On the characterization of nuclear many-body correlations in the ab initio approach

Alberto Scalesi

To cite this version:

Alberto Scalesi. On the characterization of nuclear many-body correlations in the ab initio approach. Nuclear Theory [nucl-th]. Université Paris-Saclay, 2024. English. NNT : 2024UPASP070 . tel-04727415

HAL Id: tel-04727415
https://theses.hal.science/tel-04727415v1

Submitted on 9 Oct 2024

Thèse de doctorat

NNT: 2024UPASP070

On the characterization of nuclear many-body correlations in the *ab initio* approach

De la caractérisation des corrélations à N corps dans l'approche ab initio nucléaire

Thèse de doctorat de l'université Paris-Saclay

École doctorale n° 576
Particules, Hadrons, Énergie et Noyau : Instrumentation, Imagerie, Cosmos et Simulation (PHENIICS)
Spécialité de doctorat : Physique nucléaire
Référent : Faculté des sciences d'Orsay

Thèse préparée au **Département de physique nucléaire (Université Paris-Saclay, CEA)**, sous la direction de **Vittorio SOMÀ**, Ingénieur de recherche, la co-direction de **Thomas DUGUET**, Ingénieur de recherche et le co-encadrement de **Mikael FROSINI**, Ingénieur de recherche

Thèse soutenue à Paris-Saclay, le 17 septembre 2024, par

Alberto SCALESI

Composition du jury

Membres du jury avec voix délibérative

Gaute HAGEN Professeur, Laboratoire National d'Oak Ridge	Président & Rapporteur
Andreas EKSTRÖM Professeur associé (HDR equiv.), Université Technologique de Chalmers	Rapporteur & Examinateur
Karim BENNACEUR Directeur de recherche, IP2I, Lyon	Examinateur
Angela GARGANO Directrice de recherche, Institut National de Physique Nucléaire, Naples	Examinatrice

université
PARIS-SACLAY

ÉCOLE DOCTORALE
Particules, hadrons, énergie et noyau :
instrumentation, imagerie, cosmos
et simulation (PHENIICS)

Titre: De la caractérisation des corrélations à N corps dans l'approche *ab initio* nucléaire

Mots clés: méthodes *ab initio*, structure nucléaire, problème quantique à N corps

Résumé: La branche *ab initio* de la théorie de la structure nucléaire s'est traditionnellement concentrée sur l'étude des noyaux de masse légère à moyenne et des systèmes principalement sphériques. Les développements actuels visent à étendre cette approche aux noyaux de masse élevée et aux systèmes à double couche ouverte. L'étude de ces systèmes représente un défi qualitatif et quantitatif. Par conséquent, différentes stratégies doivent être conçues pour capturer efficacement les corrélations dominantes qui ont le plus d'impact sur les observables d'intérêt. Bien qu'il existe en principe des méthodes exactes pour résoudre l'équation de Schrödinger non relativiste pour un hamiltonien nucléaire donné, les limitations pratiques des simulations numériques rendent un tel espoir vain pour la plupart des isotopes. Cela nécessite une hiérarchisation des corrélations mises en jeu dans les différents systèmes nucléaires. La plupart des techniques *ab initio* reposent sur un calcul initial de type 'champ moyen', généralement effectué via la méthode Hartree-Fock (HF), qui fournit un état de référence contenant la majeure partie des corrélations contribuant aux propriétés nucléaires globales. Lorsqu'on s'attaque à des systèmes à couche ouverte, il s'est avéré particulièrement pratique de briser les symétries du Hamiltonien au niveau du champ moyen pour inclure efficacement les corrélations statiques apparaissant dans les noyaux superfluides (via la théorie HF-Bogoliubov, HFB) ou déformés (via la méthode HF déformée, dHF). Le présent travail contribue à cette ligne de recherche en proposant et en explorant de nouvelles techniques à N-corps applicables à tous les systèmes nucléaires exploitant cette idée de brisure de symétrie,

La technique *ab initio* la plus simple applicable au-delà du champ moyen est la théorie des perturbations à N-corps. Le premier résultat de ce travail est la démonstration qu'une théorie des perturbations incorporant la brisure de la symétrie de rotation (dBMBPT) et employant des interactions nucléaires modernes peut déjà décrire qualitativement les principales observables nucléaires, telles que l'énergie de liaison et le rayon de l'état fondamental. Étant donné que la théorie des perturbations constitue une méthode peu coûteuse permettant d'effectuer des études systématiques sur large partie de la carte des noyaux, une partie du présent travail est consacrée à ouvrir la voie à de tels calculs à grande échelle.

Afin de pousser les calculs à N-corps vers une plus grande précision, une nouvelle technique *ab initio* est ensuite introduite, à savoir la méthode des fonctions de Green-Dyson autoconsistantes déformées (dDSCGF). Cette approche nonperturbative (c'est-à-dire sommant un nombre infini de contributions perturbatives) permet de calculer une grande variété de quantités utiles, à la fois pour l'état fondamental du noyau ciblé et pour les états excités des systèmes voisins. En outre, elle s'étend naturellement en direction des réactions nucléaires afin d'évaluer, par example, les potentiels optiques.

Étant donné le coût de calcul élevé des méthodes nonperturbatives à N-corps, la dernière section présente des approches possibles pour rendre ces calculs plus efficaces. En particulier, la base des orbitales naturelles est introduite et étudiée dans le contexte des systèmes déformés. Ainsi, il est prouvé que cette technique permet d'utiliser des bases beaucoup plus petites, réduisant ainsi de manière significative le coût final des simulations numériques et étendant leur domaine d'application.

En conclusion, les développements présentés dans ce travail ouvrent des voies nouvelles et prometteuses en vue de la description *ab initio* des noyaux lourds à couches ouvertes.

Title: On the characterization of nuclear many-body correlations in the *ab initio* approach
Keywords: *ab initio* methods, nuclear structure, quantum many-body problem

Abstract: The *ab initio* branch of nuclear structure theory has traditionally focused on the study of light to mid-mass nuclei and primarily spherical systems. Current developments aim at extending this focus to heavy-mass nuclei and doubly open-shell systems. The study of such systems is qualitatively and quantitatively challenging. Hence, different strategies must be designed to efficiently capture the dominant correlations that most significantly impact the observables of interest. While in principle exact methods exist to solve the non-relativistic Schrödinger equation for a given Nuclear Hamiltonian, practical limitations in numerical simulations make such an approach impossible for most isotopes. This calls for a hierarchical characterization of the main correlations at play in the various nuclear systems. Most *ab initio* techniques rely on an initial mean-field calculation, typically carried out via the Hartree-Fock (HF) method, which provide a reference state containing the principal part of the correlations contributing to bulk nuclear properties. When tackling open-shell systems, it has been proven particularly convenient to break symmetries at mean-field level to effectively include the static correlations arising in superfluid (via HF-Bogoliubov theory, HFB) or deformed nuclei (via deformed HF, dHF). The present work contributes to this research line by proposing end exploring novel symmetry-breaking many-body techniques applicable to all nuclear systems.

The simplest *ab initio* technique that can be applied on top of the mean-field is many-body perturbation theory. The first result of this work is the demonstration that symmetry-breaking perturbation theory (dBMBPT) based on state-of-the-art nuclear interactions can already qualitatively describe the main nuclear observables, such as ground-state energies and radii. Given that perturbation theory constitutes a cheap and efficient way to perform systematic studies of different nuclei across the nuclear chart, a part of the present work is dedicated to pave the way to such large-scale calculations.

In order to push many-body calculations to higher precision, a novel *ab initio* technique is then introduced, namely the deformed Dyson Self-Consistent Green's function (dDSCGF) method. Such a non-perturbative (i.e., resumming an infinite number of perturbation-theory contributions) approach allows one to compute a wide variety of quantities of interest, both for the ground state of the targeted nucleus and for excited states of neighbouring systems. In addition, it naturally bridges to nuclear reactions giving access to, e.g., the evaluation of optical potentials.

Given the high computational cost of non-perturbative many-body methods, the final section introduces possible approaches to make such calculations more efficient. In particular, the Natural Orbital basis is introduced and investigated in the context of deformed systems. Eventually, it is proven that this technique enables the use of much smaller basis sets, thus significantly decreasing the final cost of numerical simulations and enlarging their reach. All together, the developments reported in the present work open up new and promising possibilities for the *ab initio* description of heavy-mass and open-shell nuclei.

Resumé en français

La branche *ab initio* de la théorie de la structure nucléaire s'est traditionnellement concentrée sur l'étude des noyaux de masse légère à moyenne et des systèmes principalement sphériques. Les développements actuels visent à étendre cette approche aux noyaux de masse élevée et aux systèmes à double couche ouverte. L'étude de ces systèmes représente un défi qualitatif et quantitatif. Par conséquent, différentes stratégies doivent être conçues pour capturer efficacement les corrélations dominantes qui ont le plus d'impact sur les observables d'intérêt. Bien qu'il existe en principe des méthodes exactes pour résoudre l'équation de Schrödinger non relativiste pour un hamiltonien nucléaire donné, les limitations pratiques des simulations numériques rendent un tel espoir vain pour la plupart des isotopes. Cela nécessite une hiérarchisation des corrélations mises en jeu dans les différents systèmes nucléaires. La plupart des techniques *ab initio* reposent sur un calcul initial de type 'champ moyen', généralement effectué via la méthode Hartree-Fock (HF), qui fournit un état de référence contenant la majeure partie des corrélations contribuant aux propriétés nucléaires globales. Lorsqu'on s'attaque à des systèmes à couche ouverte, il s'est avéré particulièrement pratique de briser les symétries du Hamiltonien au niveau du champ moyen pour inclure efficacement les corrélations statiques apparaissant dans les noyaux superfluides (via la théorie HF-Bogoliubov, HFB) ou déformés (via la méthode HF déformée, dHF). Ces corrélations sont des corrélations à long range et contribuent à donner un caractère collectif aux nucléons dans le noyau. Elles sont commodément incluses dans les calculs théoriques au niveau du champ moyen, car si leur étude n'était abordée que dans le cadre du calcul au-delà du champ moyen, cela nécessiterait des ressources informatiques trop élevées. Le présent travail contribue à cette ligne de recherche en proposant et en explorant de nouvelles techniques à N-corps applicables à tous les systèmes nucléaires exploitant cette idée de brisure de symétrie,

La technique *ab initio* la plus simple applicable au-delà du champ moyen est la théorie des perturbations à N-corps. Le premier résultat de ce travail est la démonstration qu'une théorie des perturbations incorporant la brisure de la symétrie de rotation (dBMBPT) et employant des interactions nucléaires modernes peut déjà décrire qualitativement les principales observables nucléaires, telles que l'énergie de liaison et le rayon de l'état fondamental. Étant donné que la théorie des perturbations constitue une méthode peu coûteuse permettant d'effectuer des études systématiques sur large partie de la carte des noyaux, une partie du présent travail est consacrée à ouvrir la voie à de tels calculs à grande échelle.

Afin de pousser les calculs à N-corps vers une plus grande précision, une nouvelle technique *ab initio* est ensuite introduite, à savoir la méthode des fonctions de Green-Dyson autoconsistantes déformées (dDSCGF). Cette approche nonperturbative (c'est-à-dire sommant un nombre infini de contributions perturbatives) permet de calculer une grande variété de quantités utiles, à la fois pour l'état fondamental du noyau ciblé et pour les états excités des systèmes voisins. En outre, elle s'étend naturellement en direction des réactions nucléaires afin d'évaluer, par example, les potentiels optiques.

Étant donné le coût de calcul élevé des méthodes nonperturbatives à N-corps, la dernière section présente des approches possibles pour rendre ces calculs plus efficaces. En particulier, la base des orbitales naturelles est introduite et étudiée dans le contexte des systèmes déformés. Ainsi, il est prouvé que cette technique permet d'utiliser des bases beaucoup plus petites, réduisant ainsi de manière significative le coût final des simulations numériques et étendant leur domaine d'application.

En conclusion, les développements présentés dans ce travail ouvrent des voies nouvelles et prometteuses en vue de la description *ab initio* des noyaux lourds à couches ouvertes.

This work was supported by the European Union's Horizon 2020 research and innovation program under grant agreement No 800945 – NUMERICS – H2020-MSCA-COFUND-2017.

Acknowledgements

If these three years have flown by, it is also thanks to the people who have been by my side. First and foremost, thank you to my family for all the support that has allowed me to be here.

Second, I must thank the people who started it all: thank you to Enrico, Xavier, Gianluca and Carlo for introducing me to this field and for always being patient in your explanations. If I felt immediately welcomed into the research community, it is mostly thanks to you.

My team of supervisors has been the best I could have hoped for. Thanks to Vittorio for putting up with all my requests and easing all my worries. Many times I pretended to go to the hallway to fill my water bottle, but it was just an excuse to see if you were in the office so I could ask my questions, and you were always ready to help. Your calmness has been an inspiration. Thanks to Thomas for teaching me the rigor and technical foundations necessary in the field. And thank you for all the great insights raised during the countless lunches and discussions we have had. Every time you brought up a new discussion, I felt enriched. Thanks Mikael for the trust you placed in me by allowing me to use the HFB code. Thanks also for all the technical discussions we've had about codes. They have been very stimulating, and I hope to continue having them in the future.

Thanks to the members of my jury: G. Hagen, A. Ekström (see you soon!), K. Bennaceur and A. Gargano. Thanks for reading the manuscript and agreeing to be part of my defense panel.

Thanks to my flatmate Alberto for sharing these three years with me. If they have been lighter, it is also due to our mutual venting sessions that allowed us to get through these years with more peace of mind.

Thanks to Peter for always being by my side and for gifting me the monkey: it will always be with me.

Thanks to all the friends who participated in the countless D&D and bouldering sessions: it was fun!

Thanks to Andrea L., Benjamin, Pepijn, Gianluca, Lars, Andrea P., Kevin, Antoine, Zhibo, Xiang, Qiuping and the other PhD students and PostDocs that I have met over the years. You have created an environment in which I felt comfortable and allowed me to spend these three years with more ease.

And of course, a big thank you to all my friends from Italy, who have always supported me despite my limited presence in the area.

List of Acronyms

χEFT	Chiral Effective Field Theory
HF	Hartree-Fock
dHF	Axially-deformed Hartree-Fock
HFB	Hartree-Fock-Bogoliubov
dHFB	Axially-deformed Hartree-Fock-Bogoliubov
MBPT	Many-body perturbation theory
dMBPT	Axially-deformed Many-body perturbation theory
BMBPT	Bogoliubov Many-body perturbation theory
sBMBPT	Spherical Bogoliubov Many-body perturbation theory
dBMBPT	Axially-deformed Bogoliubov Many-body perturbation theory
CC	Coupled-cluster
CCD	Coupled-cluster doubles
sBCCSD	Spherical coupled-cluster singles-doubles
dCC	Axially-deformed coupled-cluster
dCCSD	Axially-deformed coupled-cluster singles-doubles
dCCSDT	Axially-deformed coupled-cluster singles-doubles-triples
SRG	Similarity renormalization group
IMSRG	In-medium similarity renormalization group
VS-IMSRG	Valence-space in-medium similarity renormalization group
EFA	Equal-filling approximation
ZP	Zero-pairing
EDF	Energy density functional
SCGF	Self-consistent Green's function
sGSCGF	Spherical Gorkov Self-consistent Green's function
dDSCGF	Axially-deformed Dyson Self-consistent Green's function

PGCM	Projected Generator Coordinate Method
sHO	Spherical Harmonic Oscillator
ME	Matrix Element
NAT	Natural Orbital
BAR	Baranger
IT	Importance Truncation
1B	One-body
2B	Two-body
3B	Three-body

Contents

Introduction

Atomic nuclei are complex many-body systems characterized by the interplay of three of the four fundamental forces: the strong, the weak and the electromagnetic interactions. The rich diversity of phenomena characterizing nuclei makes the development of a unique theory for their description far from being accomplished nowadays. In nuclear structure studies, static properties of atomic nuclei at low energies are meaningfully investigated using point-like nucleons displaying a non-relativisitc kinematic as degrees of freedom, i.e. solving the time-independent non-relativistic A-nucleon Schrödinger equation

$$H |\Psi_k^A\rangle = E_k^A |\Psi_k^A\rangle , \tag{0.1}$$

whose eigenvalues deliver the A-body energies E_k^A. The obstacles making such an *ab initio* description of nuclear systems very challenging are encapsulated by the two main elements entering such a A-body Schrödinger equation.

The first is the input Hamiltonian operator H composed by an easy-to-handle kinetic energy term and a hard-to-handle interaction term, the latter being itself decomposed into two-, three- and in general up to A-body contributions. Historically, many approaches have been designed to model the interactions entering the Hamiltonian. The current paradigm allowing to do so in a systematic manner while anchoring the construction into the underlying gauge theory of the strong force, i.e. quantum chromodynamics (QCD), is given by a set of Effective Field Theories (EFT) focusing on different energy scales [1, 2]. For what concerns the low-energy domain, Chiral EFT (χEFT) [3] delivers the state-of-the-art scheme to describe atomic nuclei even though some challenges remain to be overcome within this framework, in particular the non-renormalizable character of currently available χEFT interactions based on the traditional Weinberg power-counting [4].

The second element concerns the output many-body wave function $|\Psi_k^A\rangle$. While it can be determined exactly in few-body systems, the exponential growth of the A-body Hilbert space with particle number quickly calls for systematic approximations. The goal of approximations performed within the frame of so-called expansion many-body methods [5] is to include correlations contributing the most to nuclear observables at low-orders in the expansion. In turn, this allows reducing the scaling to a low polynomial cost, which can be handled by modern supercomputers. However, those most relevant correlations differ in nature depending on the nucleus under consideration. In order to characterize them, it is first necessary to introduce a nuclear classification based on the naïve occupation of single-nucleon energy shells emerging from a spherical mean-field approximation.

- *Doubly closed-shell systems*: nuclei for which the highest occupied neutron and proton energy shells are full such that a non-zero energy gap separate them from the unoccupied shells. These nuclei were the first to be investigated via expansion methods based on a spherically-symmetric Slater determinant reference state and are dominated by so-called dynamical correlations associated with a large number of subleading n-particle/n-hole excitations on top of the reference state.

- *Open-shell systems*: nuclei for which the neutron and/or the proton highest occupied energy shell is only partially occupied. These nuclei constitute around 90% of the nuclear chart [6]. The absence of an energy gap between the last occupied and first empty states in the reference state induces the appearance of strong collective, i.e. static, correlations that cannot be incorporated in a controlled fashion by expanding the exact solution via particle-hole excitations on top of the degenerate reference state. Handling such static correlations requires either the use of multi-reference expansion techniques [7, 8] or the reference state to break $U(1)$ ($SU(2)$) symmetry associated with particle number (angular momentum) conservation in singly (doubly) open-shell nuclei [6, 9]. Once static correlations have been taken care of at the level of the (multi) reference state, dynamical correlations can be safely captured on top via an expansion expressed in terms of elementary excitations on the reference state.

While the definition of the Hamiltonian and the determination of the many-body solutions have so far been presented as two separate problems, they happen to be strongly entangled. The characteristics, i.e. intrinsic resolution scale and highest interaction rank, of the Hamiltonian employed to solve the A-body Schrödinger equation have a strong impact on the applicability of a given many-body expansion method. Indeed, the solution obtained for a given nucleus is satisfactory only when a convergence is reached with respect to the

- *Truncation of the A-body Hilbert space*: the size of the A-body Hilbert space limits numerical calculations in terms of (i) memory required to store elementary objects and (ii) CPU time required for the calculations. The size of the A-body Hilbert space needed to converge a calculation strongly depends on the nature of the Hamiltonian and increases with the nuclear mass. A chapter of this manuscript is dedicated to the development of a method to limit such a numerical bottleneck.

- *Truncation of the many-body expansion*: the vast majority of the calculations shown in this manuscript are based on a preliminary mean-field calculation delivering a reference state already capturing crucial static correlations by breaking $U(1)$ and/or $SU(2)$ symmetries. The subsequent beyond-mean field expansion dedicated to efficiently including dynamical correlations at low orders is either realized via a simple and inexpensive many-body perturbation theory or via more elaborate and accurate non-perturbative techniques. The choice of the approach strongly depends on the characteristics of the Hamiltonian and, to a lesser extent, on the system under consideration. This works as a motivation for the development of the novel deformed Dyson Self-Consistent Green's Function (dDSCGF) method introduced in this work.

Only nuclear Hamiltonians making possible, for a large range of nuclei, to reach convergence with respect to the above two parameters based on available modern supercomputers are of interest to many-body practitioners. Similarity renormalization group (SRG) trasnsformations [10] introduced two decades ago to 'soften' χEFT Hamiltonians via a decoupling of low and high momenta have been instrumental to construct such operators.

This work advances the state-of-the-art in different directions: first of all, it demonstrates comprehensively that breaking $SU(2)$ symmetry is necessary for studying doubly open-shell systems while maintaining polynomial computational cost. Second, a significant portion of the manuscript is dedicated to developing a new $SU(2)$ non-perturbative method. Finally, it examines the role of techniques to mitigate the computational cost of beyond mean-field calculations.

The manuscript is organized as follows: Chapters 1 and 2 introduce the theoretical background necessary to understand the basic ingredients of the manuscript. Chapter 3 pedagogically displays how correlations impacting nuclear binding energies of closed and open-shell nuclei can be efficiently included in *ab initio* expansion methods based on symmetry-breaking reference states. Chapter 4 works as an intermezzo presenting an application of deformed many-body perturbation theory to address state-of-the-art experimental measurements. Chapter 5 introduces the novel dDSCGF *ab initio* method dedicated to the accurate description of doubly open-shell nuclei whereas Chapter 6 analyzes the use of the deformed natural basis to alleviate the numerical cost of such calculations. Chapter 7 focuses on the threefold puzzle characterizing Calcium isotopes between the $N = 40$ and $N = 48$ neutron shell closures, highlighting the solutions to the first two parts while leaving the third one as an unsolved mystery. Finally, on top of the partial conclusions that can be found at the end of each chapter, some overall conclusions are drawn. The manuscript ends with a set of Appendices including details that have not been incorporated in the text for the sake of readability.

Chapter 1.

Prelude – Why break symmetries?

Ideally, Eq. (0.1) should be solved exactly for a given input Hamiltonian H. In practice, the intrinsic exponential scaling of such a task with the size of the system strongly limits the applicability range of exact methods to few-body systems. In order to extend the reach of many-body techniques to higher masses, correlation-expansion approaches have been developed in the last two decades to provide improvable approximations to the exact many-body wave function at polynomial cost n_B^p, where n_B represents the number of states included in the basis of the one-body Hilbert space $\mathcal{H}_1$ and p is fixed by the order at which the many-body expansion is truncated. Such methods build dynamical correlations on top of a suitably chosen *reference state* via set of elementary excitations, as depicted in Fig. 1.1 for a spherically-symmetric Slater determinant reference state.

Different correlations-expansion methods exist, i.e. many-body perturbation theory (MBPT) [11], coupled-cluster (CC) [12], in-medium similarity renormalization group (IMSRG) [13] and self-consistent Green's function (SCGF) [14] approaches. While these methods based on a spherically-symmetric Slater determinant reference state have delivered a successful description of doubly closed-shell nuclei, difficulties related to the choice of that reference state arise when addressing open-shell systems. In order to intuitively understand why such a version of expansion methods breaks down for in open-shell nuclei, consider the analytical expression of the second-order contribution to the energy in spherical MBPT (sMBPT):

$$\Delta E^{(2)} = -\frac{1}{4} \sum_{\alpha\beta\lambda\mu} \frac{\langle \alpha\beta | H_1 | \lambda\mu \rangle \langle \lambda\mu | H_1 | \alpha\beta \rangle}{\varepsilon_\alpha + \varepsilon_\beta - \varepsilon_\lambda - \varepsilon_\mu}, \tag{1.1}$$

where λ and μ (α and β) denote occupied, i.e. 'hole', (unoccupied, i.e. 'particle') single-particle states in the spherically-symmetric reference Slater determinant whereas H_1 is the so-called residual part associated with the appropriate partitioning of the Hamiltonian $H = H_0 + H_1$. When an open-shell nucleus is considered, the energies of the last

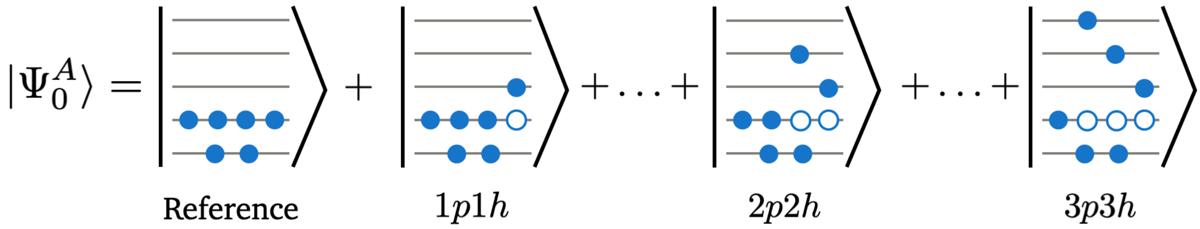

Figure 1.1. Schematic representation of the particle-hole expansion performed by correlation-expansion methods on top of a reference state.

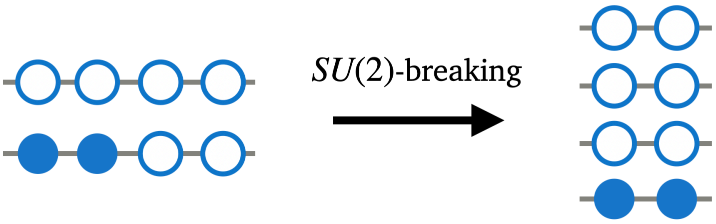

Figure 1.2. Schematic representation of the lift of the particle-hole degeneracy occurring in an open shell via the breaking of $SU(2)$ symmetry.

occupied and first unoccupied single-particle states are equal as schematically represented on the left-hand side of Fig. 1.2. This characteristic leads to a problematic degeneracy of the spherically-symmetric Slater determinant reference state with respect to elementary particle-hole excitations, eventually translating into a null denominator in Eq. (1.1).

In order to extend the applicability of such methods to open-shell systems, a solution, first employed in Gorkov self-consistent Green's function calculations of singly open-shell nuclei[1] [16, 17], corresponds to allowing the reference state to break suitable symmetries of the Hamiltonian characterized by the symmetry group G_{Ham} inherited from QCD. There are essentially two symmetries that can be usefully broken by the reference state.

- *Global-gauge symmetry* $U(1)$[2] associated with particle-number conservation. Its breaking requires the use of more general Bogoliubov reference states and corresponds to the emergence of strong static correlations associated with the superfluid character of neutrons or (and) protons in singly (doubly) open-shell nuclei.
- *Rotational symmetry* $SU(2)$ associated with angular-momentum conservation. Its breaking requires the use of spatially deformed Slater determinant or Bogoliubov reference states and signal the emergence of strong quadrupolar correlations associated with the rotational character of doubly open-shell nuclei.

In both cases, the breaking of the symmetry allows the reference state to capture static correlations at mean-field cost[3] and further lifts its degeneracy with respect to elementary excitations, as schematically shown in Fig. 1.2 for a deformed Slater determinant reference state, ultimately avoiding to have any null denominator in Eq. (1.1).

Eventually, symmetries should be restored in order to properly reflect the fundamental symmetries of the underlying Hamiltonian. Symmetry restorations techniques have been developed so far in the case of CC and MBPT [18, 19] and constitute a challenge to be numerically implemented given their significant computational cost.

---

[1] While this constituted the first such implementation for *ab initio* correlation-expansion methods, symmetry-breaking concepts have been employed long before in nuclear structure theory, especially in the context of energy density functionals [15].

[2] Since two isotopic species are at play in atomic nuclei, $U(1)$ is here used as a shorthand notation for global-gauge symmetry with respect to both proton and neutron number, i.e. $U(1)_N \otimes U(1)_Z$.

[3] Such static correlations could only be resummed at much higher costs via a particle-hole like expansion.

Chapter 2.

Theoretical framework – Bogoliubov, or on the pairing

2.1. The nuclear Hamiltonian

2.1.1. Operator structure

In *ab initio*, the nuclear Hamiltonian in the intrinsic frame is typically truncated up three-body forces and reads

$$H = T + V + W, \tag{2.1}$$

where T represents the intrinsic kinetic energy whereas V and W represent respectively two- and three-body interactions. Representing in second quantization the chosen basis of the one-body Hilbert space $\mathcal{H}_1$ by two sets of anti-commuting creation and annihilation operators, $c^\dagger_\alpha$ and c_α, satisfying the anticommutation rules

$$\{c_\alpha, c_\beta\} = 0\,, \tag{2.2a}$$
$$\{c^\dagger_\alpha, c^\dagger_\beta\} = 0\,, \tag{2.2b}$$
$$\{c_\alpha, c^\dagger_\beta\} = \delta_{\alpha\beta}\,, \tag{2.2c}$$

Eq. (2.1) can be re-written as

$$\begin{aligned} H = {} & \sum_{\alpha\delta} \left(1 - \frac{1}{A}\right) t^{lab}_{\alpha\delta} c^\dagger_\alpha c_\delta \\ & + \frac{1}{(2!)^2} \sum_{\alpha\beta\delta\varepsilon} (\bar{v}^{NN}_{\alpha\beta\delta\varepsilon} - \bar{t}^{cm}_{\alpha\beta\delta\varepsilon}) c^\dagger_\alpha c^\dagger_\beta c_\varepsilon c_\delta \\ & + \frac{1}{(3!)^2} \sum_{\alpha\beta\gamma\delta\varepsilon\varphi} \bar{w}_{\alpha\beta\gamma\delta\varepsilon\varphi} c^\dagger_\alpha c^\dagger_\beta c^\dagger_\gamma c_\varphi c_\varepsilon c_\delta \,. \end{aligned} \tag{2.3}$$

Here $t^{lab}_{\alpha\delta}$ represents the one-body (1B) matrix element of the kinetic energy in the laboratory frame and $\bar{t}^{cm}_{\alpha\beta\delta\varepsilon}$ the two-body (2B) matrix element for the contribution of the center-of-mass kinetic energy that is subtracted from the Hamiltonian in the laboratory frame

$$T^{cm} = \frac{1}{m_N A} \sum_{i<j} \vec{p}_i \cdot \vec{p}_j, \tag{2.4}$$

m_N and A being respectively the mass of the nucleon and the particle-number operator [20]. In Eq. 2.3, two-body (three-body [3B]) matrix elements are anti-symmetric with respect to the exchange of the first-two and last-two (any two among the first-three and last-three) indices.

2.1.2. χEFT Hamiltonians

Calculations in the present work have been carried out employing different types of χEFT Hamiltonians:

- NNLO$_{\text{sat}}$ (bare) [21], which has been proven able to accurately reproduce energies and charge radii up to mid-mass nuclei;
- NNLO$_{\text{sat}}$ (2.4) and NNLO$_{\text{sat}}$ (2.0) [22], which constitute the SRG-evolved version of the NNLO$_{\text{sat}}$ (bare) bare interaction, respectively down to the momentum scales $2.4\,\text{fm}^{-1}$ and $2.0\,\text{fm}^{-1}$;
- ΔNNLO$_{\text{go}}$ (394) and ΔNNLO$_{\text{go}}$ (450) [23], which explicitly include Δ isobar degrees of freedom in the fit of the LECs;
- EM 1.8/2.0 [24], a soft interaction that allows to accurately predict binding energies but largely underestimates charge radii, based on the two-body potential from [25];
- NN+3N(lnl) [26], whose two-body part is given by [25] similarly to the case of the EM 1.8/2.0 interaction, and includes a combination of local and non-local regulators;
- NN(N^{4}LO)+3N(lnl)E7 [27], analogous to the NN+3N(lnl) interaction but with a 2-body part truncated at the fifth order (N^{4}LO) in the chiral expansion and the addition of a subleading term that enhances the strength of the spin-orbit interaction in the three-body sector.

The main parameters that characterize different interactions are:

- the value of the Low-Energy Constants (LECs) employed in the theory, typically fitted on few-body and many-body systems;
- the value of the cutoff employed in the χEFT interactions;
- if the interaction is SRG-evolved, the value of the flow parameter;
- the order truncation in the χEFT expansion (LO, NLO, NNLO, N^{3}LO, ...).

When a χEFT Hamiltonian is employed in a many-body calculation, such parameters influence the rate of convergence with respect to the size of the model space and the many-body expansion and the values of the computed observables.

2.1.3. Spherical harmonic oscillator matrix elements

Ab initio applications require the representation of operators on a single-particle basis. The most notable and long-time employed single-particle basis in nuclear structure is the spherical Harmonic Oscillator (sHO) basis. Different reasons lay behind its success: first of all, the sHO potential is rather optimal to describe well-bound closed-shell nuclei [28]. Second, the specific analytical structure of sHO wave functions allows for various simplifications that are useful to expand operators relevant for nuclear structure studies. Finally, it allows for an exact separation of intrinsic and center-of-mass motions [29], which justifies the application of Eq. (2.3) for the calculation of the MEs of the intrinsic Hamiltonian.

Greek letters are used in this manuscript to label a set of five quantum numbers for the sHO basis:

$$\alpha \equiv \{n_\alpha, j_\alpha, m_\alpha, l_\alpha, t_\alpha\} = \{n_\alpha, j_\alpha, m_\alpha, \pi_\alpha, t_\alpha\}, \tag{2.5}$$

$e_{\max}$	n_B
2	40
4	140
6	336
8	660
10	1144
12	1820
14	2720

Table 2.1. Number of sHO one-body basis states n_B for a given $e_{\max}$ truncation. For each isospin, the number of sHO one-body basis states is $n_B^P = n_B^N \equiv n_B/2$.

where n_α indicates the principal quantum number, j_α the total angular momentum, m_α the projection of the total angular momentum along the quantization axis, l_α the orbital angular momentum, π_α the parity ($\pi_a = (-1)^{l_\alpha}$) and t_α the projection of the isospin along the quantization axis. A bar over Greek letters indicates the definition

$$\bar{\alpha} \equiv \{n_\alpha, j_\alpha, -m_\alpha, l_\alpha, t_\alpha\} = \{n_\alpha, j_\alpha, -m_\alpha, \pi_\alpha, t_\alpha\}. \tag{2.6}$$

Quantum numbers n_α and l_α allow to order single-particle sHO states according to their energies

$$E^{\text{sHO}} = \hbar\omega\left(2n + l + \frac{3}{2}\right). \tag{2.7}$$

Whenever adding a one-body spin-orbit potential to the sHO, energy levels with $l > 0$ are further split into two subshells differing by the quantum numbers $j = l \pm 1/2$ and coined as spin-orbit partners. Such ordering of single-particle states is depicted in Fig. A.1 from App. A and it is referred to as the Bohr-Mottelson shell model.

The dimension n_B of the sHO basis, i.e. the range of the index α, is set by selecting neutron and proton states according to an $e_{\max} \equiv 2n_\alpha + l_\alpha$ truncation. The values of n_B corresponding to $2 \leq e_{\max} \leq 14$ are displayed in Tab. 2.1. Furthermore, an additional truncation typically characterizes three-body matrix elements and is given by the parameter

$$e_{3\max} \equiv 2n_\alpha + l_\alpha + 2n_\beta + l_\beta + 2n_\gamma + l_\gamma. \tag{2.8}$$

The spatial extension of sHO wave functions can be tuned via the choice of the frequency $\hbar\omega$ of the harmonic oscillator potential[1]. Even if *ab initio* calculations become independent of that choice when a large enough $e_{\max}$ is employed, a particular value of $\hbar\omega$ can help optimize the convergence of the calculation for a given $e_{\max}$. For any choice of the oscillator frequency, though, all sHO basis states display a wrong asymptotic behavior at large distances, i.e. they fall off as Gaussian functions, which makes it difficult to reproduce the exponential tail of the one-nucleon density distribution.

Spherical harmonic oscillator MEs of two- and three-body interactions employed for the calculations presented in this manuscript have been produced in different ways:

---

[1] In the present work, following the typical approach in *ab initio*, $\hbar\omega$ is chosen to deliver the lowest value of ground-state energy for each studied case. While this choice is well-motivated for mean-field calculations due to the variational nature of the problem, its application to beyond mean-field calculations is questionable. Nevertheless, since beyond mean-field calculations generally show regular convergence to the lowest values of the ground-state energy as the size of the model space increases or as the single-particle wave functions become better suited to describe the nucleus, this criterion for choosing $\hbar\omega$ is also applied to such calculations.

- NNLO_{sat} (bare), $\Delta\text{NNLO}_{\text{go}}$ (394), $\Delta\text{NNLO}_{\text{go}}$ (450) and EM 1.8/2.0 MEs up to $e_{3\text{max}} = 16$ have been generated with the `NuHamil` code [30].
- EM 1.8/2.0 MEs at $e_{3\text{max}} = 18$ have been generated by H. Hergert.
- NNLO_{sat} (2.4), NNLO_{sat} (2.0), NN+3N(lnl) and NN(N^{4}LO)+3N(lnl)E7 MEs have been produced by P. Navrátil.
- Non-local three-body momentum-space MEs employed for the generation of sHO MEs with the `NuHamil` code have been computed by K. Hebeler [31].

Center-of-mass kinetic energy corrections appearing in Eq. (2.3) have been calculated according to the equations displayed in Ref. [32].

2.1.4. Two-body rank reduction of three-body operators

The direct utilization of the MEs of the three-body interaction W in Eq. (2.1) in correlation-expansion methods requires the storage and manipulation of six-indexes tensors. Even exploiting anti-symmetry relations, such an object remains too complicated to explicitly handle in terms of the memory required to store it and the computational time necessary for its manipulation. However, taking into account three-body operators remains possible at the level of mean-field calculations. Such upside can be exploited to perform the so-called normal-ordered two-body (NO2B) approximation, that allows to capture the relevant effects of three-body interactions while working with two-body operators [33, 34]. The NO2B approximation relies on the normal-ordering of the Hamiltonian with respect to a Slater determinant through Wick's theorem and can be applied to Slater determinants that are characterized by the same symmetries as the underlying Hamiltonian.

Nevertheless, the direct extension of such a procedure to expansion methods based on a symmetry-breaking reference state would lead to an approximate Hamiltonian with lower symmetries than the full Hamiltonian. This is to be avoided in order to attribute the symmetry breaking to the sole expansion method used and not to the rank-reduction step of three-nucleon interactions. In order to overcome this problem, a new technique has been recently proposed [35]. Such approach allows to effectively approximate an n-body operator by rank-reducing it to a sum of terms of lower rank (up to $k < n$) via a convolution with a symmetry-invariant one-body density matrix ρ that can originate from any symmetry-conserving auxiliary many-body state.

For the present manuscript, the interest is in reducing ($n = 3$)-body operators into a sum of effective ($k = 0, 1, 2$)-body ones. As proven in Ref. [35], this can be accomplished by defining the three tensors

$$h^{(0)}[\rho] \equiv \frac{1}{3!} \sum_{\alpha\beta\gamma\delta\varepsilon\varphi} \bar{w}_{\alpha\beta\gamma\delta\varepsilon\varphi} \rho_{\varphi\gamma} \rho_{\varepsilon\beta} \rho_{\delta\alpha}, \tag{2.9a}$$

$$h^{(1)}_{\alpha\delta}[\rho] \equiv \left(1 - \frac{1}{A}\right) t^{lab}_{\alpha\delta} - \frac{1}{2!} \sum_{\beta\gamma\varepsilon\varphi} \bar{w}_{\alpha\beta\gamma\delta\varepsilon\varphi} \rho_{\varphi\gamma} \rho_{\varepsilon\beta}, \tag{2.9b}$$

$$h^{(2)}_{\alpha\beta\delta\varepsilon}[\rho] \equiv (\bar{v}^{NN}_{\alpha\beta\delta\varepsilon} - \bar{t}^{cm}_{\alpha\beta\delta\varepsilon}) + \sum_{\gamma\varphi} \bar{w}_{\alpha\beta\gamma\delta\varepsilon\varphi} \rho_{\varphi\gamma}, \tag{2.9c}$$

entering the rank-reduced effective 2B Hamiltonian

$$H^{2\text{B}}[\rho] = h^{(0)}[\rho] + \frac{1}{(1!)^2} \sum_{\alpha\delta} h^{(1)}_{\alpha\delta}[\rho] c^\dagger_\alpha c_\delta + \frac{1}{(2!)^2} \sum_{\alpha\beta\delta\varepsilon} h^{(2)}_{\alpha\beta\delta\varepsilon}[\rho] c^\dagger_\alpha c^\dagger_\beta c_\varepsilon c_\delta. \tag{2.10}$$

Symmetry-breaking calculations presented in this manuscript are based on the effective 2B Hamiltonian in Eq. (2.10). The one-body density matrix ρ employed is the normal density matrix of a spherical Hartree-Fock-Bogoliubov (HFB) calculation [35].

For simplicity of notation, in the following $h^{(0)}$ will be used to denote the 0-body part of the rank-reduced Hamiltonian, while $t_{\alpha\delta} \equiv h^{(1)}_{\alpha\delta}$ and $\bar{v}_{\alpha\beta\delta\varepsilon} \equiv h^{(2)}_{\alpha\beta\delta\varepsilon}$ will denote respectively the matrix elements of the 1- and 2-body parts.

2.2. Bogoliubov algebra

Let us consider the set $\{\beta_{\kappa_1}, \beta^\dagger_{\kappa_2}\}$ of so-called *quasiparticle* creation and annihilation operators obeying the anti-commutation rules

$$\{\beta_{\kappa_1}, \beta_{\kappa_2}\} = 0\,, \tag{2.11a}$$
$$\{\beta^\dagger_{\kappa_1}, \beta^\dagger_{\kappa_2}\} = 0\,, \tag{2.11b}$$
$$\{\beta_{\kappa_1}, \beta^\dagger_{\kappa_2}\} = \delta_{\kappa_1\kappa_2}\,, \tag{2.11c}$$

and related to the set of creation and annihilation operators introduced in Eq. (2.2) through the *Bogoliubov transformation* [36]

$$\beta_\kappa \equiv \sum_\lambda U^*_{\lambda\kappa} c_\lambda + V^*_{\lambda\kappa} c^\dagger_\lambda\,, \tag{2.12a}$$
$$\beta^\dagger_\kappa \equiv \sum_\lambda V_{\lambda\kappa} c_\lambda + U_{\lambda\kappa} c^\dagger_\lambda\,, \tag{2.12b}$$

or equivalently in matrix form

$$\begin{pmatrix} \beta \\ \beta^\dagger \end{pmatrix} \equiv \mathcal{W}^\dagger \begin{pmatrix} c \\ c^\dagger \end{pmatrix}, \tag{2.13}$$

where the Bogoliubov matrix $\mathcal{W}$ was introduced according to

$$\mathcal{W} = \begin{pmatrix} U & V^* \\ V & U^* \end{pmatrix}. \tag{2.14}$$

Equations (2.11) impose that $\mathcal{W}$ is a unitary matrix

$$\mathcal{W}^\dagger \mathcal{W} = \mathcal{W}\mathcal{W}^\dagger = I\,, \tag{2.15}$$

the first equality leading to

$$U^\dagger U + V^\dagger V = 1\,, \tag{2.16a}$$
$$V^T U + U^T V = 0\,, \tag{2.16b}$$
$$U U^\dagger + V^* V^T = 1\,, \tag{2.16c}$$
$$V U^\dagger + U^* V^T = 0\,, \tag{2.16d}$$

and the second one to equivalent identities.

The Bogoliubov product state is defined (up to a phase) as the normalized vacuum for the set of quasiparticle operators defined in Eqs. (2.11):

$$\beta_\kappa \left|\Phi\right\rangle = 0 \qquad \forall\kappa\,. \tag{2.17}$$

A possible explicit representation of the Bogoliubov vacuum is given by

$$|\Phi\rangle \equiv \mathcal{C} \prod_{\kappa} \beta_{\kappa} |0\rangle \,, \tag{2.18}$$

where $\mathcal{C}$ denotes a complex normalization constant ensuring that $\langle\Phi|\Phi\rangle = 1$. It is easy to verify that $|\Phi\rangle$ is not an eigenstate of the particle-number operator A and therefore breaks $U(1)$ gobal-gauge symmetry[2].

The Bogoliubov vacuum can be equivalently characterized by the associated one-body normal and anomalous density matrices respectively defined as

$$\rho_{\lambda_1\lambda_2} \equiv \frac{\langle\Phi|c^{\dagger}_{\lambda_2} c_{\lambda_1}|\Phi\rangle}{\langle\Phi|\Phi\rangle}, \tag{2.19a}$$

$$\kappa_{\lambda_1\lambda_2} \equiv \frac{\langle\Phi|c_{\lambda_2} c_{\lambda_1}|\Phi\rangle}{\langle\Phi|\Phi\rangle}, \tag{2.19b}$$

and possibly rewritten in matrix form in terms of the two matrices making up the Bogoliubov transformation

$$\rho = V^* V^T, \tag{2.20a}$$

$$\kappa = V^* U^T = -U V^{\dagger}. \tag{2.20b}$$

Exploiting fermionic anti-commutation relations, is it easy to prove that ρ and κ are respectively hermitian ($\rho^{\dagger} = \rho$) and skew-symmetric ($\kappa^T = -\kappa$), i.e.

$$\rho_{\mu\nu} = \rho^*_{\mu\nu} \,, \tag{2.21a}$$

$$\kappa_{\nu\mu} = -\kappa_{\mu\nu} \,. \tag{2.21b}$$

Finally, Eqs. (2.19a) and (2.19b) can be combined to define the *generalized density matrix*

$$\mathcal{R} \equiv \begin{pmatrix} \rho & \kappa \\ -\kappa^* & 1-\rho^* \end{pmatrix}, \tag{2.22}$$

which can be proven to be hermitian ($\mathcal{R}^{\dagger} = \mathcal{R}$), idempotent ($\mathcal{R}^2 = \mathcal{R}$) and diagonal in the quasiparticle basis with eigenvalues 0 and 1

$$\mathcal{W}^{\dagger} \mathcal{R} \mathcal{W} = \begin{pmatrix} 0 & 0 \\ 0 & 1 \end{pmatrix}. \tag{2.23}$$

2.3. The Hartree-Fock-Bogoliubov equations

The mean-field HFB approximation constitutes the typical approach delivering the reference Bogoliubov state, already incorporating pairing correlations, around which the exact solution will be expanded later on using a specific expansion method of choice. In such an approach, nucleons are represented as non-interacting quasiparticles moving in a self-consistent mean-field potential. Across the manifold of Bogoliubov vacua $|\Phi\rangle$, the best mean-field approximation to the ground-state of the system is selected by employing the Ritz variational principle

$$\delta \frac{\langle\Phi|H|\Phi\rangle}{\langle\Phi|\Phi\rangle} = 0 \,. \tag{2.24}$$

---

[2] While this is true in general, in the limit in which the Bogoliubov vacuum reduces to a Slater determinant (see the discussion in Sec. 2.3.1) $U(1)$ symmetry is not broken.

Since the Bogoliubov vacuum does not carry a well defined number of particles, the requirement that the average number of particles is equal to the number of particles of the system is imposed

$$\langle\Phi|A|\Phi\rangle = A\,, \tag{2.25}$$

throughout the minimization.

This is done by introducing the *grand-canonical potential* defined from the Hamiltonian H as

$$\Omega \equiv H - \lambda A\,, \tag{2.26}$$

where λ is a Lagrange multiplier, allowing to replace Eq. (2.24) via

$$\mathcal{E}[\mathcal{R}] \equiv \frac{\langle\Phi|\Omega|\Phi\rangle}{\langle\Phi|\Phi\rangle} \tag{2.27}$$

while controlling that the average particle number remains fixed to the physical value. Further requiring that the Bogoliubov transformation is unitary (or equivalently $\mathcal{R}$ is idempotent), the minimization

$$\delta\{\mathcal{E}[\mathcal{R}] + \mathrm{Tr}[\Lambda(\mathcal{R}^2 - \mathcal{R})]\} = 0, \tag{2.28}$$

is effectively done, where Λ labels a matrix of Lagrange multipliers. Introducing the *HFB Hamiltonian*

$$\mathcal{H} \equiv \frac{\partial\mathcal{E}[\mathcal{R}]}{\partial\mathcal{R}} = \begin{pmatrix} h-\lambda & \Delta \\ -\Delta^* & -(h-\lambda)^* \end{pmatrix}, \tag{2.29}$$

where h and Δ represent respectively the *Hartree-Fock field* and the *Bogoliubov field*

$$h - \lambda \equiv \frac{\partial\mathcal{E}[\mathcal{R}]}{\partial\rho^*}\,, \tag{2.30}$$

$$\Delta \equiv \frac{\partial\mathcal{E}[\mathcal{R}]}{\partial\kappa^*}\,, \tag{2.31}$$

Eq. (2.28) can be written as

$$\mathcal{H} + \mathcal{R}\Lambda + \Lambda\mathcal{R} - \Lambda = 0\,. \tag{2.32}$$

Two equations are obtained respectively multiplying the lhs of Eq. (2.32) from the left and from the right by $\mathcal{R}$. Subtracting the two and exploiting the idempotency of $\mathcal{R}$, one obtains

$$[\mathcal{H}, \mathcal{R}] = 0\,. \tag{2.33}$$

Since Eq. (2.23) displays a diagonality of $\mathcal{R}$ in the quasiparticle basis, the U and V matrices for the Bogoliubov transformation in Eq. (2.12) can be determined by solving the Hartree-Fock-Bogoliubov equations

$$\mathcal{H}\begin{pmatrix} U \\ V \end{pmatrix}_k = \begin{pmatrix} h-\lambda & \Delta \\ -\Delta^* & -(h-\lambda)^* \end{pmatrix}\begin{pmatrix} U \\ V \end{pmatrix}_k = E_k\begin{pmatrix} U \\ V \end{pmatrix}_k, \tag{2.34}$$

i.e. diagonalizing the Hartree-Fock-Bogoliubov Hamiltonian. Since h and Δ depend on the eigenvectors U and V, the numerical implementation of Eq. (2.34) requires an iterative solution.

Taking the expectation value of H on the HFB vacuum and applying the Wick theorem [37], it follows that the total energy of the system is given by

$$E^{\mathrm{HFB}} = h^{(0)} + \sum_{\alpha\beta} t_{\alpha\beta}\rho_{\beta\alpha} + \frac{1}{2}\sum_{\alpha\beta\gamma\delta} \bar{v}_{\alpha\beta\gamma\delta}\rho_{\delta\beta}\rho_{\gamma\alpha} + \frac{1}{4}\sum_{\alpha\beta\gamma\delta} \bar{v}_{\alpha\beta\gamma\delta}\kappa_{\alpha\beta}\kappa_{\gamma\delta}\,. \tag{2.35}$$

2.3.1. Reduction to Hartree-Fock equations

Consider the limit case in which the Bogoliubov vacuum (Eq. (2.18)) reduces to a Slater determinant

$$|\Phi\rangle = \prod_{\lambda=1}^{A} c_\lambda^\dagger |0\rangle \, , \tag{2.36}$$

where the A occupied single-particle states are denoted with $(\lambda, \mu, \ldots)$ whereas all the others are empty and denoted with $(\alpha, \beta, \ldots)$. The Bogoliubov transformation (Eq. (2.12)) leads to the following connection between quasiparticle and single-particle creation and annihilation operators

$$\beta_\alpha = c_\alpha, \qquad \beta_\alpha^\dagger = c_\alpha^\dagger, \tag{2.37a}$$
$$\beta_\lambda^\dagger = c_\lambda, \qquad \beta_\lambda = c_\lambda^\dagger, \tag{2.37b}$$

such that

$$V_{\alpha\kappa} = 0, \qquad U_{\alpha\kappa} = \delta_{\alpha\kappa}, \tag{2.38a}$$
$$V_{\lambda\kappa} = \delta_{\lambda\kappa}, \qquad U_{\lambda\kappa} = 0. \tag{2.38b}$$

The normal and anomalous density matrices (Eqs. (2.19a) and (2.19b)) reduce to

$$\rho_{\alpha\kappa} = 0, \qquad \kappa_{\alpha\kappa} = 0, \tag{2.39a}$$
$$\rho_{\lambda\kappa} = \delta_{\lambda\kappa}, \qquad \kappa_{\lambda\kappa} = 0, \tag{2.39b}$$

which combined with Eq. (2.31) shows that the Bogoliubov field vanishes ($\Delta = 0$).

The Hartree-Fock-Bogoliubov equation (Eq. (2.34)) simplifies into

$$\begin{pmatrix} h-\lambda & 0 \\ 0 & -(h-\lambda)^* \end{pmatrix} \begin{pmatrix} U_k \\ V_k \end{pmatrix} = E_k \begin{pmatrix} U_k \\ V_k \end{pmatrix} . \tag{2.40}$$

Given that the Lagrange multiplier λ entering Eq. (2.26) must be located in between the last occupied and the first empty level in order for the reference Slater determinant to contain A nucleons, the positive HFB eigenvalues E_κ of Eq. (2.34) are given by

$$E_\kappa \equiv \begin{cases} \varepsilon_\alpha - \lambda & \text{if} \quad \kappa = \alpha, \\ \lambda - \varepsilon_\lambda & \text{if} \quad \kappa = \lambda, \end{cases} \tag{2.41}$$

where the hole and particle single-particle energies come from solving the two separate *Hartree-Fock* (HF) equations according to

$$hU_\alpha = \varepsilon_\alpha U_\alpha, \tag{2.42a}$$
$$hV_\lambda^* = \varepsilon_\lambda V_\lambda^*. \tag{2.42b}$$

The total energy in the HF basis is now obtained from Eq. (2.35) discarding the term depending on the anomalous density matrix

$$E^{\text{HF}} = h^{(0)} + \sum_{\lambda=1}^{A} t_{\lambda\lambda} + \frac{1}{2} \sum_{\lambda\mu=1}^{A} \bar{v}_{\lambda\mu\lambda\mu}. \tag{2.43}$$

2.3.2. Normal ordering of operators

Once the Bogoliubov reference state has been obtained, a generic n-body operator O commuting with the particle-number operator A can be normal-ordered with respect to it according to[3]

$$\begin{aligned} O &\equiv \sum_{m=0}^{n} \sum_{\substack{i,j=0 \\ i+j=2m}}^{2n} \frac{1}{i!j!} \sum_{\kappa_1 \dots \kappa_{i+j}} O^{ij}_{\kappa_1 \dots \kappa_{i+j}} \beta^\dagger_{\kappa_1} \dots \beta^\dagger_{\kappa_i} \beta_{\kappa_{i+j}} \dots \beta_{\kappa_{i+1}} \\ &\equiv \sum_{m=0}^{n} \sum_{\substack{i,j=0 \\ i+j=2m}}^{2n} O^{ij} \\ &\equiv \sum_{m=0}^{n} O^{[2m]}. \end{aligned} \tag{2.44}$$

A tensor $O^{ij}_{\kappa_1 \dots \kappa_{i+j}}$ is antisymmetric with respect to the permutation of the first i or the last j indices

$$O^{ij}_{\kappa_1 \dots \kappa_i \kappa_{i+1} \dots \kappa_{i+j}} = \varepsilon(\sigma_\mu)\varepsilon(\sigma_\nu) O^{ij}_{\sigma_\mu(\kappa_1 \dots \kappa_i)\sigma_\nu(\kappa_{i+1} \dots \kappa_{i+j})}, \tag{2.45}$$

where $\varepsilon(\sigma_\mu)$ $(\varepsilon(\sigma_\nu))$ represents the signature of the permutation of the first i (last j) operators. The quantity $O^{[2m]}$ collects all the terms containing $2m$ quasi-particle operators

$$O^{[2m]} \equiv \sum_{\substack{i,j=0 \\ i+j=2m}}^{2n} O^{ij}, \tag{2.46}$$

knowing that a given term O^{ij} gathers i (j) quasi-particle creation (annihilation) operators according to

$$O^{ij} \equiv \frac{1}{i!j!} \sum_{\kappa_1 \dots \kappa_{i+j}} O^{ij}_{\kappa_1 \dots \kappa_i \kappa_{i+1} \dots \kappa_{i+j}} \beta^\dagger_{\kappa_1} \dots \beta^\dagger_{\kappa_i} \beta_{\kappa_{i+j}} \dots \beta_{\kappa_{i+1}}. \tag{2.47}$$

2.4. Bogoliubov Many-body Perturbation Theory

2.4.1. Partitioning

The grand potential is split into an *unperturbed part* Ω_0 and a *residual part* Ω_1:

$$\Omega = \Omega_0 + \Omega_1, \tag{2.48}$$

where Ω_0 must be suitably chosen to lift particle-hole degeneracies, as illustrated in Ch. 1. The unperturbed part of Eq. (2.48) can be written as

$$\Omega_0 \equiv \Omega^{00} + \sum_{\kappa} E_\kappa \beta^\dagger_\kappa \beta_\kappa, \tag{2.49}$$

with $E_\kappa > 0$ obtained from solving Eq. (2.34). With such a definition, the Bogoliubov vacuum is the ground state of Ω_0

$$\Omega_0 \left|\Phi\right\rangle = \Omega^{00} \left|\Phi\right\rangle, \tag{2.50}$$

---

[3] Since the rank-reduced Hamiltonian of Eq. (2.10) is presently employed, the constant term O^{00} sums $\bar{h}^{(0)}$ with the contributions deriving from the one and two-body terms through the normal-ordering procedure.

whereas the many-body states obtained by performing quasi-particle excitations of the vacuum

$$|\Phi^{\kappa_1\kappa_2}\rangle \equiv \beta^\dagger_{\kappa_1}\beta^\dagger_{\kappa_2}\dots|\Phi\rangle \tag{2.51}$$

happen to be its excited states

$$\begin{aligned}
\Omega_0\,|\Phi^{\kappa_1\kappa_2\cdots}\rangle &= \Omega^{00}\,|\Phi^{\kappa_1\kappa_2\cdots}\rangle + \sum_\kappa E_\kappa\beta^\dagger_\kappa\beta_\kappa\,|\Phi^{\kappa_1\kappa_2\cdots}\rangle \\
&= \Omega^{00}\,|\Phi^{\kappa_1\kappa_2\cdots}\rangle + \sum_\kappa E_\kappa\beta^\dagger_\kappa\beta_\kappa\beta^\dagger_{\kappa_1}\beta^\dagger_{\kappa_2}\dots|\Phi\rangle \\
&= \Omega^{00}\,|\Phi^{\kappa_1\kappa_2\cdots}\rangle + \sum_\kappa E_\kappa\left(\sum_{\kappa_i}\delta_{\kappa\kappa_i}\right)|\Phi^{\kappa_1\kappa_2\cdots}\rangle \\
&= [\Omega^{00} + E_{\kappa_1} + E_{\kappa_2} + \dots]\,|\Phi^{\kappa_1\kappa_2\cdots}\rangle \\
&\equiv [\Omega^{00} + E_{\kappa_1\kappa_2\dots}]\,|\Phi^{\kappa_1\kappa_2\cdots}\rangle\,.
\end{aligned} \tag{2.52}$$

The fact that $E_\kappa > 0$ causes a well-defined energy separation between the vacuum $|\Phi\rangle$ and quasiparticle excited states, lifting the particle-hole degeneracy that charaterizes open-shell systems (see the discussion in Ch. 1).

2.4.2. Expansion

Based on the above partitioning of the grand potential, the perturbative expansion can be carried out purely algebraically or diagrammatically [11, 38]. For a two-body observable O commuting with the Hamiltonian ($O \equiv H, \Omega, A$), the correlation correction is given by the superfluid generalization of Goldstone's formula [39]

$$\Delta O = \langle\Phi|\,O\sum_{k=1}^{+\infty}\left(\frac{1}{\Omega^{00}-\Omega_1}\Omega_1\right)^k|\Phi\rangle_{\text{conn}}\,, \tag{2.53}$$

where the subscript 'conn' indicates that only connected diagrams contribute to the expansion. While the unperturbed contribution is nothing but the expectation value of O in the Bogoliubov reference state

$$\langle\Phi|O|\Phi\rangle = O^{00}, \tag{2.54}$$

the second- and third-order contributions based on the HFB reference state are the first non-zero corrections and read as

$$O^{(2)} = -\frac{1}{24}\sum_{\kappa_1\kappa_2\kappa_3\kappa_4}\frac{O^{40}_{\kappa_1\kappa_2\kappa_3\kappa_4}\Omega^{04}_{\kappa_1\kappa_2\kappa_3\kappa_4}}{E_{\kappa_1\kappa_2\kappa_3\kappa_4}}, \tag{2.55a}$$

$$O^{(3)} = \frac{1}{8}\sum_{\kappa_1\kappa_2\kappa_3\kappa_4\kappa_5\kappa_6}\frac{\Omega^{40}_{\kappa_1\kappa_2\kappa_3\kappa_4}O^{22}_{\kappa_3\kappa_4\kappa_5\kappa_6}\Omega^{04}_{\kappa_5\kappa_6\kappa_1\kappa_2}}{E_{\kappa_1\kappa_2\kappa_3\kappa_4}E_{\kappa_5\kappa_6\kappa_1\kappa_2}}. \tag{2.55b}$$

2.4.3. One-body density matrix

Given the dHFB unperturbed vacuum $|\Phi\rangle$ at hand, the dBMBPT($p = 2, 3$) many-body state at second and third order in perturbation theory reads as

$$\begin{aligned}|\Psi^{(p)}\rangle =&|\Phi\rangle \\ &+ \frac{1}{(1)!}\sum_{\kappa_1\kappa_2} C^{20}_{\kappa_1\kappa_2}(p)|\Phi^{\kappa_1\kappa_2}\rangle \\ &+ \frac{1}{(4)!}\sum_{\kappa_1\ldots\kappa_4} C^{40}_{\kappa_1\kappa_2\kappa_3\kappa_4}(p)|\Phi^{\kappa_1\kappa_2\kappa_3\kappa_4}\rangle \\ &+ \frac{1}{(6)!}\sum_{\kappa_1\ldots\kappa_6} C^{60}_{\kappa_1\kappa_2\kappa_3\kappa_4\kappa_5\kappa_6}(p)|\Phi^{\kappa_1\kappa_2\kappa_3\kappa_4\kappa_5\kappa_6}\rangle\,,\end{aligned} \tag{2.56}$$

where $|\Phi^{\kappa_1\cdots\kappa_{2q}}\rangle$ denotes elementary excitations obtained via the action of $2q$ quasi-particle creation operators on $|\Phi\rangle$. The presence of single, double and triple excitations signals that the bulk of dynamical correlations is captured by $|\Psi^{(p)}\rangle$[4].

Let us introduce the BMBPT(2,3) one-body density matrices in the quasi-particle basis

$$\tilde{\rho}^{(2,3)}_{\kappa_1\kappa_2} \equiv \frac{\langle\Psi^{(2,3)}|\beta^\dagger_{\kappa_1}\beta_{\kappa_2}|\Psi^{(2,3)}\rangle}{\langle\Psi^{(2,3)}|\Psi^{(2,3)}\rangle}, \tag{2.57a}$$

$$\tilde{\kappa}^{(2,3)}_{\kappa_2\kappa_2} \equiv \frac{\langle\Psi^{(2,3)}|\beta_{\kappa_1}\beta_{\kappa_2}|\Psi^{(2,3)}\rangle}{\langle\Psi^{(2,3)}|\Psi^{(2,3)}\rangle}, \tag{2.57b}$$

where the expression of the numerators and denominators in terms of $C_{\kappa_1\kappa_2}$ and $C_{\kappa_1\kappa_2\kappa_3\kappa_4}$ can be found in Ref. [40]. Next, the normal BMBPT(2,3) one-body density matrix in the single-particle basis defined as

$$\rho^{(2,3)}_{\alpha\beta} = \frac{\langle\Psi^{(2,3))}|c^\dagger_\alpha c_\beta|\Psi^{(2,3))}\rangle}{\langle\Psi^{(2,3))}|\Psi^{(2,3))}\rangle} \tag{2.58}$$

can be obtained from $\tilde{\rho}^{(2,3)}$ and $\tilde{\kappa}^{(2,3)}$ via the inverse of Eq. (2.12), and assuming that time-reversal symmetry is conserved, under the form

$$\begin{aligned}\rho^{(2,3)}_{\alpha\beta} = \rho^{\text{HFB}}_{\alpha\beta} + \sum_{\kappa_1\kappa_2}\Big[&U_{\kappa_2\beta}\tilde{\rho}_{\kappa_1\kappa_2}U^*_{\kappa_1\alpha} - V_{\beta\kappa_2}\tilde{\rho}_{\kappa_1\kappa_2}V^*_{\kappa_1\alpha}+ \\ &- V_{\beta\kappa_2}\tilde{\kappa}_{\kappa_2\kappa_1}U_{*\kappa_1\alpha} + U_{\kappa_2\beta}\tilde{\kappa}_{\kappa_2\kappa_1}V_{\alpha\kappa_1}\Big],\end{aligned} \tag{2.59}$$

where $\rho^{\text{HFB}}_{\alpha\beta}$ is given by Eq. (2.19a).

2.4.4. Reduction to many-body perturbation theory

Rewriting the operator string $\beta^\dagger_\kappa\beta_\kappa$ based on Eqs. (2.37)

$$\beta^\dagger_\kappa\beta_\kappa = (c^\dagger_\alpha\delta_{\kappa\alpha} + c_\lambda\delta_{\kappa\lambda})(c_\alpha\delta_{\kappa\alpha} + c^\dagger_\lambda\delta_{\kappa\lambda}) = \begin{cases} c^\dagger_\alpha c_\alpha & \text{if} \quad \kappa = \alpha, \\ c_\lambda c^\dagger_\lambda & \text{if} \quad \kappa = \lambda. \end{cases} \tag{2.60}$$

---

[4] For reference, the explicit expressions of the second-order coefficients $C^{20}_{\kappa_1\kappa_2}(2)$ and $C^{40}_{\kappa_1\kappa_2\kappa_3\kappa_4}(2)$ can be found in Ref. [35]. Since $|\Psi^{(2)}\rangle$ does not contain triple excitations, one has $C^{60}_{\kappa_1\kappa_2\kappa_3\kappa_4\kappa_5\kappa_6}(2) = 0$.

and using Eq. (2.41), the unperturbed grand potential (Eq. (2.49)) becomes

$$\Omega_0 = \Omega^{00} + \sum_{\alpha=A+1} (\varepsilon_\alpha - \lambda) c^\dagger_\alpha c_\alpha + \sum_{\lambda=1}^{A} (\lambda - \varepsilon_\lambda) c_\lambda c^\dagger_\lambda. \tag{2.61}$$

The excited states of Ω_0 are generated here through particle-hole excitations of the Slater determinant $|\Phi\rangle$

$$|\Phi^{\alpha\beta\ldots}_{\lambda\mu\ldots}\rangle = c^\dagger_\alpha c_\lambda \ldots c^\dagger_\beta c_\mu \ldots |\Phi\rangle \,, \tag{2.62}$$

with the associated eigenvalues

$$\Omega_0 \, |\Phi^{\alpha\beta\ldots}_{\lambda\mu\ldots}\rangle = [\Omega^{00} + \varepsilon_\alpha + \varepsilon_\beta + \ldots - \varepsilon_\lambda - \varepsilon_\mu - \ldots] \, |\Phi^{\alpha\beta\ldots}_{\lambda\mu\ldots}\rangle \,. \tag{2.63}$$

Clearly, the Lagrange multiplier λ does not play any active role such that one can redefine the problem in terms of the Hamiltonian, thus using the partitioning

$$H = H_0 + H_1, \tag{2.64}$$

with the normal-ordered unperturbed part

$$H_0 \equiv E^{\text{HF}} + \sum_{\alpha=A+1} \varepsilon_\alpha c^\dagger_\alpha c_\alpha - \sum_{\lambda=1}^{A} \varepsilon_\lambda c_\lambda c^\dagger_\lambda \tag{2.65}$$

having the same excitation spectrum as Ω_0 in Eq. (2.63). While the unperturbed contribution to the energy is nothing but

$$\langle\Phi|H|\Phi\rangle = E^{HF}, \tag{2.66}$$

the second-order contribution is given by

$$\Delta E^{(2)} = -\frac{1}{4} \sum_{\alpha\beta\lambda\mu} \frac{|\bar{v}_{\alpha\beta\lambda\mu}|^2}{\varepsilon_\alpha + \varepsilon_\beta - \varepsilon_\lambda - \varepsilon_\mu}. \tag{2.67}$$

2.5. Axial deformation

While many-body methods breaking $U(1)$ symmetry require a dedicated Bogoliubov-based formalism to be worked out, the breaking of $SU(2)$ symmetry simply demands a straightforward adaption of the $SU(2)$-conserving equations.

The formalism designed above can be easily adapted to the case of axial deformation by specifying that the many-body tensors at play only display a block-diagonal structure with respect to quantum numbers m, π and t. This feature relates to the assumption that the many-body states at play carry good isospin, parity and projection of the total angular momentum ($|\Psi\rangle \equiv |\Psi^{M\Pi T}\rangle$). Since rotational symmetry is broken, J is not a good quantum number anymore and many-body tensors are not diagonal with respect to the total angular momentum quantum number.

In this context, a measure of the collectivity of the symmetry-breaking solutions is given by the *axial deformation* parameter β_2

$$\beta_2 \equiv \frac{4\pi}{3AR_0^2} \, q_{20} \,, \tag{2.68}$$

where $R_0 \equiv 1.2\, A^{1/3}\,\mathrm{fm}$ and q_{20} is the expectation value of the *axial quadrupole moment* one-body operator $Q_{20} \equiv r^2 Y_{20}(\theta, \phi)$, with $Y_{20}(\theta, \phi)$ a spherical harmonic (see Eq. (G.5) from App. G) with quantum numbers $l = 2$ and $m = 0$.

The dHF(B) unperturbed state $|\Phi\rangle$ at play in d(B)MBPT (and similarly in dCC [9] and dDSCGF [6]) breaks rotational invariance. Consequently, the quasi-particle basis[5] labelling the many-body tensors at play in the deformed method of interest [41] is characterized by the set of quantum numbers

$$\alpha \equiv (N_\alpha, \pi_\alpha, m_\alpha, t_\alpha)\,, \tag{2.69}$$

where N_α denotes a novel principal quantum number. While π_α and m_α remain good quantum numbers[6], it is not anymore the case for j_α and l_α.

While the block-diagonal structure of the equations presented above specified to axial symmetry is not explicitly reported, the complete derivation of the equations at play in axially-deformed Hartree-Fock (dHF) and axially-deformed self-consistent Green's function (dSCGF) methods can be found in Ch. 5.

2.6. Accessing ground-state energies of odd-even systems

The description of odd-systems constitutes a challenging task for *ab initio* expansion methods given the breaking of time-reversal symmetry induced by the odd nucleon. In the HFB method, a proposed perturbative procedure consists of adding a quasiparticle on top of the vacuum state of the even-even neighboring nucleus. However this procedure displays issues linked to the particle number of the odd-even system that is to be described.

In order to overcome this problem, the HFB calculation can be performed while constraining the even-number-parity vacuum to carry the appropriate odd average number of particles [42]. Creating on top of it the quasi-particle carrying the lowest quasi-particle energy allows to properly approximate the total energy of the odd-even system.

While such a procedure was originally formulated within HFB theory, it is presently adapted to approximate BMBPT(2,3) calculations for odd systems. The even-number-parity vacuum carrying the odd average particle number is employed as a reference state to perform the perturbative expansion. The energy for the odd-system is then determined by adding the smallest HFB quasi-particle energy to the BMBPT(2,3) total energy.

---

[5] In case the unperturbed state is a deformed Hartree-Fock Slater determinant, the quasi-particle basis relates trivially to the deformed Hartree-Fock single-particle basis. In case the unperturbed state is a deformed Hartree-Fock-Bogoliubov state, it corresponds to the actual deformed Bogoliubov quasi-particle basis.

[6] While it can be further broken [41], the rotational symmetry around the z axis is presently conserved, i.e. the unperturbed state remains axially symmetric.

Chapter 3.

Impact of correlations on nuclear binding energies

Contents

3.1. Introduction

Predictions based on *ab initio* nuclear structure calculations are currently moving to heavier systems [43–47] and/or doubly open-shell nuclei [8, 9, 41, 48]. One ambition of such developments is to efficiently capture the dominant many-body correlations at play. As introduced in Ch. 1, many-body correlations can be separated in two different categories. The first category concerns so-called *dynamical* correlations carried by all nucleons and delivering the bulk of the correlation energy. Dynamical correlations are well captured by a sum of many low-rank elementary, e.g. particle-hole, excitations out of a well-chosen unperturbed state. The second category concerns so-called *static* correlations that strongly impact the ground-state of open-shell nuclei and are driven by the valence nucleons. While being largely subleading, static correlations vary quickly with the number of valence nucleons and, as such, strongly impact differential quantities as well as spectroscopic observables. Such correlations can be efficiently captured via an optimal choice of the unperturbed state [7, 11].

In this context, the present chapter aims at pedagogically analyze the impact of many-body correlations on binding energies and associated differential quantities, i.e. first- and second-order derivatives with respect to the (even) neutron number. To do so, the study is conducted along neighboring Calcium ($Z = 20$) and Chromium ($Z = 24$) isotopic chains spanning a large range of (even) neutron numbers from $N = 12$ till $N = 50$. Most of Ca isotopes are of singly open-shell character whereas most of Cr isotopes are of doubly open-shell character. Comparing the behavior of binding energies along these isotopic chains allows one to illustrate the roles played by static and dynamical correlations in the two types of nuclei and the capacity of *ab initio* many-body methods to efficiently capture them by employing an optimal formulation. In order to control how some of the identified features depend on the nuclear mass, additional calculations are performed along the Tin ($Z = 50$) isotopic chain from $N = 50$ till $N = 82$.

The present chapter is organized as follows. Before starting with actual calculations, Sec. 3.2 presents a summary of the main sources of uncertainty that characterize *ab initio* methods. Section 3.3 briefly introduces the numerical calculations performed in the present study. In Sec. 3.4, the results obtained at the spherical mean-field level are analyzed, pointing to specific deficiencies that need to be remedied by the addition of correlations. In Sec. 3.5, low-order dynamical correlations on top of the spherical mean-field are proven to correct all such shortcomings to a high degree in Ca isotopes. In Sec. 3.6, the inclusion of static correlations either via a complete diagonalization in the valence space or via the explicit breaking of rotational symmetry is shown to be critical to obtain an equally good description of Cr isotopes.

3.2. Sources of uncertainty in many-body methods

As discussed in the Introduction, the solution of the many-body Schrödinger equation (Eq. (0.1)) requires (i) the modelling of the nuclear Hamiltonian H and (ii) the determination of the many-body wave function $|\Psi_k^A\rangle$ through a many-body calculation. Different sources of uncertainty are involved at different levels of such procedure. For what concerns the determination of the LECs characterizing the nuclear interaction alone, rigorous methods have been developed in past years to estimate the uncertainty associated to the fitting procedure [50, 51]. When it comes to other sources of error, specific evaluations must be performed in different regions of the nuclear chart since their impact is typically mass-dependent. Nuclear interactions carry mainly three sources of uncertainty.

- *Truncation in the χEFT expansion*: it requires the generation of the interaction at different orders in the EFT. It can be then quantified, e.g., through the simple estimation illustrated in [52].

- *SRG evolution*: Hamiltonians pre-processed via SRG techniques are usually truncated at the 3B level, which spoils the unitary character of the transformation. To evaluate the corresponding impact on nuclear observables, one needs to repeat the many-body calculation at different values of the SRG flow parameter. The variation is a measure of the associated uncertainty.

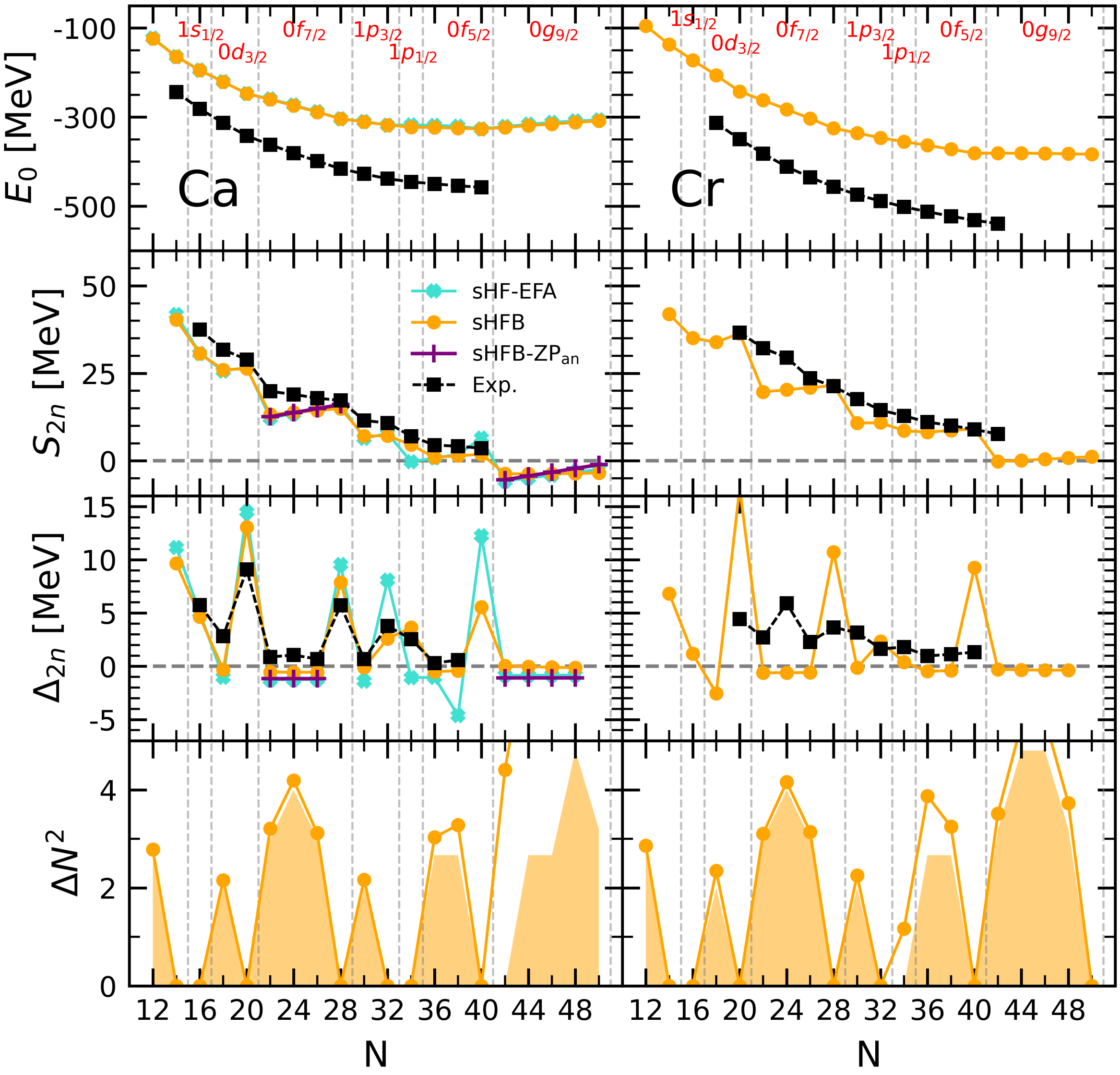

Figure 3.1. Systematics along Ca (*left panel*) and Cr (*right panel*) isotopic chains. First line: sHFB and sHF-EFA absolute binding energy against experimental data. Second (third) line: sHFB and sHF-EFA two-neutron separation energy (two-neutron shell gap) against experimental data. Between ^{42}Ca and ^{48}Ca ($0f_{7/2}$ shell) as well as between ^{62}Ca and ^{70}Ca ($0g_{9/2}$ shell), sHFB-ZP semi-analytical results are also shown. Fourth line: sHFB neutron-number variance against the minimal possible variance in sHFB calculations (shaded area) [49]. The sequence of the underlying neutron canonical shells are also displayed.

- *Rank-reduction of three-body operators*: past studies [53] showed that the error induced by the rank-reduction of three-body operators [35] (see Sec. 2.1.4) on ground-state energies of light- to mid-mass nuclei is below 1%.

The first two sources of uncertainties can be sizeable and at the same time are difficult to evaluate. Particular estimates point to a few (up to 5) percent impact on ground-state properties (see e.g. [54]).

The projection of operators on a single-particle basis delivers a one-body model-space that must be suitably truncated. As already illustrated, such truncation is typically performed via the e_{max} and $e_{3\text{max}}$ sHO parameters.

- e_{max} *truncation*: ground-state energies and radii can be extrapolated to $e_{\text{max}} \to \infty$ by studying the infrared behavior of sHO wave functions in an effective box [55, 56]. Such extrapolation however requires several calculations at different values of e_{max} and $\hbar\omega$. With this at hand, one can evaluate the error associated with a given e_{max}.

- $e_{3\text{max}}$ *truncation*: more empirical extrapolations procedures can be devised (see e.g. [44]), which also require several calculations varying the value of $e_{3\text{max}}$. A statistical analysis can also provide associated uncertainties.

For the model-space truncations ($e_{\text{max}} = 10 - 12$ and $e_{3\text{max}} = 16 - 18$) and mass-range ($A = 18 - 70$) studied in this manuscript, these two sources of uncertainty are typically subleading compared to the other ones.

Lastly, three additional sources of error characterize many-body methods.

- *Many-body truncation*: the error strongly depends on the 'softness' of the Hamiltonian and on the mass of the system under study. For soft Hamiltonians (e.g. EM 1.8/2.0), truncating the perturbative expansion at second order already allows to get close (typically 1-2%) to an exact reference [6]. For 'harder' interactions, high-momentum contributions become non-negligible and require non-perturbative methods to be properly taken into account. Several parts of this manuscript present a comparison of various many-body methods, from which the convergence of the many-body expansion and associated uncertainties can be deduced case by case.

- *Breaking of particle-number symmetry*: equations from [57] allow to estimate of the impact of particle number projection on the total energy. Large-scale calculations [6] up to mid-mass nuclei that are not presented in this manuscript showed that the uncertainty associated does not exceed 1% in all the cases considered.

- *Breaking of rotational symmetry*: for ground-state energies, past studies [9, 48] indicate that angular-momentum projection yields an additional 1-2% at the CCD level. Given that the effect strongly depends on the deformation, it may vary abruptly across isotopic chains and impact differential quantities like two-neutron separation energies or two-neutron gaps.

While efforts to fully characterize uncertainties associated to dBMBPT calculations are currently underway [6], given (i) the large variety of many-body methods and interactions employed here and (ii) the exploratory nature of many of the developments discussed in the present manuscript, the choice of not displaying theoretical error bars have been made. One should refer to the present discussion to estimate case by case theoretical uncertainties.

3.3. Numerical calculations

Ab initio many-body calculations in this chapter are carried out employing a one-body sHO basis characterized by the frequency $\hbar\omega = 12\,\text{MeV}$. All states up to $e_{\text{max}} = 12$ are included. The representation of three-body operators is further restricted by only employing three-body states up to $e_{3\text{max}} = 18\,(24)$ in Ca and Cr (Sn) isotopes.

Calculations are performed using the EM 1.8/2.0 Hamiltonian. This particular Hamiltonian is employed because it is empirically known to give an excellent reproduction of binding energies in the mid-mass region [58].

The present study is based on three complementary expansion many-body methods. First, the spherical Hartree-Fock Bogoliubov (sHFB) mean-field approximation plus second-order Bogoliubov many-body perturbation theory (sBMBPT(2)) correction [38, 59] is employed. As a non-perturbative complement to sBMBPT(2), spherical Bogoliubov coupled cluster with singles and doubles (sBCCSD) [46, 60] calculations are also carried out. Third comes the axially-deformed Hartree-Fock Bogoliubov (dHFB) mean-field approximation plus second-order Bogoliubov many-body perturbation theory (dBMBPT(2)) correction[1] [35, 41].

Available valence-space in-medium similarity renormalization group (VS-IMSRG(2)) results in Ca and Cr isotopes [58] based on the same Hamiltonian[2] are presently employed as a reference given that static and dynamical correlations generated within the valence space are accounted for to all orders via the diagonalization of the associated effective Hamiltonian. Notice that calculations along complete Ca and Cr isotopic chains require a reset of the valence space below $N = 20$ and above $N = 40$. The data presently employed correspond to the choice of valence spaces delivering the most optimal results [58].

Experimental data (as well as extrapolated data) for nuclear ground-state energies shown in all the present work are taken from [63].

3.4. Spherical mean-field approximation

The baseline of more advanced treatment based on a many-body expansion is given by the mean-field approximation restricted to spherical symmetry [5]. Because the present study targets open-shell systems, the minimal version presently considered is given by sHFB that can naturally capture pairing correlations via the breaking of $U(1)$ symmetry associated with particle-number conservation [36] (see the discussion in Ch. 2).

3.4.1. Calcium chain

Systematic sHFB results along the Ca isotopic chain are displayed in the left panels of Fig. 3.1. In the first line, one observes that sHFB calculations significantly underbind experimental data, e.g. by more than 100 MeV in ^{48}Ca, in a way that increases with neutron excess. Such a quantitative defect is expected from a mean-field approximation in the context of *ab initio* calculations. Indeed, while static neutron-neutron pairing

---

[1] dHFB and dBMBPT calculations in the present manuscript are carried out with the `PAN@CEA` numerical suite [41].

[2] The numerical setting is slightly different given that these calculations employ $e_{\text{max}} = 14$ and $e_{3\text{max}} = 16$ while extrapolations in e_{max} are performed to obtain infrared convergence [61]. The effects of 3N interactions between valence nucleons is captured via the ensemble normal-ordering of Ref. [62].

correlations are incorporated within sHFB, one is missing dynamical correlations whose inclusion account for a significant fraction of the binding energy [5, 8, 11, 64].

The evolution of binding energies can be scrutinized via the two-neutron separation energy

$$S_{2n}(N,Z) \equiv E(N-2,Z) - E(N,Z) \tag{3.1}$$

displayed in the second line of Fig. 3.1. Because $S_{2n}(N,Z)$ is a first derivative of the binding energy $E(N,Z)$ with respect to (even) neutron number, the large offset seen in the first line has disappeared. Eventually, the S_{2n} from sHFB slightly underestimate experimental data overall such that adding dynamical correlations is expected to correct for this quantitative discrepancy.

The main characteristics of the experimental S_{2n}, i.e. the sudden drops at $N = 20$ and 28, and to a lesser extent at $N = 32$ and 34, as well as the smooth evolution in between, are well accounted for by sHFB results. However, crucial differences are revealed upon closer inspection. First, the amplitude of the drops at $N = 20$ and 28 is too large and the trend in between, i.e. while filling the $0f_{7/2}$ shell, is qualitatively wrong. Correlated with the too large drop at $N = 20$, the S_{2n} value in ^{42}Ca is significantly too low. Further adding neutrons, S_{2n} increases linearly throughout the $0f_{7/2}$ shell instead of decreasing linearly as for experimental data[3].

Given that $S_{2n}(N,Z)$ is the first derivative of the binding energy, the patterns identified above relate to specific features of the binding energies that could not be fully appreciated in the first line of Fig. 3.1 due to the large scale employed. S_{2n} evolves linearly with the number a_v of nucleons in the valence shell for both sHFB results and experiment data and this implies that $E(N,Z)$ is essentially quadratic in between two closed-shell isotopes. The fact that S_{2n} starts from too low of a value in sHFB calculations in the open-shell relates to the fact that the linear decrease of $E(N,Z)$ is not pronounced enough such that the difference to the data increases throughout the shell. Finally, the fact that S_{2n} is rising linearly instead of decreasing linearly indicates that the sHFB energy is concave instead of being convex.

These characteristics can be pinned down quantitatively by looking at the third line of Fig. 3.1 displaying the so-called two-neutron shell gap

$$\Delta_{2n}(N,Z) \equiv S_{2n}(N,Z) - S_{2n}(N+2,Z)\,. \tag{3.2}$$

Whenever Δ_{2n} displays a sudden increase, the amplitude of the spike provides an empirical measure of the extra stability associated with a mean-field picture of a closed-shell nucleus displaying a large Fermi gap. Otherwise, Δ_{2n} is linked to the second derivative, i.e. the curvature, of the smoothly evolving binding energy (see App. C for details).

The left panel displaying Δ_{2n} in Fig. 3.1 confirms the two patterns identified above. First, the amplitude of the spikes at $N = 20$ and $N = 28$ are too large by 4.0 and 2.1 MeV, respectively[4]. Second, the essentially constant character of the experimental Δ_{2n} between

---

[3] While the same patterns are at play when going through ^{48}Ca, the size of the $1p_{3/2}$ shell is too small to make the rising slope of sHFB results really visible. The highly degenerate $0g_{9/2}$ shell between ^{62}Ca and ^{70}Ca is more favorable in this respect even though the slope of the sHFB results is actually zero in this case. These nuclei are anyway predicted to be unbound and there is no experimental data yet to be confronted with.

[4] Contrarily, the sudden increase is correctly reproduced for $N = 32$ and $N = 34$. It seems that the larger is the over-stability in the data, i.e. the more pronounced is the magic character of the isotope, the larger is the sHFB exaggeration.

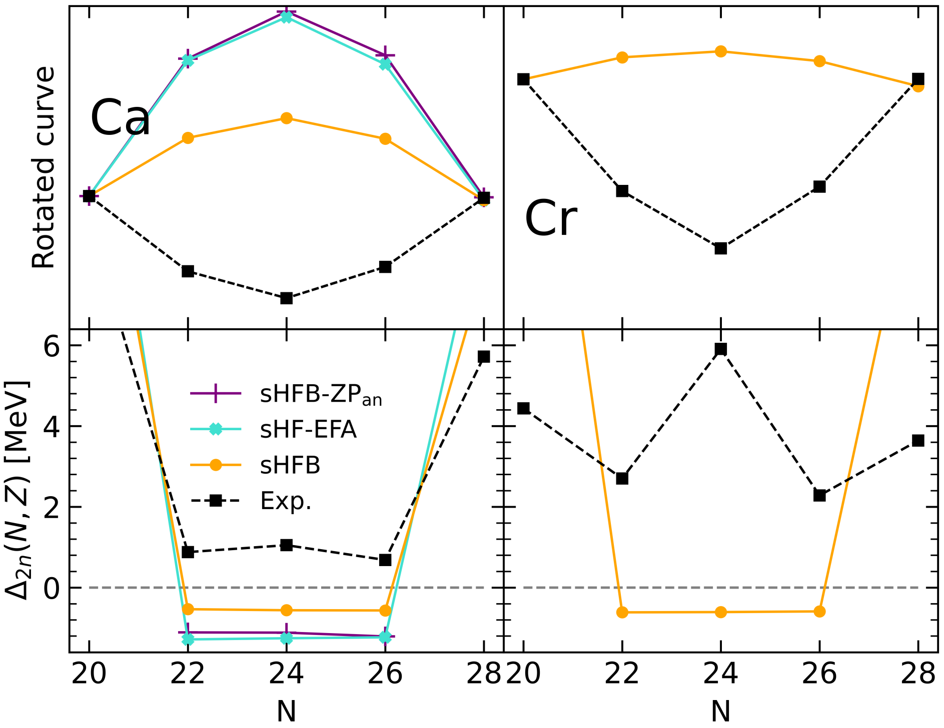

Figure 3.2. Energy curvature of Ca (*left panels*) and Cr (*right panels*) isotopes between $N = 20$ and $N = 28$ ($0f_{7/2}$ shell). Upper panels: energies rescaled to $N = 20$ and $N = 28$ (see text for details). Bottom panels: two-neutron shell gap Δ_{2n}. Experimental data are compared to sHFB results. For Ca isotopes, results from sHF-EFA and sHFB-ZP semi-analytical results are also shown.

^{42}Ca and ^{48}Ca is well captured by sHFB calculations but the associated value is negative instead of positive, i.e. to a very good approximation the sHFB energy is indeed quadratic with the number of valence nucleons a_v but it is concave instead of being convex[5].

Eventually, the issue associated with the curvature of the energy can be even better appreciated from the left panels of Fig. 3.2 focusing on the isotopes between $N = 20$ and $N = 28$. While the bottom panel shows Δ_{2n}, the upper panel displays the total energy rescaled to $N = 20$ and rotated around that point such that the value at $N = 28$ is aligned with it. This effectively removes the overall shift between the different curves along with the linear trend between the two closed-shell isotopes. Both panels make clear that, while experimental energies of Ca isotopes are essentially quadratic and convex between two closed-shell isotopes, sHFB calculations generate a quadratic dependence of energies whose curvature carries the wrong sign.

3.4.2. Analytical investigation

The wrong qualitative behavior of the sHFB energy along semi-magic chains was already visible in past calculations [46, 59, 65] based on different chiral Hamiltonians. It seems to indicate that this behavior is deeply rooted into the spherical mean-field approximation based on realistic nuclear Hamiltonians. This expectation can in fact be confirmed

---

[5] Between ^{62}Ca and ^{70}Ca, where there is no experimental data, Δ_{2n} is constant but actually null such that the sHFB energy is rather linear with a_v.

analytically as demonstrated below.

In order to proceed, one must first make a crucial observation thanks to the results shown on the last line of Fig. 3.1 comparing the neutron-number variance in the sHFB calculation to the *minimal* variance obtained in the zero-pairing limit of sHFB theory (sHFB-ZP) [49]. As already noticed [65], chiral Hamiltonians typically generate only little static pairing at the mean-field level[6], i.e. the computed neutron-number variance is indeed very close to the minimal variance in most open-shell isotopes, except in ^{56,58}Ca and for nuclei in the continuum. As visible from the left panels of Fig. 3.1, this is confirmed by the proximity of sHFB results to those obtained from spherical Hartree-Fock calculations performed within the equal-filling approximation [70] (sHF-EFA) that do not include pairing correlations by construction. Results are indeed very close overall, except in ^{56,58}Ca ($0f_{5/2}$ shell) where sHFB better reproduces experimental values for S_{2n} and Δ_{2n}. As for the curvature within open-shells, the left panels of Fig. 3.2 reveals that the curvature of sHF-EFA results also carries the wrong sign but is such that the concavity is even more pronounced than for sHFB, i.e. the weak pairing correlations present within the $0f_{7/2}$ shell in sHFB do improve the situation compared to the case where pairing would indeed be strictly zero.

Based on this observation, the sHFB energy of an open-shell nucleus relative to the closed-shell (CS) core[7] can be, to a good approximation, expressed analytically as a function of a_v and of specific 2N and 3N interaction matrix elements within sHFB-ZP and sHF-EFA. Both cases are worked out in details in App. B. Since both variants provide almost identical numerical results, only the simpler sHF-EFA expressions are reported here whereas the complete set of formulae valid in sHFB-ZP can be found in App. B.

Canonical single-particle states $\kappa \equiv (n_\kappa, l_\kappa, j_\kappa, m_\kappa, t_\kappa)$ diagonalizing the one-body density matrix $\rho^{\text{sHF-EFA}}$ gather in shells carrying degeneracy $d_\kappa \equiv 2j_\kappa + 1$ characterized by the single-particle energies $\varepsilon_\kappa = \varepsilon_{\breve{\kappa}}$ (see Eq. 3.5 below) where $\breve{\kappa} \equiv (n_\kappa, l_\kappa, j_\kappa, t_\kappa)$. For a system with A (even) nucleons, these shells separate into three categories in sHF-EFA:

1. $\varepsilon_{\breve{h}}$ denoting 'hole states',
2. $\varepsilon_{\breve{v}}$ denoting 'valence states',
3. $\varepsilon_{\breve{p}}$ denoting 'particle states' ,

such that $A - a_v$ nucleons fill the hole states whereas $0 < a_v \leq d_v$ nucleons occupy the valence shell.

Given this setting, one eventually obtains the total energy of an open-shell nucleus relative to the CS core along with the corresponding two-neutron separation energy and two-neutron shell gap as

$$\begin{aligned}\Delta E^{\text{sHF-EFA}}(a_v) &\equiv E^{\text{sHF-EFA}}(a_v) - E^{\text{sHF-EFA}}(0) \\ &= \alpha_{\breve{v}} a_v + \frac{\beta_{\breve{v}}}{2} a_v^2 \,, \qquad (3.3a)\end{aligned}$$

---

[6] In an *ab initio* setting, pairing properties such as the odd-even mass staggering are expected to largely originate from (i.e. required to account for) higher-order processes associated with the exchange of *collective* medium fluctuations between paired particles [66–69]. Achieving a quantitative description of pairing properties from first principles constitutes a major challenge for *ab initio* nuclear structure theory [65].

[7] The following considerations can be meaningfully applied only to *singly* open-shell nuclei, since they rely on the existence of a spherical core and highly-degenerate shells on top of it.

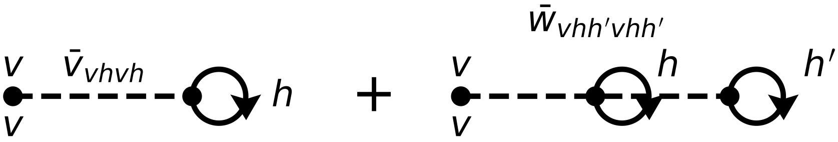

Figure 3.3. First-order interaction energy contributions to the valence-shell single-particle energy $\varepsilon_{\breve{v}}^{\text{CS}}$ computed in the closed-shell core.

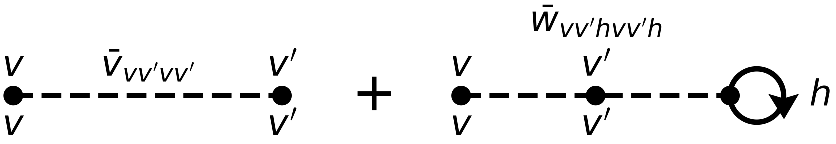

Figure 3.4. First-order contributions to the valence-shell effective two-body matrix elements $\bar{\boldsymbol{v}}_{vv'vv'}$.

$$
\begin{aligned}
S_{2n}^{\text{sHF-EFA}}(a_v) &= -2\alpha_{\breve{v}} - 2\beta_{\breve{v}}(a_v - 1)\,, &&(3.3\text{b})\\
\Delta_{2n}^{\text{sHF-EFA}}(a_v) &= 4\beta_{\breve{v}}\,, &&(3.3\text{c})
\end{aligned}
$$

with

$$
\begin{aligned}
\alpha_{\breve{v}} &= \varepsilon_{\breve{v}}^{\text{CS}}\\
&\equiv t_{vv} + \sum_{h} \bar{v}^{NN}_{vhvh} + \frac{1}{2}\sum_{hh'} \bar{w}_{vhh'vhh'}\,, &&(3.4\text{a})\\
\beta_{\breve{v}} &= \frac{1}{d_v}\sum_{m_{v'}}^{d_v}\left(\bar{v}^{NN}_{vv'vv'} + \sum_{h}\bar{w}_{vv'hvv'h}\right)\\
&\equiv \frac{1}{d_v}\sum_{m_{v'}}^{d_v}\bar{\boldsymbol{v}}_{vv'vv'}\,, &&(3.4\text{b})
\end{aligned}
$$

where $\bar{v}^{NN}_{\alpha\beta\delta\varepsilon}$ has been defined in Eq. (2.3). Equation (3.3a) proves that the sHF-EFA energy is indeed quadratic[8] in the number of valence nucleons throughout any given open-shell. The coefficient $\alpha_{\breve{v}}$ of the linear term is nothing but the mean-field single-particle energy of the valence shell computed in the CS core $\varepsilon_{\breve{v}}^{\text{CS}}$, whose interaction energy contributions are displayed diagrammatically in Fig. 3.3. The coefficient $\beta_{\breve{v}}$ of the quadratic term, i.e. the curvature of the energy, is given by the *average* over the valence magnetic substates of the diagonal valence-shell two-body matrix elements[9] $\bar{\boldsymbol{v}}_{vv'vv'}$ displayed diagrammatically in Fig. 3.4. Such an averaging corresponds to the *monopole* valence-shell matrix element per valence state. As visible from Eq. (3.3b), $-2\varepsilon_{\breve{v}}^{\text{CS}}$ sets the initial value of S_{2n}[10] whereas $-2\beta_{\breve{v}}$ drives its linear evolution throughout the open-shell. Eventually, Δ_{2n} extracts $4\beta_{\breve{v}}$.

Extracting $\varepsilon_{\breve{v}}^{\text{CS}}$ and $\bar{\boldsymbol{v}}_{vv'vv'}$ numerically from the presently employed chiral Hamiltonian (see Tab. 3.1), the semi-analytical results from Eqs. (3.3)-(3.4) (in fact of their sHFB-ZP

---

[8] As shown in App. B, the 3N interaction actually induces the presence of a cubic term in the energy. However, present numerical applications demonstrate that it is negligible for all nuclei under consideration such that it can be dropped altogether in the present discussion.

[9] As seen from Eq. (3.4b), $\bar{\boldsymbol{v}}_{vv'vv'}$ includes the effective contribution obtained by averaging the 3N interaction over the CS core.

[10] As seen from Tab. 3.1, the relation $|\alpha_{\breve{v}}| \gg |\beta_{\breve{v}}|$ holds in practice such that the starting value of $S_{2n}^{\text{sHF-EFA}}$ $(a_v = 2)$ in the open shell is essentially dictated by $\varepsilon_{\breve{v}}^{\text{CS}}$.

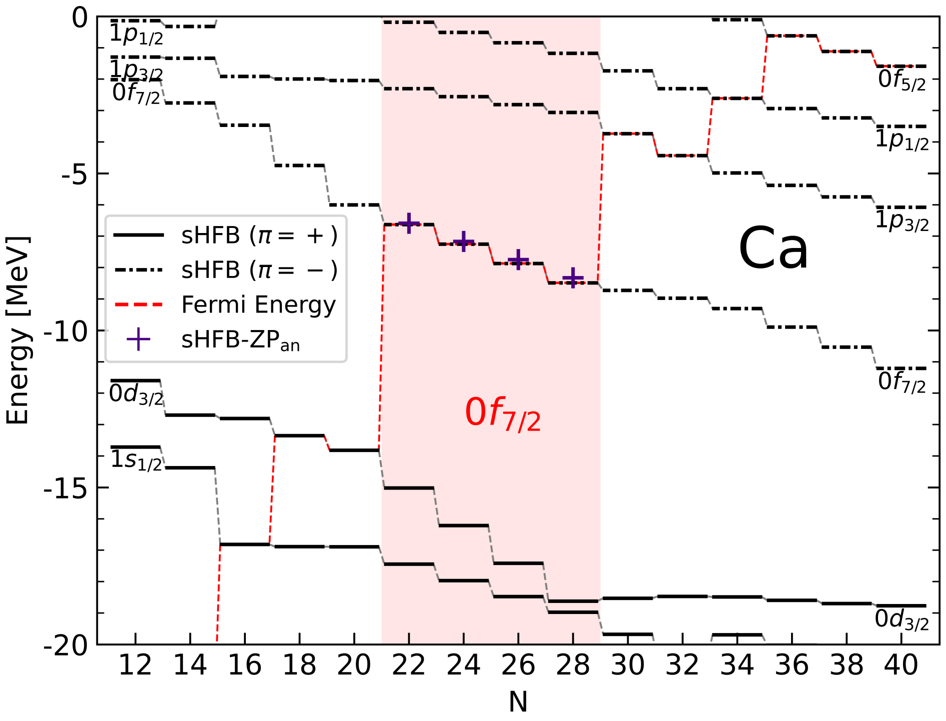

Figure 3.5. Neutron canonical single-particle energies $\varepsilon_{\breve{k}}$ from sHFB calculations along the Ca isotopic chain. Semi-analytical sHFB-ZP results for $\varepsilon_{0f_{7/2}}$ are also shown between ^{40}Ca and ^{48}Ca.

Open shell	$\alpha_{\breve{v}}$ (MeV)	$\beta_{\breve{v}}$ (MeV)
$0f_{7/2}$	-6.005	-0.290
$0g_{9/2}$	2.976	-0.270

Table 3.1. Coefficient of the linear and quadratic term of the HFB-ZP energy (Eq. (B.7)-(B.8)) extracted numerically for two neutron valence shells along the Ca isotopic chain using the EM 1.8/2.0 Hamiltonian [24]. The coefficient of the cubic term $\gamma_{\breve{v}}$ is numerically zero in all cases.

counterparts; see App. B) are superimposed on the left panels of Fig. 3.1 between ^{42}Ca and ^{48}Ca ($0f_{7/2}$ valence shell) as well as between ^{62}Ca and ^{70}Ca ($0g_{9/2}$ valence shell). The results perfectly match the numerical sHF-EFA curves, that are themselves very close to sHFB results. Looking at the left panels of Fig. 3.2, one indeed sees the fully quantitative agreement between sHF-EFA and the semi-analytical results.

The semi-analytical results first clarify that, in an *ab initio* setting, the reason why in a given open shell:

1. E^{sHFB} loses energy relatively to experiment,

2. S_{2n}^{sHFB} starts from too low a value,

relates directly to the fact that the mean-field valence-shell single-particle energy in the CS core $\varepsilon_{\breve{v}}^{\mathrm{CS}}$ delivered by χEFT interactions is systematically too small in absolute, i.e. non negative enough. This is accompanied with the fact that the effective mass is too low at the mean-field level, as testified by the too large (value) decrease of S_{2n}^{sHFB} ($\Delta_{2n}^{\mathrm{sHFB}}$), which is actually a key reason why pairing correlations are so weak. Second, the fact that:

1. E^{sHFB} is concave,
2. S_{2n}^{sHFB} is rising,
3. $\Delta_{2n}^{\text{sHFB}}$ is negative,

throughout open shells, in opposition to experimental data, relates to the attractive character of the monopole valence-shell matrix element delivered by χEFT interactions.

Interestingly, the above features are typically *not* displayed by sHFB calculations based on *effective* and empirical energy density functionals (EDF), see e.g. [71]. Indeed, EDFs are tailored via a fit to empirical data to implicitly incorporate the dominant effect of dynamical correlations. In practice, this generally results into a significantly larger effective mass[11] and into much stronger pairing correlations since the pairing part of the functional is typically adjusted to reproduce experimental pairing gaps at the sHFB level. At the same time, it is striking that EDF parametrizations only tailored to reproduce many-body calculations of infinite nuclear matter and employed in finite nuclei at the strict mean-field level, i.e. without an explicit account of dynamical correlations on a nucleus-by-nucleus basis, do display the features identified above [71].

The above observations are also consistent with the evolution of canonical single-particle energies throughout an open shell, and more specifically of the valence-shell single-particle energy itself. In the sHF-EFA approximation, it can easily be shown that its evolution with a_v is linear

$$\varepsilon_{\check{v}}^{\text{sHF-EFA}}(a_v) = \varepsilon_{\check{v}}^{\text{CS}} + \beta_{\check{v}} a_v \, , \tag{3.5}$$

the coefficient of the slope being given by $\beta_{\check{v}}$. As visible in Fig. 3.5, neutron canonical single-particle energies do evolve linearly within a given open-shell. In particular, the evolution of $\varepsilon_{0f_{7/2}}$ between ^{40}Ca and ^{48}Ca is perfectly reproduced using Eq. (3.5) (in fact its sHFB-ZP counterpart; see App. B). Eventually, this linear down-slopping evolution is fully correlated with the concavity of the binding energy.

3.4.3. Chromium chain

Having characterized sHFB results along the semi-magic Ca isotopic chain, the focus turns now to doubly open-shell Cr isotopes.

As seen in the upper-right panel of Fig. 3.1, the global trend of sHFB binding energies is similar, relative to the data, than for Ca isotopes. Looking through the magnifying glass of S_{2n} and Δ_{2n}, experimental data do not however display the characteristic patterns identified along the Ca chain. In particular, S_{2n} decreases more gradually such that the sudden drops (sudden spikes in Δ_{2n}), e.g. at $N = 20$ and 28, have all disappeared. Contrarily, a small bump (spike) is now visible in S_{2n} (Δ_{2n}) for $N = 24$, i.e. in ^{44}Cr located in the middle of the $0f_{7/2}$ shell. These changes are not at all accounted for by sHFB results that closely follow those obtained previously. Indeed, in addition to displaying the defects identified along the Ca isotopic chain, sHFB results further fail to capture the qualitative modifications seen in the data, i.e. sHFB results keep a strong memory of the underlying spherical shell structure whose fingerprints are no longer visible along the Cr isotopic chain.

---

[11] Even though Δ_{2n} is traditionally left to overestimate experimental data at shell closures in EDF calculations to leave some room for additional correlations, it does so on a much smaller scale than in present sHFB *ab initio* calculations that overestimate Δ_{2n} at, e.g. $N = 20$ by 4 MeV.

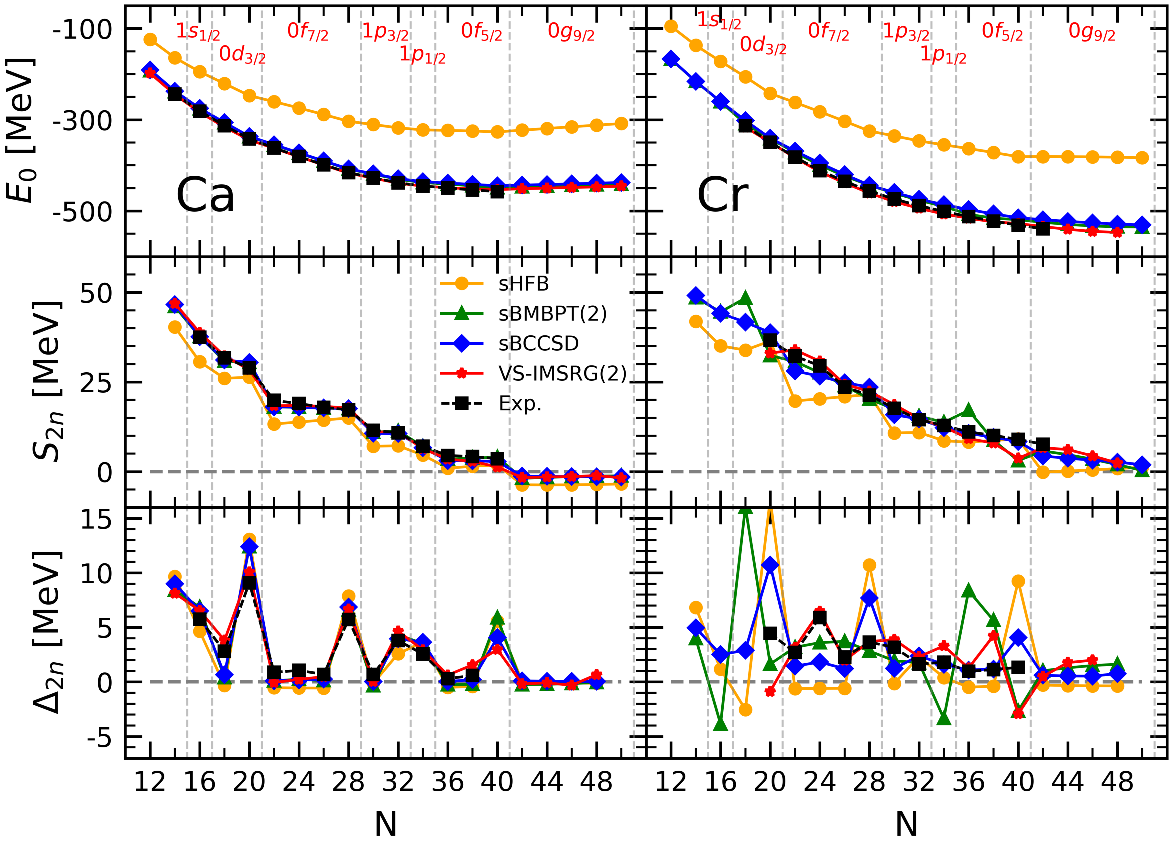

Figure 3.6. Results of sHFB, sBMBPT(2), sBCCSD and VS-IMSRG(2) calculations against experimental data along Ca (*left panels*) and Cr (*right panels*) isotopic chains. Upper panels: absolute binding energy. Middle panels: two-neutron separation energy. Lower panels: two-neutron shell gap.

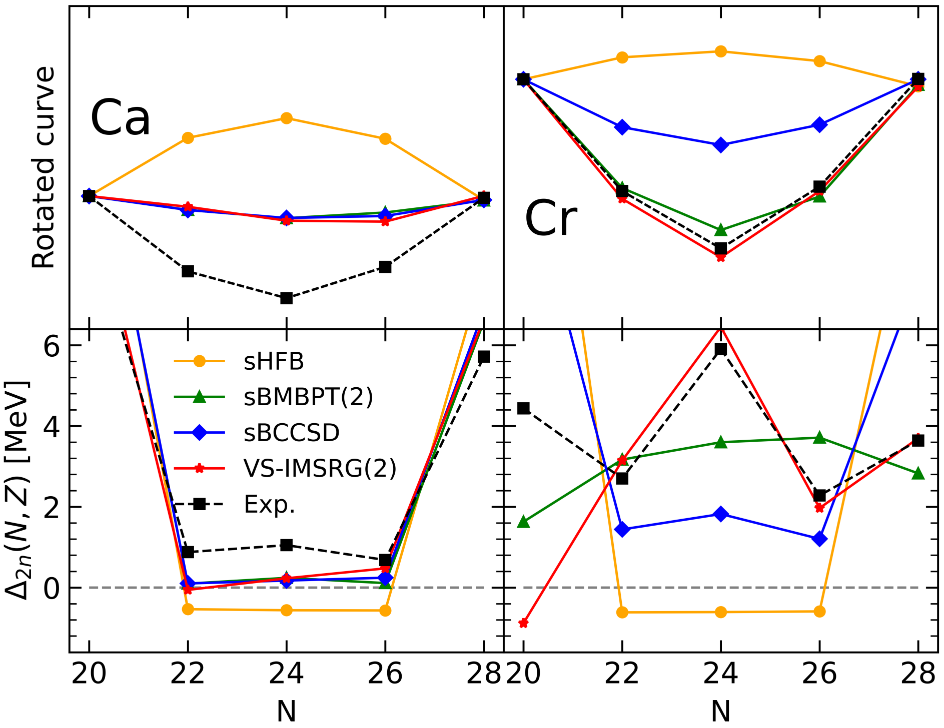

Figure 3.7. Same as Fig. 3.2 for sHFB, sBMBPT(2), sBCCSD and VS-IMSRG(2).

3.5. Spherical beyond mean-field corrections

Based on the previous analysis, the goal is now to assess whether consistently adding dynamical correlations via sBMBPT(2), sBCCSD or VS-IMSRG(2) can correct for the shortcomings identified at the sHFB level.

3.5.1. Calcium chain

As seen in the upper-left panel of Fig. 3.6, dynamical correlations compensate for the underbinding observed at the sHFB level such that all three methods reproduce well experimental binding energies along the Ca isotopic chain with the presently employed Hamiltonian. This is particularly true for VS-IMSRG(2) whose root-mean-square error to the data is equal to 1.9 MeV, while it is equal to 7.3 and 8.8 MeV for BMBPT(2) and BCCSD, respectively. In particular, the increasing underbinding of sHFB results as a function of neutron excess is essentially compensated for.

The improvement goes indeed beyond a plain shift as can be inferred from the middle-left panel of Fig. 3.6. Indeed, S_{2n} are systematically improved against experimental data for all three methods. First, S_{2n} are globally increased by up to about 5 MeV. Second, the amplitudes of the sudden drops at magic numbers are reduced. As visible from the bottom-left panel, the two-neutron shell gap at $N = 20$ is reduced from 13 MeV in sHFB to 8.6 MeV in VS-IMSRG(2), which is comparable to the experimental value of 9.1 MeV. In sBMBPT(2) and sBCCSD the reduction is not pronounced enough, the Δ_{2n} being equal to 12.4 MeV in both cases, thus showing that low-rank elementary excitations are not enough to produce a fully quantitative picture of the $N = 20$ magicity. While sBCCSD is third-order-complete, it is of interest to investigate how much including genuine fourth-order triple excitations, e.g. by going to (approximate) BCCSDT, can help in this respect [72].

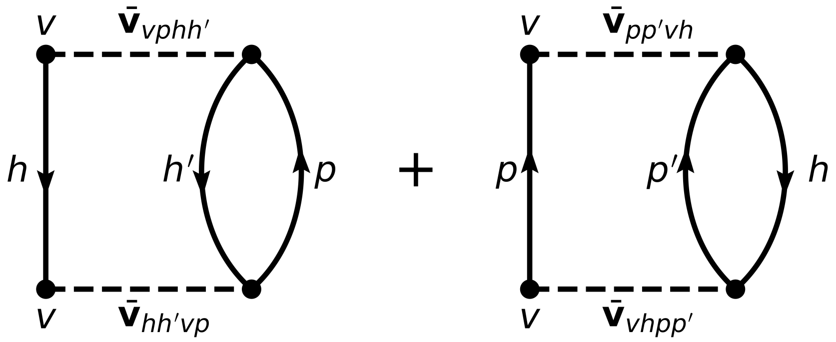

Figure 3.8. Second-order (on-shell) diagonal self-energy correction $\Sigma_{v}^{(2)}$ to the valence-shell single-particle energy computed in the closed-shell core. *Left diagram*: $1p2h$ diagram. *Right diagram*: $2p1h$ diagram.

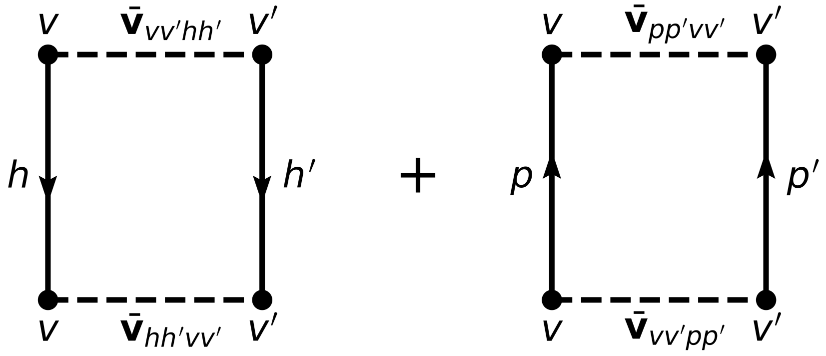

Figure 3.9. Second-order (on-shell) correction $\bar{\boldsymbol{v}}^{(2)}_{vv'vv'}$ to the diagonal valence-shell effective two-body matrix elements. *Left diagram*: hole-hole diagram. *Right diagram*: particle-particle diagram.

In spite of the $N = 20$ two-neutron shell gap being still overestimated in sBMBPT(2) and sBCCSD, the S_{2n} at the beginning of each open shell is increased to be in much better agreement with experimental data. For example, dynamical correlations bring S_{2n} in ^{42}Ca from 13.3 MeV in sHFB to 18.0 and 18.1 MeV in BMBPT(2) and BCCSD, respectively, as well as to 18.6 MeV in VS-IMSRG(2), which compares favorably with the experimental value of 19.8 MeV. Third, the wrong linear increase throughout any given open shell is corrected for, as can be seen for example between ^{42}Ca and ^{48}Ca. This reflects the improvement of the curvature of the energy throughout open shells that can be better appreciated from the left-panels of Fig. 3.7 that focuses on the $0f_{7/2}$ shell. Dynamical correlations turn the energy from beyond concave at the sHFB level to being convex, in a way that is essentially identical with the three employed methods.

Eventually, the agreement with data for S_{2n} and Δ_{2n} along the Ca chain is qualitatively and quantitatively satisfying for all three methods even though the $N = 20$ magicity is still exaggerated in BMBPT(2) and BCCSD and the convexity throughout the $0f_{7/2}$ shell is not pronounced enough compared to experimental data for all three methods, which points to yet missing correlations. A detailed analysis of the connection between the lack of convexity in the energy and the inability of presently employed *ab initio* methods to correctly reproduce the (infamous) evolution of charge radii between ^{40}Ca and ^{48}Ca [73] is carried out in Ch. 7.

3.5.2. Analytical investigation

As demonstrated in Sec. 3.4.2, the deficiencies of sHFB can be understood via a semi-analytical analysis performed in the zero-pairing limit. The capacity of dynamical correlations to correct for those shortcomings is now analyzed in a similar manner within the frame of sMBPT(2). As demonstrated in App. B.4, the mean-field result of Eq. (3.3) can be extended, for $a_v \geq 2$, to

$$S^{(2)}_{2n}(a_v) = -2\varepsilon^{\mathrm{CS}(2)}_{\breve{v}} - 2\beta^{(2)}_{\breve{v}}(a_v - 1)\,, \tag{3.6a}$$

$$\Delta^{(2)}_{2n}(a_v) = 4\beta^{(2)}_{\breve{v}}\,, \tag{3.6b}$$

where the second-order (on-shell) valence-shell single-particle energy and averaged valence-shell interaction computed in the CS core

$$\varepsilon^{\mathrm{CS}(2)}_{\breve{v}} \equiv \varepsilon^{\mathrm{CS}}_{\breve{v}} + \Sigma^{(2)}_{\breve{v}}(\varepsilon^{\mathrm{CS}}_{\breve{v}})\,, \tag{3.7a}$$

$$\beta^{(2)}_{\breve{v}} \equiv \frac{1}{d_v}\sum_{m_{v'}}^{d_{\breve{v}}} \left(\bar{\boldsymbol{v}}_{vv'vv'} + \bar{\boldsymbol{v}}^{(2)}_{vv'vv'}(\varepsilon^{\mathrm{CS}}_{\breve{v}})\right)\,, \tag{3.7b}$$

involve the (on-shell) valence-shell self-energy and two-body effective interaction corrections

$$\begin{aligned}\Sigma^{(2)}_{\breve{v}}(\varepsilon^{\mathrm{CS}}_{\breve{v}}) = &+\frac{1}{2}\sum_{hh'p}\frac{|\bar{\boldsymbol{v}}_{hh'vp}|^2}{\varepsilon^{\mathrm{CS}}_{p} + \varepsilon^{\mathrm{CS}}_{\breve{v}} - \varepsilon^{\mathrm{CS}}_{h} - \varepsilon^{\mathrm{CS}}_{h'}} \\ &-\frac{1}{2}\sum_{pp'h}\frac{|\bar{\boldsymbol{v}}_{vhpp'}|^2}{\varepsilon^{\mathrm{CS}}_{p} + \varepsilon^{\mathrm{CS}}_{p'} - \varepsilon^{\mathrm{CS}}_{h} - \varepsilon^{\mathrm{CS}}_{\breve{v}}}\,,\end{aligned} \tag{3.8a}$$

$$\begin{aligned}\bar{\boldsymbol{v}}^{(2)}_{vv'vv'}(\varepsilon^{\mathrm{CS}}_{\breve{v}}) = &+\frac{1}{2}\sum_{hh'}\frac{|\bar{\boldsymbol{v}}_{hh'vv'}|^2}{2\varepsilon^{\mathrm{CS}}_{\breve{v}} - \varepsilon^{\mathrm{CS}}_{h} - \varepsilon^{\mathrm{CS}}_{h'}} \\ &-\frac{1}{2}\sum_{pp'}\frac{|\bar{\boldsymbol{v}}_{vv'pp'}|^2}{\varepsilon^{\mathrm{CS}}_{p} + \varepsilon^{\mathrm{CS}}_{p'} - 2\varepsilon^{\mathrm{CS}}_{\breve{v}}}\,,\end{aligned} \tag{3.8b}$$

displayed diagrammatically in Figs. 3.8 and 3.9, respectively. The self-energy correction collects a positive ($2h1p$) contribution and a negative ($2p1h$) contribution. Similarly, the valence-shell interaction correction collects a positive (hole-hole) contribution and a negative (particle-particle) contribution.

As seen from Eqs. (3.6)–(3.8), and in agreement with the results shown in the middle-left panel of Fig. 3.6 and analyzed in the present section, dynamical correlations modify both the starting value and the slope of S_{2n} in the valence-shell. For example, the negative second-order self-energy correction $\Sigma^{(2)}_{0f_{7/2}}$ lowers $\varepsilon^{\mathrm{CS}(2)}_{0f_{7/2}}$ in such a way that S_{2n} computed in sBMBPT(2) increases from 13.28 to 18.02 MeV in ^{42}Ca to almost match the experimental value (19.84 MeV). This effect relates to the coupling of a propagating nucleon to $2h1p$ and $2p1h$ configurations as represented in Fig. 3.8, the latter winning over the former[12]. Consistently, the second-order correction to the average $0f_{7/2}$ valence-shell effective interaction is repulsive, with the hole-hole contribution winning over the particle-particle one.

---

[12] The lowering of $\varepsilon_{0f_{7/2}}$ is not accompanied by a decrease of Δ_{2n} in ^{40}Ca in sBMBPT(2) and sBCCSD, contrary to sVS-IMSRG(2), i.e. $\varepsilon_{0d_{3/2}}$ is lowered as much as $\varepsilon_{0f_{7/2}}$. Thus, the needed increase of the effective mass associated with the compression of on-shell single-particle energies is not accounted for by low-order corrections to sHFB.

In the present calculation, such a correction is larger in absolute value than the mean-field contribution and manages to turn the total energy from being concave to being convex, i.e. it makes S_{2n} decrease linearly between ^{42}Ca and ^{48}Ca as for experimental data[13]. Still, and as can be seen from the bottom-left panel of Fig. 3.7, the positive curvature $\beta^{(2)}_{0f_{7/2}} = 25\,\text{keV}$[14] is not large enough[15] compared to experimental data ($\Delta_{2n}/4 \approx 220\,\text{keV}$ in $^{42-46}$Ca), thus pointing to yet missing many-body correlations as discussed earlier on.

3.5.3. Chromium chain

While the deficiencies observed at the sHFB were shown to be qualitatively and quantitatively corrected via the consistent addition of dynamical correlations in Ca isotopes, it remains to be seen to which extent this is the case along the Cr isotopic chain.

As seen in the upper-right panel of Fig. 3.6, correlations brought by sBMBPT(2), sBCCSD and VS-IMSRG(2) provide the bulk of the missing binding along the Cr chain as well, even though the end values are globally further away from experimental data than for Ca isotopes. While the rms error to the data is 1.9, 7.3 and 8.8 MeV for VS-IMSRG(2), sBMBPT(2) and sBCCSD in Ca isotopes, it becomes 4.0, 10.6 and 14.7 MeV in Cr isotopes, respectively; i.e. the deterioration is more pronounced for sBMBPT(2) and sBCCSD.

Looking at the middle- and bottom-right panels of Fig. 3.6, sBMBPT(2) and sBCCSD are seen to improve the reproduction of experimental S_{2n} and Δ_{2n} compared to sHFB. Still, the level of agreement is neither on the same level as in Ca isotopes nor on the same level as for VS-IMSRG(2) in those Cr isotopes. The large spikes of Δ_{2n} seen at $N = 20, 28$ and 40 for sHFB are only slightly diminished in sBCCSD calculations, thus wrongly keeping the imprint of the spherical magic numbers. Even if the behavior throughout the $0f_{7/2}$ shell is improved, as can also be appreciated from the left panels of Fig. 3.7, it remains quite remote from experimental data. As for sBMBPT(2) results, Δ_{2n} bear little resemblance to experimental data and are clearly not credible.

Contrarily, the S_{2n} and Δ_{2n} predicted by VS-IMSRG(2) are both in qualitative and quantitative agreement with experimental data[16]. Indeed, the disappearance of the spikes at $N = 20, 28$ and 40, as well as the appearance of a new one for $N = 24$, are perfectly reproduced. This demonstrates that the exact diagonalization of the effective Hamiltonian within the fp shell is able to capture crucial static correlations that are not accounted for by low-rank excitations on top of a spherical mean field via sBMBPT(2) and sBCCSD.

3.6. Deformed unperturbed state

Even if challenges still remain to be overcome to achieve high accuracy in describing specific quantities that are impacted by collective fluctuations (e.g. superfluidity and radii

---

[13] The amount by which S_{2n} is increased at the start of the open-shell and the fact that its slope is actually inverted depend on the Hamiltonian under use; see Refs. [65, 74] for examples where the qualitative defects of the sHFB results are not actually corrected via the inclusion of low-order dynamical correlations.

[14] This value is essentially constant throughout the valence shell.

[15] The same is true for sBCCSD and VS-IMSRG(2) calculations as can be inferred from the bottom-left panel of Fig. 3.7.

[16] The slight degradation observed in the vicinity on $N = 20$ and 40 is attributable to the need to reset the valence space.

between ^{40}Ca and ^{48}Ca that will be discussed in Ch. 7), the discussion above demonstrates that polynomially-scaling expansion methods built on top of a spherical Bogoliubov reference state and implemented to rather low truncation orders deliver a good account of mid-mass doubly closed-shell and singly open-shell nuclear ground states. Contrarily, doubly open-shell nuclei require the inclusion of specific static correlations that can hardly be incorporated following this strategy, i.e. they require a full diagonalization of the effective Hamiltonian in an appropriate valence space, thus compromising with the polynomial scaling that will eventually become crucial in heavy nuclei.

On a principle level, the solution delivered by expansion many-body methods is eventually independent of the unperturbed state whenever all terms in the expansion series are summed up – provided that the expansion series actually converges [75–80]. In practice however, the interesting question relates to how close to the exact solution one can be at the most economical cost. In this context, it is believed that dominant static correlations can be efficiently captured in doubly open-shell nuclei via an appropriate redefinition of the unperturbed state, at the price of breaking [9, 41] (and eventually restoring [8, 18, 48, 81, 82]) rotational symmetry associated with angular-momentum conservation. The present section wishes to pedagogically illustrate that a quantitative description of doubly open-shell nuclei can indeed be achieved at (low) polynomial cost via dBMBPT(2) calculations performed on top of a deformed HFB unperturbed state.

3.6.1. Calcium chain

Results of systematic dHFB, dBMBPT(2), as well as VS-IMSRG(2) calculations of Ca isotopes are displayed on the left-hand panels of Fig. 3.10. Comparing those to the results shown before on the left-hand panels of Fig. 3.6, it is clear that allowing the mean-field solution to deform does not lead to any significant modification along the Ca isotopic chain. Indeed, and as demonstrated by the lower panel of Fig. 3.10, almost all Ca isotopes do not take advantage of this possibility at the mean-field level[17]. The fact that static correlations associated with quadrupolar deformations are not emerging from the calculation is consistent with the fact sBMBPT(2) and sBCCSD results were already satisfactory as discussed extensively in Sec. 3.5.

3.6.2. Chromium chain

As the comparison of the right-hand panels of Figs. 3.6 and 3.10 illustrates, the energetic of doubly open-shell Cr isotopes is instead strongly impacted by the breaking of rotational symmetry. Indeed, most Cr isotopes do acquire a large intrinsic deformation[18] as seen in the lower-right panel of Fig. 3.10. While the overall rms error of total binding energies remains similar in sBMBPT(2) and dBMBPT(2), the *evolution* with N is strongly impacted as can be inferred from the behavior of S_{2n} and Δ_{2n}.

As a matter of fact, the qualitative (quantitative) reproduction of S_{2n} (Δ_{2n}) is already excellent at the deformed mean-field level, i.e. all deficiencies identified in sHFB results are already corrected by dHFB. In particular, the fictitious shell closures at $N = 20, 28$ and

---

[17] The few isotopes that do deform, i.e. ^{32,44,46,68,70}Ca, only acquire a small intrinsic deformation.

[18] Interestingly, neutron deficient isotopes $^{34-42}$ are predicted to display a strong oblate-prolate oscillation. Isotopes between $N = 20$ and $N = 28$ all display a large prolate deformation, which slowly fades away towards $N = 40$. Eventually, the prolate deformation suddenly increases again going across $N = 40$ and stays large until the predicted neutron drip line at $N = 48$.

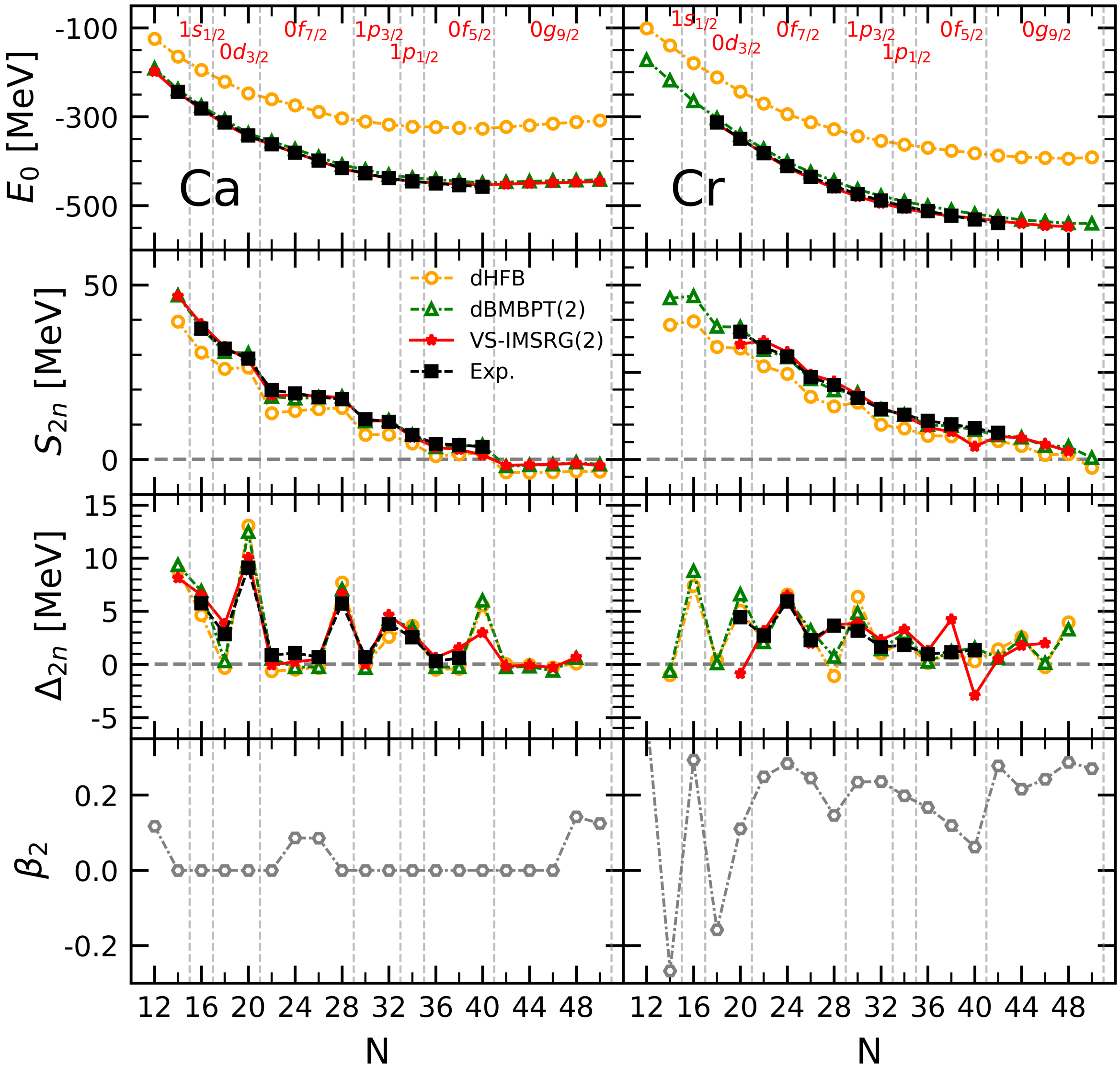

Figure 3.10. Systematic dHFB, dBMBPT(2) and VS-IMSRG(2) calculations against experimental data along Ca (*left panels*) and Cr (*right panels*) isotopic chains. *First line*: absolute binding energy. *Second line*: two-neutron separation energy. *Third line*: two-neutron shell gap. Fourth line: intrinsic axial quadrupole deformation of the dHFB solution.

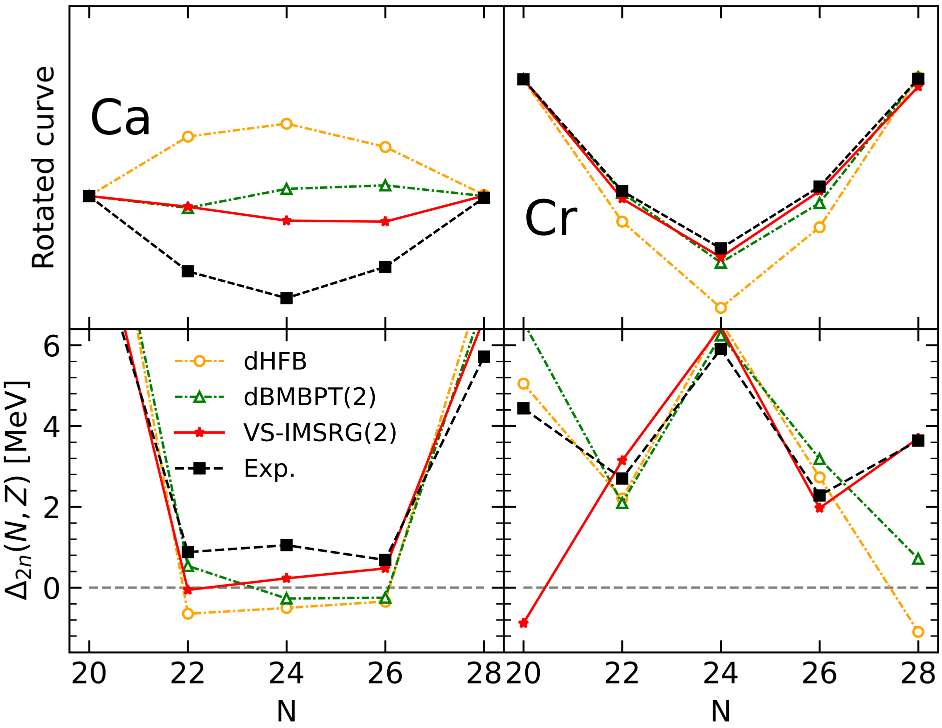

Figure 3.11. Same as Fig. 3.2 for dHFB, dBMBPT(2) and VS-IMSRG(2).

40 have disappeared in dHFB results. Eventually, dynamical correlations added on top of dHFB via dBMBPT(2) increase S_{2n} systematically to reach an excellent agreement with both VS-IMSRG(2) results and experimental data. While the rms error to experimental S_{2n} was 2.9 MeV for sBMBPT(2) (5.8 MeV for sHFB), it is 0.9 MeV for dBMBPT(2) (4.4 MeV for dHFB), which is to be compared to 2.2 MeV for VS-IMSRG(2).

Focusing on the $0f_{7/2}$ shell, the right panels of Fig. 3.11 show that the curvature of the energy is already very well captured at the dHFB level, while it was qualitatively wrong for both sHFB and sBMBPT(2), and becomes almost as good as with VS-IMSRG(2) for dBMBPT(2).

These results demonstrate that static correlations in doubly open-shell nuclei can be qualitatively and quantitatively seized via polynomially-scaling expansion methods built on top of a deformed reference state and implemented to rather low truncation order.

3.7. Tin chain

As a last step, the discussion is extended to semi-magic Sn isotopes between ^{100}Sn and ^{132}Sn, i.e. going through the sub-shell closures at $N = 58, 64, 66$ and 70 located between the $N = 50$ and 82 major shell closures. In Fig. 3.12, S_{2n} and Δ_{2n} computed from mean-field and beyond-mean-field calculations with and without breaking rotational symmetry are displayed.

It is clear that experimental data does not show any fingerprint of the sub-shell closures, i.e. S_{2n} decreases linearly between $N = 52$ and 82 such that Δ_{2n} is flat. Contrarily, sHFB results strongly reflect the presence of those sub-shell closures in a way that is consistent with the behavior seen in Ca isotopes, i.e. S_{2n} are too low overall and rise linearly throughout open-shells, especially along the highly degenerate $0g_{7/2}$ and $0h_{11/2}$

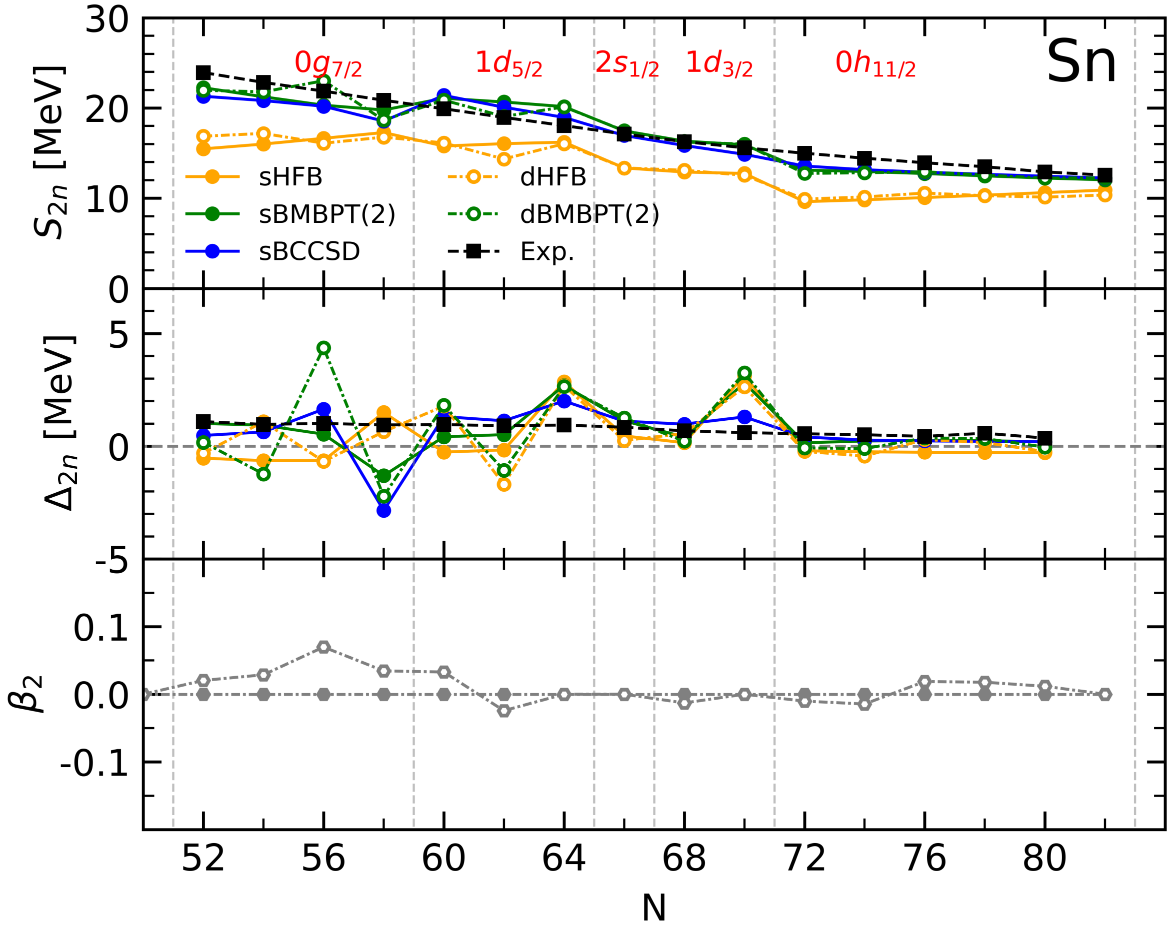

Figure 3.12. Results from sHFB, sBMBPT(2), sBCCSD, dHFB and dBMBPT(2) calculations against experimental data along the Sn isotopic chain. *First panel*: two-neutron separation energy. *Second panel*: two-neutron shell gap. *Third panel*: intrinsic axial quadrupole deformation of sHFB and dHFB solutions.

shells.

Dynamical correlations brought on top of sHFB via sBMBPT(2) and sBCCSD largely ameliorate the situation, i.e. S_{2n} are increased overall and the behavior throughout open-shells are corrected. However, the imprint of the sub-shell closures remain visible.

The larger mass combined with the weak pairing correlations induced by χEFT interactions at the mean-field level makes several semi-magic Sn isotopes take advantage of deformation if authorized to do so[19] as can be seen from the lower panel of Fig. 3.12. Still, the axial quadrupole deformation parameter remains small in all cases. As in Ca isotopes, the wrong trend of S_{2n} with N observed at the sHFB level is thus not corrected by dHFB calculations and dBMBPT(2) eventually deliver very similar results to sBMBPT(2).

3.8. Conclusions

In order to extend the reach of *ab initio* calculations to heavy doubly open-shell nuclei in the future, the most efficient strategy to incorporate dominant many-body correlations at play in (heavy) nuclei must be identified. With this in mind, the present chapter analyzed in details the impact of many-body correlations on binding energies of Calcium and Chromium isotopes with an (even) neutron number ranging from $N = 12$ to $N = 50$.

Using an empirically-optimal (soft) χEFT-based Hamiltonian, binding energies computed in the spherical mean-field approximation were first shown to display specific shortcomings in semi-magic Ca isotopes. In addition to being associated (as expected) to a significant underbinding, the corresponding energy was shown to evolve qualitatively incorrectly throughout (highly degenerate) open shells, i.e. whereas the linear decrease with the number of valence nucleons is too slow, the quadratic term makes the energy concave instead of being convex. Relying on the observation that χEFT-based interactions generate very little pairing at the spherical mean-field level, these two features could be related analytically to the fact that (i) single-particle energies are not enough bound and that (ii) the monopole valence-shell two-body matrix elements is attractive.

Next, the consistent addition of dynamical correlations at polynomial cost via, e.g., low-order perturbation theory was shown to correct the deficiencies identified at the spherical mean-field level. This decisive improvement could also be understood analytically. Eventually, it is possible to reach a description of semi-magic Ca isotopes on essentially the same quantitative level as valence-space in-medium similarity renormalization group calculations, which rely on the diagonalization of the effective Hamiltonian in the fp valence space. Either way, some yet missing correlation energy was identified between ^{40}Ca and ^{48}Ca that could be correlated with the (infamous) difficulty to describe the evolution of the charge radius between those two isotopes.

Moving to doubly open-shell Cr isotopes, calculations based on a spherical mean-field reference state could not appropriately reproduce the binding energy evolution. However, allowing this unperturbed state to break rotational symmetry proved to be sufficient to capture the static correlations responsible for the phenomenological modifications observed between the two isotopic chains and that otherwise need the diagonalization of the effective Hamiltonian in large valence spaces. Semi-magic Sn isotopes behave similarly to lighter Ca isotopes with a spherical mean-field delivering qualitatively wrong patterns

---

[19] This is again at variance with mean-field calculations based on effective EDFs. Indeed, the strong built-in pairing typically constrains all Sn isotopes to remain spherical between $N = 50$ and $N = 82$ in that case.

that are corrected by the consistent addition of low-order dynamical correlations.

Eventually, the work carried out in the present chapter demonstrates in a pedagogical way that polynomially-scaling expansion methods based on unperturbed states possibly breaking (and restoring) symmetries constitute an optimal route to extend *ab initio* calculations to heavy closed- and open-shell nuclei.

The presence of shell closures along isotopic chains has been proven to be relevant in order to establish which *ab initio* technique is more suitable for the study of specific nuclear systems. Before moving to the direction of including more correlations in the beyond mean-field expansion of the total wave function (Ch. 5), the next chapter (Ch. 4) presents a small digression on the dependence of neutron shell closures on the isotonic chain considered. Such discussion is relevant because it shows that shell closures predicted by the spherical shell model (Fig. A.1) are often eclipsed by a re-ordering of the energetic levels to a configuration that the nuclear system finds more energetically favorable. Being such re-adjustment of energy levels interpretable in terms of an increase of collectivity, deformed *ab initio* methods are a suitable choice for their study.

Chapter 4.

Interlude – $N = 20$ island of inversion

Contents

Being an inexpensive but accurate method for the description of nuclear bulk observable, dBMBPT not only constitutes an optimal tool for large-scale calculations[1] [6], but can also be easily employed for specific studies. As an example, the present chapter discusses a recent application that allowed to compare dBMBPT results with state-of-the-art experimental measurements.

In the past months, a new precise evaluation of atomic masses have been performed at the TRIUMF's ISAC facility. Neutron-rich Magnesium and Sodium isotopes have been produced and transmitted to TRIUMF's Ion Trap for Atomic and Nuclear science (TITAN) for the mass measurement. The isotopes involved in the experiment are $^{31-33}$Na and $^{31-35}$Mg. The new results allowed to significantly reduce the uncertainty associated to existing masses [63] and gave a small correction (in the order of $\simeq 0.1\,\mathrm{MeV}$) to their values.

---

[1] Given the relatively easy access that dBMBPT provides to ground-state energies, charge radii, and deformation parameters, the large-scale calculations mentioned in this manuscript are intended to be performed for a wide range of nuclei, from light to heavy, estimating such parameters and derived quantities.

The interest in this specific region of the Segrè chart is connected to the study of the $N = 20$ shell closure, a standard magic number predicted by the spherical shell model (see Fig. A.1) [83, 84]. As one moves south of ^{36}S and ^{34}Si, where this gap is still large, the shell closure becomes weaker and eventually collapses to give rise to one of the so-called *islands of inversion*. There, one can interpret nuclear data in terms of a drastic change in the underlying shell structure, in particular inducing an inversion in the position of standard shell-model orbitals. Experimentally, a minimum for the $N = 20$ two-neutron gap is found for Magnesium at $Z = 12$. An interesting open issue is whether such gap remains small or rather increases when going further down in proton number, all the way to Oxygen isotopes where the magicity of the unbound ^{28}Si has been recently questioned [85]. The disappearance (and possible reappearance) of shell closures is typically linked with the onset of collectivity and deformation. Hence, it is natural to try applying the dBMBPT to this study.

Because the publication of the new measurements is currently undergoing [86], results are still reserved and cannot be shown in the present manuscript. However, data from [63] are qualitatively similar enough to the new ones such that the discussion that follows remains valid. The study performed in the present chapter employs the dBMBPT(3) method with the EM 1.8/2.0 and the NN(N^{4}LO)+3N(lnl)E7 interactions. VS-IMSRG(2) results with the EM 1.8/2.0 interaction [86] are also shown for comparison.

In order to validate the accuracy of dBMBPT(3) in the mass region of interest, drip lines for Ne, Na and Mg isotopes have been first determined. Such analysis is important because it allows to quantify the reliability of the method and interactions used in the mass region of interest. Results are shown in Fig. 4.1. One-neutron separation energies have been calculated through the definition

$$S_{1n}(N, Z) \equiv E(N-1, Z) - E(N, Z)\,, \tag{4.1}$$

while two-neutron separation energies have been calculated accordingly to Eq. (3.1). Moving along an isotopic chain increasing the value of N, the drip line is found in correspondence of the last nucleus that displays positive values of both S_{1n} and S_{2n}. For Neon isotopes, while the experiment predicts the drip line in correspondence of ^{34}Ne, dBMBPT(3) calculations for the EM 1.8/2.0 and NN(N^{4}LO)+3N(lnl)E7 interaction locate it respectively in correspondence of ^{32}Ne and ^{30}Ne. For what concerns Sodium isotopes, only the S_{2n} is shown since the dBMBPT(3) does not allow to compute odd-odd nuclei (the treatment of odd system illustrated in Sec. 2.6 being valid only for the odd-even ones). Nevertheless, one can still look at the S_{2n} alone and find the theoretically predicted drip line in correspondence of ^{35}Na, while the (tentative[2]) experimental one is at the level of ^{38}Na. Finally, calculations performed for Magnesium isotopes display full agreement with experimental data in predicting the dripline for ^{40}Mg. Overall, dBMBPT(3) calculations are fairly accurate and capture the main experimental trends. Even if not all driplines are reproduced, most of the discrepancies lie within theoretical uncertainties once the latter are thoroughly estimated. Importantly, as discussed in the remaining part of this chapter, the present application focuses two-neutron shell gaps Δ_{2n} (Eq. (3.2)), which are relative separation energies are thus insensitive to a global shift of the S_{1n} and S_{2n} values.

The novel experiment performed in TRIUMF allowed to accurately determine the experimental Δ_{2n} gap for ^{31}Na and ^{32}Mg, and decrease the associated uncertainties with respect to [63]. Fig. 4.2 shows the two-neutron shell gap as a function of $N = 20$ isotones. Moving across the isotonic chain decreasing the number of protons, VS-IMSRG(2)

---

[2] The neutron drip line is experimentally determined only up to Neon [87].

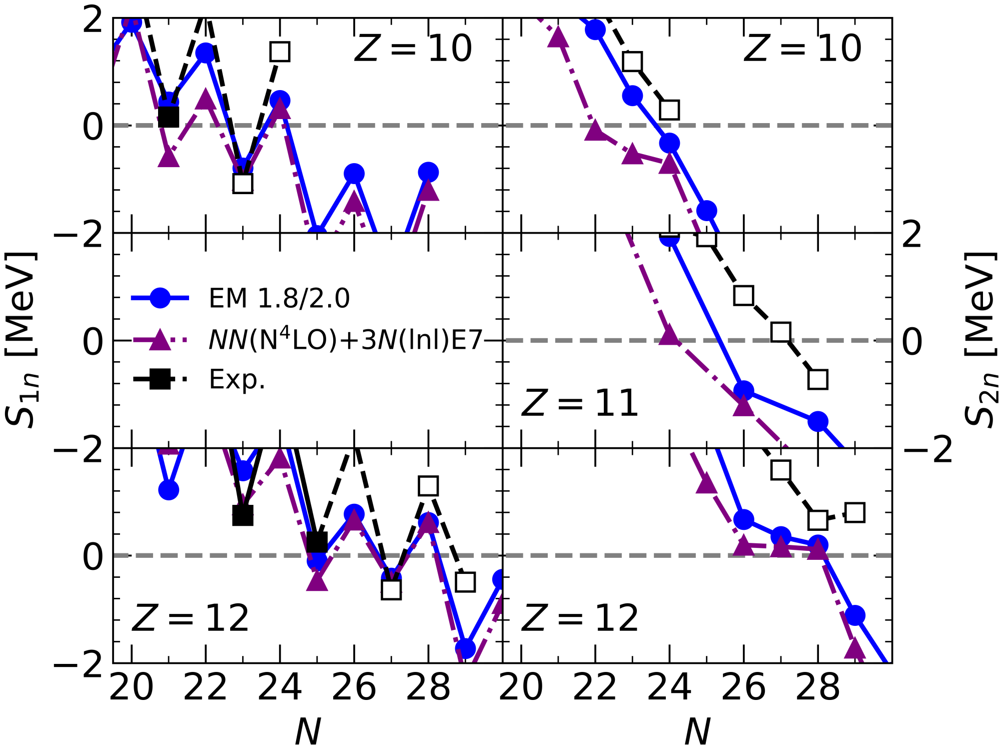

Figure 4.1. One- and two-neutron separation energies (respectively in *left* and *right* panels) for Neon (*upper panels*), Sodium (*central panels*) and Magnesium (*bottom panels*) isotopic chains. S_{1n} results for Sodium are absent because the present many-body approach can not access odd-odd systems. Calculations are performed with the dBMBPT(3) method in $e_{\max} = 10$ at the optimal $\hbar\omega$ for each case. EM 1.8/2.0 three-body MEs are in $e_{3\max} = 18$ while $NN(\mathrm{N}^4\mathrm{LO}){+}3N(\mathrm{lnl})\mathrm{E7}$ ones are in $e_{3\max} = 16$. Experimental data are taken from [63]. While measured data are represented with full squares, empty squares label extrapolated data.

results display the same trend as the experiment for $Z = 13$, 12 and 11, the latter one being $\approx 0.8\,\mathrm{MeV}$ far from the experiment. For $Z = 10$ and 9, VS-IMSRG(2) values keep increasing, while the extrapolated data predict the opposite trend. For what concerns dBMBPT(3) with the same interaction (EM 1.8/2.0), the trend looks different since the Δ_{2n} decreases all the way from $Z = 13$ to 10, remaining close to the experiment only at $Z = 11$ and increasing from $Z = 10$ to $Z = 9$ similarly to VS-IMSRG(2). dBMBPT(3) calculations carried out with the $NN(\mathrm{N}^4\mathrm{LO}){+}3N(\mathrm{lnl})\mathrm{E7}$ interaction still largely overestimate the Δ_{2n} at $Z = 13$. Furthermore, similarly to the other dBMBPT(3) calculations, they predict an inversion of trend between $Z = 12$ and 11. Overall, dBMBPT(3) results with the $NN(\mathrm{N}^4\mathrm{LO}){+}3N(\mathrm{lnl})\mathrm{E7}$ interaction are more close to experimental data than the analogous EM 1.8/2.0 ones, while VS-IMSRG(2) still displays the best results in terms of compatibility with the experiment.

The results presented in this chapter highlight how a qualitative description can be already achieved at the level of deformed BMBPT calculations even in a challenging region as one of the islands of inversion, where collective correlations dictate the evolution of nuclear structure. Nevertheless, the study also shows that the accuracy of present *ab initio* methods and nuclear interactions still needs to be increased to be a quantitative

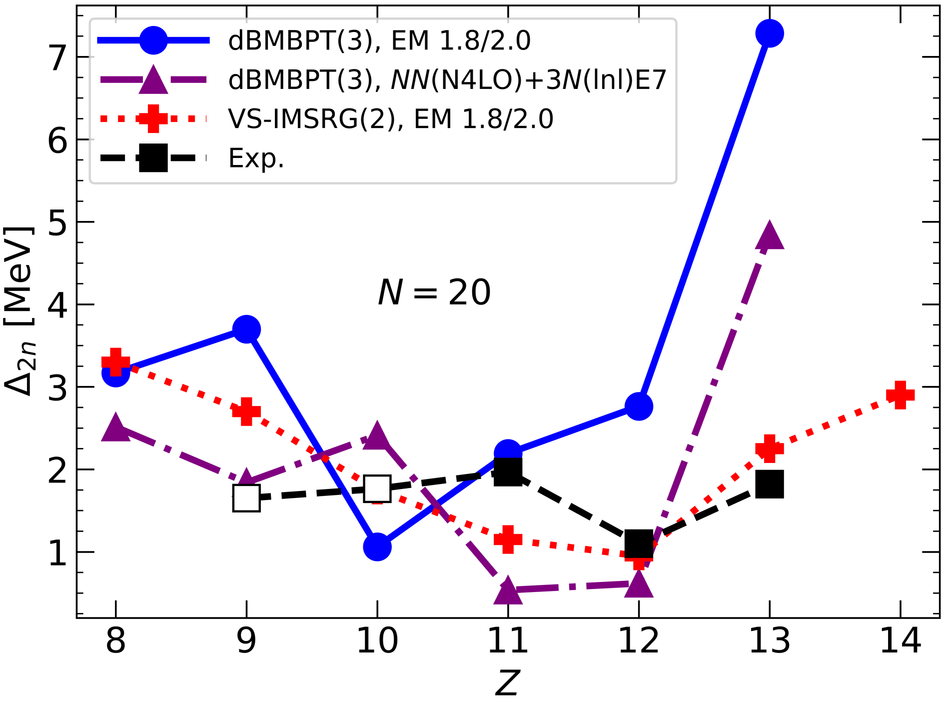

Figure 4.2. Experimental and theoretical two-neutron shell gaps at $N = 20$ for various proton numbers. Results from different many-body methods and interactions (see text for details) are displayed together with experimental data taken from [63]. While measured data are represented with full squares, empty squares label extrapolated data.

tool for the analysis and interpretation of highly precise modern mass measurements.x

In order to push in the direction of increasing the precision of deformed *ab initio* methods, the following chapter (Ch. 5) extends the reach of dBMBPT to a non-perturbative self-consistent method able to incorporate in the calculation summations of infinite number of diagrams.

Chapter 5.

Deformed Dyson self-consistent Green's function

5.1. Introduction

In previous chapters, many-body perturbation theory built on symmetry-breaking reference states was proven to be a convenient and reliable tool to systematically explore bulk properties of medium-mass nuclei, irrespectively of their open- or closed-shell character. The main strength of dBMBPT resides in the low computational cost of low-order calculations. However, such a method is not as flexible and as complete as other, more advanced, many-body techniques. In particular, its application strongly relies on the use of low-momentum interactions. In addition, observables other than ground-state bulk properties are harder to access. A non-perturbative method that has been extensively developed and applied to the description of atomic nuclei in recent years is the self-consistent Green's function approach [14, 88, 89]. While this technique has been extended to $U(1)$-symmetry breaking reference states in the so-called Gorkov framework to address semi-magic nuclei [16], a deformed SCGF implementation amenable to the description of the much larger set of doubly open-shell nuclei is currently missing. The aim of the this chapter is to introduce such a formalism, discuss its numerical implementation and present the first realistic applications to singly and doubly open-shell mid-mass nuclei.

The dBMBPT formalism introduced in Ch. 2 can handle reference states breaking both $SU(2)$ symmetry and $U(1)$ symmetry. While the same route could be followed for SCGF, the resulting numerical implementation would be very heavy and hard to cope with. Instead, the strategy followed here is to build the correlated GFs on states that break solely $SU(2)$ rotational invariance. The rationale supporting this choice is based on three elements:

1. large-scale calculations [6] of open-shell nuclei[1] show that, when starting from state-of-the-art χEFT interactions, dHFB (as well as dBMBPT) solutions with non-zero deformation very rarely also break particle-number symmetry, i.e., only $1-2\,\%$ of the studied nuclei that break $SU(2)$ symmetry also spontaneously break $U(1)$ symmetry;
2. while paying the price of breaking both symmetries at the same time can be afforded at dBMBPT(2) level, it would significantly limit the applicability of a more costly method like SCGF;
3. once $SU(2)$ is broken, it is not necessary to further break $U(1)$ symmetry in even-even nuclei to lift the degeneracy problem of the reference state with respect to

---

[1] Results from a subset of those calculations were discussed in Ch. 3 and 4.

elementary excitations discussed in Ch. 1, i.e. any expansion method based on a reference state that breaks $SU(2)$ but not $U(1)$ is well defined.

For these reasons, restricting a SCGF generalisation to the sole $SU(2)$ breaking constitutes an optimal option at this point in time. As shown in the following sections, the resulting deformed Dyson Self-Consistent Green's function (dSCGF) formalism is able to deliver an accurate description of doubly open-shell systems across a significant range of nuclei.

5.2. Theoretical framework

5.2.1. Basic elements

Green's function-based techniques have been extensively applied to *ab initio* nuclear structure studies [14]. The versatility of such methods allows to determine bulk properties of nuclei such as ground state energy and radii, as well as excitation spectra and optical potentials. While most of *ab initio* techniques are based on the explicit manipulation of the total wave function $|\Psi_k^A\rangle$ [11, 13, 90], Green's function (GF) methods rely on the knowledge of the *single-particle propagator* [88, 91], also referred to as '1-body' or '2-point' GF

$$i g_{\alpha\beta}(t_\alpha - t_\beta) = i g^{2-\mathrm{pt}}_{\alpha\beta}(t_\alpha - t_\beta) \equiv \langle \Psi_0^A | \mathcal{T}[c_\alpha(t_\alpha) c^\dagger_\beta(t_\beta)] | \Psi_0^A \rangle \, . \tag{5.1}$$

Here $\mathcal{T}$ represents the *time ordering* operator and $c^\dagger_\alpha(t_\alpha)$ ($c_\alpha(t_\alpha)$) is the creation (annihilation) operator in the Heisenberg picture. The one-body propagator $g_{\alpha\beta}$ only depends on the time difference $t_\alpha - t_\beta$ due to time-translational invariance. If $t_\alpha > t_\beta$ ($t_\alpha < t_\beta$), the GF represents the probability amplitude to add a particle (hole) to $|\Psi_0^A\rangle$ at time t_α in a single-particle basis state α and let it propagate to a time t_β where it is removed from a (possibly different) single-particle basis state β. It is straightforward to generalize Eq. (5.1) to higher-body GFs, e.g.

$$i g^{4-\mathrm{pt}}_{\alpha\gamma\beta\delta}(t_\alpha, t_\gamma, t_\beta, t_\delta) \equiv \langle \Psi_0^A | \mathcal{T}[c_\gamma(t_\gamma) c_\alpha(t_\alpha) c^\dagger_\beta(t_\beta) c^\dagger_\delta(t_\delta)] | \Psi_0^A \rangle \, , \tag{5.2a}$$

$$i g^{6-\mathrm{pt}}_{\alpha\gamma\varepsilon\beta\delta\varphi}(t_\alpha, t_\gamma, t_\varepsilon, t_\beta, t_\delta, t_\varphi) \equiv \langle \Psi_0^A | \mathcal{T}[c_\varepsilon(t_\varepsilon) c_\gamma(t_\gamma) c_\alpha(t_\alpha) c^\dagger_\beta(t_\beta) c^\dagger_\delta(t_\delta) c^\dagger_\varphi(t_\varphi)] | \Psi_0^A \rangle \, . \tag{5.2b}$$

The 1-body GF itself contains a wealth of information about the structure of the A-nucleon system, including the response to the addition or removal of one particle. The latter in turn provides information on the $A \pm 1$ neighbouring systems and elastic nucleon-nucleus scattering. To access such properties, it is convenient to convert Eq. (5.1) in its spectral representation through a Fourier transform,

$$\begin{aligned} g^{2-\mathrm{pt}}_{\alpha\beta}(\omega) &\equiv g_{\alpha\beta}(\omega) \\ &= \int d\tau_{\alpha\beta} \, e^{i\omega\tau_{\alpha\beta}} g_{\alpha\beta}(\tau_{\alpha\beta}) \\ &\equiv \sum_n \frac{\langle \Psi_0^A | c_\alpha | \Psi_n^{A+1} \rangle \langle \Psi_n^{A+1} | c^\dagger_\beta | \Psi_0^A \rangle}{\omega - (E_n^{A+1} - E_0^A) + i\eta} + \sum_k \frac{\langle \Psi_k^{A-1} | c_\alpha | \Psi_0^A \rangle \langle \Psi_0^A | c^\dagger_\beta | \Psi_k^{A-1} \rangle}{\omega - (E_n^A - E_0^{A-1}) - i\eta} \\ &\equiv \sum_n \frac{(\mathcal{X}_\alpha^n)^* \mathcal{X}_\beta^n}{\omega - \varepsilon_n^+ + i\eta} + \sum_k \frac{\mathcal{Y}_\alpha^k (\mathcal{Y}_\beta^k)^*}{\omega - \varepsilon_k^- - i\eta} , \end{aligned} \tag{5.3}$$

where $\tau_{\alpha\beta} \equiv t_\alpha - t_\beta$ and the operators c_α and $c^\dagger_\alpha$ are now in Schrödinger's picture [91]. The last line of Eq. (5.3) defines the so-called Källén-Lehmann representation of the single-particle propagator. The convention employed in this manuscript is to use the Latin letter

n (k) to label states in the $A+1$ ($A-1$) system. Equation (5.3) allows to straightforwardly access two important quantities.

1. From the numerator, the *transition amplitudes*

   $$\mathcal{X}^n_\alpha \equiv \langle\Psi^{A+1}_n|c^\dagger_\alpha|\Psi^A_0\rangle\,, \tag{5.4a}$$
   $$\mathcal{Y}^k_\alpha \equiv \langle\Psi^{A-1}_k|c_\alpha|\Psi^A_0\rangle\,, \tag{5.4b}$$

   can be obtained from which the elements of the spectroscopic probability matrices associated with one-nucleon addition and removal processes can be computed according to

   $$(S^+_n)_{\alpha\beta} \equiv \langle\Psi^A_0|c_\alpha|\Psi^{A+1}_n\rangle\,\langle\Psi^{A+1}_n|c^\dagger_\beta|\Psi^A_0\rangle\,, \tag{5.5a}$$
   $$(S^-_k)_{\alpha\beta} \equiv \langle\Psi^A_0|c^\dagger_\alpha|\Psi^{A-1}_n\rangle\,\langle\Psi^{A-1}_n|c_\beta|\Psi^A_0\rangle\,. \tag{5.5b}$$

   An important quantity that can be built out from the transition amplitude $\mathcal{Y}^k_\alpha$ is the one-body density matrix

   $$\rho_{\alpha\beta} \equiv \langle\Psi^A_0|c^\dagger_\beta c_\alpha|\Psi^A_0\rangle = \int_{C\uparrow} g_{\alpha\beta}(\omega)\frac{d\omega}{2\pi i} = \sum_k (\mathcal{Y}^k_\beta)^*\mathcal{Y}^k_\alpha, \tag{5.6}$$

   where $C\uparrow$ represents a contour closed on the upper imaginary energy plane. This object can be used to determine any one-body observable in the A-body system, as well as other properties of the system such as the axial deformation (see Sec. 5.5.1 and 5.5.2). The trace of the matrices in Eqs. (5.5) applied over the one-body Hilbert space delivers the *spectroscopic factors*

   $$SF^+_n \equiv \mathrm{Tr}_{\mathcal{H}_1}[\boldsymbol{S}^+_n] = \sum_{\alpha\in\mathcal{H}_1} |\mathcal{X}^n_\alpha|^2, \tag{5.7a}$$
   $$SF^-_k \equiv \mathrm{Tr}_{\mathcal{H}_1}[\boldsymbol{S}^-_k] = \sum_{\alpha\in\mathcal{H}_1} |\mathcal{Y}^k_\alpha|^2, \tag{5.7b}$$

   that quantify the sums of probabilities that an eigenstate of the $A+1$ ($A-1$) system can be described as the addition (removal) of a nucleon to (from) a single-particle state on top of the A-body ground state.

2. From the denominator, the poles

   $$\varepsilon^+_n = E^{A+1}_n - E^A_0\,, \tag{5.8a}$$
   $$\varepsilon^-_k = E^A_0 - E^{A-1}_k\,, \tag{5.8b}$$

   represent respectively one-particle addition and removal energies from the ground state of the A-body system to eigenstates of the $A\pm1$ systems.

In summary, the knowledge of the single-particle propagator in its spectral representation allows to determine the energies of ground and excited states of neighbouring $A\pm1$ nuclei (see Fig. 5.1), as well as the probability amplitudes to reach such eigenstates from the A-body ground state. The determination of analogous information for excited states of the A-body system itself requires instead the knowledge of the 2-body Green's function, typically expressed in terms of the polarization propagator [88].

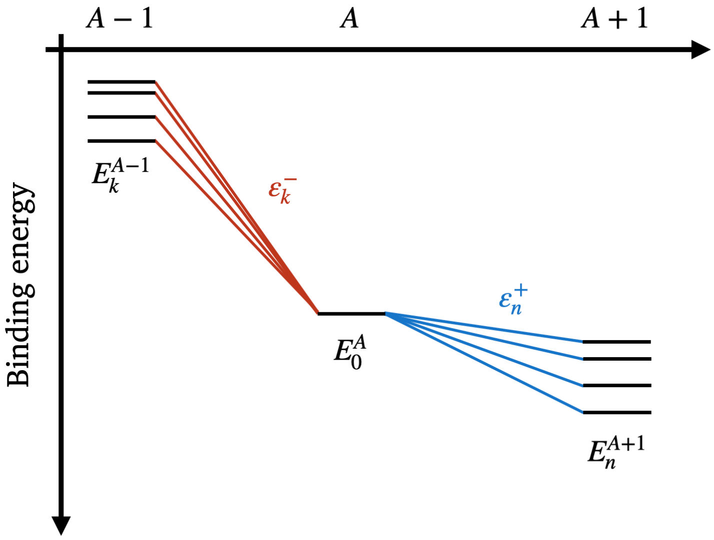

Figure 5.1. Schematic representation of the $A-1$ and $A+1$ energy spectra accessible from the ground-state of the A-body system through the knowledge of the 1B-Green's function poles.

5.2.2. Dyson equation

The 1-B Green's function is fully determined by solving the Dyson equation

$$g_{\alpha\beta}(\omega) = g^{(0)}_{\alpha\beta}(\omega) + \sum_{\gamma\delta} g^{(0)}_{\alpha\gamma}\, \Sigma^{\star}_{\gamma\delta}(\omega)\, g_{\delta\beta}(\omega). \tag{5.9}$$

Here $g^{(0)}_{\alpha\beta}(\omega)$ represents an ansatz or reference propagator (usually referred to as *unperturbed* propagator). Correspondingly, the full GF $g_{\alpha\beta}(\omega)$ is called *correlated* or *dressed* propagator. The *irreducible self-energy* $\Sigma^{\star}_{\gamma\delta}(\omega)$ represents the energy-dependent potential felt by a nucleon due to its interaction with the medium. At positive energies, it can be formally related to the Feshbach optical potential for nucleon-nucleus elastic scattering [92]. Equation (5.9) is diagrammatically represented in Fig. 5.2. Numerically, such equation can be solved iteratively by re-inserting the dressed propagator into the right-hand-side until convergence.

In principle, the exact knowledge of the self-energy allows to determine exactly the dressed propagator. In practice, the self-energy needs to be approximated in numerical calculations and different strategies exist to accomplish such a goal. The standard approximation scheme employed in *ab initio* nuclear structure, which will be employed in the present work, is given by the Algebraic Diagrammatic Construction at order n (ADC(n)) [93]. The first ADC order for the self-energy expansion (ADC(1)) reduces the Dyson equation to the standard Hartree-Fock equation.

The Dyson equation in Eq. (5.9) corresponds to a re-writing of the non-relativistic Schrödinger equation, Eq. (0.1), in terms of Green's functions. Recasting the Schrödinger equation in the form of a self-consistent equation is non-trivial and can be achieved following two different paths:

1. the equation-of-motion technique;

2. the perturbative expansion of the single-particle propagator.

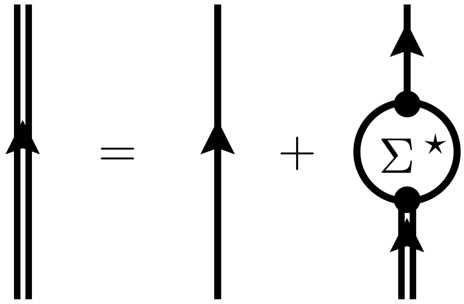

Figure 5.2. Diagrammatic representation of the Dyson equation. *Single lines* represent the unperturbed propagator and *double lines* represent the dressed propagator.

Since the present work does not aim at providing a comprehensive overview of Green's functions but simply at introducing the basic concepts, only the second path is sketched in the following. For full details on the two derivations the reader is referred to [88].

For both procedures, it is first necessary to introduce the splitting of the Hamiltonian

$$H = \underbrace{T+U}_{\equiv H_0} + \underbrace{V+W-U}_{\equiv H_1} \tag{5.10}$$

into an *unperturbed part* H_0 and a *perturbation* H_1. U labels an auxiliary one-body potential that is arbitrary but, in practice, must be suitably chosen to optimize the convergence of the perturbation series. The choice of U defines a reference state $|\Phi_0^A\rangle$, the lowest eigenstate of H_0, and the associated unperturbed propagator

$$i g^{(0)}_{\alpha\beta}(t_\alpha - t_\beta) \equiv \langle \Phi_0^A | \mathcal{T}[c^I_\alpha(t_\alpha) c^{I\dagger}_\beta(t_\beta)] | \Phi_0^A \rangle \,, \tag{5.11}$$

where the superscript 'I' indicates that the corresponding operators are now represented in the interaction picture. Exploiting the properties of the time-evolution operator, Eq. (5.11) can then be perturbatively expanded with respect to H_1

$$\begin{aligned} g_{\alpha\beta}(t_\alpha - t_\beta) = & - i \sum_{n=0}^{+\infty} \frac{1}{n!} \int dt_1 \ldots \int dt_n \\ & \times \langle \Psi_0^A | \mathcal{T}[H_1(t_1) \ldots H_1(t_n) c^I_\alpha(t_\alpha) c^{I\dagger}_\beta(t_\beta)] | \Psi_0^A \rangle_{\text{conn}} \,, \end{aligned} \tag{5.12}$$

where the subscript 'conn' indicates that only connected diagrams must be retained when applying Wick's theorem. The Fourier transform of Eq. (5.12) to the energy domain contains interaction terms that can be recast into the irreducible self-energy, reading

$$\begin{aligned} g_{\alpha\beta}(\omega) = & \, g_{0\,\alpha\beta}(\omega) \\ & + \sum_{\gamma\delta} g_{0\,\alpha\gamma}(\omega) \Sigma^*_{\gamma\delta}(\omega) g_{0\,\delta\beta}(\omega) \\ & + \sum_{\gamma\delta\varepsilon\varphi} g_{0\,\alpha\gamma}(\omega) \Sigma^*_{\gamma\delta}(\omega) g_{0\,\delta\varepsilon}(\omega) \Sigma^*_{\varepsilon\varphi}(\omega) g_{0\,\varphi\beta} \\ & + \ldots . \end{aligned} \tag{5.13}$$

Since the infinite sum of all terms after the first self-energy coincides with the full propagator itself, by gathering them together the Dyson equation (5.9) is recovered.

5.2.3. Algebraic diagrammatic construction method

The irreducible[2] self-energy entering Eq. (5.9) can be split into 3 different parts

$$\Sigma^{\star}_{\alpha\beta}(\omega) = -u_{\alpha\beta} + \Sigma^{(\infty)}_{\alpha\beta} + \widetilde{\Sigma}_{\alpha\beta}(\omega), \tag{5.14}$$

where the matrix element of the auxiliary potential $u_{\alpha\beta}$ has been isolated from the proper self-energy. The quantity $\Sigma^{(\infty)}_{\alpha\beta}$ represents the *static* part of the self-energy and it can be thought of as the mean field that a nucleon feels due to its interaction with the other nucleons. It can be obtained by taking the limit of the full self-energy to $\omega \to \pm\infty$. On the other hand, $\widetilde{\Sigma}_{\alpha\beta}(\omega)$ represents the *dynamical* part of the self-energy that includes information about dynamical excitations of the system. Whilst the contribution $\Sigma^{(\infty)}_{\alpha\beta}$ can be included exactly in a numerical calculation, $\widetilde{\Sigma}_{\alpha\beta}(\omega)$ is the hard-to-handle part of the total self-energy and different strategies can be designed in order to approximate it. While the simplest technique constitutes in truncating the perturbative expansion at a defined order, more refined methods have been developed in the last decades to include resummation of infinite perturbative contributions. The route adopted in this work, which is the typical choice in *ab initio* nuclear structure, is the ADC truncation.

The ADC method has been widely employed in quantum chemistry in the past [93–95]. Recently, it has been successfully imported in nuclear structure [16, 96, 97]. The unique characteristic of the ADC(n) approach is that, in addition to including all perturbative contributions up to order n, it maintains the analytical structure of the exact self-energy. This guarantees that certain key properties are preserved, namely the non-violation of causality and the possibility to recast Dyson's equation as an energy-independent eigenvalue problem, as discussed in Sec. 5.2.4. The starting point of the ADC is the following spectral representation of the exact self-energy

$$\begin{aligned}\Sigma^{*}_{\alpha\beta}(\omega) = &- u_{\alpha\beta} + \Sigma^{(\infty)}_{\alpha\beta} \\ &+ \sum_{rr'} M^{\dagger}_{\alpha,r} \left[\frac{1}{\omega - [E^{>} + C]_{r,r'} + i\eta} \right]_{r,r'} M_{r',\beta} \\ &+ \sum_{ss'} N_{\alpha,s} \left[\frac{1}{\omega - (E^{<} + D) - i\eta} \right]_{s,s'} N^{\dagger}_{s',\beta},\end{aligned} \tag{5.15}$$

where $E^{>}$ and $E^{<}$ denote the unperturbed energies of forward (fw) and backward (bw) *intermediate state configurations* (ISCs). Those represent configurations beyond the single-particle model that encode the complex many-body dynamics, labelled by indices r and s in the particle-addition ($2p1h$, $3p2h$, …) and particle-removal ($2h1p$, $3h2p$, …) channel respectively. Coupling matrices M and N connect single-particle states to ISCs, while matrices C and D describe couplings between two ISCs. While the latter are dense matrices, $E^{>}$ and $E^{<}$ are diagonal in the ISC space, i.e. $E^{>}_{rr'} = \delta_{rr'} E^{>}_{r}$ and $E^{<}_{ss'} = \delta_{ss'} E^{<}_{s}$.

Next, the building blocks of such spectral representation are expanded as follows.

- Coupling matrices M and N are expanded in perturbation

$$M_{r,\alpha} = M^{(\mathrm{I})}_{r,\alpha} + M^{(\mathrm{II})}_{r,\alpha} + M^{(\mathrm{III})}_{r,\alpha} + \dots \tag{5.16a}$$

$$N_{\alpha,s} = N^{(\mathrm{I})}_{\alpha,s} + N^{(\mathrm{II})}_{\alpha,s} + N^{(\mathrm{III})}_{\alpha,s} + \dots \tag{5.16b}$$

---

[2] In the diagrammatic language, this object indeed contains only *one-particle irreducible* contributions, i.e. diagrams that can not be split into two by cutting only one fermionic line. The remaining *one-particle reducible* diagrams are then generated by subsequent insertions of $\Sigma^{\star}$, as evident from Eq. (5.13).

$$\Sigma^{(1)}_{\alpha\beta}(\omega) =$$

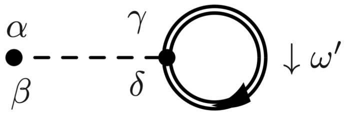

Figure 5.3. Diagram contributing to the first-order approximation of the self-energy in the ADC scheme.

- Denominators are expanded in a power series

$$\frac{1}{A-B} = \frac{1}{A} + \frac{1}{A}B\frac{1}{A-B} = \frac{1}{A} + \frac{1}{A}B\frac{1}{A} + \frac{1}{A}B\frac{1}{A}B\frac{1}{A} + \cdots , \tag{5.17}$$

with $(A, B) = (\omega - E^{>}, C)$ and $(A, B) = (\omega - E^{<}, D)$ respectively.

This defines a perturbative expansion for the whole dynamical self-energy, which reads as

$$\begin{aligned}
\widetilde{\Sigma}_{\alpha\beta}(\omega) \;=\; & \sum_r M^{(\mathrm{I})\dagger}_{\alpha r}\left[\frac{1}{\omega - E^{>}_r + \mathrm{i}\eta}\right] M^{(\mathrm{I})}_{r\beta} \\
& + \sum_r M^{(\mathrm{II})\dagger}_{\alpha r}\left[\frac{1}{\omega - E^{>}_r + \mathrm{i}\eta}\right] M^{(\mathrm{I})}_{r\beta} + \sum_r M^{(\mathrm{I})\dagger}_{\alpha r}\left[\frac{1}{\omega - E^{>}_r + \mathrm{i}\eta}\right] M^{(\mathrm{II})}_{r\beta} \\
& + \sum_{rr'} M^{(\mathrm{I})\dagger}_{\alpha r}\left[\frac{1}{\omega - E^{>}_r + \mathrm{i}\eta}\right] C_{rr'}\left[\frac{1}{\omega - E^{>}_{r'} + \mathrm{i}\eta}\right] M^{(\mathrm{I})}_{r'\beta} + \dots \\
& + \sum_s N^{(\mathrm{I})}_{\alpha s}\left[\frac{1}{\omega - E^{<}_s - \mathrm{i}\eta}\right] N^{(\mathrm{I})\dagger}_{s\beta} \\
& + \sum_s N^{(\mathrm{II})}_{\alpha s}\left[\frac{1}{\omega - E^{<}_s - \mathrm{i}\eta}\right] N^{(\mathrm{I})\dagger}_{s\beta} + \sum_s N^{(\mathrm{I})}_{\alpha s}\left[\frac{1}{\omega - E^{<}_s - \mathrm{i}\eta}\right] N^{(\mathrm{II})\dagger}_{s\beta} \\
& + \sum_{ss'} N^{(\mathrm{I})}_{\alpha s}\left[\frac{1}{\omega - E^{<}_s - \mathrm{i}\eta}\right] D_{ss'}\left[\frac{1}{\omega - E^{<}_{s'} - \mathrm{i}\eta}\right] N^{(\mathrm{I})\dagger}_{s'\beta} + \dots ,
\end{aligned} \tag{5.18}$$

where the first and fourth lines represent respectively *fw* and *bw* second-order contributions, the remaining terms corresponding to third-order contributions and the dots to higher-order contributions.

Finally, the various terms entering Eq. (5.18) are determined by matching them, at each order n, to the standard perturbative expansion of the dynamical self-energy. Below the explicit matching at second order, i.e. the ADC(2) truncation employed in the present work, is given.

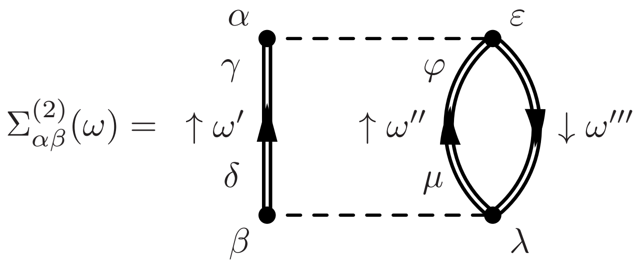

Figure 5.4. Diagram contributing to the second-order approximation of the self-energy in the ADC scheme.

First-order self-energy

The first-order contribution to the self-energy is represented in Fig. 5.3 and reads as

$$\begin{aligned}\Sigma^{(1)}_{\alpha\beta}(\omega) &= -i\int_{C^{\uparrow}} \frac{d\omega'}{2\pi} \sum_{\gamma\delta} \bar{v}_{\alpha\gamma\beta\delta}\, g_{\delta\gamma}(\omega') \\ &= -i\int_{C^{\uparrow}} \frac{d\omega'}{2\pi} \sum_{\gamma\delta} \bar{v}_{\alpha\gamma\beta\delta} \sum_{n} \frac{(\mathcal{X}^{n}_{\delta})^{*}\mathcal{X}^{n}_{\gamma}}{\omega - \varepsilon^{+}_{n} + i\eta} - i\int_{C^{\uparrow}} \frac{d\omega'}{2\pi} \sum_{\gamma\delta} \bar{v}_{\alpha\gamma\beta\delta} \sum_{k} \frac{\mathcal{Y}^{k}_{\delta}(\mathcal{Y}^{k}_{\gamma})^{*}}{\omega - \varepsilon^{-}_{k} - i\eta} \\ &= \sum_{\gamma\delta} \bar{v}_{\alpha\gamma\beta\delta} \sum_{k} \mathcal{Y}^{k}_{\delta}(\mathcal{Y}^{k}_{\gamma})^{*} \\ &= \sum_{\gamma\delta} \bar{v}_{\alpha\gamma\beta\delta}\, \rho_{\delta\gamma}\,,\end{aligned} \tag{5.19}$$

Second-order self-energy

At second-order, only one diagram contributes to the self-energy (Fig. 5.4) reading as

$$\begin{aligned}\Sigma^{(2)}_{\alpha\beta}(\omega) &= \frac{1}{8\pi^{2}} \int d\omega' d\omega'' d\omega''' \sum_{\gamma\delta\varepsilon\varphi\mu\lambda} \bar{v}_{\alpha\varepsilon\gamma\varphi}\bar{v}_{\delta\mu\beta\lambda}\, g_{\gamma\delta}(\omega')g_{\varphi\mu}(\omega'')g_{\lambda\varepsilon}(\omega''')\delta(\omega - \omega' - \omega'' - \omega''') \\ &= \frac{1}{2}\int \frac{d\omega'}{2\pi}\frac{d\omega''}{2\pi} \sum_{\gamma\delta\varepsilon\varphi\mu\lambda} \bar{v}_{\alpha\varepsilon\gamma\varphi}\bar{v}_{\delta\mu\beta\lambda}\, g_{\gamma\delta}(\omega')g_{\varphi\mu}(\omega'')g_{\lambda\varepsilon}(\omega' + \omega'' - \omega) \\ &= \frac{1}{2}\int \frac{d\omega'}{2\pi}\frac{d\omega''}{2\pi} \sum_{\substack{\gamma\delta\varepsilon\varphi\mu\lambda \\ n_1 n_2 n_3 \\ k_1 k_2 k_3}} \bar{v}_{\alpha\varepsilon\gamma\varphi}\bar{v}_{\delta\mu\beta\lambda} \left\{ \frac{\mathcal{X}^{n_1}_{\gamma}\mathcal{X}^{n_1 *}_{\delta}}{\omega' - \varepsilon^{+}_{n_1} + i\eta} + \frac{\mathcal{Y}^{k_1 *}_{\gamma}\mathcal{Y}^{k_1}_{\delta}}{\omega' - \varepsilon^{+}_{k_1} - i\eta} \right\} \\ &\quad \times \left\{ \frac{\mathcal{X}^{n_2}_{\varphi}\mathcal{X}^{n_2 *}_{\mu}}{\omega'' - \varepsilon^{+}_{n_2} + i\eta} + \frac{\mathcal{Y}^{k_2 *}_{\varphi}\mathcal{Y}^{k_2}_{\mu}}{\omega'' - \varepsilon^{+}_{k_2} - i\eta} \right\} \\ &\quad \times \left\{ \frac{\mathcal{X}^{n_3}_{\lambda}\mathcal{X}^{n_3 *}_{\varepsilon}}{\omega' + \omega'' - \omega - \varepsilon^{+}_{n_3} + i\eta} + \frac{\mathcal{Y}^{k_3 *}_{\lambda}\mathcal{Y}^{k_3}_{\varepsilon}}{\omega' + \omega'' - \omega - \varepsilon^{-}_{k_3} - i\eta} \right\} \\ &= \frac{1}{2} \sum_{\substack{\gamma\delta\varepsilon\varphi\mu\lambda \\ n_1 n_2 n_3 \\ k_1 k_2 k_3}} \bar{v}_{\alpha\varepsilon\gamma\varphi}\bar{v}_{\delta\mu\beta\lambda} \left\{ \frac{\mathcal{X}^{n_1}_{\gamma}\mathcal{X}^{n_1 *}_{\delta}\mathcal{X}^{n_2}_{\phi}\mathcal{X}^{n_2 *}_{\mu}\mathcal{Y}^{k_3 *}_{\lambda}\mathcal{Y}^{k_3}_{\varepsilon}}{\omega - (\varepsilon^{+}_{n_1} + \varepsilon^{+}_{n_2} - \varepsilon^{-}_{k_3}) + i\eta} + \frac{\mathcal{Y}^{k_1 *}_{\gamma}\mathcal{Y}^{k_1}_{\delta}\mathcal{Y}^{k_2 *}_{\phi}\mathcal{Y}^{k_2}_{\mu}\mathcal{X}^{n_3}_{\lambda}\mathcal{X}^{n_3 *}_{\varepsilon}}{\omega - (\varepsilon^{-}_{k_1} + \varepsilon^{-}_{k_2} - \varepsilon^{+}_{n_3}) - i\eta} \right\}.\end{aligned} \tag{5.20}$$

ADC(2)

The comparison of Eq. (5.18) with Eq.(5.20) allows to identify the first-order coupling matrices $M^{(\mathrm{I})}$ and $N^{(\mathrm{I})}$, as well as the corresponding unperturbed energies. By construction, interaction matrices C and D are zero at this order. One thus has

$$\begin{aligned}
M^{(\mathrm{I})}_{r\alpha} &= M_{n_1 n_2 k_3 \alpha} = \frac{1}{\sqrt{2}} \sum_{\mu\nu\lambda} \mathcal{X}^{n_1}_{\mu}\, \mathcal{X}^{n_2}_{\mu}\, \mathcal{Y}^{k_3}_{\lambda}\, \bar{v}_{\mu\nu\alpha\lambda}\,, && (5.21a)\\
E^{>}_{r} &= E^{>}_{n_1 n_2 k_3} = \mathrm{diag}\left(\varepsilon^{+}_{n_1} + \varepsilon^{+}_{n_2} - \varepsilon^{-}_{k_3}\right)\,, && (5.21b)\\
C_{r,r'} &= C_{n_1 n_2 k_3, n'_1 n'_2 k'_3} = 0\,, && (5.21c)\\
N^{(\mathrm{I})}_{s\alpha} &= N_{k_1 k_2 n_3 \alpha} = \frac{1}{\sqrt{2}} \sum_{\mu\nu\lambda} \mathcal{Y}^{k_1}_{\mu}\, \mathcal{Y}^{k_2}_{\nu}\, \mathcal{X}^{n_3}_{\lambda}\, \bar{v}_{\mu\nu\alpha\lambda}\,, && (5.21d)\\
E^{<}_{s} &= E^{<}_{k_1 k_2 n_3} = \mathrm{diag}\left(\varepsilon^{+}_{k_1} + \varepsilon^{+}_{k_2} - \varepsilon^{-}_{n_3}\right)\,, && (5.21e)\\
D_{s,s'} &= D_{k_1 k_2 n_3, k'_1 k'_2 n'_3} = 0\,, && (5.21f)
\end{aligned}$$

where the collective indexes $r \equiv (n_1, n_2, k_3)$ and $s \equiv (k_1, k_2, n_3)$ relative to *pph* and *hhp* ISCs, respectively, have been specified.

5.2.4. Solution of the Dyson equation

Once an appropriate approximation to the self-energy have been established, the Dyson equation (5.9) can be solved. A summary of the main steps leading to a form suitable for a numerical implementation is given here for the ADC(2) scheme, while details can be found in, e.g., Ref. [98]. First of all, let us define the collective index i

$$\varepsilon_i \longrightarrow \begin{cases} \varepsilon^{+}_{n} & \text{for particle states} \\ \varepsilon^{-}_{k} & \text{for hole states} \end{cases} \quad \text{and} \quad \mathcal{Z}^{i}_{\alpha} \longrightarrow \begin{cases} (\mathcal{X}^{n}_{\alpha})^{*} & \text{for particle states} \\ \mathcal{Y}^{k}_{\alpha} & \text{for hole states} \end{cases} \tag{5.22}$$

grouping together hole and particle states. Since the direct solution of Eq. (5.9) can be problematic due to energy denominators, an equivalent eigenvalue equation can be obtained extracting the poles of the single-particle propagator

$$\lim_{\omega \to \varepsilon_i} (\omega - \varepsilon_i) \left\{ g_{\alpha\beta}(\omega) = g^{(0)}_{\alpha\beta}(\omega) + g^{(0)}_{\alpha\gamma}(\omega) \Sigma^{*}_{\gamma\delta}(\omega) g_{\delta\beta}(\omega) \right\}, \tag{5.23}$$

which leads to

$$\mathcal{Z}^{i}_{\alpha} (\mathcal{Z}^{i}_{\beta})^{*} = g^{(0)}_{\alpha\gamma}(\omega) \Sigma^{*}_{\gamma\delta}(\omega) \mathcal{Z}^{i}_{\delta} (\mathcal{Z}^{i}_{\beta})^{*} \Big|_{\omega = \varepsilon_i} . \tag{5.24}$$

Dividing both sides of Eq. (5.24) by $(\mathcal{Z}^{i}_{\beta})^{*}$ and exploiting the fact that $[g^{(0)}(\omega)]^{-1} = \omega - H_0$, the following eigenvalue equation is obtained

$$\begin{aligned}
\varepsilon_i \mathcal{Z}^{i}_{\alpha} &= \sum_{\delta} \left\{ t + u + \Sigma^{*}(\omega) \right\}_{\alpha\delta} \mathcal{Z}^{i}_{\delta} \Big|_{\omega = \varepsilon_i} \\
&= \sum_{\delta} \Bigg\{ t_{\alpha\delta} + \Sigma^{(\infty)}_{\alpha\delta} + \sum_{r} M^{\dagger}_{\alpha r} \frac{1}{\omega - E^{>}_{r} + i\eta} M_{r\delta} \\
&\qquad + \sum_{s} N^{\dagger}_{\alpha s} \frac{1}{\omega - E^{<}_{s} - i\eta} N_{s\delta} \Bigg\} \mathcal{Z}^{i}_{\delta} \Big|_{\omega = \varepsilon_i} .
\end{aligned} \tag{5.25}$$

This equation is manifestly energy dependent but does not depend on the auxiliary potential U introduced in Eq. (5.14). Equation (5.25) is numerically demanding since, given the dependence on ω, many diagonalizations are required for the extraction of the desired eigenvalues. In order to overcome this problem, new quantities $\mathcal{W}$ and $\mathcal{V}$ are conveniently defined as

$$\left[\varepsilon_i - E_r^>\right] \mathcal{W}_r^i \equiv \sum_\delta M_{r\delta} \mathcal{Z}_\delta^i \,, \tag{5.26a}$$

$$\left[\varepsilon_i - E_s^<\right] \mathcal{V}_s^i \equiv \sum_\delta N_{s\delta} \mathcal{Z}_\delta^i \,, \tag{5.26b}$$

where the limit $i\eta \to 0$ was taken. Equation (5.25) is then recast into a large-dimensional energy-independent matrix diagonalization problem

$$\begin{pmatrix} t_{\alpha\delta} + \Sigma_{\alpha\delta}^{(\infty)} & M_{\alpha r}^\dagger & N_{\alpha s}^\dagger \\ M_{r\delta} & E_r^> & 0 \\ N_{s\delta} & 0 & E_s^< \end{pmatrix} \begin{pmatrix} \mathcal{Z}_\delta^i \\ \mathcal{W}_r^i \\ \mathcal{V}_s^i \end{pmatrix} = \varepsilon_i \begin{pmatrix} \mathcal{Z}_\alpha^i \\ \mathcal{W}_r^i \\ \mathcal{V}_s^i \end{pmatrix} , \tag{5.27}$$

where the eigenvectors satisfy the normalization condition

$$\sum_\alpha |\mathcal{Z}_\alpha^i|^2 + \sum_r |\mathcal{W}_r^i|^2 + \sum_s |\mathcal{V}_s^i|^2 = 1. \tag{5.28}$$

Equation (5.27) constitutes the final equation implemented in the numerical code.

5.2.5. $U(1)$-symmetry breaking Gorkov framework

The Dyson framework introduced in the previous sections can be generalized to the study superfluid systems. This can be accomplished by a formalism that allows building the SCGF expansion on top of a particle-number-symmetry breaking reference state. Such a method has been developed in nuclear structure in the frame of Gorkov Self-Consistent Green's functions (GSCGF). While Gorkov ADC(2) [16, 17] has been operational for some time, Gorkov ADC(3) has been recently formalized [97].

The GSCGF method is based on a many-body wave function without a well-defined number of particles, i.e. which can be described as the superposition

$$|\Psi_0\rangle = \sum_A^{\text{even}} |\Psi_0^A\rangle \,. \tag{5.29}$$

The single-particle propagator is then generalized to a set of four *Gorkov propagators* [99]

$$ig_{\alpha\beta}^{11}(t_\alpha - t_\beta) \equiv \langle \Psi_0 | \mathcal{T}[c_\alpha(t_\alpha) c_\beta^\dagger(t_\beta)] | \Psi_0 \rangle \,, \tag{5.30a}$$

$$ig_{\alpha\beta}^{12}(t_\alpha - t_\beta) \equiv \langle \Psi_0 | \mathcal{T}[c_\alpha(t_\alpha) \eta_\beta c_{\bar\beta}^\dagger(t_\beta)] | \Psi_0 \rangle \,, \tag{5.30b}$$

$$ig_{\alpha\beta}^{21}(t_\alpha - t_\beta) \equiv \langle \Psi_0 | \mathcal{T}[\eta_\alpha c_{\bar\alpha}(t_\alpha) c_\beta^\dagger(t_\beta)] | \Psi_0 \rangle \,, \tag{5.30c}$$

$$ig_{\alpha\beta}^{22}(t_\alpha - t_\beta) \equiv \langle \Psi_0 | \mathcal{T}[\eta_\alpha c_{\bar\alpha}(t_\alpha) \eta_\beta c_{\bar\beta}^\dagger(t_\beta)] | \Psi_0 \rangle \,, \tag{5.30d}$$

that can be gathered together via the *Nambu notation* [100, 101]

$$i\boldsymbol{g}_{\alpha\beta}(t_\alpha - t_\beta) \equiv i \begin{pmatrix} g_{\alpha\beta}^{11}(t_\alpha - t_\beta) & g_{\alpha\beta}^{12}(t_\alpha - t_\beta) \\ g_{\alpha\beta}^{21}(t_\alpha - t_\beta) & g_{\alpha\beta}^{22}(t_\alpha - t_\beta) \end{pmatrix} . \tag{5.31}$$

The Dyson equation generalizes for the Gorkov propagators as the *Gorkov equation*

$$\boldsymbol{g}_{\alpha\beta}(\omega) = \boldsymbol{g}_{0\,\alpha\beta}(\omega) + \sum_{\gamma\delta} \boldsymbol{g}_{0\,\alpha\gamma}(\omega)\boldsymbol{\Sigma}^{*}_{\gamma\delta}(\omega)\boldsymbol{g}_{\gamma\beta}(\omega), \tag{5.32}$$

where the self-energy is now a four-component matrix

$$\boldsymbol{\Sigma}^{*}_{\alpha\beta}(\omega) \equiv \begin{pmatrix} \Sigma^{*11}_{\alpha\beta}(\omega) & \Sigma^{*12}_{\alpha\beta}(\omega) \\ \Sigma^{*21}_{\alpha\beta}(\omega) & \Sigma^{*22}_{\alpha\beta}(\omega) \end{pmatrix} \tag{5.33}$$

whose elements are to be approximated employing the ADC expansion.

The Gorkov SCGF formalism has been successfully employed in the description of singly open-shell systems [14, 26, 65] and constitutes a state-of-the art tool to study the impact of superfluidity in atomic nuclei.

5.3. Working equations

The matrix form of Dyson's equation (5.27) translates into different explicit expressions depending on the symmetries at play in a given implementation. In the following, the working equations are specified to the case of deformed axially-symmetric many-body states. For this purpose, let us assume that many-body states carry good isospin (T_0), parity (Π) and angular momentum projection (M). On the other hand, since rotational symmetry is broken, good total angular momentum J is lost. Furthermore, let us consider the ground-state of an even-even system characterized by $M^{\Pi} = 0^{+}$.

5.3.1. Transition amplitudes and one-body density matrix

Let us start from the expressions of the transition amplitudes $\mathcal{X}^{n}_{\alpha}$ and $\mathcal{Y}^{k}_{\alpha}$ defined in Eqs. (5.4). Given the parity operator

$$\Pi \left|\alpha\right\rangle = \pi_\alpha \left|\alpha\right\rangle \ , \tag{5.34}$$

the creation operator $a^{\dagger}_{\alpha}$ can be taken to satisfy the relation

$$\Pi c^{\dagger}_{\alpha} \Pi^{\dagger} = \pi_\alpha c^{\dagger}_{\alpha} \, , \tag{5.35}$$

whose expectation value with respect to states $|\Psi_n\rangle$ and $|\Psi_0\rangle$ reads

$$\langle \Psi^{A+1}_{n} | \Pi c^{\dagger}_{\alpha} \Pi^{\dagger} | \Psi^{A}_{0} \rangle = \pi_\alpha \langle \Psi^{A+1}_{n} | c^{\dagger}_{\alpha} | \Psi^{A}_{0} \rangle \ . \tag{5.36}$$

On the left-hand side, the action of the parity operator on the states gives

$$\langle \Psi^{A+1}_{n} | \Pi c^{\dagger}_{\alpha} \Pi^{\dagger} | \Psi^{A}_{0} \rangle = \pi_n \Pi \langle \Psi^{A+1}_{n} | c^{\dagger}_{\alpha} | \Psi^{A}_{0} \rangle \, , \tag{5.37}$$

which implies $\pi_\alpha = \pi_n \Pi$. For a positive-parity ground state this leads to $\pi_\alpha = \pi_n$. Similarly, the additive property of isospin projection implies implies $t_\alpha = t_n$. Finally, symmetry relations involving angular momentum projections m can be exploited. Following App. D.2 one can prove that the operator $c^{\dagger}_{\alpha}$ is the (m_α)-th components of an Axial Tensor (AT). Employing Eq. (D.8), one then demonstrates the identity $m_\alpha + M = m_n$, which reduces to $m_\alpha = m_n$ since in the present case $M = 0$.

Collecting together the relations obtained for isospin, parity and angular momentum projections, it follows that the spectroscopic amplitude $\mathcal{X}_\alpha^n$ assumes the block structure

$$\begin{aligned} \mathcal{X}_\alpha^n &= \delta_{t_\alpha t_n} \delta_{\pi_\alpha \pi_n} \delta_{m_\alpha, m_n} \langle \Psi_n^{A+1} | c_\alpha^\dagger | \Psi_0^A \rangle \\ &\equiv \delta_{t_\alpha t_n} \delta_{\pi_\alpha \pi_n} \delta_{m_\alpha m_n} \mathcal{X}_{N_\alpha N_k}^{[m\pi t]_\alpha} \,. \end{aligned} \tag{5.38a}$$

Proceeding in the same way for $(\mathcal{Y}_\alpha^k)^*$, Eq. (D.8) imposes the condition $m_\alpha + m_k = M = 0$ and one finds

$$\begin{aligned} (\mathcal{Y}_\alpha^k)^* &= \delta_{t_\alpha t_n} \delta_{\pi_\alpha \pi_n} \delta_{-m_\alpha m_k} \langle \Psi_0^A | c_\alpha^\dagger | \Psi_k^{A-1} \rangle \\ &\equiv \delta_{t_\alpha t_k} \delta_{\pi_\alpha \pi_k} \delta_{-m_\alpha m_k} (\mathcal{Y}_{N_\alpha N_k}^{[m\pi t]_\alpha})^* \,. \end{aligned} \tag{5.38b}$$

The spectroscopic amplitude $\mathcal{Y}_\alpha^k$ than displays the same block-diagonal structure than in Eq. (5.38b)[3].

These definitions also lead to the following block-diagonal structure for the one-body density matrix

$$\begin{aligned} \rho_{\alpha\beta} &= \sum_k (\mathcal{Y}_\beta^k)^* \mathcal{Y}_\alpha^k \\ &= \delta_{t_\alpha t_\beta} \delta_{\pi_\alpha \pi_\beta} \delta_{m_\alpha m_\beta} \sum_{N_k} (\mathcal{Y}_{N_\beta N_k}^{[m\pi t]_\alpha})^* \mathcal{Y}_{N_\alpha N_k}^{[m\pi t]_\alpha} \\ &\equiv \delta_{t_\alpha t_\beta} \delta_{\pi_\alpha \pi_\beta} \delta_{m_\alpha m_\beta} \, \rho_{N_\alpha N_\beta}^{[m\pi t]_\alpha} \,. \end{aligned} \tag{5.39}$$

5.3.2. First-order self-energy

Next, let us consider the mean-field-like part of the Dyson matrix, i.e. the upper-left submatrix reading as

$$\begin{aligned} h_{\alpha\gamma} &\equiv t_{\alpha\gamma} + \Sigma_{\alpha\gamma}^{(\infty)} \\ &= t_{\alpha\gamma} + \sum_{\beta\delta} \bar{v}_{\alpha\beta\gamma\delta} \, \rho_{\delta\beta} \,, \end{aligned} \tag{5.40}$$

where the expression for $\Sigma_{\alpha\gamma}^{(\infty)}$ was derived in Eq. (5.3). Employing Eq. (5.39) and exploiting the fact that the kinetic-energy and two-body interaction matrix elements conserve isospin, parity and angular-momentum projection, i.e. specifically

$$\begin{aligned} t_{\alpha\gamma} &= \delta_{t_\alpha t_\gamma} \, \delta_{\pi_\alpha \pi_\gamma} \, \delta_{m_\alpha m_\gamma} t_{\alpha\gamma} \\ &\equiv \delta_{t_\alpha t_\gamma} \, \delta_{\pi_\alpha \pi_\gamma} \, \delta_{m_\alpha m_\gamma} \, t_{N_\alpha N_\gamma}^{[m\pi t]_\alpha} \,, \end{aligned} \tag{5.41a}$$

$$\begin{aligned} \bar{v}_{\alpha\beta\gamma\delta} &= \delta_{t_\alpha + t_\beta, t_\gamma + t_\delta} \, \delta_{\pi_\alpha \pi_\beta, \pi_\gamma \pi_\delta} \, \delta_{m_\alpha + m_\beta, m_\gamma + m_\delta} \, \bar{v}_{\alpha\beta\gamma\delta} \\ &\equiv \delta_{t_\alpha + t_\beta, t_\gamma + t_\delta} \, \delta_{\pi_\alpha \pi_\beta, \pi_\gamma \pi_\delta} \, \delta_{m_\alpha + m_\beta, m_\gamma + m_\delta} \, \bar{v}_{N_\alpha N_\beta N_\gamma N_\delta}^{[m\pi t]_{\alpha\beta = \gamma\delta}} \,, \end{aligned} \tag{5.41b}$$

where the notation

$$[m\pi t]_{\alpha\beta=\gamma\delta} \equiv \begin{cases} t_\alpha + t_\beta = t_\gamma + t_\delta \\ \pi_\alpha \pi_\beta = \pi_\gamma \pi_\delta \\ m_\alpha + m_\beta = m_\gamma + m_\delta \end{cases} \tag{5.42}$$

---

[3] An alternative way to prove directly the block structure of $\mathcal{Y}_\alpha^k$ without passing through its conjugate is illustrated in App. D

has been employed, one can rewrite Eq. (5.40) as

$$
\begin{aligned}
h_{\alpha\gamma} &= t_{\alpha\gamma} + \sum_{\beta\delta} \bar{v}_{\alpha\beta\gamma\delta}\, \rho_{\delta\beta} \\
&= \delta_{t_\alpha t_\gamma}\, \delta_{\pi_\alpha \pi_\gamma}\, \delta_{m_\alpha m_\gamma}\, t^{[m\pi t]_\alpha}_{N_\alpha N_\gamma} + \delta_{t_\alpha t_\gamma}\, \delta_{\pi_\alpha \pi_\gamma}\, \delta_{m_\alpha m_\gamma} \sum_{N_\beta N_\delta} \sum_{m_\delta \pi_\delta t_\delta} \bar{v}^{[m\pi t]_{\alpha\beta=\gamma\delta}}_{N_\alpha N_\beta N_\gamma N_\delta}\, \rho^{[m\pi t]_\delta}_{N_\delta N_\beta} \\
&\equiv \delta_{t_\alpha t_\gamma}\, \delta_{\pi_\alpha \pi_\gamma}\, \delta_{m_\alpha m_\gamma}\, h^{[m\pi t]_\alpha}_{N_\alpha N_\gamma}\,.
\end{aligned}
\tag{5.43}
$$

5.3.3. Second-order self-energy

Let us now consider Eq. (5.21a). Inserting the block structure of the spectroscopic amplitudes, Eqs. (5.38), and exploiting the properties of the 2B potential, Eq. (5.41b), one obtains

$$
\begin{aligned}
M_{n_1 n_2 k_3 \alpha} = \frac{1}{\sqrt{2}} \sum_{\mu\nu\lambda} & \delta_{t_{n_1} t_\mu} \delta_{t_{n_2} t_\nu} \delta_{t_{k_3} t_\lambda} \delta_{\pi_{n_1} \pi_\mu} \delta_{\pi_{n_2} \pi_\nu} \delta_{\pi_{k_3} \pi_\lambda} \delta_{m_{n_1} m_\mu} \delta_{m_{n_2} m_\nu} \delta_{-m_{k_3} m_\lambda} \\
& \times \mathcal{X}^{[m\pi t]_{n_1}}_{N_{n_1} N_\mu} \mathcal{X}^{[m\pi t]_{n_2}}_{N_{n_2} N_\nu} \mathcal{Y}^{[m\pi t]_{k_3}}_{N_{k_3} N_\lambda} \delta_{t_\mu + t_\nu, t_\alpha + t_\lambda} \delta_{\pi_\mu \pi_\nu, \pi_\alpha \pi_\lambda} \delta_{m_\mu + m_\nu, m_\alpha + m_\lambda} \\
& \times \bar{v}^{[m\pi t]_{\mu\nu=\alpha\lambda}}_{N_\mu N_\nu N_\alpha N_\lambda} \\
= \delta_{t_{n_1} + t_{n_2}, t_\alpha + t_{k_3}} & \delta_{\pi_{n_1} \pi_{n_2}, \pi_\alpha \pi_{k_3}} \delta_{m_{n_1} + m_{n_2}, m_\alpha - m_{k_3}} \\
& \times \frac{1}{\sqrt{2}} \sum_{N_\mu N_\nu N_\lambda} \mathcal{X}^{[m\pi t]_{n_1}}_{N_{n_1} N_\mu} \mathcal{X}^{[m\pi t]_{n_2}}_{N_{n_2} N_\nu} \mathcal{Y}^{[m\pi t]_{k_3}}_{N_{k_3} N_\lambda} \bar{v}^{[m\pi t]_{n_1 n_2 = \alpha \bar{k}_3}}_{N_{n_1} N_{n_2} N_\alpha N_{k_3}} \\
\equiv \delta_{t_{n_1} + t_{n_2}, t_\alpha + t_{k_3}} & \delta_{\pi_{n_1} \pi_{n_2}, \pi_\alpha \pi_{k_3}} \delta_{m_{n_1} + m_{n_2}, m_\alpha - m_{k_3}} M^{[m\pi t]_{n_1 n_2 = \alpha \bar{k}_3}}_{N_{n_1} N_{n_2} N_{k_3} N_\alpha}\,,
\end{aligned}
\tag{5.44a}
$$

where for barred indices the angular-momentum projection has to be taken with a minus sign. Similarly, starting from Eq. (5.21d) one finds

$$
\begin{aligned}
N_{k_1 k_2 n_3 \alpha} = \frac{1}{\sqrt{2}} \sum_{\mu\nu\lambda} & \delta_{t_{k_1} t_\mu} \delta_{t_{k_2} t_\nu} \delta_{t_{n_3} t_\lambda} \delta_{\pi_{k_1} \pi_\mu} \delta_{\pi_{k_2} \pi_\nu} \delta_{\pi_{n_3} \pi_\lambda} \delta_{-m_{k_1} m_\mu} \delta_{-m_{k_2} m_\nu} \delta_{m_{n_3} m_\lambda} \\
& \times \mathcal{Y}^{[m\pi t]_{k_1}}_{N_{k_1} N_\mu} \mathcal{Y}^{[m\pi t]_{k_2}}_{N_{k_2} N_\nu} \mathcal{X}^{[m\pi t]_{n_3}}_{N_{n_3} N_\lambda} \\
& \times \delta_{t_\mu + t_\nu, t_\alpha + t_\lambda} \delta_{\pi_\mu \pi_\nu, \pi_\alpha \pi_\lambda} \delta_{m_\mu + m_\nu, m_\alpha + m_\lambda} \bar{v}^{[m\pi t]_{\mu\nu=\alpha\lambda}}_{N_\mu N_\nu N_\alpha N_\lambda} \\
= \delta_{t_{k_1} + t_{k_2}, t_{n_3} + t_\alpha} & \delta_{\pi_{k_1} \pi_{k_2}, \pi_{n_3} \pi_\alpha} \delta_{-m_{k_1} - m_{k_2}, m_\alpha m_{n_3}} \\
& \times \frac{1}{\sqrt{2}} \sum_{N_\mu N_\nu N_\lambda} \mathcal{Y}^{[m\pi t]_{k_1}}_{N_{k_1} N_\mu} \mathcal{Y}^{[m\pi t]_{k_2}}_{N_{k_2} N_\nu} \mathcal{X}^{[m\pi t]_{n_3}}_{N_{n_3} N_\lambda} \bar{v}^{[m\pi t]_{\mu\nu=\alpha\lambda}}_{N_\mu N_\nu N_\alpha N_\lambda} \\
\equiv \delta_{t_{k_1} + t_{k_2}, t_{n_3} + t_\alpha} & \delta_{\pi_{k_1} \pi_{k_2}, \pi_{n_3} \pi_\alpha} \delta_{-m_{k_1} - m_{k_2}, m_\alpha m_{n_3}} N^{[m\pi t]_{\bar{k}_1 \bar{k}_2 = \alpha n_3}}_{N_{k_1} N_{k_2} N_{n_3} N_\alpha}\,.
\end{aligned}
\tag{5.44b}
$$

Eventually, the diagonal part of the Dyson matrix is given by the two diagonal matrices $E^{>}$ and $E^{<}$ defined in Eqs. (5.21b) and (5.21e) respectively. Even if these quantities do not explicitly depend on the single-particle index α, the block structures of M and N constrain the values r and s can assume in a fixed symmetry block of the Dyson matrix.

5.3.4. Block-diagonal structure of ADC(2) equations

Collecting all block-diagonal structures derived in the previous sections, i.e. Eqs. (5.43) and (5.44), and recalling that addition and removal amplitudes obey

$$
\mathcal{Z}^i_\delta = \delta_{t_\delta t_i} \delta_{\pi_\delta \pi_i} \delta_{m_\delta m_i} \mathcal{Z}^{[m\pi t]_\delta}_{N_\delta N_i}\,,
\tag{5.45}
$$

one can now rewrite Eqs. (5.26) according to the block-diagonal form

$$\left[\varepsilon_i - E^{>}_{n_1 n_2 k_3}\right] \mathcal{W}^{[m\pi t]_{n_1 n_2 = i\bar{k}_3}}_{N_{n_1} N_{n_2} N_{k_3} N_i} = \sum_{N_\delta} M^{[m\pi t]_{n_1 n_2 = \delta\bar{k}_3}}_{N_{n_1} N_{n_2} N_{k_3} N_\delta} \mathcal{Z}^{[m\pi t]_\delta}_{N_\delta N_i} \,, \tag{5.46a}$$

$$\left[\varepsilon_i - E^{<}_{k_1 k_2 n_3}\right] \mathcal{V}^{[m\pi t]_{\bar{k}_1 \bar{k}_2 = i n_3}}_{N_{k_1} N_{k_2} N_{n_3} N_i} = \sum_{N_\delta} N^{[m\pi t]_{\bar{k}_1 \bar{k}_2 = \delta n_3}}_{N_{k_1} N_{k_2} N_{n_3} N_\delta} \mathcal{Z}^{[m\pi t]_\delta}_{N_\delta N_i} \,, \tag{5.46b}$$

where the block-diagonal $\mathcal{W}$ and $\mathcal{V}$ amplitudes are defined as

$$\mathcal{W}^{i}_{n_1 n_2 k_3} \equiv \delta_{t_{n_1}+t_{n_2}, t_i + t_{k_3}} \delta_{\pi_{n_1}\pi_{n_2}, \pi_i \pi_{k_3}} \delta_{m_{n_1}+m_{n_2}, m_i - m_{k_3}} \mathcal{W}^{[m\pi t]_{n_1 n_2 = i\bar{k}_3}}_{N_{n_1} N_{n_2} N_{k_3} N_i} , \tag{5.47a}$$

$$\mathcal{V}^{i}_{k_1 k_2 n_3} \equiv \delta_{t_{k_1}+t_{k_2}, t_{n_3} + t_i} \delta_{\pi_{k_1}\pi_{k_2}, \pi_{n_3} \pi_i} \delta_{-m_{k_1}-m_{k_2}, m_i m_{n_3}} \mathcal{V}^{[m\pi t]_{\bar{k}_1 \bar{k}_2 = i n_3}}_{N_{k_1} N_{k_2} N_{n_3} N_i} \,. \tag{5.47b}$$

With these formulae at hand, the full Dyson matrix Eq. (5.27) can be re-written in a block-diagonal form. As an example, the first row reads as

$$\begin{aligned} \varepsilon_i \mathcal{Z}^{[m\pi t]_\alpha}_{N_\alpha N_i} = & \sum_{N_\delta} [t + \Sigma^{(\infty)}]^{[m\pi t]_\alpha}_{N_\alpha N_\delta} \mathcal{Z}^{[m\pi t]_\delta}_{N_\delta N_i} + \sum_{N_{n_1} N_{n_2} N_{k_3}} M^{[m\pi t]_{n_1 n_2 = \alpha\bar{k}_3}}_{N_{n_1} N_{n_2} N_{k_3} N_\alpha} \mathcal{W}^{[m\pi t]^{n_1 n_2 = i\bar{k}_3}}_{N_{n_1} N_{n_2} N_{k_3} N_i} \\ & + \sum_{N_{k_1} N_{k_2} N_{n_3}} N^{[m\pi t]_{\bar{k}_1 \bar{k}_2 = \alpha n_3}}_{N_{k_1} N_{k_2} N_{n_3} N_\alpha} \mathcal{V}^{[m\pi t]_{\bar{k}_1 \bar{k}_2 = i n_3}}_{N_{k_1} N_{k_2} N_{n_3} N_i} \,. \end{aligned} \tag{5.48}$$

In practical calculations, the eigenvalue problem is thus solved for different symmetry blocks of the single-particle index α.

5.4. Computational aspects

This section addresses the main challenges that arise when implementing the equations discussed in Sec. 5.3. The methods used to tackle these challenges and limit the cost of numerical calculations are illustrated and the associated errors are evaluated.

5.4.1. Dimensions of the eigenvalue problem

As explained in Sec. 5.2.4, the Dyson equation is most suitably solved in terms of the energy-independent eigenvalue problem (5.27). The latter was specified for the case of interest, i.e. for axially-deformed calculations, in Sec. 5.3.4. While the energy-independent character simplifies the determination of the poles of the single-particle propagator (which are straightforwardly identified with the eigenvalues of Eq. (5.27)), the drawback of this

$e_{\max}$	^{16}O	^{48}Ca	^{132}Sn	^{208}Pb
2	447	-	-	-
4	6480	9993	-	-
6	32 973	77 688	104 851	66 052
8	108 486	292 447	577 461	643 729
10	280 011	802 046	1 833 425	2 373 192

Table 5.1. Number of rows in the largest symmetry block of the forward dynamical part of the Dyson matrix displayed for four different sample nuclei as a function of $e_{\max}$.

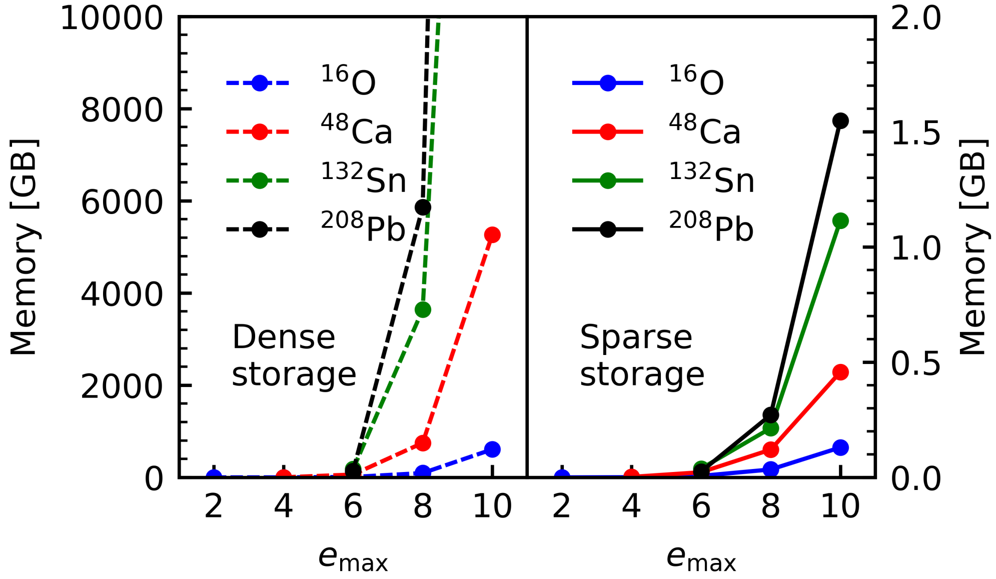

Figure 5.5. Memory required to store the largest symmetry block of the ADC(2,3) Dyson matrix in double precision. The figure compares the naive numerical implementation where all the elements of the block are stored (*left panel*) with the optimal ADC(2) implementation where only non-zero elements of the matrix are kept in memory (*right panel*). At the ADC(3) level, one has to exploit the sparsity of the matrix to reduce storage costs.

form relates to the large dimensions of the resulting Dyson matrix. This is particularly severe in the case of the present m-scheme implementation that builds on a sizeable single-particle basis to begin with.

As an example, Tab. 5.1 illustrates the dimensions of largest block of the Dyson matrix when built from a HF propagator for different nuclei and model spaces. One can appreciate the rapid increase with the model-space size, which translates in linear dimensions of the order of $10^5 - 10^6$ for realistic bases. Apart from the associated CPU runtime, this may pose problems in terms of memory for both the storage of the matrix elements and the subsequent diagonalization. While the former does indeed constitute a bottleneck for high-order ($n \geq 3$) ADC(n) truncations where one has to deal with dense matrices, the diagonality of the $E^{>}$ and $E^{<}$ matrices at the ADC(2) level makes it less troublesome (see Fig. 5.5 for an illustration). Still, the full matrix has to be eventually diagonalized, which constitutes a non-trivial numerical exercise.

While the numbers given above correspond to using an uncorrelated HF propagator to build the Dyson matrix to be diagonalized, the self-consistent character of the ADC(2) equations increases in fact dramatically the matrix dimensions. Indeed, self-consistency is achieved by an iterative solution of Dyson's equation, i.e. via successive diagonalizations of the Dyson matrix starting from the first step described above. At each step, many more new poles of the 1B propagator are generated and, in principle, enter the calculation of the dynamical self-energy in the following iteration. While, on the one hand, this process builds the many-body correlations characterizing the interacting system (i.e., *dresses* the single-particle propagator), it leads on the other hand to an exponential growth in the matrix dimensions that has to be controlled in practice.

5.4.2. Krylov projection

In order to contain the rapid increase of the Dyson matrix dimensions, an efficient strategy has been developed in the context of Green's functions [102, 103] based on *Krylov projection* techniques. While such projection is usually taylored (e.g., in no-core shell model calculations [104]) to best approximate the extreme eigenvalues of a large matrix, one is here rather interested in preserving as much as possible the properties of the spectral strength distribution associated with the dressed propagator, which include information on quasiparticle poles across a large energy range. For this reason, and since the most relevant poles are located around the Fermi surface, the Krylov projection is performed separately on the *fw* and *bw* energy denominators of the dynamical self-energy. The reduced matrices are re-inserted into the full Dyson matrix, to obtained a projected version of it that is eventually diagonalized exactly.

In practice, the Krylov projection is typically performed in SCGF via the *multi-pivot Lanczos algorithm*. A complete illustration of the procedure is reported in App. E. Schematically, the algorithm yields projectors, or Lanczos matrices, $\mathcal{L}^>$ and $\mathcal{L}^<$ for each symmetry block of the Dyson matrix and for the two separate forward and backward contributions. The projectors are subsequently applied to the submatrices of the original matrix as follows

$$E'^{>}_{ll'} \equiv \sum_r (\mathcal{L}^>)^\dagger_{lr} E^>_r \mathcal{L}^>_{rl'}, \tag{5.49a}$$

$$E'^{<}_{ll'} \equiv \sum_s (\mathcal{L}^<)^\dagger_{ls} E^<_s \mathcal{L}^<_{sl'}, \tag{5.49b}$$

$$M'_{l\alpha} \equiv \sum_r (\mathcal{L}^>)^\dagger_{lr} M_{r\alpha}, \tag{5.49c}$$

$$N'_{l\alpha} \equiv \sum_s (\mathcal{L}^<)^\dagger_{ls} N_{s\alpha}, \tag{5.49d}$$

where l, l', s, and s' are indexes relative to ISCs. While the single-pivot Lanczos algorithm projects a diagonal matrix (such as the ADC(2) $E^>$ and $E^<$) to a tri-diagonal one, the presently employed multi-pivot version produces a projected matrix that, in addition, displays non-zero rows and columns in correspondence of the addition of a new pivot. The resulting structure is depicted in Fig. 5.6 and is referred to as *fishbone-like* structure.

Numerically, the bottleneck of the Lanczos algorithm is represented by the matrix-vector products (E.3) involving matrices with very large dimensions. However, at the ADC(2) the diagonality of $E^>$ and $E^<$ can be exploited to recast the matrix-vector product into an element-wise product. The same properties also simplifies the matrix products in Eqs. (5.49a) and (5.49b).

Since the goal is to project a matrix on a smaller subspace, two questions arise.

1. What is an optimal choice for the initial matrix of pivots, that is in principle arbitrary?

2. What is an optimal choice for the number of pivots N_p and the related number of iterations per pivot N_l (i.e., which value of N_l reflects on a satisfactory approximation of the quantities of interest)?

As for the first question, literature lacks of systematic studies for the optimal choice of the pivots. In this work, the choice made in [103] is considered, which consists in taking

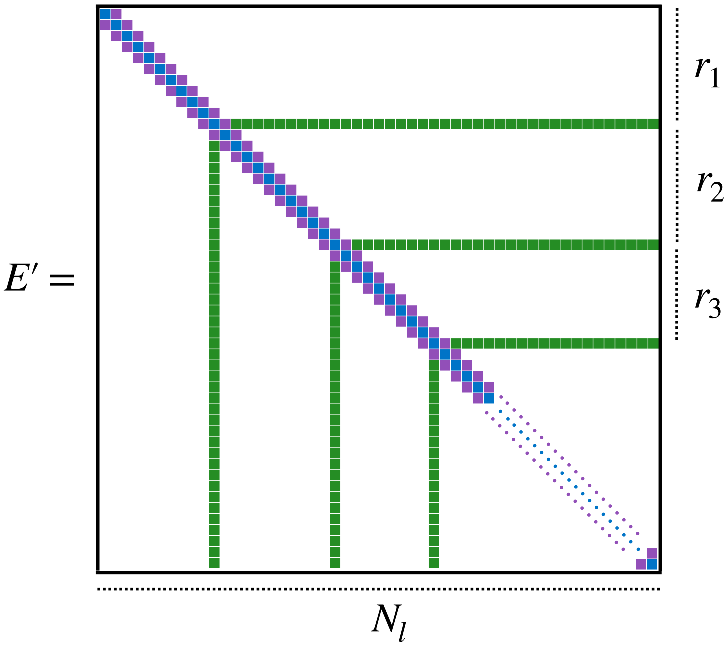

Figure 5.6. Fishbone-like structure appearing in the projection of a diagonal matrix with the multi-pivot Lanczos algorithm.

as a set of pivot vectors

$$p_\kappa^{i,fw} = \left\{ \sum_\alpha M_\alpha^h \mathcal{Y}_\alpha^i, \sum_\alpha M_\alpha^p \mathcal{X}_\alpha^i \right\}, \tag{5.50a}$$

$$p_\kappa^{i,bw} = \left\{ \sum_\alpha N_\alpha^h \mathcal{Y}_\alpha^i, \sum_\alpha N_\alpha^p \mathcal{X}_\alpha^i \right\}, \tag{5.50b}$$

where h (p) is an index running over the holes (particles) of a symmetry block and $\kappa = \{h, p\}$ is a collective index for holes and particles. The two objects in curl brackets in Eqs. (5.50) represent the two set of columns of the pivot matrix. If a certain symmetry block does not contain any hole or particle state, a single random pivot is taken.

For what concerns the optimal number of iterations per pivot, Fig. 5.7 illustrates the sensitivity of the ground-state energy of different nuclei on N_l for a set of three different χEFT interactions. In most cases an acceptable precision is reached after only a few Lanczos iterations, with just two Lanczos iterations often delivering 0.5% of relative error. There is no clear degradation of the quality of the approximation with respect to the nuclear mass except for the case of ^{72}Cr with the NNLO$_{\text{go}}$(450) interaction, where it is clear that the convergence is not reached before $N_l = 10$ iterations. This is presumably due to a combination of the high mass of the nucleus and the hardness of the interaction employed.

To complement Fig. 5.7, Tab. 5.2 shows the computational time required to perform different numbers of Lanczos iterations for the same set of nuclei. For a fixed value of N_l, the numerical cost increases almost proportionally with respect to the nuclear mass. Overall, one can conclude that 10 Lanczos iterations represent a good compromise between the accuracy of the calculation (the error never exceeds 0.4% in all the tests performed) and the computational time required. In the following, therefore, $N_l = 10$ is always used.

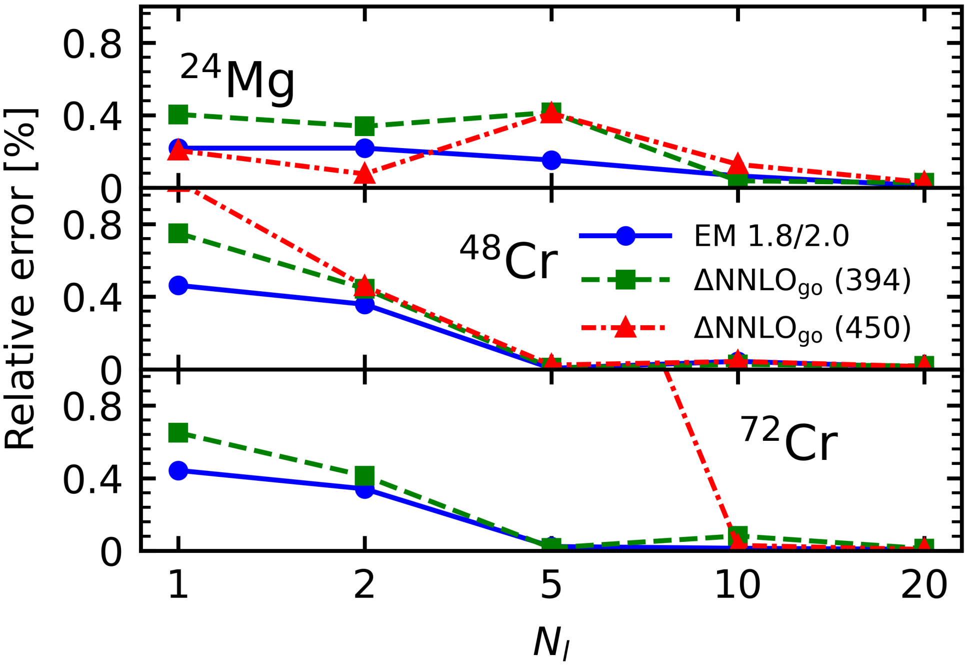

Figure 5.7. Convergence of the total energy computed for ^{24}Mg, ^{48}Mg and ^{72}Cr for the EM 1.8/2.0, the ΔNNLO$_{\text{go}}$ (394) and the ΔNNLO$_{\text{go}}$ (450) interactions, as a function of the number of iterations per pivot N_l. The total energy is represented on the y-axis as the relative error with respect to a calculation performed with $N_l = 30$ that is assumed to be converged. Calculations are carried out in $e_{\text{max}} = 8$ and the optimal $\hbar\omega$ for the sHO matrix elements has been employed for each case.

N_l	^{24}Mg	^{48}Cr	^{72}Cr
1	0.001	0.001	0.001
2	0.002	0.005	0.008
5	0.039	0.075	0.105
10	0.318	0.594	0.939
20	2.532	4.849	7.520
30	8.666	16.314	28.462

Table 5.2. CPU time (in hours) required to perform one Lanczos reduction of the forward and backward part of the second-order self-energy computed using HF one-body propagators as a function of the number of iterations per pivot N_l. The data are obtained employing 128 OpenMP threads. Calculations are performed in $e_{\text{max}} = 8$.

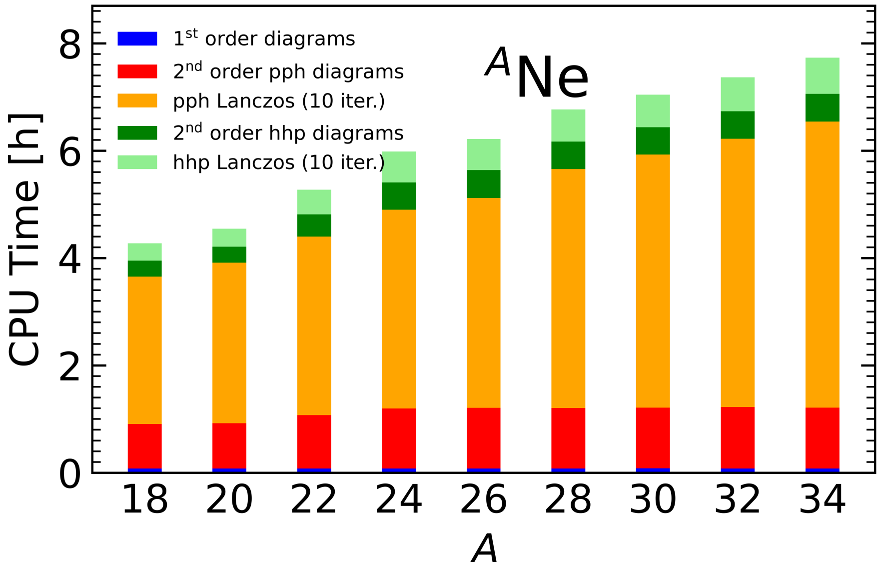

Figure 5.8. Times required (i) to compute first- and second-order self-energies based on HF one-body propagators and (ii) to perform Lanczos iterations of the forward (*pph*) and backward (*hhp*) part of the Dyson matrix. Results are displayed for the Neon isotopic chain computed with $e_{\text{max}} = 10$.

5.4.3. Self-consistency

The self-consistent solution of the Dyson equation requires the re-evaluation of the Dyson matrix multiple times until a chosen convergence criterion is satisfied. Per se, this constitutes a challenge because it requires the re-calculation of second-order diagrams and the subsequent re-application of the Lanczos algorithm multiple times. As an illustration, Fig. 5.8 displays the typical CPU times needed for the different steps of a realistic ADC(2) computation. One observes that the CPU time is dominated by the 2p-1h channel and more specifically to the Lanczos projection of it.

In self-consistent calculations such costs have to be paid several times. In fact, the situation is even more challenging given that the number of poles in the one-body propagator, and thus the size of Dyson matrix, increases dramatically at each step of self-consistent procedure. In the following, two strategies to tackle such a problem are discussed.

Partial self-consistency

A first possibility to control the increase in the number of poles is to compute second-order diagrams only at the first iteration and subsequently ‘freeze’ them, i.e. update only the static self-energy $\Sigma^{(\infty)}$ in the successive iterations. This constitutes a significant advantage given that first-order self-energy contributions are relatively inexpensive to compute and that the size of the Dyson matrix remains fixed. Such procedure is denoted as the ‘sc0’ approximation.

Figure 5.9 examines the efficiency of this approximation compared to full self-consistent (‘sc’) calculations (discussed in the following) for the Ca and Cr isotopic chains. Generally, sc0 provides excellent results, departing by less than 0.2% in most cases. Interestingly, there seems to be a weak correlation between the performance of the sc0 approximation

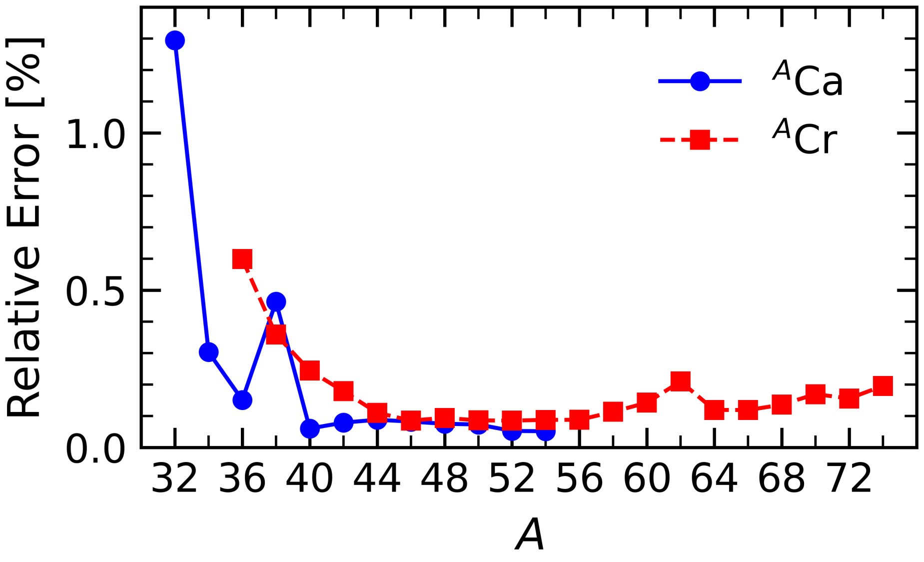

Figure 5.9. Relative error of the ground-state energy of Calcium and Chromium isotopes computed with the sc0 approximation against full self-consistent calculations. Calculations are performed with the EM 1.8/2.0 interaction in $e_{\text{max}} = 12$ and $\hbar\omega = 12\,\text{MeV}$.

and the mass number. The difference assumes sizeable values only in the region $A = 32 - 38$, then decreases and remains constant at low values before slightly increasing again for the mass range $A > 56$.

It is however important to stress the fact that, unlike the full self-consistent case, an sc0 calculation does depend on the particular reference state delivering the input unperturbed propagator. Specifically, in the example of Fig. 5.9 a HF calculation performed for the same nucleus and the same Hamiltonian was used to generate such reference state. In general, an unwise choice of the unperturbed propagator can lead to much greater differences between sc0 and the corresponding sc calculation.

Optimized reference state and full self-consistency

In order to perform a fully self-consistent calculation, strategies must be designed to tackle the dynamical part of the self-energy. The method employed in this work is taken from Ref. [105]. The main idea is to effectively 'reduce' the dimension of the dressed propagator obtained at the end of a given iteration by converting it into a mean-field-like propagator, i.e. a 1B GF with the same number of poles as the HF one, thus maintaining the size of the Dyson matrix fixed. Such a propagator is denoted as the *optimized reference state* (OpRS) propagator and can be written as

$$g^{\text{OpRS}}_{\alpha\beta}(\omega) = \sum_{n \notin F} \frac{(\phi^n_\alpha)^* \phi^n_\beta}{\omega - \varepsilon^{\text{OpRS}}_n + i\eta} + \sum_{k \in F} \frac{\phi^k_\alpha (\phi^k_\beta)^*}{\omega - \varepsilon^{\text{OpRS}}_k - i\eta}, \tag{5.51}$$

where F represents the set of occupied states. While diagonalizing the Baranger one-body Hamiltonian [106, 107], i.e. the HF-like field computed from the correlated one-body density matrix delivers such a similar object, it typically does not constitute an efficient choice. The reason is that a correlated HF propagator does not conserve the key properties of the full spectral function, which can be encoded in the (inverse[4]) moments

$$M^{p}_{\alpha\beta} = \sum_{n} \frac{(\mathcal{X}^{n}_{\alpha})^{*}\mathcal{X}^{n}_{\beta}}{[E_F - \varepsilon^{+}_{n}]^{p}} + \sum_{k} \frac{\mathcal{Y}^{k}_{\alpha}(\mathcal{Y}^{k}_{\beta})^{*}}{[E_F - \varepsilon^{-}_{k}]^{p}}, \qquad p = 0, 1, 2, \dots \tag{5.52}$$

with E_F representing the Fermi energy (separately determined for neutrons and protons)

$$E_F \equiv \frac{\varepsilon^{+}_{0} + \varepsilon^{-}_{0}}{2} = \frac{E^{A+1}_{0} + E^{A-1}_{0}}{2} \,. \tag{5.53}$$

A better strategy thus consists in requiring that the OpRS propagator reproduces the lowest moments of the fully correlated spectral distribution. In particular, demanding that moments with $p = 0, 1$ are conserved, i.e.

$$M^{0,OpRS}_{\alpha\beta} = M^{0}_{\alpha\beta}, \tag{5.54a}$$

$$M^{1,OpRS}_{\alpha\beta} = M^{1}_{\alpha\beta} \,, \tag{5.54b}$$

leads to an OpRS propagator having the same number of poles as the mean-field one.

Overall, the procedure to perform self-consistent dSCGF calculations is defined as follows.

1. The reference propagator is determined solving dHF equations (at the first iteration) or by reducing a pre-existing dressed propagator to an OpRS one (for successive iterations).
2. Second-order self-energies are computed by evaluating Eqs. (5.21).
3. The Krylov projection is performed by means of the Lanczos algorithm.
4. First-order self-energies are computed from Eq. (5.19).
5. The Dyson matrix is diagonalized and the correlated propagator is determined.

The procedure is repeated from step [4-5] for partial self-consistency (sc0) or from step [1-5] for full self-consistency (sc), until convergence. The corresponding workflow is summarized in Fig. 5.10.

In order to illustrate how self-consistency is achieved in practical calculations, Fig. 5.11 shows the convergence of the ADC(2) ground-state energy of ^{20}Ne for different choices of the unperturbed propagator. Specifically, using a dHF propagator from:

1. ^{20}Ne computed with ΔNNLO$_{\text{go}}$ (394) interaction (same nucleus and Hamiltonian used for the ADC(2) calculation);
2. ^{20}Ne computed with NNLO$_{\text{sat}}$ (bare) interaction (same nucleus than the ADC(2) calculation but different Hamiltonian);
3. ^{24}Mg computed with NNLO$_{\text{sat}}$ (bare) interaction (different nucleus and Hamiltonian than the ADC(2) calculation).

---

[4] Considering the *inverse* moment allows to enhance the importance of the spectral distribution around the Fermi surface, i.e. the most relevant part of the energy domain.

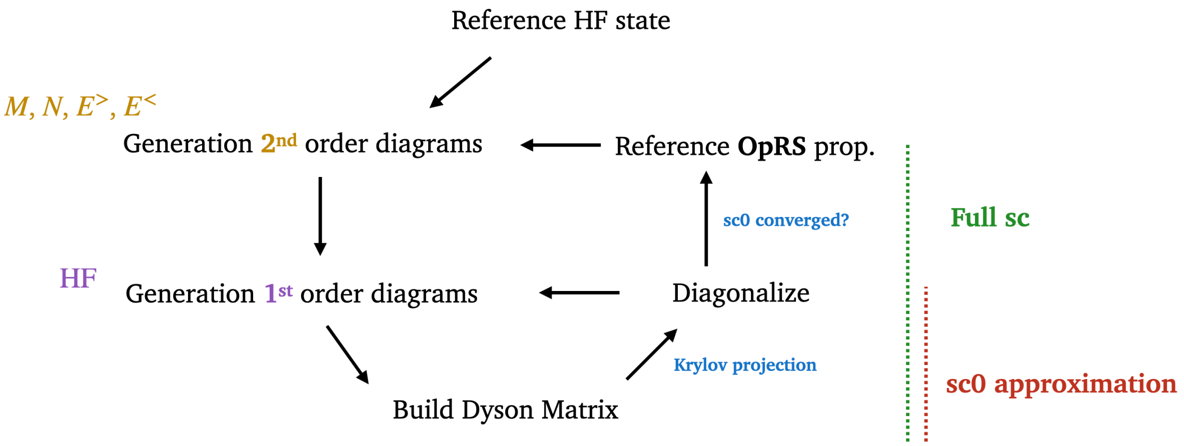

Figure 5.10. Workflow representing the approximation schemes employed to reach two different degrees of self-consistency, sc0 and sc.

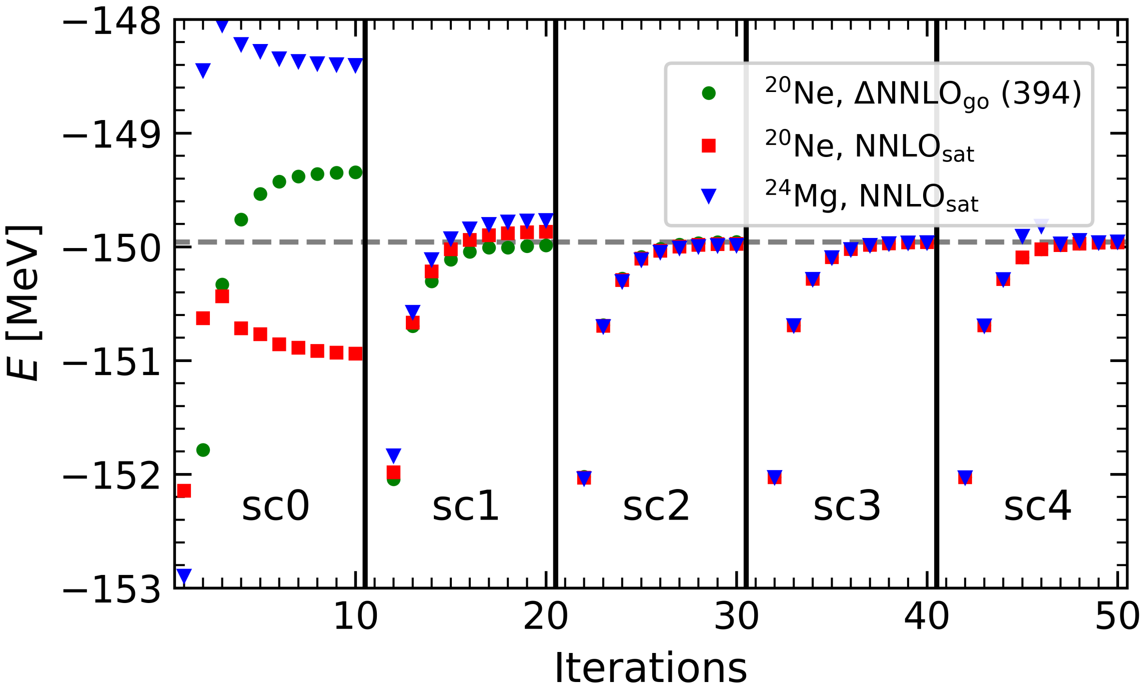

Figure 5.11. Numerical proof of the self-consistency in SCGF at ADC(2) level. Three-different dHF reference states (determined for the nucleus and the interaction indicated in the legend) have been chosen to perform an ADC(2) calculation in $e_{\text{max}} = 6$ for ^{20}Ne with the ΔNNLO$_{\text{go}}$(394) interaction with $\hbar\omega = 16\,\text{MeV}$.

Eventually, all calculations converge to the same total energy, which demonstrates numerically the self-consistent character of the GF scheme. Still, the way the correct result is approached varies depending on the initial reference state. The first calculation converges the fastest both in terms of getting closer to the final result already at the sc0 level and as overall convergence with respect to the full sc cycle. Such an approach is thus applied for all calculations presented in Sec. 5.5. In general, nevertheless, an excellent stability is observed for all cases, which confirms the appropriateness of the chosen implementation.

5.5. Results

Having outlined the theoretical background of axially-deformed Dyson SCGF at second-order, dubbed as dDSCGF(2), as well as the approximations employed to make numerical calculations doable, it is now time to apply such newly-developed technique to the study of open-shell systems and confront it with existing state-of-the-art calculations. In particular, here dDSCGF(2) results are presented for different medium-mass isotopic chains (Neon, Argon, Calcium and Chromium) and compared to those of other *ab initio* methods, namely:

1. dBMBPT(2)), extensively discussed in Ch. 2;
2. spherical Gorkov SCGF at second order (sGSCGF(2)) [65], discussed in in Sec. 5.2.5;
3. axially-deformed coupled-cluster method with the inclusion of singles and doubles (dCCSD) [9];
4. axially-deformed coupled-cluster method with the inclusion of singles, doubles and triples (dCCSDT-1), where the triples are included through the linearized approximation [9].

dHF and dDSCGF(2) calculations presented in this manuscript have been performed with a new numerical suite developed in the context of the present thesis. Even tough such suite is here presently employed in combination with sHO and dNAT bases, it can be used in combination with any generic spherical basis read from file [32] for the expansion of all the operators of interest.

5.5.1. Ground-state energies

Working equations

In SCGF the ground-state energy of the A-body system can be computed by means of the Galitski-Migdal-Koltun (GMK) sum rule, which is based on the sole knowledge of the single-particle propagator [108, 109]. When the effective Hamiltonian of Eq. (2.10) is employed, the GMK formula reads as

$$\begin{aligned} E_0^{\text{GMK}} &= h^{(0)} + \frac{1}{2\pi}\int_{-\infty}^{\varepsilon_F^-} d\omega \sum_{\alpha\beta}(t_{\alpha\beta} + \omega\delta_{\alpha\beta}) \operatorname{Im} g_{\beta\alpha}(\omega) \\ &= h^{(0)} + \frac{1}{2\pi}\int_{-\infty}^{\varepsilon_F^-} d\omega \sum_{\alpha\beta}(t_{\alpha\beta} + \omega\delta_{\alpha\beta}) \sum_k \mathcal{Y}_\beta^k (\mathcal{Y}_\alpha^k)^* \delta(\omega - \varepsilon_k) \\ &= h^{(0)} + \frac{1}{2}\sum_{\alpha\beta} t_{\alpha\beta}\rho_{\beta\alpha} + \frac{1}{2}\sum_\alpha \sum_k \varepsilon_k \mathcal{Y}_\alpha^k (\mathcal{Y}_\alpha^k)^* \,. \end{aligned} \tag{5.55}$$

It is instructive to see how the above formula reduces to the standard HF energy when an ADC(1) propagator is employed. In that case, Dyson's equation simply reads as

$$\sum_{\beta}\Big[t_{\alpha\beta}+\sum_{\gamma\delta}\bar{v}_{\alpha\gamma\beta\delta}\rho_{\delta\gamma}\Big]\mathcal{Y}^{k}_{\beta}=\varepsilon_k\mathcal{Y}^{k}_{\alpha}\,, \tag{5.56}$$

where the analytical expression for $\Sigma^{(\infty)}$ has been inserted. Multiplying on the right by $(\mathcal{Y}^{k}_{\alpha})^*$ leads to

$$\sum_{\beta}\Big[t_{\alpha\beta}+\sum_{\gamma\delta}\bar{v}_{\alpha\gamma\beta\delta}\rho_{\delta\gamma}\Big]\mathcal{Y}^{k}_{\beta}(\mathcal{Y}^{k}_{\alpha})^*=\varepsilon_k\mathcal{Y}^{k}_{\alpha}(\mathcal{Y}^{k}_{\alpha})^*\,. \tag{5.57}$$

Plugging Eq. (5.57) into Eq. (5.55) leads to

$$\begin{aligned}E_0^{\text{GMK}}&=h^{(0)}+\frac{1}{2}\sum_{\alpha\beta}t_{\alpha\beta}\,\rho_{\beta\alpha}+\frac{1}{2}\sum_{\alpha\beta}\sum_{k}\Big[t_{\alpha\beta}+\sum_{\gamma\delta}\bar{v}_{\alpha\gamma\beta\delta}\,\rho_{\delta\gamma}\Big]\mathcal{Y}^{k}_{\beta}(\mathcal{Y}^{k}_{\alpha})^*\\&=h^{(0)}+\sum_{\alpha\beta}t_{\alpha\beta}\,\rho_{\beta\alpha}+\frac{1}{2}\sum_{\alpha\beta\gamma\delta}\bar{v}_{\alpha\gamma\beta\delta}\,\rho_{\delta\gamma}\,\rho_{\beta\alpha},\end{aligned} \tag{5.58}$$

where Eq. (5.6) has been employed. The equation for the total energy in the HF case (Eq. (2.43)) is indeed recovered.

Compared to other many-body methods, one of the advantages of the SCGF approach is the ability to easily access odd-even nuclei neighbouring the targeted A-body system (see Fig. 5.1 and associated discussion in Sec. 5.2.1). As a result, in addition to the A-body ground-state energy computed via the GMK sum rule, energies of the $A \pm 1$ neighbours (including those of the ground-states) are automatically available[5]. Since the same odd-even nucleus can be accessed from two different even-even systems, in the following, ground-state energies of odd-even nuclei are computed from both even-even neighbours and an average between the two is taken as the final result[6].

Finally, it is worth commenting on the fact that, even if the Dyson formalism does not formally break particle-number symmetry as in the Gorkov scheme, actual calculations deliver slightly wrong number of particles. This is related to the way Fermi energies are determined in the present method, i.e. by adding one by one quasi-hole fragments until the right number of neutrons and protons are reached. Given that this sum increments the occupation in a discrete fashion, in practice one can rarely reach exactly the right number of particles. For the calculations discussed in this chapter, in average, the number of protons and neutrons is typically exceeded by 0.3 units. Presently, a rudimentary correction is employed for total energies (see discussion around Fig. 5.13). In addition, the actual (computed) particle number is considered when it appears explicitly in the expression for a given observable. While such a problem is in principle mitigated when pushing the ADC expansion to higher orders, possible strategies to correct it already at the ADC(2) level are left for future works.

Neon isotopic chain

Before focusing on binding energies, let us have a look at the degree of deformation associated with the dHF and dDSCGF(2) solutions. Even if it is not an observable, the

---

[5] In principle, to properly extract $A \pm 1$ energies one should additionally perform separate calculations with the corresponding $A \pm 1$ centre-of-mass corrections. This is however not done in the present work given its exploratory character.

[6] In cases where the two evaluations differ by more than 500 keV the procedure is assumed to be unreliable and no value is given.

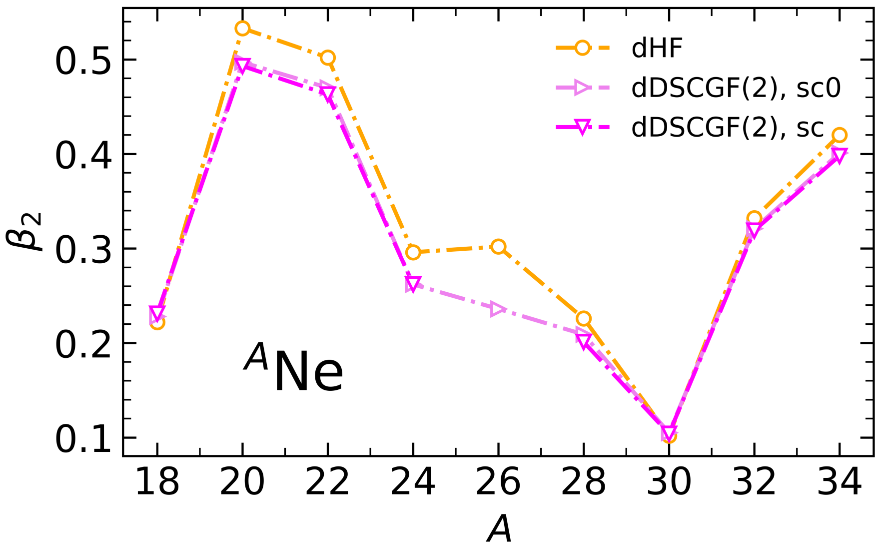

Figure 5.12. Axial deformation parameter along Neon isotopes for different *ab initio* methods: dHF, dDSCGF(2) with the sc0 approximation and fully self-consistent dDSCGF(2). All calculations employ the ΔNNLO$_{\rm go}$ (394) interaction with $\hbar\omega = 16\,$MeV, $e_{\rm max} = 10$ and $e_{\rm 3max} = 16$.

axial deformation parameter β_2, defined in Eq. (2.68), is indeed an important indicator characterizing the collectivity of the many-body state under consideration. Figure 5.12 displays the β_2 values of the dHF and dDSCGF(2) solutions along the Neon isotopic chain. The overall trend is qualitatively in line with previous studies [54], with local minima corresponding to standard neutron closures at $N = 8$ and $N = 20$[7]. Furthermore, β_2 tend to decrease with the progressive inclusion of dynamical correlations, i.e. except in ^{18}Ne and ^{30}Ne where the three results are similar, dHF always displays the largest deformation, followed by dDSCGF(2) computed with the sc0 approximation and by the fully self-consistent dDSCGF(2), the latter two results being always close to each other. The fact that the value of β_2 tends to decrease as more correlations are included in the calculation does make sense. Indeed, a good $J = 0$ state (having $\beta_2 = 0$ by construction) is to be recovered in the limit in which the many-body problem is solved exactly[8]. The small difference between the two dDSCGF(2) approximations reflect the similarity, in terms of many-body content, of the two computational schemes.

Moving to ground-state energies, results obtained along the Neon isotopic chain with the ΔNNLO$_{\rm go}$ (394) Hamiltonian are displayed in Fig. 5.13 for dDSCGF(2), dBMBPT(2), dCCSD and dCCSDT-1 calculations, as well as from experimental data. All calculations follow a similar trend, with dDSCGF(2) systematically located below dBMBPT(2) and surprisingly close to dCCSDT-1, where the latter typically adds 10% of the dCCSD correlation energy on top of it. The fact that dBMBPT(2) gains over dCCSD as neutron excess

---

[7] While other *ab initio* calculations predict ^{30}Ne to be spherical [54], there are indications that such a solution actually corresponds to the second 0^+ state, the ground state instead being characterized by a large deformation.

[8] However, nothing imposes that such a limit is reached monotonically in any given expansion method based on a deformed reference state such that the presently observed decrease was not necessarily expected.

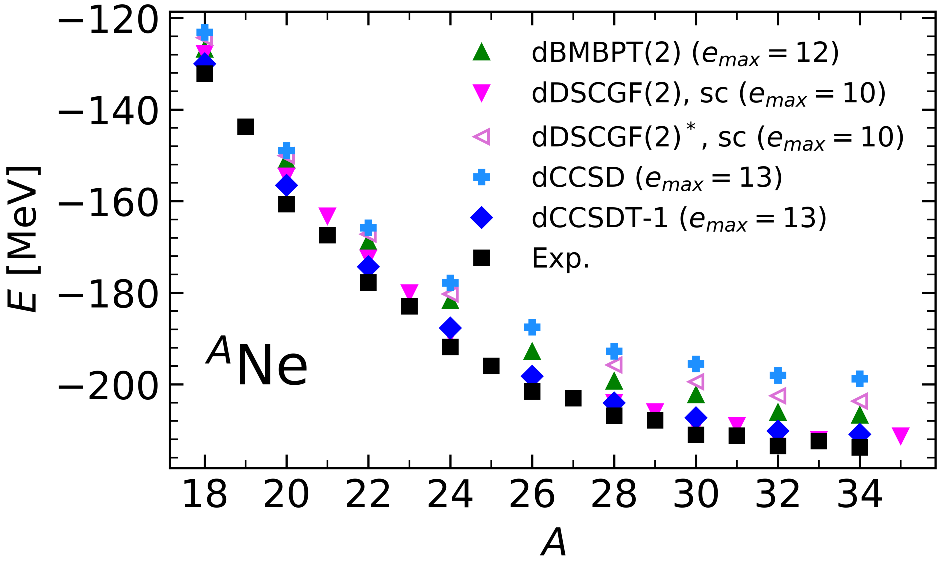

Figure 5.13. Ground-state energy along Neon isotopes computed with different *ab initio* methods. All calculations employ the $\Delta\text{NNLO}_{\text{go}}$ (394) Hamiltonian with $\hbar\omega = 16\,\text{MeV}$. Coupled-cluster data are taken from [9]. dDSCGF(2) values for ^{25}Ne, ^{26}Ne and ^{27}Ne are not shown since the self-consistent loop did not converge for ^{26}Ne. Experimental data are also shown for comparison.

increases is consistent with what has been observed along semi-magic isotopic chains [46]. The largest root mean square (rms) error with respect to the experiment along the chain is for dCCSD, amounting to 13.6 MeV whereas dBMBPT(2) follows with a rms deviation of 8.2 MeV. Eventually, dCCSDT-1 and dDSCGF(2) display an error of 3.4 MeV and 2.9 MeV respectively. Even if not shown in Fig. 5.13, dBMBPT(2) and dDSCGF(2) calculations of ^{36}Ne indicate that the drip line is predicted in ^{34}Ne for the presently employed Hamiltonian, which is in agreement with recent experimental results [87].

The surprising closeness of dCCSDT-1 and dDSCGF(2) is in fact due to the contamination of dDSCGF(2) results by the wrong particle number. To roughly evaluate its impact, a naive correction is presently performed for even isotopes by subtracting from the neutron and proton contributions to the GMK energy the corresponding particle-number excess times the energy per nucleon. This produces the rescaled dDSCGF(2)* curve in Fig. 5.13 that is shifted up by $[3.4, 9.2]$ MeV ($[2.7, 4.3]\%$) compared to dDSCGF(2), the shift increasing with the neutron excess. Even though this curve must be taken with a grain of salt due to the naive character of the subtraction scheme used, it shows, as expected, that dDSCGF(2)* is eventually much closer to dBMBPT(2) than to dCCSDT-1. This analyzes calls for an actual control of the (average) particle number in future dSCGF calculations. As for the present thesis, dDSCGF(2)* results based on the naive rescaling are employed in (most of) the figures below.

Argon isotopic chain

Although most of the Ar isotopes qualify as doubly open-shell systems, being only two protons away from the semi-magic Calcium chain the deformation is expected to be play a lesser role than in the strongly collective Neon isotopes. As a result, breaking rotational

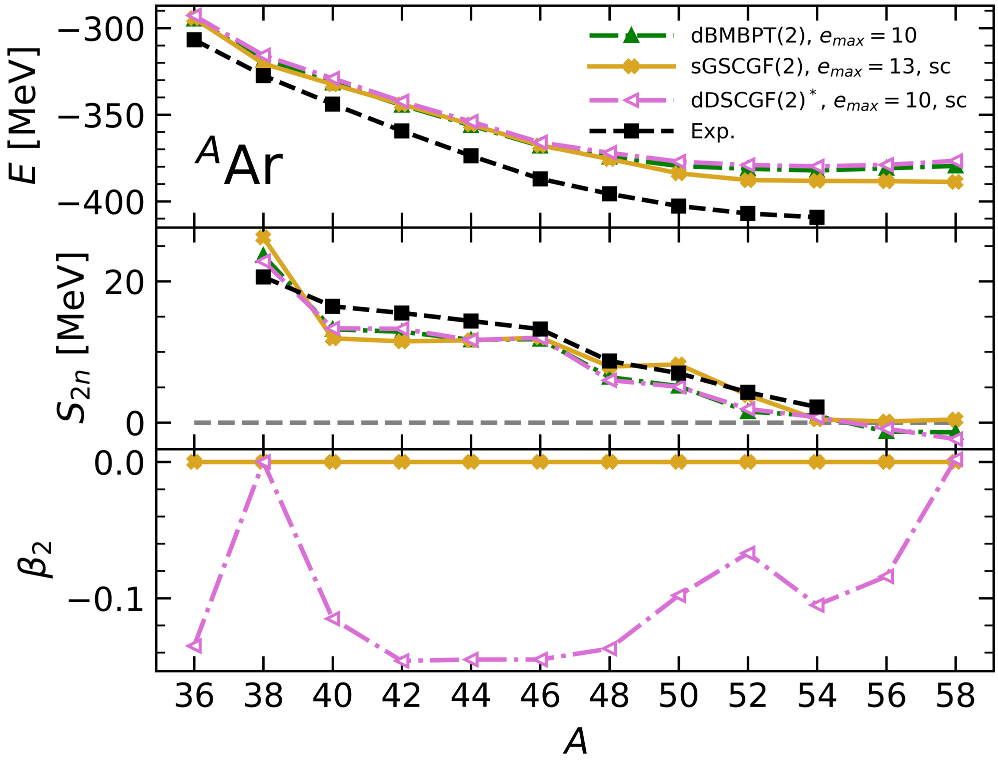

Figure 5.14. Ground-state energy (*top panel*), two-neutron separation energy (*middle panel*) and axial deformation (*bottom panel*) of Argon isotopes obtained from dDSCGF(2)* ($e_{\text{max}} = 10$), dBMBPT(2) ($e_{\text{max}} = 10$) and sGSCGF(2) ($e_{\text{max}} = 13$) calculations based on the NN+$3N$(lnl) Hamiltonian and the sHO frequency $\hbar\omega = 18\,\text{MeV}$.

invariance might not be strictly necessary here and one can attempt to perform *spherical* $U(1)$-symmetry breaking many-body calculations, i.e. results in $^{36-58}$Ar coming from both dDSCGF(2)* ($e_{\text{max}} = 10$) and sGSCGF(2) ($e_{\text{max}} = 13$) calculations with the NN+$3N$(lnl) Hamiltonian are confronted in Fig. 5.14 for total energies, two-neutron separation energies and deformation parameters. Also shown are dBMBPT(2) ($e_{\text{max}} = 10$) results and experimental values where applicable.

One first observes that dDSCGF(2)* energies are essentially identical to dBMBPT(2) ones and systematically above sGSCGF(2) ones. The latter feature, which increases with neutron excess, relates to the limitation to $e_{\text{max}} = 10$ in deformed calculations[9] compared to $e_{\text{max}} = 13$ employed to obtain converged sGSCGF(2) results[10]. Moving to two-neutron separation energies, the trend obtained via dBMBPT(2) and dDSCGF(2) is in better agreement with the experimental one than with sGSCGF(2), thus showing the benefit brought by the explicit deformation. In particular, and even though it is not perfect, the exaggerated drop at $N = 20$ is significantly improved. Eventually, experimental two-neutron separation energies are still underestimating, which either points to yet missing

---

[9] Argon isotopes also benefit from pairing correlations in sGSCGF(2) calculations but this only accounts for a small portion of the shift down. As for dBMBPT, it is only true about ^{44}Ar and ^{48}Ar given that the deformed reference state is unpaired for all the other isotopes.

[10] Results from sGSCGF(2) calculations with $e_{\text{max}} = 10$ are not reported on the figure because several isotopes could not be converged. For isotopes that could be converged, dDSCGF(2)* binding energies are indeed typically 3 to 6 MeV below sGSCGF(2) ones.

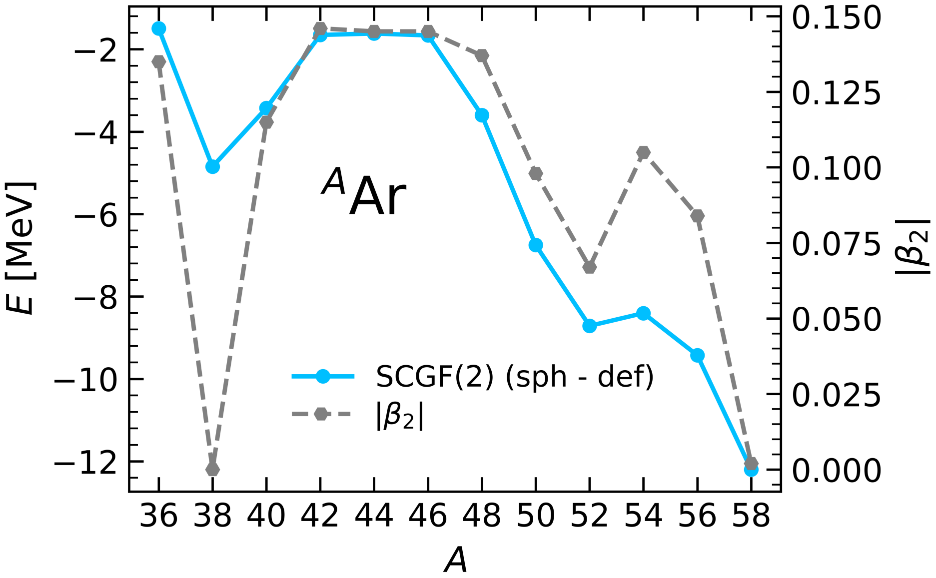

Figure 5.15. Energy difference between dDSCGF(2)* ($e_{\text{max}} = 10$) and sGSCGF(2) ($e_{\text{max}} = 13$) calculations (see *left y-axis*) compared to the axial deformation computed from dDSCGF(2) (see *right y-axis*). Results are obtained with the NN+3N(lnl) Hamiltonian for $\hbar\omega = 18$ MeV.

correlations or to a deficiency of the NN+3N(lnl) Hamiltonian.

In order to further examine the features of deformed ADC(2) calculations, it is instructive to compare the deformation parameter β_2 against the energy difference between spherical and deformed calculations[11]. Such a comparison is shown in Fig. 5.15. One observes a remarkable correlation between both quantities, the energy difference being essentially proportional to the magnitude of the deformation parameter. This result corroborates the findings of Ref. [65], where the deviation from experimental data of sGSCGF(2) calculations across several isotopic chains around Calcium, including Argon, was found to be strongly correlated with deformation estimates.

Calcium and Chromium isotopic chain

Having at hand a novel non-perturbative method to study open-shell system, it is relevant to revisit the study of Calcium and Chromium isotopic chains extensively discussed in Ch. 3. Figures 5.16 and 5.17 complement previously discussed results with the dDSCGF(2) data. Once again, dDSCGF(2) closely follows dBMBPT(2) along both isotopic chains, which is again a testimony of the soft character of the EM 1.8/2.0 Hamiltonian. Even for a sensitive observable such as two-neutron gaps, one can hardly see differences between the two. Contrary to the results obtained in Ar isotopes with the NN+3N(lnl) Hamiltonian, two-neutron separation energies are on par with experiment. Even though it should be firmly addressed by computing Ar (Ca and Cr) isotopes with the EM 1.8/2.0 (NN+3N(lnl)) Hamiltonian, this difference seems to point to a shortcoming of the NN+3N(lnl) Hamiltonian.

---

[11] Due to the different e_{max} values employed, only the evolution of this energy difference is pertinent, not its overall size.

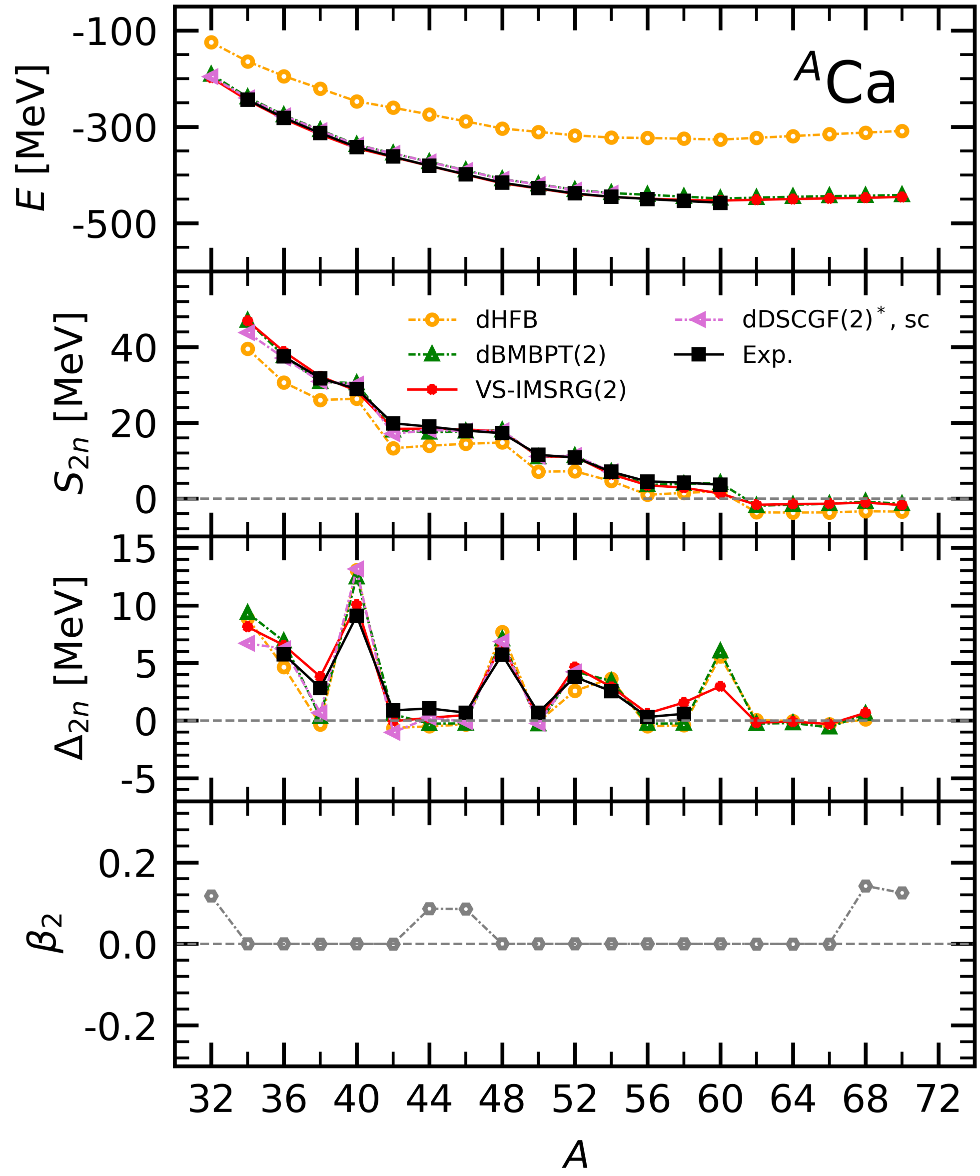

Figure 5.16. Systematic dHFB ($e_{\mathrm{max}} = 12$), dBMBPT(2) ($e_{\mathrm{max}} = 12$), dDSCGF(2)* ($e_{\mathrm{max}} = 10$) and VS-IMSRG(2) ($e_{\mathrm{max}} = 12$) calculations against experimental data along the Ca isotopic chain. *First line*: absolute binding energy. *Second line*: two-neutron separation energy. *Third line*: two-neutron shell gap. Fourth line: intrinsic axial quadrupole deformation of the dHFB solution. Results are obtained with the EM 1.8/2.0 Hamiltonian and $\hbar\omega = 12\,\mathrm{MeV}$.

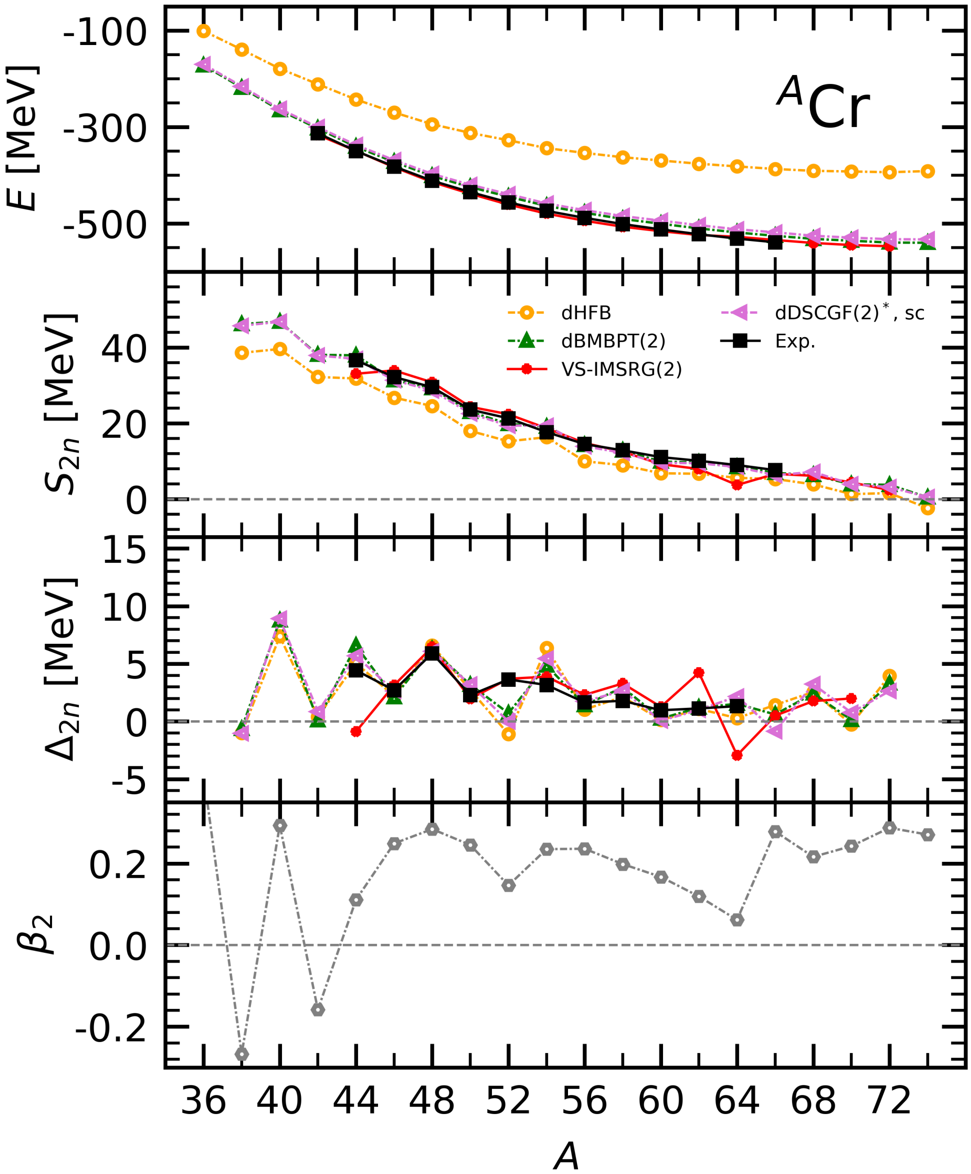

Figure 5.17. Same as Fig. 5.16 for the Chromium isotopic chain.

5.5.2. Charge radii

Another key nuclear structure observable is the root-mean-square *charge radius* defined as $R_{ch} \equiv \sqrt{\langle r^2_{ch} \rangle}$, with

$$\langle r^2_{ch} \rangle \equiv \langle r^2_{pt-p} \rangle + \langle R^2_p \rangle + \frac{N}{Z} \langle R^2_n \rangle + \frac{3\hbar^2}{4m^2_p c^2} + \langle r^2_{so} \rangle \ , \tag{5.59}$$

where the point-proton radius $\langle r^2_{pt-p} \rangle$ is corrected for proton and neutron charge radii, respectively equal to $\langle R^2_p \rangle = 0.7079\,\text{fm}^2$ [110] and $\langle R^2_n \rangle = -0.1149\,\text{fm}^2$ [111], for the relativistic Darwin-Foldy term $(3\hbar^2)/(4m^2_p c^2)$ and for a spin-orbit contribution $\langle r^2_{so} \rangle$. The latter is included via a formula derived within a spherical mean-field approximation [112]. The point-proton radius is computed in the intrinsic frame as

$$\langle r^2 \rangle_{pt-p} \simeq \frac{1}{A} \sum_{\alpha\beta} u^{pt-p}_{\alpha} \langle \alpha | \vec{r}^{\,2} | \beta \rangle \, \rho_{\beta\alpha} - \frac{1}{A^2} \sum_{\alpha\beta\gamma\delta} u^{pt-p}_{\alpha\gamma} \langle \alpha\gamma | \vec{r}_1 \cdot \vec{r}_2 | \beta\delta \rangle \, \rho_{\beta\alpha} \, \rho_{\delta\gamma} \, , \tag{5.60}$$

where $\vec{r}_i$ represents the position of the i-th nucleon. The approximate sign comes from the fact that the two-body operator on the right-hand side should be in principle convoluted with the (correlated) two-body density matrix and not with the product of two (correlated) one-body density matrices, which is too burdensome to compute in practice. As described in Ref. [113], the coefficients u^{pt-p}_{α} and $u^{pt-p}_{\alpha\gamma}$ read respectively as

$$u^{pt-p}_{\alpha} = \begin{cases} \dfrac{A(A-2)+Z}{ZA} & \text{if } \alpha \text{ labels a proton state} \\ \dfrac{1}{A} & \text{if } \alpha \text{ labels a neutron state} \end{cases} \tag{5.61}$$

and

$$u^{pt-p}_{\alpha\beta} = \begin{cases} \dfrac{2A-Z}{Z} & \text{if } \alpha \text{ and } \beta \text{ label proton states} \\ \dfrac{A-Z}{Z} & \text{if } \alpha \text{ and } \beta \text{ label a proton and a neutron state} \\ -1 & \text{if } \alpha \text{ and } \beta \text{ label neutron states.} \end{cases} \tag{5.62}$$

Charge radii calculated with dDSCGF(2) along the Neon isotopic chain with ΔNNLO$_{\text{go}}$ (394) and ΔNNLO$_{\text{go}}$ (450) Hamiltonians are compared in Fig. 5.18 with those obtained from dCCSDT-1 calculations. With the ΔNNLO$_{\text{go}}$ (394) Hamiltonian, SCGF and CC results display the same trend, with a local maximum and a local minimum in ^{20}Ne and ^{24}Ne, respectively. For what concerns the ΔNNLO$_{\text{go}}$ (450) interaction, the trend is again similar but the minimum obtained in ^{24}Ne for dCCSDT-1 and experiment is shifted to ^{26}Ne for dDSCGF(2). Overall the Green's function results are about 0.02 −0.05 fm above the coupled-cluster ones. Such a discrepancy might be due to the different model space employed in the two calculations and the different truncations employed in both many-body expansions.

5.5.3. One-nucleon addition and removal processes

Interpreting spectra

As discussed in Sec. 5.2.1, the Lehmann representation of the single-particle propagator, Eq. (5.3), provides key informations about $A\pm1$ systems. In particular, the poles of the 1B

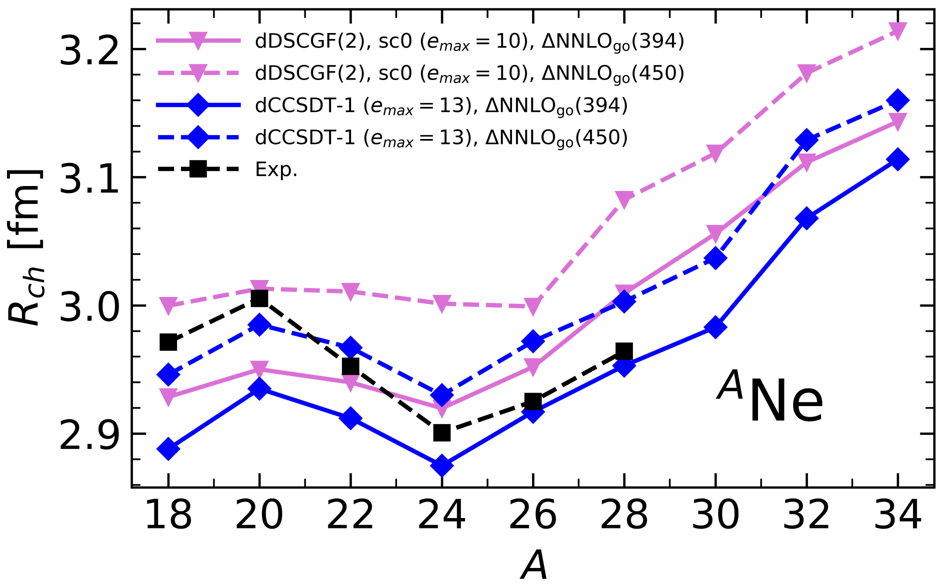

Figure 5.18. Charge radius computed for the Neon isotopic chain for the ΔNNLO$_{go}$ (394) and the ΔNNLO$_{go}$ (450) interaction, with corresponding sHO energies $\hbar\omega = 16$ and 12 MeV. Coupled-cluster data are taken from [9] while experimental data are taken from [111].

Green's function deliver one-nucleon addition and removal energies to the A-body ground state and thus provide excitation spectra in the odd neighbours. While such spectra can be straightforwardly compared to experimental ones in calculations that conserve spherical symmetry (see, e.g. [26, 114–116]), in the present approach the impossibility to firmly assign a good angular momentum to the poles of the GF poses an interpretation problem. While this can (and should) be solved in the future by formulating a symmetry-restored version of deformed SCGF theory, a short-term solution might be devised by learning from other methods exploiting deformation, e.g. the Nilsson shell model.

Examples

In this context, let us inspect some examples of such spectra and associated spectroscopic factors. These quantities are conveniently encoded, for both one-nucleon addition and removal processes, into the spectral strength distribution

$$\begin{aligned}\mathcal{S}(\omega) &\equiv \mathrm{Tr}_{\mathcal{H}_1}\Big[\mathbf{S}^{+}(\omega)\Big] + \mathrm{Tr}_{\mathcal{H}_1}\Big[\mathbf{S}^{-}(\omega)\Big] \\ &= \sum_{n\in\mathcal{H}_{A+1}} SF_n^{+}\,\delta(\omega-\varepsilon_n^{+}) + \sum_{k\in\mathcal{H}_{A-1}} SF_k^{-}\,\delta(\omega-\varepsilon_k^{-})\,.\end{aligned} \tag{5.63}$$

Let us start with the doubly closed-shell nucleus ^{40}Ca whose HF solution does not break rotational symmetry and can thus be labelled with $j^{\pi} = 0^{+}$ even if the calculation is implemented in m-scheme. Figure 5.19 displays the associated spectral strength distribution in several neutron positive-parity symmetry blocks computed at the ADC(1) level with the NN+3N(lnl) Hamiltonian. The addition (removal) of one neutron accesses eigenstates in ^{39}Ca (^{41}Ca), the two channels being separated by the Fermi energy in the figure. The fact that all peaks have $SF^{\pm} = 1$ is a consequence of the independent-particle character of the

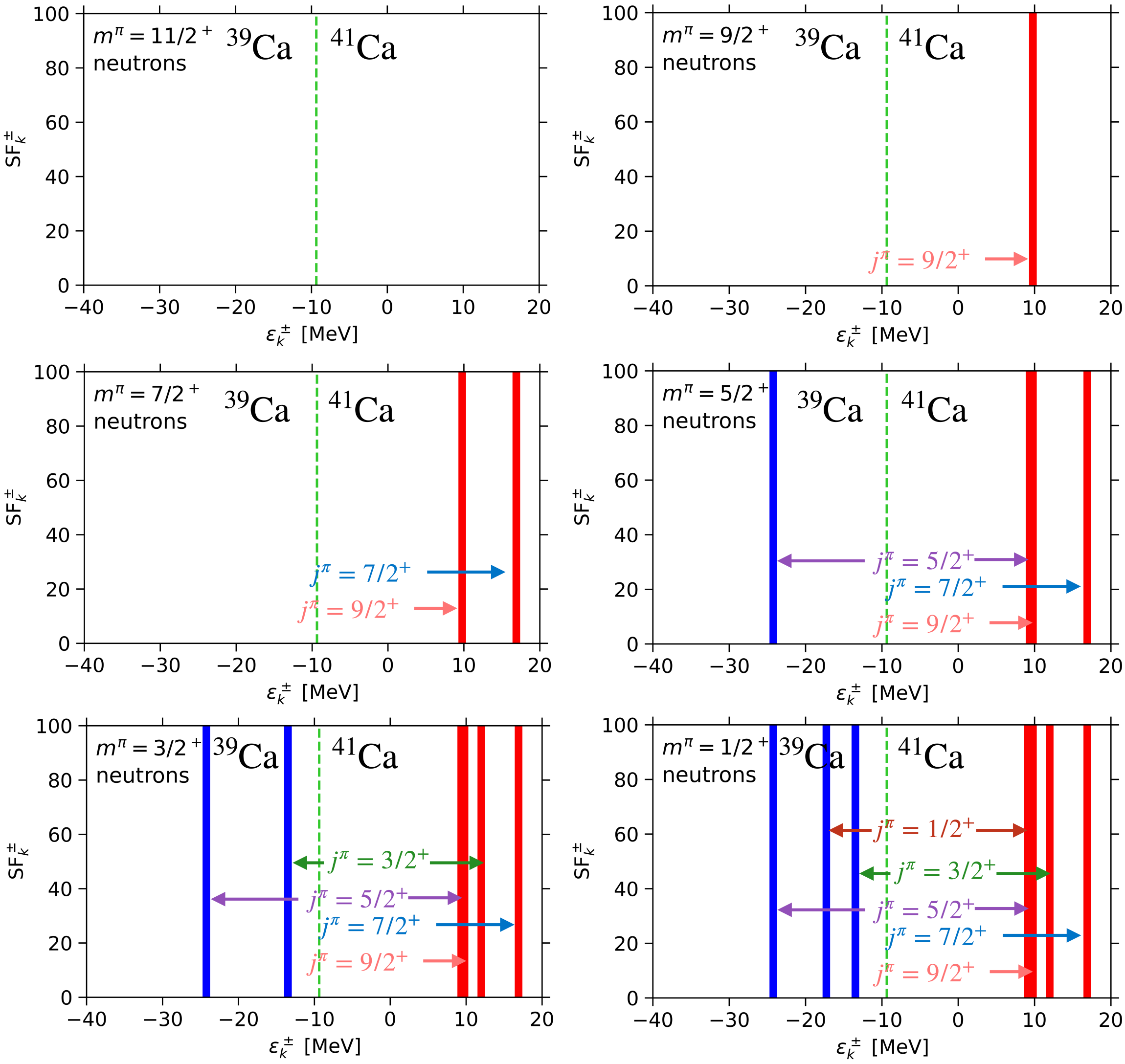

Figure 5.19. Neutron spectral strength distribution computed in ^{40}Ca at the ADC(1) level. Starting from the top and moving from left to right, the 6 panels show the spectral strength for different positive-parity symmetry blocks of the Dyson equation where the value of m constantly decreases. Everywhere, the green dashed line represents the neutron Fermi energy (Eq. (5.53)). According to the procedure described in the text, angular momenta are identified for each peak and labelled correspondingly on the plot. Results are relative to the NN+$3N$(lnl) Hamiltonian and employ $\hbar\omega = 18\,\mathrm{MeV}$ with $e_{\max} = 10$.

ADC(1), i.e. HF, approximation. Given that rotational symmetry is not spontaneously broken in ^{40}Ca, each state in the $A \pm 1$ systems is expected to carry a good j^π quantum number and should thus display a degeneracy with respect to the angular-momentum projection m, i.e., each state should appear at the same energy in each $|m| \leq j$ block.

Starting from the top left panel, no peak is visible in the $m^\pi = 11/2^+$ block in the displayed energy range. Going to the $m^\pi = 9/2^+$ block, a state appears in the additional channel to ^{41}Ca at $\varepsilon_n^+ \approx 10$. Since this peak is not present in the previous block, it can safely be assigned $j^\pi = 9/2^+$. Analogously, in the $m^\pi = 7/2^+$ block a new state appears in the additional channel, while the $j^\pi = 9/2^+$ state already identified in the $m^\pi = 9/2^+$ block is indeed present at the same energy. The new peak can thus be assigned $j^\pi = 7/2^+$. One can proceed similarly for all the remaining blocks with states also appearing in the removal channel to ^{39}Ca.

The same exercise performed for the fragmented strength distribution obtained at the ADC(2) level shown in Fig. F.1 of App. F leads to analogous conclusions. In the limit of zero deformation, one can thus straightforwardly recover a well-defined and unambiguous physical spectrum from the m-scheme implementation.

Let us now move to ^{58}Ca for which the dHF reference state displays the small axial deformation $\beta_2 = -0.03$. The corresponding spectral distribution computed at the ADC(2) level is shown in Fig. 5.20. Proceeding as before, i.e. starting from the $m^\pi = 11/2^+$ block and moving step-by-step to blocks with smaller values of m, it becomes immediately clear that this the clean angular momentum assignment is no longer possible. The slight deformation of ^{58}Ca is already enough to trigger some m-dependence in the distribution that prevents from firmly assigning good j to each of the peaks. Nevertheless, in most cases the variations of the horizontal position and height of the peak remains small, such that one can still identify its dominant j character.

Moving to ^{46}Ca whose dHF reference state displays the mild deformation $\beta_2 = 0.08$, the angular momentum mixing is already too significant for all quasi-particle and quasi-hole states as seen in Fig. F.2 presented in App. F. Consequently, the procedure does not allow a firm angular momentum assignment such that one is only left with labelling final states with m and π.

5.6. Conclusions

The first applications of the newly developed deformed DSCGF approach establish it as a promising tool in the landscape of *ab initio* many-body techniques. While results are close to dBMBPT(2) for soft nuclear interactions, the non-perturbative nature of the method allows one to cover a wider range of χEFT Hamiltonians. Furthermore, the versatility of the approach and the variety of observables at hand in a single calculation make it an attractive alternative to existing nuclear structure methods applicable to singly and doubly open-shell nuclei. Indeed, the numerical techniques exposed in the present chapter make calculations doable at a moderate computational cost.

As a first follow-up of this work, a proper particle-number adjustment was shown to be necessary to perform accurate dDSCGF calculations. This will be done by introducing a Lagrange term controlling the average particle number while solving Dyson's equation.

Next, a numerical optimization is required to push calculations to larger values of $e_{\max}$ and N_l. This can be accomplished both by optimizing specific routines of the numerical code and by implementing a multi-node parallelization to distribute the computation of the many-body tensors at play across different CPU nodes.

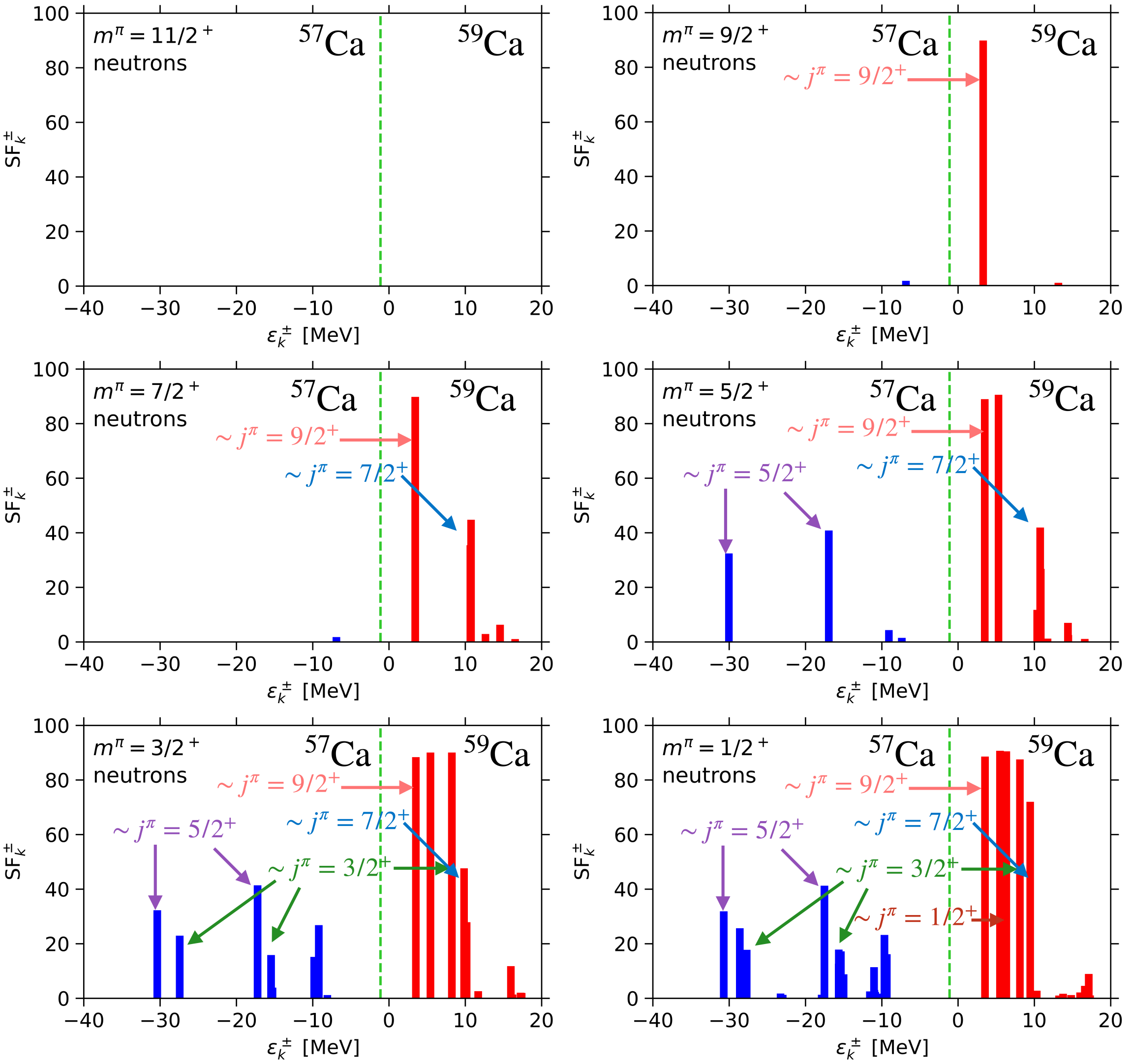

Figure 5.20. Same as Fig. 5.19 but for the ADC(2) approximation and ^{58}Ca. While a good angular momentum cannot be firmly associated to the various peaks anymore, labels are still displayed in the plot to tentatively identify the main J contribution.

Another important future development concerns the enrichment of the many-body content, e.g. by pushing the dDSCGF expansion to the ADC(3) truncation level. While this has been recently accomplished for spherical DSCGF calculations [96], the m-scheme setting necessary to tackle deformed systems makes a similar development much more challenging in the present case. A possible interesting alternative is the so-called 'extended ADC(2)' approximation [96] whose truncation level resides between ADC(2) and ADC(3). This approximation includes full ladder and ring diagrams summations through the introduction of non-zero C and D terms in Eq. (5.27). Although less costly than the full ADC(3), such a scheme does however reduce considerably the sparsity of the Dyson matrix and will require an decisive optimization of the numerical code, such as the already-mentioned multi-node parallelization.

In absence of angular-momentum conservation, the interpretation of spectral strength distributions associated to one-nucleon addition and removal processes must rely on the phenomenological know-how developed in the past in the context of the Nilsson model [117]. On the longer term, the objective is to formulate a symmetry-conserving SCGF calculation for open-shell nuclei. Typically, this can be done following two different routes:

1. the first option is to break symmetries at the mean-field level, build a symmetry-breaking beyond mean-field expansion on top of it and eventually restore the symmetries. A full restoration of the rotational symmetry, similarly to what can be done for MBPT and CC [18, 19, 48], is still to be developed;

2. the second option is to employ a multi-reference state (which can be obtained e.g. from a Projected Generator Coordinate Method (PGCM) calculation) that does not break symmetries but that is informed by the correlations relevant for the description of open-shell nuclei. Such formalism has been recently developed in Quantum Chemistry [118, 119] for the ADC expansion and still needs to be adapted to the nuclear structure case.

In order to push the technique presented in this chapter to the next many-body order, i.e. dDCSGF(3), numerical optimizations will probably not be sufficient. The size of the Dyson matrix at ADC(3) level is indeed extremely limiting for numerical applications. In order to overcome such obstacle, the next chapter (Ch. 6) aims at adapting a long-time known technique to accelerate the convergence rate of *ab initio* applications with respect to the size of the model space to the study of deformed systems.

Chapter 6.

Deformed natural orbitals

Contents

6.1. Introduction

As discussed in Ch. 2, *ab initio* calculations are typically carried out by representing relevant quantities (wave functions, operators, density matrices, etc.) on a basis of the A-body Hilbert space $\mathcal{H}_\text{A}$, itself obtained as the tensor-product of bases of the one-body Hilbert space $\mathcal{H}_1$. Because of finite computational resources, the infinite-dimensional basis of $\mathcal{H}_\text{A}$ has to be truncated to perform practical calculations, either directly or via a truncation of the underlying one-body basis. Eventually, the size of the truncated basis impacts both the cost of handling (in terms of storage and RAM) the Hamiltonian tensors constituting the input of a given simulation and the cost of solving the many-body Schrödinger equation (in terms of storage, RAM and CPU time) to determine the many-body tensors (wave function, density matrices...) constituting the output. Clearly, the accuracy of a calculation depends on the appropriateness of the chosen basis truncation[1], which itself depends on the characteristics of the employed basis. While attaining a suitable error[2] does not generally constitute a difficulty in light nuclei, it may become challenging in medium-mass nuclei and ultimately limits the application of state-of-the-art techniques to heavy systems, especially when aiming at doubly open-shell nuclei and/or at solving the many-body Schrödinger equation with sub-percent accuracy; see Ref. [41] for a detailed discussion.

Several strategies are currently pursued to alleviate the computational cost of many-body calculations (at fixed accuracy). First, importance truncation (IT) [22, 120–122] and tensor factorisation (TF) [41, 123–126] techniques aim at reducing the storage and CPU footprints of input and output tensors while working in a given one-body basis of choice, typically the eigenbasis of the one-body (sHO) Hamiltonian. A second approach, the one followed in the present chapter, consists of optimising in a first step the nature of the one-body basis in order to reach faster convergence with respect to the cardinality of that basis. Eventually, the two strategies can be combined to push the limits of state-of-the-art calculations.

Despite the advantages that the sHO basis offers (see the discussion in Sec. 2.1.3), the fact that sHO wave functions decay at long distances as a Gaussian function rather than as an exponential one makes difficult in practice to represent weakly-bound many-body states or to bridge to nuclear reactions.

While the optimisation of one-body basis states is central in electronic structure calculations [127, 128], the use of alternatives to the sHO basis has received limited attention in nuclear physics, with only a few exceptions [129–132]. In the present case, the interest is not in exploring alternative bases that would be given *a priori* but rather to employ a *nucleus-dependent* basis that is informed of the characteristics of the system under consideration, i.e. a basis that reflects the bulk of many-body correlations in order to best accelerate the convergence (with respect to the one-body basis size) of a subsequent high-accuracy calculation of those correlations.

A successful choice in this respect is provided by the natural (NAT) orbital basis [127, 133, 134] obtained by diagonalising the one-body density matrix of the correlated state under consideration. In particular, a faster convergence of ground-state observables has been found both in exact diagonalisation techniques [135] applicable to light nuclei, and in calculations of doubly closed-shell nuclei based on symmetry-conserving expansion methods [121, 136]. While natural orbitals have also been recently employed in deformed coupled-cluster calculations [9], a detailed study of their performance in symmetry-breaking expansion methods applicable to all nuclei is currently missing.

The first goal of the present chapter is thus to investigate the use of the NAT basis in expansion methods based on superfluid and deformed reference states dedicated to singly and doubly open-shell nuclei. Because symmetry-breaking methods necessitate a much larger number of one-body basis states than symmetry conserving ones, their optimisation is even more compelling. To do so, dBMBPT at second and third order is employed to

---

[1] This is sometimes referred to as the *model-space* truncation.

[2] The mode-space uncertainty must be similar to or smaller than the other sources of error in the many-body calculation.

both generate the one-body density matrix from which the NAT basis is extracted and compute ground-state energy out of which the accelerated convergence is characterized. The second objective of this chapter is to compare the benefits obtained using the NAT basis and IT techniques before combining both tools.

The chapter is organized as follows. Section 6.2 introduces the main theoretical and computational ingredients, including details on the extraction of the natural basis. Section 6.3 compares the performance of the NAT and sHO bases in open-shell nuclei. Section 6.4 examines possible alternatives to the NAT basis and provides further insight by analyzing the behavior of the associated single-particle wave functions. In Sec. 6.5 the NAT basis is compared to IT and combined with it. Section 6.6 presents the advantages that the NAT basis brings to the dDSCGF(2) method presented in Ch. 5. Finally, Sec. 6.7 summarizes the main conclusions and discusses possible future developments.

6.2. Formalism and computational setting

6.2.1. Many-body method

The goal is to extract *approximate* natural orbitals from a many-body state informed of bulk of many-body correlations via a calculation that is significantly less costly than the one of interest. A low-order deformed Bogoliubov many-body perturbation theory [35, 137] calculation based on a dHFB unperturbed state is ideally suited to do so across a significant part of the nuclear chart, independently of the closed-, singly open- and doubly open-shell character of the nucleus under consideration[3]. While the objective is to eventually perform non-perturbative calculations of open-shell nuclei[4], dBMBPT is also used in most of the present chapter to validate the acceleration offered by the use of the NAT basis.

6.2.2. Deformed natural orbital basis

Definition

Having defined the dBMBPT(p) state $|\Psi^{(p)}\rangle$ in Eq. (2.56), the associated normal one-body density matrix relative to normalized many-body wave functions can be computed in the sHO basis as in Eq. (2.58)[5]:

$$\begin{aligned}\rho^{(p)}_{\alpha\beta} &\equiv \langle\Psi^{(p)}|c^\dagger_\beta c_\alpha|\Psi^{(p)}\rangle \\ &\equiv \delta_{m_\alpha m_\beta}\delta_{\pi_\alpha\pi_\beta}\delta_{t_\alpha t_\beta}\,\rho^{[m\pi t]_\alpha\,(p)}_{n_\alpha j_\alpha n_\beta j_\beta}\,,\end{aligned} \tag{6.1}$$

and diagonalized according to

$$\sum_\beta \rho^{(p)}_{\alpha\beta} C^{(p)}_{\beta\gamma} = \lambda^{(p)}_\gamma C^{(p)}_{\alpha\gamma}\,. \tag{6.2}$$

---

[3] The method used to generate the NAT basis will be indicated in square brackets, e.g. ‘NAT[dBMBPT(2)]’ denotes the NAT basis obtained from a second-order dBMBPT density matrix. Whenever the unperturbed state is actually unpaired, ‘dHF’ or ‘dMBPT’ can be used to label the calculation in use.

[4] One typically has in mind to perform deformed coupled cluster (dCC) [9, 48] or Dyson self-consistent Green’s function calculations (dDSCGF) [6] based on a deformed reference state.

[5] For reference, the explicit expression of $\rho^{(2)}$ can be found in Ref. [35].

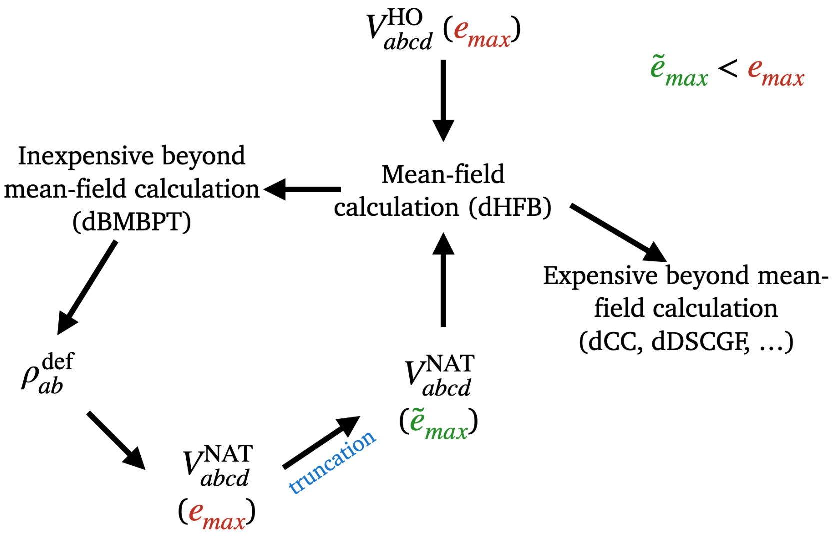

Figure 6.1. Workflow of the generation of the NAT basis via a dBMBPT calculation, leading to a redefinition of the interaction matrix elements for a subsequent many-body calculation.

The eigenstates of $\rho^{(p)}$ are nothing but the deformed NAT[dBMBPT(p)] basis states whose eigenvalues $\lambda^{(p)}_\gamma$ denote their average occupation in $|\Psi^{(p)}\rangle$. In Eq. (6.2), the eigenvectors provide the unitary transformation between the sHO basis $\{|\varphi_\alpha\rangle; \alpha = 1, \dots, n_B\}$ and the NAT[dBMBPT(p)] basis $\{|\phi^{(p)}_\gamma\rangle; \gamma = 1, \dots, n_B\}$

$$C^{(p)}_{\alpha\gamma} \equiv \langle\varphi_\alpha|\phi^{(p)}_\gamma\rangle \,. \tag{6.3}$$

Algorithm

In practice, the density matrix is diagonalized in each separate $[m\pi t]_\alpha$ block such that the transformation between the two bases reads as

$$|N_\alpha m_\alpha \pi_\alpha t_\alpha\rangle_{\mathrm{NAT[dBMBPT}(p)]} = \sum_{n_\alpha j_\alpha} C^{[m\pi t]_\alpha\,(p)}_{n_\alpha j_\alpha N_\alpha} \, |n_\alpha \pi_\alpha j_\alpha m_\alpha t_\alpha\rangle_{\mathrm{sHO}} \,. \tag{6.4}$$

In each $[m\pi t]_\alpha$ block, the principal quantum number N_α are arranged according to the decreasing occupation ($\lambda^{(p)}_1 \geq \lambda^{(p)}_2 \geq \dots$) of the NAT states. Based on this ordering, an *effective* $\tilde{e}_{\mathrm{max}}$ parameter[6] is defined such that the number of NAT states retained is the same as for the sHO truncated according to $e_{\mathrm{max}} = \tilde{e}_{\mathrm{max}}$[7].

Truncating the NAT[dBMBPT(p)] basis according to $\tilde{e}_{\mathrm{max}}$, the matrix elements of the one-body kinetic energy and of the two-body interaction[8] initially expressed in the sHO basis are transformed into the deformed NAT basis using Eq. (6.4). Based on this (reduced) set of matrix elements, a dHFB state is recomputed and the expansion method of choice is performed on top of it. The procedure is summarized in Fig. 6.1.

---

[6] In any given calculation, $\tilde{e}_{\mathrm{max}}$ is necessarily smaller than or equal to the e_{max} value originally used to compute the density matrix.

[7] From a general standpoint, there is a total freedom to select any subset of the NAT states as the new working basis. More optimal truncation schemes will be explored in future studies.

[8] The two-body operator does not only include the genuine two-body interaction but also the two-body part of the center-of-mass correction as well as the rank-reduced three-body interaction.

Basic properties

Natural orbitals possess the key extremum property [138]

$$\sum_{\gamma=1}^{r\leq n_B} \lambda_\gamma^{(p)} \leq \sum_{k=(1)}^{(r)\leq n_B} \rho_{\kappa\kappa}^{(p)} \tag{6.5}$$

where the diagonal elements $\rho_{\kappa\kappa}$ can here be taken in *any* one-body basis and where in the sum over $\kappa = (1), \ldots, (r)$ any set of r indices among the n_B ones can be selected. This property expresses the fact that the occupations fall as quickly as possible in the natural basis such that any subset gathering the most occupied orbitals is indeed maximally occupied. In turn, this property implies that the expansion of the many-body state on the set of Slater determinants built out of NAT states displays optimal convergence properties [138]. Thus, one expects the above property to translate into the fact that the use of the NAT basis optimally accelerate the convergence of a given many-body expansion method with respect to the $\tilde{e}_{\text{max}}$ truncation. If so, extracting natural orbitals from an inexpensive dBMBPT(p) calculation with a large enough e_{max} may authorize in a second step to converge a more expensive calculation for $\tilde{e}_{\text{max}} < e_{\text{max}}$.

A second interesting property relates to the asymptotic behavior of NAT states that can be inferred from the local nucleon density distribution given by

$$\rho^{(p)}(\vec{r}) = \sum_\gamma \lambda_\gamma^{(p)} |\phi_\gamma^{(p)}(\vec{r})|^2 \,. \tag{6.6}$$

Due to the short-range character of nuclear forces, the long-distance behavior of the one-nucleon density distribution is given by [139]

$$\rho^{(p)}(\vec{r}) \underset{r\to+\infty}{\longrightarrow} \frac{e^{-2\kappa_0\, r}}{(\kappa_0\, r)^2} \,, \tag{6.7}$$

with $\kappa_0 = \sqrt{-2m\varepsilon_0/\hbar^2}$ and where $\varepsilon_0 = \left(E_0^N - E_0^{N-1}\right)$ is minus the one-nucleon separation energy to reach the ground state of the system with one less nucleon. Because $\rho^{(p)}(\vec{r})$ decays exponentially with a rate set by the one-nucleon removal energy, and because all contributions in the right-hand side of Eq. (6.6) are strictly positive[9], all natural orbital wave-functions are localized and decay faster than $\rho^{(p)}(\vec{r})$ at long distances.

This is to be compared to the case where the many-body state reduces to a single, e.g. dHF, Slater determinant. In this case natural orbitals are nothing but HF single-particle states and Eq. (6.6) must be replaced by

$$\rho^{(\text{dHF})}(\vec{r}) = \sum_{\alpha\,\in\,\text{occ.}} |\psi_\alpha^{(\text{dHF})}(\vec{r})|^2 \,. \tag{6.8}$$

It follows that the above property only applies to the occupied ($\lambda_\alpha^{(\text{dHF})} = 1$) single-particle states in the Slater determinant, while all unoccupied ($\lambda_\alpha^{(\text{dHF})} = 0$) single-particle HF states are not constrained to decay exponentially. In fact, the latter actually oscillate to infinite distance as scattering states as soon as the corresponding HF single-particle energy is positive. These characteristics will be useful later on to analyze the results obtained with different one-body bases.

---

[9] As soon as $|\Psi^{(p)}\rangle$ does not restrict to a Slater determinant, all eigenvalues of the one-body density matrix are strictly positive in principle. In practice of course, several eigenvalues can be identified as a numerical zero.

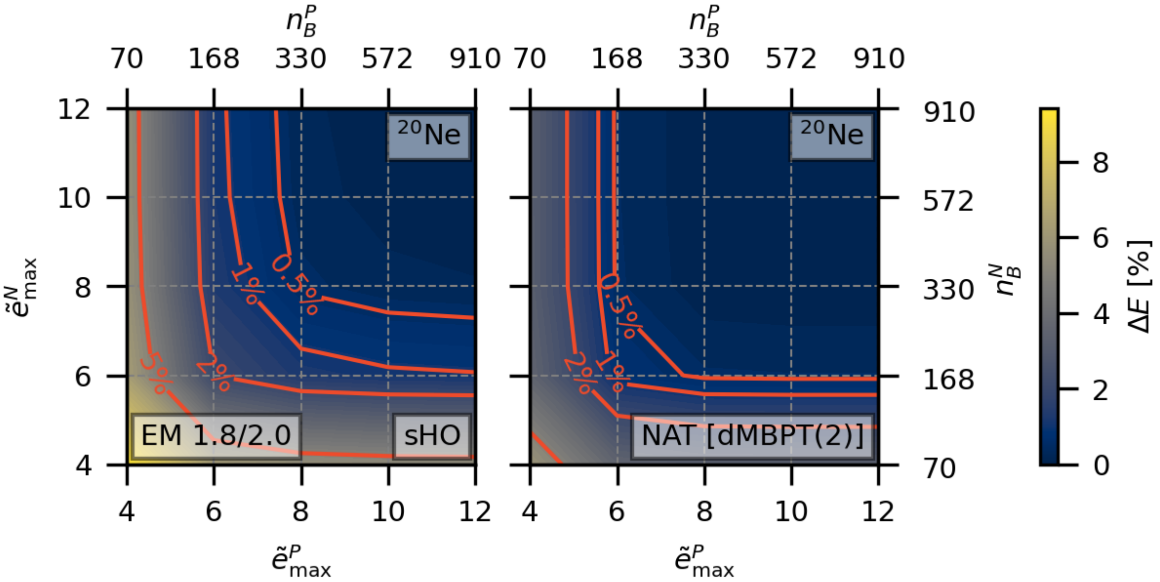

Figure 6.2. Convergence of the ^{20}Ne ground-state energy (relative to the $e_{\max} = 12$ value) computed at the dMBPT(2) level using the sHO (*left panel*) and NAT[dMBPT(2)] (*right panel*)) bases. Results are shown as a function of $\tilde{e}^N_{\max}$ and $\tilde{e}^P_{\max}$. For each basis truncation, the corresponding number of basis states are shown on the upper and right axes (See also Tab. 2.1.). Calculations are performed with the EM 1.8/2.0 Hamiltonian.

6.2.3. Hamiltonian

The two χEFT nuclear Hamiltonians NNLO$_{\text{sat}}$ (bare) and EM 1.8/2.0 are employed in the present chapter. While the second Hamiltonian is directly built as a soft representative displaying negligible coupling between low and high (relative) momentum states, the former does display significant coupling to high momenta. In order to transition from the latter to the former and characterize the impact of coupling to high momenta on the accelerated convergence induced by the NAT basis, the NNLO$_{\text{sat}}$ Hamiltonian is further evolved through a free-space similarity renormalisation group transformation (SRG) [10] in order to decouple low and high momenta. Doing so, down to the momentum scale $2.4\,\text{fm}^{-1}$ ($2.0\,\text{fm}^{-1}$), one defines the evolved NNLO$_{\text{sat}}$ (2.4) (NNLO$_{\text{sat}}$ (2.0)) Hamiltonians.

Reference calculations employ an $e_{\max} = 12$ truncation of the sHO basis. Calculations with the EM 1.8/2.0 Hamiltonian are performed with an oscillator frequency $\hbar\omega = 20\,\text{MeV}$ while results relative to NNLO$_{\text{sat}}$ (bare) are obtained with $\hbar\omega = 18\,\text{MeV}$ (except if specified otherwise). Three-body interaction matrix elements are further truncated to $e_{3\max} = 16 < 3\,e_{\max}$ before reducing the three-body interaction to an effective two-body one via the rank-reduction method developed in Ref. [35].

Based on this numerical setting the performance of a given one-body basis is characterized by computing the relative error $\Delta E[\%]$ of the dBMBPT ground-state energy obtained for a given $\tilde{e}_{\max} \leq 12$ truncation with respect to the reference results obtained for $e_{\max} = 12$.

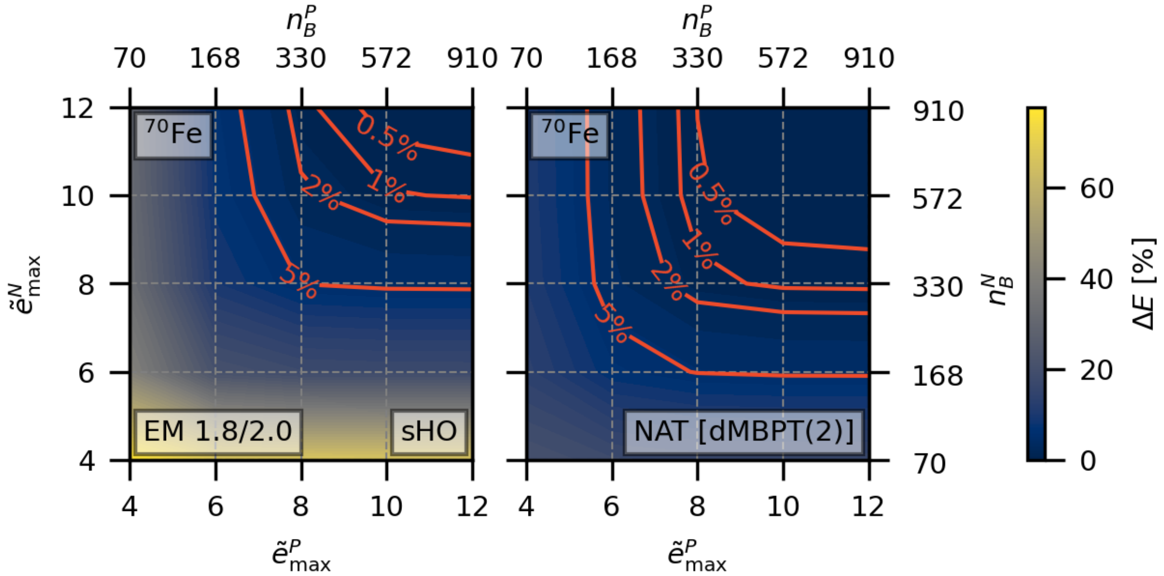

Figure 6.3. Same as Fig. 6.2 for ^{70}Fe.

6.3. NAT[dBMBPT(2)] basis performance

The goal of the present chapter is to assess the accelerated convergence obtained by using the NAT[dBMBPT(2)] basis relative to the standard sHO basis in realistic calculations of doubly open-shell nuclei. Because the NAT basis is isospin dependent, in the context of the present work the `PAN@CEA` numerical suite has been extended to handle isospin-dependent bases. In turn, this makes possible to truncate separately neutron and proton one-body basis states according to the $\tilde{e}^N_{\text{max}}$ and $\tilde{e}^P_{\text{max}}$ parameters.

6.3.1. sHO vs NAT[dBMBPT(2)] bases

The first nucleus under study is ^{20}Ne, a prolate nucleus recently investigated via various *ab initio* expansion methods [8, 9, 54]. The convergence of the ground-state energy computed with the EM 1.8/2.0 Hamiltonian is displayed in Fig. 6.2 for both the sHO and the NAT[dBMBPT(2)] bases as a function of $\tilde{e}^N_{\text{max}}$ and $\tilde{e}^P_{\text{max}}$.

The NAT basis is seen to display a faster convergence than the sHO basis, e.g. the 1% error with respect to the converged ($e_{\text{max}} = 12$) result is reached at $\tilde{e}^N_{\text{max}} = \tilde{e}^P_{\text{max}} = 8$ in the sHO basis whereas $\tilde{e}^N_{\text{max}} = \tilde{e}^P_{\text{max}} = 6$ is sufficient in the NAT basis. Because ^{20}Ne is a $N = Z$ nucleus, the gain is symmetric with respect to $\tilde{e}^N_{\text{max}}$ and $\tilde{e}^P_{\text{max}}$.

As seen from Tab. 2.1, such an advantage allows one to work with about half the number n_B of states compared to the sHO basis, which already constitutes a sizeable advantage in terms of storage and CPU time for any expansion method scaling polynomially, i.e. as n_B^q, with the one-body basis size. For state-of-the-art high-accuracy methods for which $q = 7$ or 8, the gain can be very significant.

Next, the NAT basis is tested on a heavier neutron-rich prolate ^{70}Fe nucleus; results are shown in Fig. 6.3. The error associated with the sHO basis displays an asymmetric pattern, the energy converging faster with respect to $\tilde{e}^P_{\text{max}}$ than to $\tilde{e}^N_{\text{max}}$. The use of the NAT basis essentially restores the neutron-proton symmetry and an advantage analogous to the one obtained for ^{20}Ne is observed. The fact that the benefit carries over to medium-

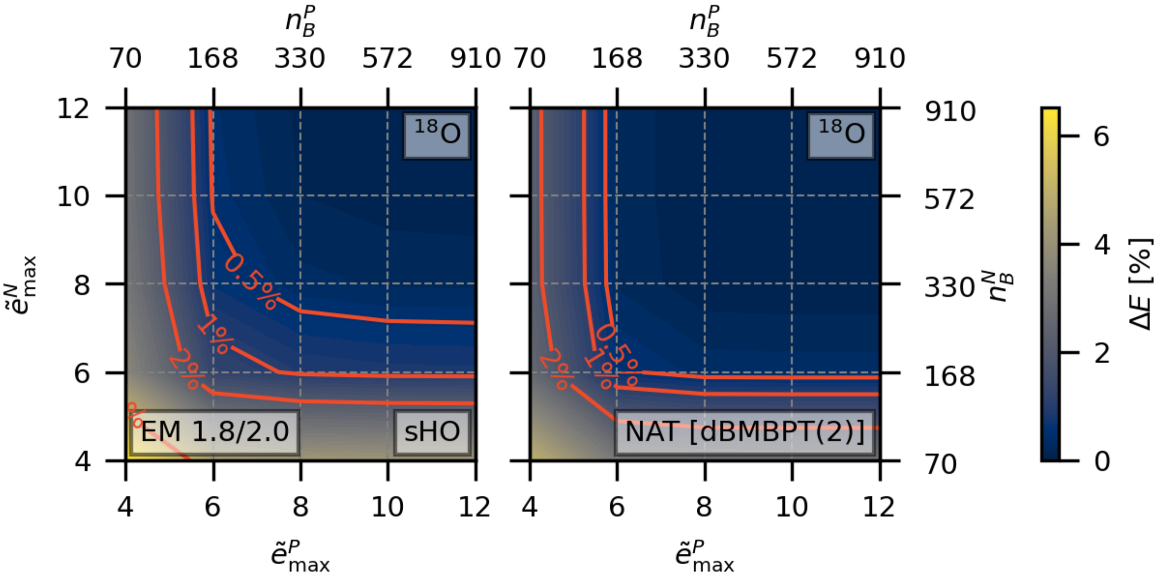

Figure 6.4. Same as Fig. 6.2 for ^{18}O.

heavy mass deformed nuclei is encouraging in view of using the NAT basis for the most computationally challenging systems in the future.

Finally, Fig. 6.4 displays results for the singly open-shell, i.e. spherical and superfluid, ^{18}O nucleus. For a small, i.e. 0.5% or 1%, error, a similar advantage to the one observed ^{20}Ne and ^{70}Fe is achieved.

6.3.2. Application to dBMBPT(3)

Having tested the performance of the NAT[dBMBPT(2)] basis through dBMBPT(2), one can employ a more advanced dBMBPT(3) calculation to further validate the conclusions. The result of such a test, reported in Fig. 6.5 for ^{18}O, indeed leads to similar conclusions as for dBMBPT(2)[10].

6.3.3. Resolution-scale dependence

The correlations encoded in a beyond-mean-field, e.g. dBMBPT(2), density matrix ultimately depend on the input Hamiltonian, and in particular on its resolution scale. It is thus important to assess the efficiency of the NAT machinery for interactions characterized by different degrees of 'softness'. To this end, the four Hamiltonians introduced in Sec. 6.2.3, spanning a significant range of resolution scales, are now considered.

Figure 6.6 shows the relative error on the dBMBPT(2) ground-state energy of ^{20}Ne and ^{56}Fe for different e_{max} ($\tilde{e}_{\text{max}}$) truncations on the sHO (NAT[dMBPT(2)]) basis. The overall behavior is similar in the two nuclei, i.e. while the error for a given e_{max} ($\tilde{e}_{\text{max}}$) decreases with the resolution scale of the Hamiltonian, the relative gain offered by the NAT basis over the sHO basis is essentially independent of it. For Hamiltonians characterized by a low resolution scale, the use of the NAT[dBMBPT(2)] basis allows a 1% error at $\tilde{e}_{\text{max}} = 6$ ($\tilde{e}_{\text{max}} = 8$) in ^{20}Ne (^{56}Fe) while the sHO basis necessitates two more major shells to

---

[10] Other possibilities, i.e. dBMBPT(2) calculations on top of NAT[dBMBPT(3)] or dBMBPT(3) calculations on top of NAT[dBMBPT(3)] have also been tried and all lead to similar results.

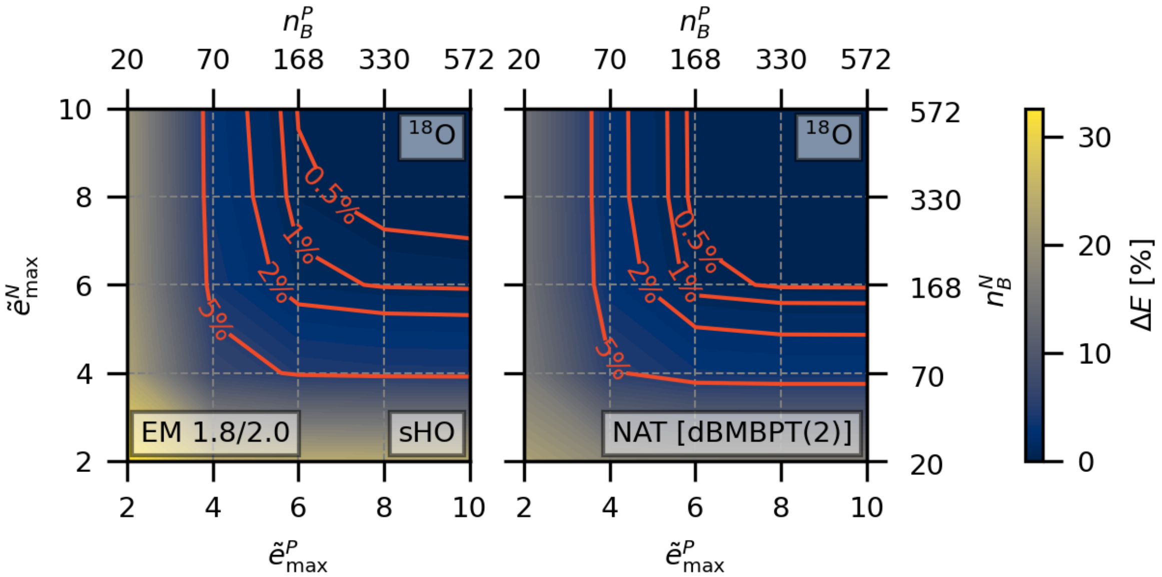

Figure 6.5. Same as Fig.6.4 but for a dBMBPT(3) calculation and an error computed relatively to the $e_{\max} = 10$ calculation.

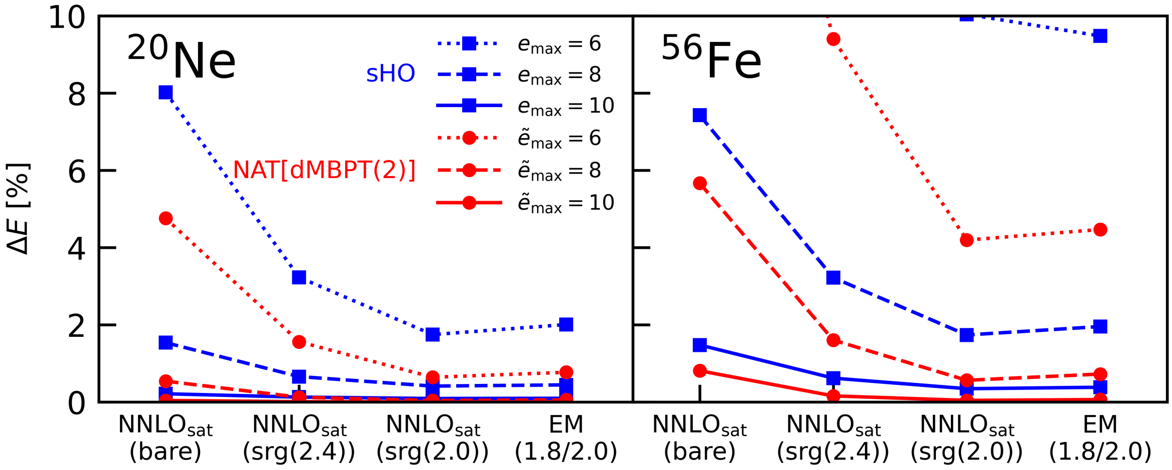

Figure 6.6. Relative error on the dBMBPT(2) ground-state energy of ^{20}Ne (left) and ^{56}Fe (right) using the sHO (NAT[dBMBPT(2)]) basis for different $e_{\max}$ ($\tilde{e}_{\max}$) truncations and the four different χEFT Hamiltonians characterized by different resolution scales.

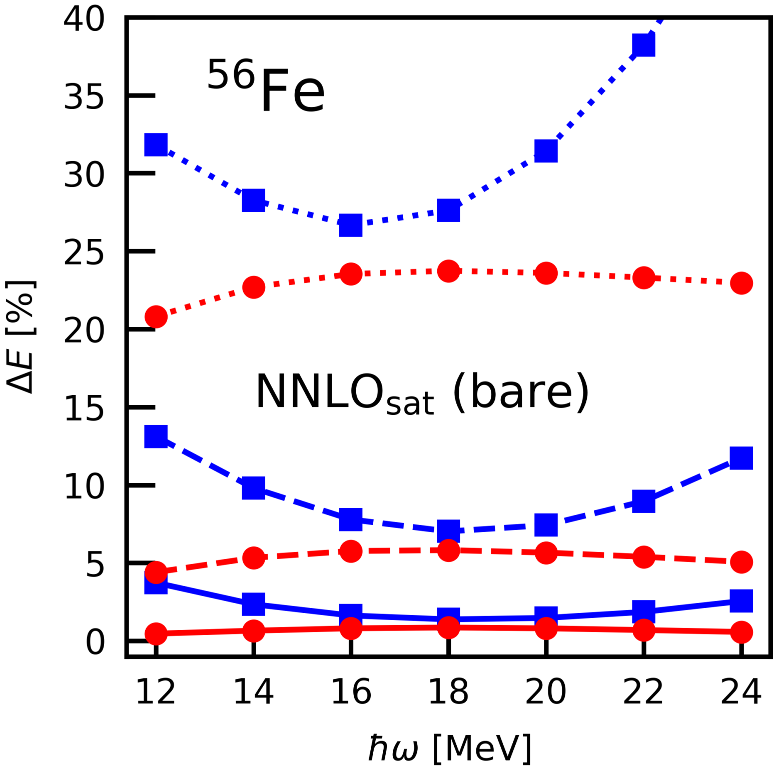

Figure 6.7. Relative error on the dBMBPT(2) ground-state energy of ^{56}Fe as a function of the oscillator frequency $\hbar\omega$ of the underlying sHO basis. Results are shown for the NNLO$_{\text{sat}}$ (bare) Hamiltonian. The legend is the same as in Fig. 6.6.

reach the same result. For the NNLO$_{\text{sat}}$ (bare) Hamiltonian characterized by the highest resolution scale, $\tilde{e}_{\text{max}} = 8$ yields a 1% error in ^{20}Ne whereas two more major shells are necessary for the sHO basis. In ^{56}Fe, however, the NAT[dBMBPT(2)] basis does not offer a significant gain over the SHO basis when targeting a 1% error.

6.3.4. $\hbar\omega$ dependence

In Ref. [136] the independence of the results obtained in closed-shell nuclei using the NAT basis generated via spherical MBPT(2) on the $\hbar\omega$ frequency of the underlying sHO basis was highlighted. An analogous study is now carried out in deformed nuclei based on the NAT[dBMBPT(2)] basis.

Figure 6.7 shows the relative error on the dBMBPT(2) ground-state energy of ^{56}Fe for the NNLO$_{\text{sat}}$ (bare) Hamiltonian[11] as a function of the oscillator frequency $\hbar\omega$ of the underlying sHO basis for different truncations of the model space. In agreement with the results obtained in closed-shell nuclei [136], the relative error is flattened for the NAT[dBMBPT(2)] basis compared to the sHO basis. This behavior originates from the fact that, the dBMBPT(2) calculation being essentially converged at $e_{\text{max}} = 12$ and thus

---

[11] As discussed in the previous section, this is the least favorable situation regarding the actual benefit of the NAT[dBMBPT(2)] basis over the sHO one. It is unimportant here given that the goal is simply to investigate how the behavior *evolves* with $\hbar\omega$.

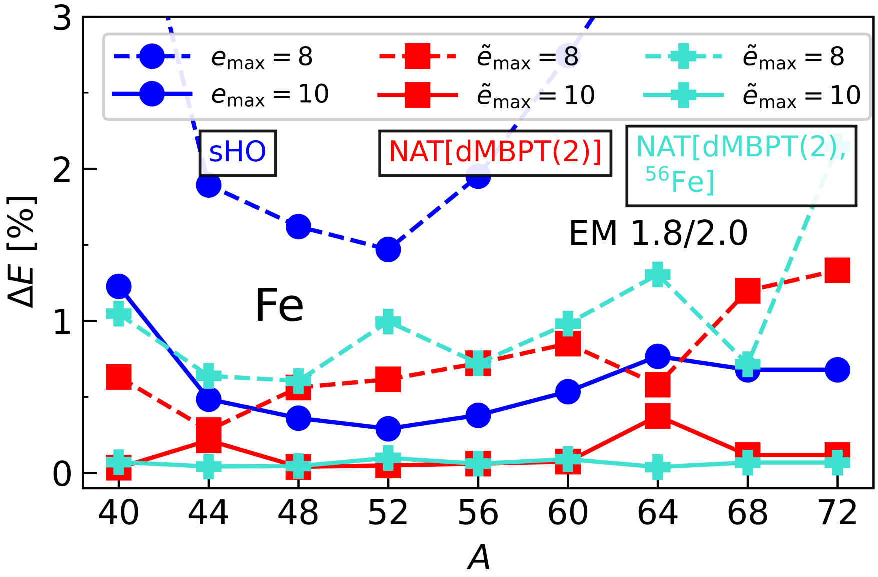

Figure 6.8. Relative error on the dBMBPT(2) ground-state energy along the Fe isotopic chain. Results are shown using both the nucleus-dependent NAT[dMBPT(2)] basis and the fixed NAT[dMBPT(2), ^{56}Fe] basis for all isotopes. Calculations were performed with the EM 1.8/2.0 Hamiltonian.

$\hbar\omega$-independent, so are the corresponding density matrices[12].

One observes that the benefit obtained from the NAT basis is minimal for $\hbar\omega = 18$ MeV, which corresponds to the optimal frequency for NNLO$_{\text{sat}}$ (bare) as far as the convergence of the results based on the sHO basis is concerned. On the other hand, the independence of the NAT basis on $\hbar\omega$ can be used to avoid searching for such an optimal frequency and thus save significant computational resources.

6.3.5. Isotopic dependence

Having characterized the performance of the NAT basis for different nuclear masses, the evolution along nine even-even iron isotopes ranging from ^{40}Fe to ^{72}Fe is now investigated. At the same time, the impact of using one fixed NAT basis extracted from, e.g., ^{56}Fe (i.e. the NAT[dMBPT(2), ^{56}Fe] basis) for all the isotopes is also studied. One might indeed expect that the characteristics of the natural orbitals do not evolve significantly along an isotopic chain or even within a given mass region. If so, the CPU time needed to repeatedly perform a dBMBPT(2) calculation to extract the NAT[dMBPT(2)] basis and transform the matrix elements of all operators at play into that basis could be avoided whenever performing a systematic study.

The results obtained along the Fe isotopic chain with the EM 1.8/2.0 Hamiltonian are displayed in Fig. 6.8. First, the benefit of using the NAT[dMBPT(2)] basis identified earlier for ^{56}Fe extends similarly to all isotopes under consideration. Second, one observes that keeping the NAT[dMBPT(2), ^{56}Fe] the same for the nine isotopes does not deteriorate the results, i.e. the gain compared to using the sHO basis remains essentially the same. This demonstrates that using NAT orbitals computed in a nearby nucleus indeed

---

[12] Further considerations about the $\hbar\omega$-dependence of the NAT orbitals are made in Sec. 6.4.3

represents a viable option. Such a study could be extended to a larger range of nuclei in the future to identify the limit of such a strategy.

6.4. Alternatives to NAT[dBMBPT(2)]

A key feature of natural orbitals relates to their capacity to carry fingerprints of correlations imprinting the many-body wave function. This is first reflected into their optimal average occupation profile (see Sec. 6.2.2), which is exploited to construct efficient truncations of the one-body basis. One might thus wonder whether other ways[13] of incorporating information about the correlated wave function into the single-particle basis provide an advantage over the sHO basis.

6.4.1. Alternatives

A first option consists in extracting the NAT basis from a deformed HFB many-body state, i.e. in using the so-called canonical basis from HFB theory [36]. Because the canonical basis is the NAT basis of a many-body state capturing static pairing correlations, canonical states are indeed known to be all localized [28] and to decay faster than the one-body local density distribution.

Instead of diagonalizing the one-body density matrix, another interesting option consists in utilizing the eigenbasis of the one-body Baranger Hamiltonian [106]

$$h^{\mathrm{BAR}}_{\alpha\beta} = t_{\alpha\beta} + \sum_{\gamma\delta} v_{\alpha\gamma\beta\delta}\, \rho_{\delta\gamma}\, , \tag{6.9}$$

where $t_{\alpha\beta}$ and $v_{\alpha\gamma\beta\delta}$ denote matrix elements of the one-body kinetic energy and of the two-body interaction, respectively. The eigenstates of h^{BAR} deliver an alternative one-body basis[14] informed from many-body correlations through the input one-body density matrix. In this case, the basis states can be ordered and truncated according to the associated eigenvalues[15] of h^{BAR}.

6.4.2. Performance

The convergence as a function of $\tilde{e}^{P}_{\max}$ (keeping $\tilde{e}^{N}_{\max} = 12$ fixed) of the dBMBPT(2) ground-state energy obtained in ^{20}Ne with the NNLO$_{\mathrm{sat}}$ (bare) Hamiltonian is displayed in Fig. 6.9 for the five following proton bases:

1. sHO basis;

---

[13] Any useful alternative must be characterized by a low computational cost to be worth considering. For instance, even though natural orbitals extracted from a more refined (and costly) calculation than dBMBPT(2) are expected to be more efficient, following this route would defy the original purpose.

[14] The Baranger (BAR) one-body basis is obtained at a similar cost as the NAT basis given that it requires to convolute the dBMBPT(2) one-body density matrix with the two-body interaction according to Eq. (6.9) prior to diagonalizing the one-body Hamiltonian h^{BAR}.

[15] These one-body eigenergies are meaningful effective single-particle energies [107, 116] and are routinely evaluated in nuclear structure calculations.

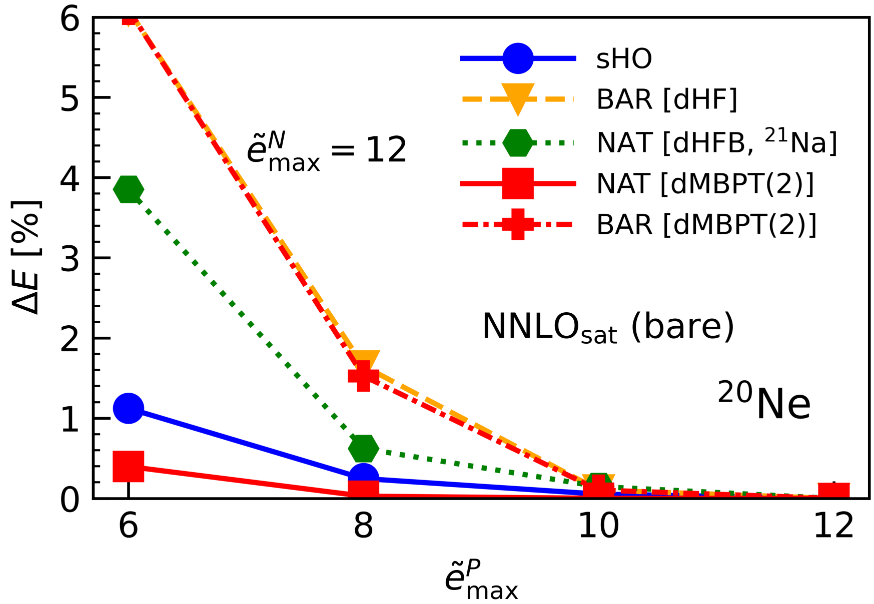

Figure 6.9. Convergence of the dBMBPT(2) ground-state energy ^{20}Ne as a function of $\tilde{e}^P_{\text{max}}$ for five different one-body bases of interest (see text for details). The neutron basis is left untruncated, i.e. $\tilde{e}^N_{\text{max}} = 12$ is used everywhere. Calculations are performed with the NNLO$_{\text{sat}}$ (bare) Hamiltonian.

2. BAR[dHF] basis[16];
3. NAT[dHFB, ^{21}Na] basis obtained from the even-number parity HFB solution of the neighbouring ^{21}Na isotone[17];
4. BAR[dMBPT(2)] basis;
5. NAT[dMBPT(2)] basis.

First, one can appreciate the clear supremacy of the NAT[dMBPT(2)] basis, which is in fact the only one performing better than the sHO basis by typically gaining two units of $\tilde{e}_{\text{max}}$ over it.

Incorporating mean-field pairing correlations into the one-body density matrix does improve over the BAR[dHF] basis but is only superior to the sHO basis for $\tilde{e}^P_{\text{max}} = 2$ (not visible on the plot), which is irrelevant given that the error is of the order of $20 - 30\%$ for such small bases. This already shows that the spatial localization of the orbitals induced by pairing correlations is beneficial but not refined enough.

The BAR[dMBPT(2)] basis and the BAR[dHF] basis display identical behaviors and provide the worst performance of all. In particular, they deliver a much slower convergence than the sHO basis. Convoluting the correlated dMBPT(2) one-body density

---

[16] The HF basis is both the NAT basis and the BAR basis associated with the HF Slater determinant. The occupations being highly degenerate (step function), such a variable does not authorize an unambiguous ordering. It is thus necessary to use Baranger (i.e. HF) single-particle energies to generate a meaningful ordering of the basis states.

[17] As for the large majority of doubly open-shell nuclei computed with ab initio interactions [137], the dHFB solution of ^{20}Ne is unpaired. A simple way to enforce pairing correlations among protons is thus to use the even number-parity solution for the neigboring isotone ^{21}Na. Given the conclusion of Sec. 6.3.5 this constitutes a well justified option.

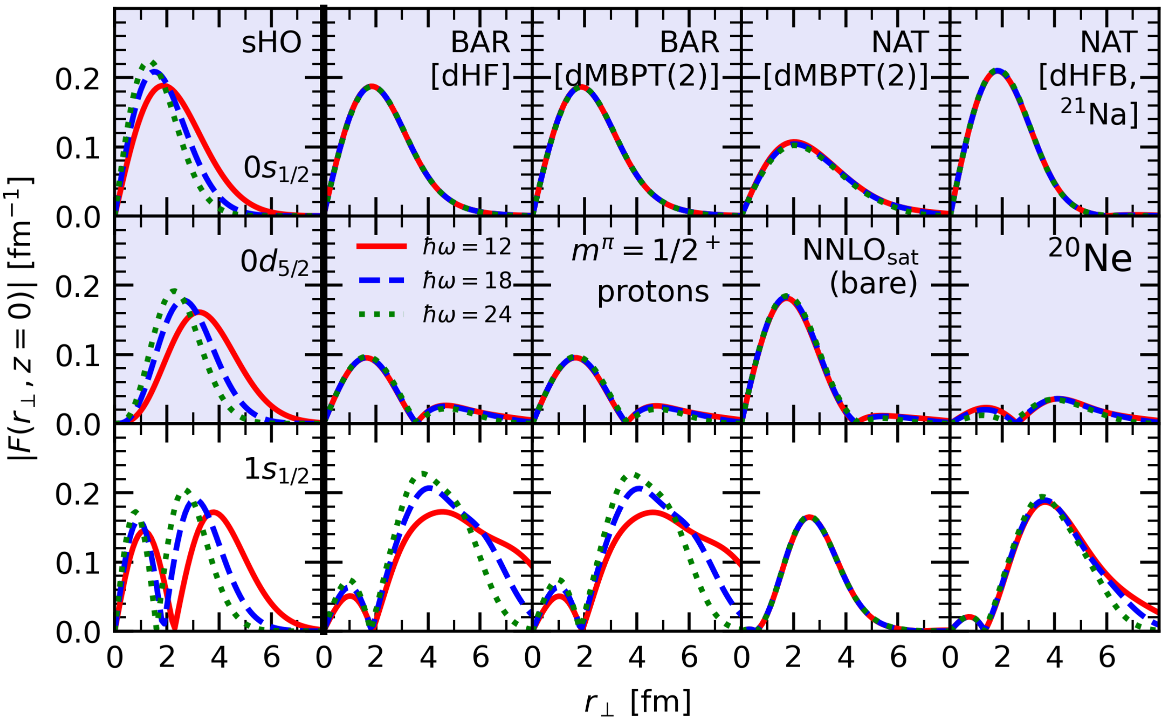

Figure 6.10. First three proton single-particle wave functions with $(m_\alpha = 1/2, \pi_\alpha = +)$ in ^{20}Ne as a function of $r_\perp$ for $z = 0$. *First column*: sHO basis including the associated (nlj) quantum numbers. *Second column*: BAR[dHF] basis. *Third column*: BAR[dBMBPT(2)] basis. *Fourth column*: NAT[dBMBPT(2)] basis. *Fifth column*: NAT[dHFB, ^{21}Na] basis. The ordering of the states from top to bottom in the NAT (BAR) bases is made according to their decreasing (increasing) average occupations (Baranger single-particle energies). One-body states that would be occupied, i.e. below the Fermi level, according to a naive filling of the shells are indicated with a grey background. Calculations are performed with the NNLO$_{\mathrm{sat}}$ (bare) Hamiltonian for three values of sHO basis frequency $\hbar\omega = 12$, 18, 24 MeV.

matrix with the two-body interaction to produce and diagonalize the Baranger one-body Hamiltonian washes out the relevant fingerprint of beyond-mean-field correlations built into that density matrix.

6.4.3. Single-particle wave functions

To better understand the behavior of the different one-body bases employed in Fig. 6.9, spatial properties of the associated wave functions are now investigated. The coordinate representation of single-particle wave functions with axial symmetry, z being the coordinate along the symmetry axis and $r_\perp$ the coordinate perpendicular to it, is detailed in App. G.

Figure 6.10 displays in each basis, for three values of sHO basis frequency $\hbar\omega = 12$, 18, 24 MeV, three representative proton single-particle wave functions, i.e. the first three proton states with $(m_\alpha = 1/2, \pi_\alpha = +)$, as a function of $r_\perp$ (fixing $z = 0$). In NAT bases, the ordering of the states from top to bottom is made according to their decreasing average occupations. In BAR bases, this ordering relates to their increasing Baranger single-particle energies. States that would be occupied in ^{20}Ne, i.e. below the Fermi level, according to a naive filling of the shells are indicated with a grey background.

Several considerations can be made by inspecting Fig. 6.10.

- *$\hbar\omega$ dependence* While the three sHO wave functions display (by construction) a dependence on the underlying sHO frequency, states *below* the Fermi level are independent of $\hbar\omega$ for the four other bases. The state *above* the Fermi level behaves, however, differently: while a significant $\hbar\omega$ dependence is observed for both BAR bases, the dependence is considerably reduced for the NAT[dHFB, ^{21}Na] state and disappears for the NAT[dMBPT(2)] one.

- *Localization* The spatial extension of the sHO states directly reflects the size of the sHO potential, determined by the frequency $\hbar\omega$. At long distances, sHO states behave as bound states decaying as Gaussian functions. In the four other bases, the spatial extension of the states below the Fermi level resembles their sHO counterpart obtained for the optimal $\hbar\omega = 18$ MeV value. Furthermore, these wave functions behave as bound-like state decaying exponentially at long distances[18]. A major difference occurs instead for the state above the Fermi level. While the $\hbar\omega$-independent state in the NAT bases is localized within the volume of the nucleus and decays exponentially at long distances, the $\hbar\omega$-dependent state in the BAR bases is delocalized given that it corresponds to a positive Baranger single-particle energy[19]. While the many-body correlations built into the dBMBPT(2) one-body density matrix efficiently localize all its eigenstates, the effect is lost when computing the Baranger Hamiltonian whose eigenstates with positive single-particle energy are scattering states independently of the correlations entering the one-body density matrix used to compute it. Eventually, one further observes that the state above the Fermi level is more localized in the NAT[dMBPT(2)] basis than in the NAT[dHFB, ^{21}Na] basis.

- *Nodes* Since both BAR and NAT states mix sHO states with different values of the principle quantum number n_α, the number of nodes in the corresponding wave

---

[18] Although hardly visible in the linear y-scale of the figure, this has been verified.

[19] This delocalization is still artificially limited by the combination of the $\hbar\omega$ and e_{max} values employed, i.e. the state would behave as a proper scattering state in the limits $\hbar\omega \to 0$ and/or $e_{\text{max}} \to \infty$.

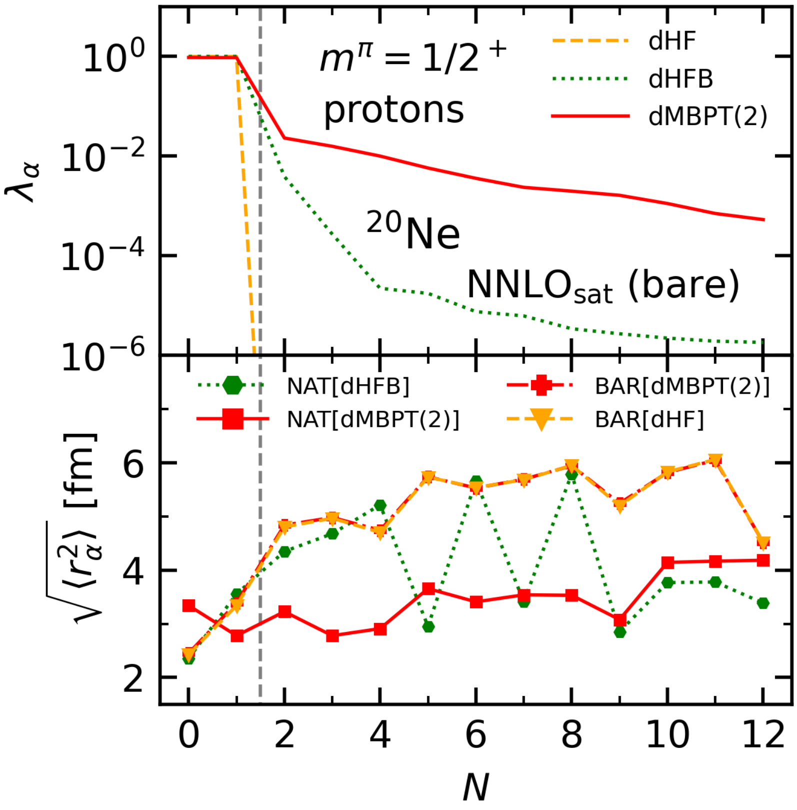

Figure 6.11. *Top panel*: eigenvalues of the dHF, dHFB(^{21}Na) and dMBPT(2) one-body density matrices. *Bottom panel*: single-particle wave function r.m.s. radius. Results are displayed for the first states in the $[m\pi t] = [1/2 + p]$ block. Calculations are performed in ^{20}Ne with NNLO$_{\text{sat}}$ (bare) and $\hbar\omega = 18\,\text{MeV}$. The vertical dashed line indicates the location of the Fermi level.

functions cannot be anticipated or easily interpreted. For instance, while the first state carries no node in the five bases, the second state displays one node in all bases but the sHO one.

The fact that all NAT[dMBPT(2)] states are similarly localized around the volume of the nucleus is what seems to distinguish this basis from the others. To validate this conjecture, the spatial extension of the basis states is now characterized over a wider range by computing the root-mean-square (r.m.s.) radius of each basis state α as

$$\begin{aligned} \sqrt{\langle r_\alpha^2 \rangle} &\equiv \sqrt{\langle \alpha | r^2 | \alpha \rangle} \\ &= 2\pi \int dr\, d\theta\, r^4 \sin\theta\, F_\alpha^2(r,\theta)\,. \end{aligned} \tag{6.10}$$

Figure 6.11 displays the first twelve eigenvalues of the dHF, dHFB(^{21}Na) and dMBPT(2) one-body density matrices in the $[m\pi t] = [1/2 + p]$ block against the r.m.s radius of the first twelve orbitals of that same block in the BAR[dHF], BAR[dMBPT(2)], NAT[dHFB, ^{21}Na] and NAT[dMBPT(2)] bases. The calculation is performed in ^{20}Ne with the NNLO$_{\text{sat}}$ (bare) Hamiltonian and the optimal frequency $\hbar\omega = 18\,\text{MeV}$. The following considerations can be made.

- Even if the natural orbitals occupations are very different for the dHF and dMBPT(2) one-body density matrices, the r.m.s radii of the BAR[dHF] and BAR[dMBPT(2)] basis states are identical, i.e. the eigenfunctions of the Baranger Hamiltonian are unchanged by the correlations built into the density matrix used to compute it.

- The spatial extension of both BAR basis states increases continuously when going from below to above the Fermi level where the r.m.s. radius of the orbitals typically reaches about 6 fm[20]. In particular, there is a large spatial mismatch between orbitals below and above the Fermi level.

- Pairing correlations built into the dHFB(^{21}Na) one-body density matrix only modify substantially the occupations of natural orbitals around the Fermi level such that the distribution of eigenvalues drop much faster than for dMBPT(2) natural orbitals. Eventually, the localization of the NAT[dHFB, ^{21}Na] orbitals is not positively affected such that their r.m.s. radius remain similar to their BAR[dHF] counterparts. The calculation was repeated[21] by boosting pairing correlations [49] to match the occupation profile displayed by the NAT[dBMBPT(2)] orbitals in Fig. 6.11. The localization of the corresponding NAT[dHFB, ^{21}Na] orbitals was not at all improved and the convergence of the dBMBPT(2) energy was by far the worst of all tested bases.

- Dynamical correlations built into the dMBPT(2) density matrix impact substantially the occupation profile of all natural orbitals. Eventually, the spatial extension of the NAT[dMBPT(2)] orbitals is more homogeneous than for the other bases; the r.m.s. radius typically remains between 3 and 4 fm for all of them. Noticeably, the first, i.e. most occupied, NAT[dMBPT(2)] state below the Fermi level is *more* extended than its counterparts in the other bases (see the first row of Fig. 6.10) such that its spatial extension is eventually more similar to states located above the Fermi level.

Figure 6.12 compares in ^{20}Ne the r.m.s. radius of the first twelve orbitals in the $[m\pi t] = [1/2 + p]$ block of the sHO, BAR[dHF], NAT[dHFB, ^{21}Na] and NAT[dMBPT(2)] bases[22], along with their average dispersion, to the dMBPT(2) r.m.s. matter radius. On average, the extension of the sHO and NAT[dMBPT(2)] orbitals are more consistent with the matter radius than for the BAR[dHF] and NAT[dHFB, ^{21}Na] basis states. Furthermore, the dispersion in the orbitals extension is the smallest for the NAT[dMBPT(2)] basis. As a matter of fact, the hierarchy in the performance of the five bases displayed in Fig. 6.9 correlates with these two spatial characteristics.

Eventually, it can be speculated that the capacity of the NAT[dMBPT(2)] basis to best converge a subsequent beyond mean-field, e.g. dBMBPT(2), calculation is correlated with the optimal spatial overlap between single-particle wave-functions below and above the Fermi level, which in turn concentrates the strength of the interaction matrix elements over the lowest lying elementary excitations. This eventually allows one to optimally build up many-body correlations as a function of $\tilde{e}_{\text{max}}$ on top of the unperturbed reference state.

---

[20] The r.m.s. radius of the orbitals with positive Baranger single-particle energies would be infinite in the limits $\hbar\omega \to 0$ and/or $e_{\text{max}} \to \infty$.

[21] The associated results are not shown in Figs. 6.9–6.11.

[22] Results for the BAR[dMBPT(2)] basis are not shown because they are identical to those obtained with the BAR[dHF] basis.

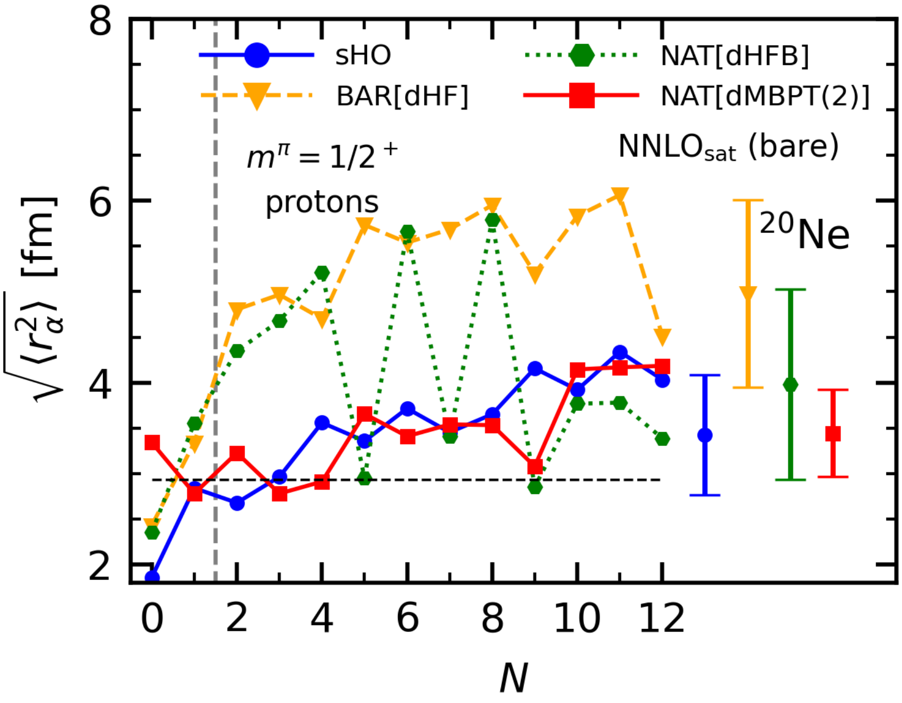

Figure 6.12. Root mean square radius of the first twelve orbitals in the $[m\pi t] = [1/2{+}p]$ block in the sHO, BAR[dHF], NAT[dHFB, ^{21}Na] and NAT[dMBPT(2)] bases. The average and dispersion of the r.m.s. over the twelve states are indicated for each of the four bases. Calculations are performed in ^{20}Ne with NNLO$_{\rm sat}$ (bare) and $\hbar\omega = 18\,\text{MeV}$. The vertical dashed line indicate the location of the Fermi level.

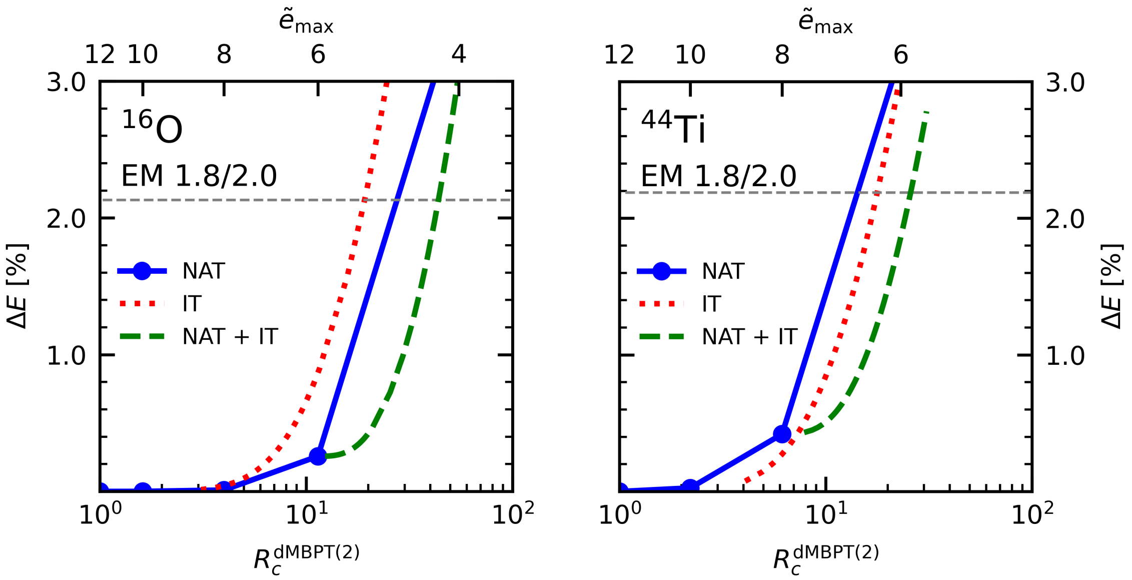

Figure 6.13. Relative error on the dBMBPT(2) energy as a function of the compression factor R_c using the NAT[dBMBPT(2)] basis, the IT technique and combining both. *Left panel*: ^{16}O. *Right panel*: ^{44}Ti. The dashed grey line represents the relative dMBPT(3) contribution to the total energy with respect to dMBPT(2). Calculations were performed with the EM 1.8/2.0 Hamiltonian.

Unfortunately, natural orbitals obtained via an even less costly (pair-boosted) HFB calculation do not display appropriate properties and do not lead to any gain over the sHO basis. For a reason that remains to be elucidated, dynamical correlations brought by second order perturbation theory and static correlations brought by (boosted) HFB can lead to essentially identical eigenvalues of the one-body density matrix (i.e. natural orbitals occupation profile), while delivering very different eigenstates (i.e. natural orbital wave functions).

6.5. Natural basis vs importance truncation

6.5.1. Importance truncation

Importance truncation (IT) constitutes another well-established technique to reduce the computational costs of nuclear structure calculations while maintaining the desired accuracy on the solution of the Schrödinger equation. The main idea is to pre-select, via an inexpensive evaluation, the most relevant elements of the many-body tensors at play in a method of interest. Using for example (B)MBPT(2) as the inexpensive pre-processing method, the second-order correction to the energy introduced in Sec. 2.4 can be schematically expressed as the sum over all entries of a mode-4 tensor

$$E^{(2)} = \frac{1}{4!} \sum_{\alpha\beta\gamma\delta} e^{(2)}_{\alpha\beta\gamma\delta} \,, \tag{6.11}$$

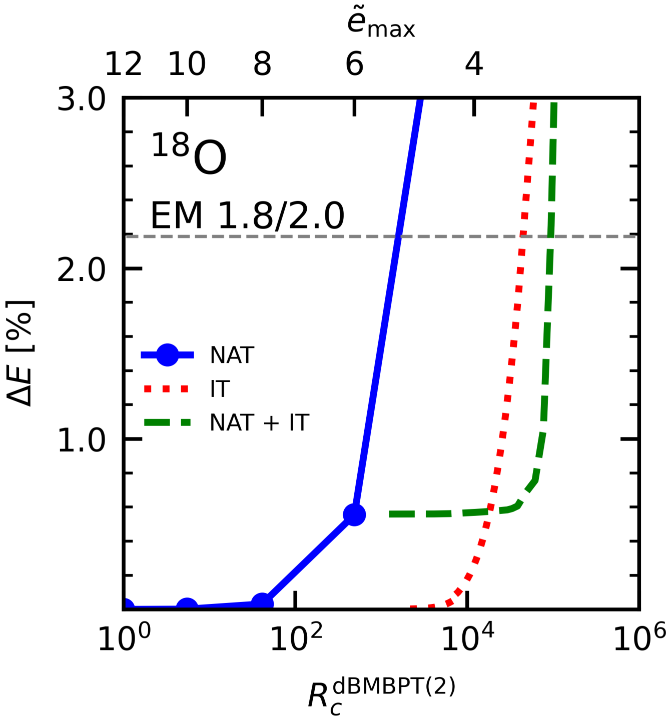

Figure 6.14. Same as Fig. 6.13 for ^{18}O.

such that all quadruplets $(\alpha, \beta, \gamma, \delta)$ corresponding to entries falling below a chosen threshold e_{IT},

$$e^{(2)}_{\alpha\beta\gamma\delta} < e_{\text{IT}} \,, \tag{6.12}$$

will be ignored in a subsequent calculation involving (a counterpart of) the mode-4 tensor, the goal being to reduce the cost of expensive diagonalisations/iterations at play in non-perturbative many-body methods. Following this strategy, IT has been successfully applied to no-core shell model [120], self-consistent Green's functions [22] and in-medium SRG [122] calculations. A comparison between IT and tensor factorisation techniques has also been performed within the frame of BMBPT [124].

6.5.2. Compression factor

To confront the respective computational gains provided by IT and natural orbitals, using (B)MBPT(2) as the validation method, the *compression factors*

$$R_c^{\text{d(B)MBPT(2)}}(e_{\text{IT}}) \equiv \frac{n_{\text{conf}}(e_{\text{max}} = 12, e_{\text{IT}} = 0)}{n_{\text{conf}}(e_{\text{max}} = 12, e_{\text{IT}})} \,, \tag{6.13a}$$

$$R_c^{\text{d(B)MBPT(2)}}(\tilde{e}_{\text{max}}) \equiv \frac{n_{\text{conf}}(e_{\text{max}} = 12, e_{\text{IT}} = 0)}{n_{\text{conf}}(\tilde{e}_{\text{max}}, e_{\text{IT}} = 0)} \,, \tag{6.13b}$$

obtained with respect to a d(B)MBPT(2) calculation in $e_{\text{max}} = 12$ and $e_{\text{IT}} = 0$) are introduced. Such a ratio quantifies the gain by comparing the number of initial tensor entries with the number of retained tensor entries: the larger the compression factor, the greater the advantage brought by the method. The compression factor associated with the NAT basis (IT) is driven by the value of $\tilde{e}_{\text{max}}$ (e_{IT}). Eventually, the number of retained entries in IT can also be translated into an effective $\tilde{e}_{\text{max}}$ value.

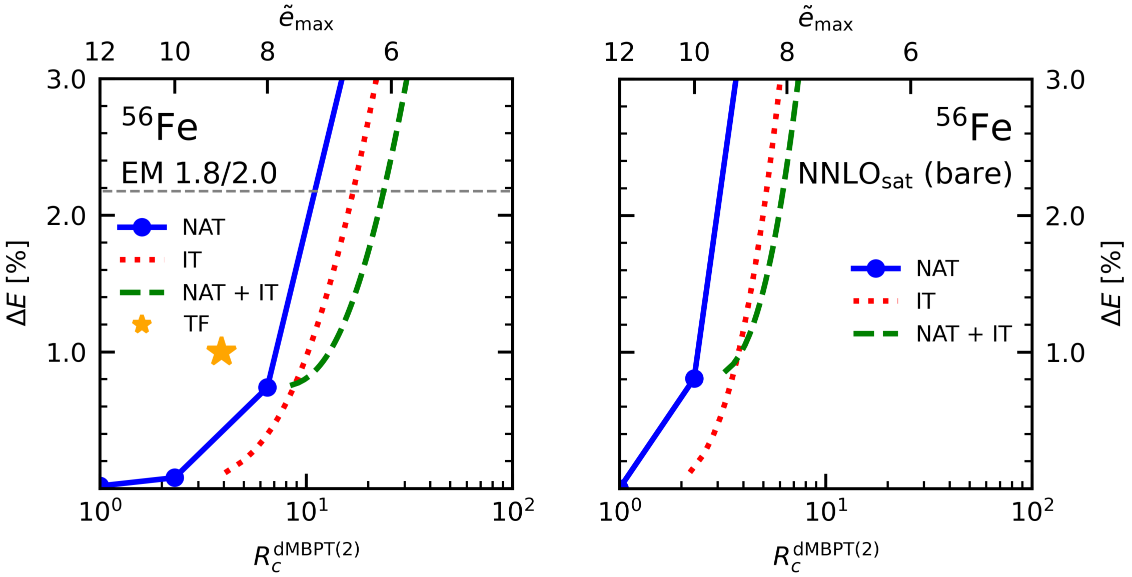

Figure 6.15. Same as Fig. 6.13 for ^{56}Fe only and the EM 1.8/2.0 (*left panel*) and NNLO$_{\text{sat}}$ (bare) (*right panel*) Hamiltonians. The compression factor obtained for $\Delta E = 1.0\%$ and $e_{\text{max}} = 12$ via tensor factorization techniques [41] is also indicated on the left panel.

6.5.3. Comparison

Figure 6.13 displays the relative error ΔE on the dMBPT(2) ground-state energy against the compression factor for NAT and IT in the doubly closed-shell (open-shell) ^{16}O (^{44}Ti) nucleus[23]. As a rule of thumb, an acceptable error in a MBPT(2) calculation is provided by the third-order contribution appearing as a horizontal dashed line in the figure.

In the limits $\tilde{e}_{\text{max}} \to 12$ or $e_{\text{IT}} \to 0$, i.e. $R_c^{\text{dMBPT(2)}} = 1$, the reference calculation is recovered. As $R_c^{\text{dMBPT(2)}}$ increases, the error ΔE evolves similarly for both approximation methods, even though the benefit obtained using the NAT[dMBPT(2)] basis is slightly superior (inferior) in ^{16}O (^{44}Ti). Eventually, an acceptable error of $\Delta E \in [1, 2]\%$ authorizes to compress the tensor at play by about one order of magnitude. Of course, the gain in non-perturbative methods pushed to high accuracy and involving mode-6 tensors to be repeatedly computed, stored and contracted is expected to be significantly higher.

The situation is different in the Bogoliubov setting, as shown in Fig. 6.14 for ^{18}O. Indeed, the necessity to rely on the Bogoliubov algebra enlarges significantly the size of the tensors at play in the reference calculation to begin with. Both compression techniques counterbalance this increase through larger compression factors than in the MBPT(2) case. While reaching an error of the order of the third-order contribution ($\Delta E \approx 2\%$) via NAT generates a compression factor of $R_c^{\text{dMBPT(2)}} \approx 10^3$, IT manages to do so while compressing the tensor by one more order of magnitude. As already observed in Ref. [22] for IT and in Ref. [41] for tensor factorization, Fig. 6.14 demonstrates that the large overhead induced by the explicit treatment of pairing correlations is to a large extent artificial and can be alleviated via different pre-processing techniques.

In order to gauge how compression factors vary with the resolution scale of the input

---

[23] The evaluation of the compression factor takes explicitly into account the fact that $U(1)$ symmetry is not broken for these two nuclei, i.e. that one can work with dMBPT(2) rather than dBMBPT(2) to begin with.

Hamiltonian, Fig. 6.15 compares the results obtained in ^{56}Fe with the EM 1.8/2.0 and the NNLO$_{\text{sat}}$ (bare) Hamiltonians. While the qualitative behavior is similar, the compression factor achieved for a given error is two orders of magnitude smaller with NNLO$_{\text{sat}}$ (bare) than with EM 1.8/2.0. Although both optimisation techniques might still bring sizeable benefits for interactions characterized by higher resolution scales, much more is to be gained with soft nuclear Hamiltonians.

6.5.4. Combination

Starting from these encouraging results, NAT and IT can in fact be combined straightforwardly, i.e. the IT can be employed based on a NAT basis truncated to an appropriate $\tilde{e}_{\text{max}}$ value. Corresponding results are shown for one particular $\tilde{e}_{\text{max}}$ value[24] in each of the panels of Figs. 6.13, 6.14 and 6.15. In all cases, combining IT with NAT does bring a further advantage, i.e. typically a factor of 2 better than the best of the two methods used separately. When using NNLO$_{\text{sat}}$ (bare) though, the additional gain is essentially negligible.

As a final comparison, the left panel of Fig. 6.15 also displays the compression factor obtained for $\Delta E = 1\%$ with tensor factorisation techniques [41]. The compression factor is about half of the one achieved using NAT or IT in this case[25].

6.6. Application to non-perturbative methods

Having validated the advantage that NAT [(d)MBPT(2)] bases bring to *ab initio* calculations, it is finally time to combine such newly-developed tool to non-perturbative methods, where the impact of NAT is expected to be beneficial. In the present case, calculations are limited to $e_{\text{max}} = 8$.[26] Since the interest is in the convergence of the relative energy with respect to a value that is assumed to be converged, such value is determined by extrapolating $e_{\text{max}} = 4$, 6 and 8 results. This goal is accomplished by the simple exponential decay function:

$$f(e_{\text{max}}, a, b, E_\infty) = a e^{-b e_{\text{max}}} + E_\infty, \tag{6.14}$$

where a, b and E_∞ represent the three parameters to be fit, the latter one representing the value of the extrapolated energy.

To this end, dDSCGF(2) calculations are performed for ^{20}Ne with the 'hardest' and the 'softest' interactions employed in this chapter, respectively the NNLO$_{\text{sat}}$ (bare) and the EM 1.8/2.0 ones.

Figure 6.16 represents such study. For what concerns results computed with the NNLO$_{\text{sat}}$ (bare) interaction, the gain that the NAT [dMBPT(2)] basis brings with respect to sHO is larger that the one obtained with the EM 1.8/2.0 interaction. This is in agreement with what seen in the case of dMBPT(2) calculations (see Fig. 6.6). sc and sc0 calculations display qualitatively the same trend for all the studied cases. With the

---

[24] Specifically, the smallest $\tilde{e}_{\text{max}}$ for which $\Delta E < 1\%$ is used.

[25] It must however be noticed that the chosen example does not correspond to one for which tensor factorization provided the best benefit [41].

[26] The self-consistent loop in SCGF sometimes gives convergence problems. Since $e_{\text{max}} = 10$ calculations proved to be harder to converge and the present implementation does not currently include sophisticated techniques to control the convergence, in the following section results are limited to $e_{\text{max}} = 8$.

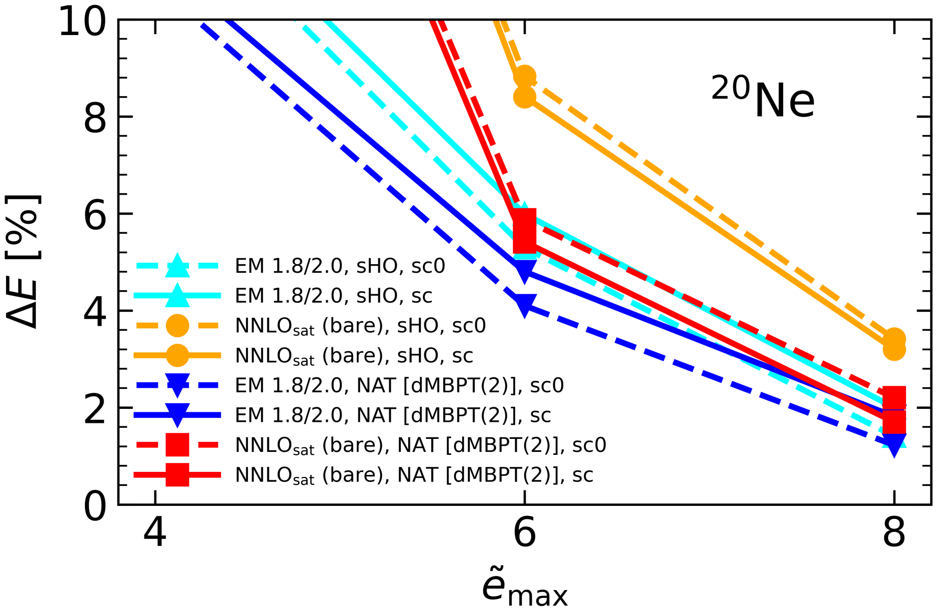

Figure 6.16. Relative error of the total energy with respect to the extrapolated $e_{\max} = +\infty$ for ^{20}Ne. sHO and NAT [dMBPT(2)] bases performance are compared for two different interactions, NNLO$_{\mathrm{sat}}$ (bare) and EM 1.8/2.0, and for the full self-consistent and partial self-consistent (sc0) approximations. $e_{3\max} = 16$ is employed and $\hbar\omega = 18$ and 20 MeV is employed respectively for the NNLO$_{\mathrm{sat}}$ (bare) and the EM 1.8/2.0 interactions.

NNLO$_{\mathrm{sat}}$ (bare) interaction the NAT [dMBPT(2)] basis brings and advantage of $\approx 4\%$ at $e_{\max} = 6$ that is reduced to $\approx 1.8\%$ at $e_{\max} = 8$. Analogous calculations with the EM 1.8/2.0 interaction reduces such gain respectively to $\approx 1\%$ and $\approx 0.5\%$.

The impact of working with a reduced model space is shown in Tab. 6.1 for the case of one single sc0 iteration. Typically, a number of sc iterations between 5 and 8 is required to reach a proper convergence of the total energy.

While results are promising, the efficiency of NAT in the dDSCGF method will need to be validated more systematically in future applications to further quantify their impact on different regions of the nuclear chart.

$e_{\max}$	time [h]
2	0.001
4	0.002
6	0.042
8	0.650
10	4.550
12	22.130

Table 6.1. Computational time (in hours) required to converge a dDSCGF(2) sc0 calculation in ^{20}Ne with 104 OpenMP processors.

6.7. Conclusions

The present chapter investigated in details the computational gain delivered from the natural basis computed via deformed second-order perturbation theory in the context of *ab initio* calculations of doubly open-shell nuclei based on expansion many-body methods using an axially deformed and superfluid reference state. In view of searching for alternative bases or for natural orbitals extracted at an even lower computational cost than deformed second-order perturbation theory, the key characteristics of natural orbitals were investigated. Eventually, the use of natural orbitals was compared to the benefit brought by other compression techniques, i.e. importance truncation and tensor factorization techniques.

The main conclusions of this study can be drawn.

- The natural orbital basis extracted via second-order many-body perturbation theory authorizes to converge calculations, e.g. dBMBPT(2,3) or dDSCGF(2), based on soft interactions to a given accuracy using about half the number of states n_B needed with the spherical harmonic oscillator basis.

- Encouraged by the dDSCGF(2) results and based on the hypothesis that such a gain extends to any many-body expansion method whose intrinsic memory load (CPU cost) scales as n_B^p (n_B^q), the benefit of using the NAT basis over the sHO basis is thus estimated to be of the order 2^p (2^q).

- Using a common reference calculation employing a sHO basis of given dimension (e.g. $e_{\text{max}} = 12$), the gain obtained via importance truncation and tensor factorization techniques is similar to the one presently achieved based on the use of the natural orbital basis.

- Employing importance truncation techniques *on top of* a NAT basis allows one to gain an additional factor of 2 in the compression of the mode-2 tensor at play in a d(B)MBPT(2) calculation compared to the benefit obtained by the best of both methods used separately.

- While the gain characterized in the present chapter is based on an e_{max}-like truncation of the natural orbital basis, there exists an entire freedom in the way the basis can be cut. Thus, the possibility to design more optimal truncation schemes needs to be investigated in the future.

- None of the alternative bases presently investigated, i.e. the natural basis extracted from Hartree-Fock and (pair-boosted) Hartree-Fock-Bogoliubov calculations or the so-called Baranger basis, was shown to provide an advantage over the spherical harmonic oscillator basis. The merit of the natural basis extracted from a second-order many-body perturbation theory seems to relate to its unique capacity to localize all its orbitals over the volume occupied by the nucleus.

- The use of NAT bases in combination with dDSCGF calculations has been shown to be beneficial. Moreover, in this case the gain (quantified by looking at Tab.6.1) is further amplified by the iterative character of the method. The use of techniques as the ones presented in the present chapter will be crucial when pushing dDSCGF(2) calculations to the third order.

Having at hand a new tool to investigate open-shell systems, the next Chapter (Ch. 7) revives part of the study performed in Ch. 3 quantitatively increasing the number of correlations included in the *ab initio* calculations.

Chapter 7.

Postlude – The threefold puzzle of Ca isotopes

Chapter 3 presented an investigation of the role of correlations in *ab initio* calculations applied to the Calcium and Chromium isotopic chains, i.e. on how the successive inclusion of many-body correlations helps reproducing experimental ground-state energies as well as its derivatives S_{2n} and Δ_{2n}. With the new dDSCGF(2) method introduced in Ch. 5 at hand and a new variant of the VS-IMSRG(2) method (described below), such a discussion can be now expanded.

7.1. Setting

Two additional quantities are presently investigated:

- the *three-point mass difference* $\Delta^{(3)}$

  $$\Delta^{(3)}(N) \equiv \frac{(-1)^N}{2}[E(N+1) - 2E(N) + E(N-1)], \tag{7.1}$$

  where N denotes the neutron number, delivers a measure of the superfluid neutron pairing gap [42, 140];

- the isotopic shift of the ground-state *mean-square charge radius*

  $$\delta \langle r^2_{\text{ch}} \rangle_{\text{A}} = \langle r^2_{\text{ch}} \rangle_{\text{A}} - \langle r^2_{\text{ch}} \rangle_{40}, \tag{7.2}$$

  relative to ^{40}Ca.

The analysis focuses on Calcium isotopes between ^{40}Ca and ^{48}Ca, i.e. while filling the neutron $0f_{7/2}$ shell. To deepen the analysis, a variant of the VS-IMSRG(2) calculations employed in Ch. 3 is presently considered. The results discussed in Ch. 3 making use of the neutron $\{0f_{7/2},\ 1p_{3/2},\ 1p_{1/2}\}$ valence space above the ^{40}Ca core[1] are now complemented with new results [141] based on the proton-neutron $\{1s_{1/2},\ 0d_{3/2},\ 0f_{7/2},\ 1p_{3/2}\}$ valence space above the ^{28}Si core[2]. These calculations 'opening' the ^{40}Ca core are denoted as VS-IMSRG(2) [^{28}Si] calculations.

---

[1] In the present chapter, such calculations are denoted as VS-IMSRG(2) [^{40}Ca].

[2] T. Miyagi, R. Stroberg and J. Holt are thanked for providing data relative to the VS-IMSRG(2) [^{28}Si] calculations.

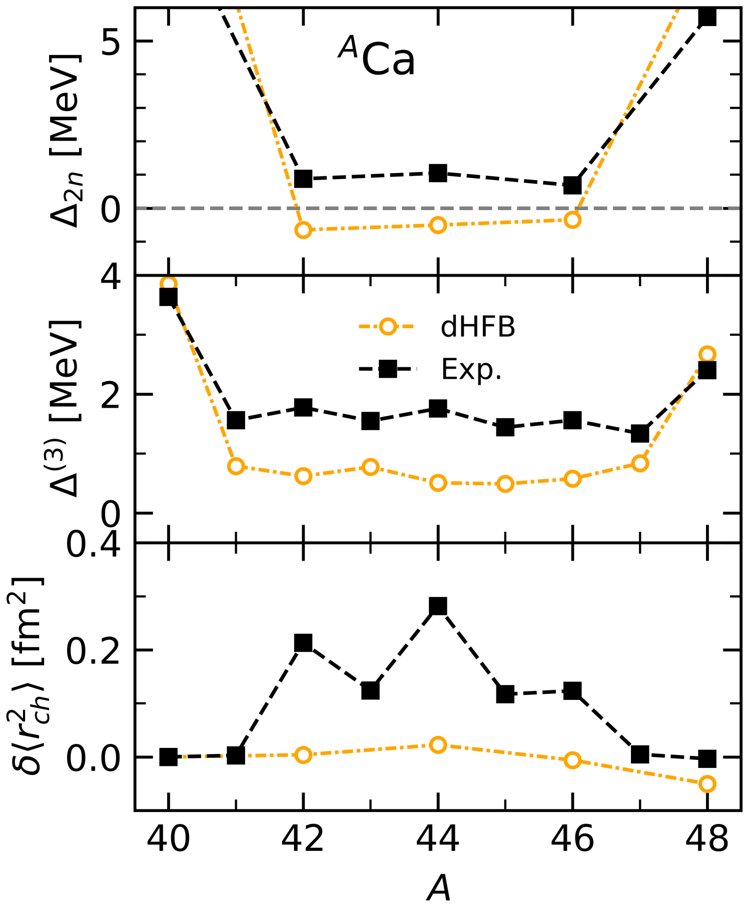

Figure 7.1. Threefold puzzle between ^{40}Ca and ^{48}Ca. Comparison of dHFB results and experimental data [63, 111] for Δ_{2n} (*top panel*), $\Delta^{(3)}$ (*middle panel*) and $\delta\,\langle r^2_{\mathrm{ch}}\rangle_{\mathrm{A}}$ (*bottom panel*).

7.2. Threefold puzzle

As visible from Fig. 7.1, the comparison of mean-field results with experimental data allows to define a threefold puzzle in $^{40-48}$Ca isotopes:

1. the second derivative of the dHF ground-state energy quantified by Δ_{2n} displays the wrong sign, i.e. the energy is concave instead of being convex;

2. deformed HF pairing gaps quantified by $\Delta^{(3)}$ only account for about 40% of the experimental value;

3. the flat trend of the dHF mean-square radius misses entirely the parabolic curve characterizing experimental values.

In the following, the capacity of different treatment of correlations beyond the mean-field to solve (partially) this threefold puzzle is analyzed.

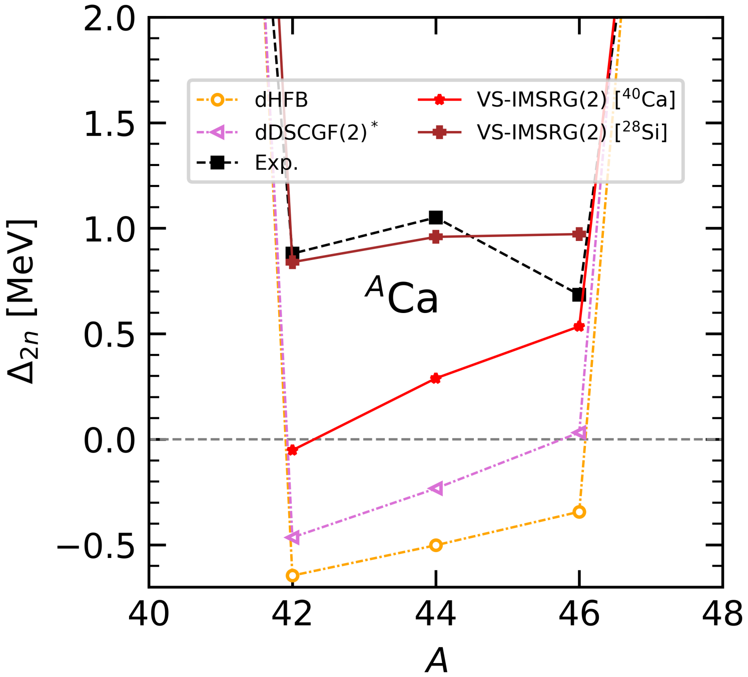

Figure 7.2. Two-neutron shell gap for even-even isotopes between ^{40}Ca and ^{48}Ca for dHF, dDSCGF(2), VS-IMSRG(2) [^{40}Ca] and VS-IMSRG(2) [^{28}Si] calculations against experimental data.

7.2.1. Curvature

As shown in Figs. 3.7 and 3.11, the inclusion of dynamical correlations improves the curvature of the energy in the direction of experimental data, i.e. the energy turns from being concave to being convex. However, the magnitude of the curvature remains underestimated. More specifically, the curvature obtained with VS-IMSRG(2) [^{40}Ca] is positive but the wrong trend with N observed at the mean-field level stays unchanged, i.e. while the experimental curvature is essentially constant around 1 MeV in $^{42-46}$Ca, the theoretical value is null in ^{42}Ca and increases linearly with N to eventually reproduce experiment in ^{46}Ca. Thus, while the full diagonalization in the fp valence-space accounts for the necessary correlations towards the end of the $0f_{7/2}$ shell, the freezing of the ^{40}Ca core does not permit, at least at the IMSRG(2) level, to deliver the right curvature all throughout the open shell.

As visible in Fig. 7.2, dDSCGF(2)* results are located in between dHFB and VS-IMSRG(2) [^{40}Ca] ones, displaying the same trend with N. Even though low-order dynamical correlations improve the situation, about half of what is captured via the full diagonalization in the fp valence-space is missing. On the other end, opening the ^{40}Ca core, VS-IMSRG(2) [^{28}Si] very much improves over VS-IMSRG(2) [^{40}Ca] in the beginning of the $0f_{7/2}$ shell and allows a quantitative reproduction of experiment all throughout. Such a behavior relates to the explicit treatment of the collective fluctuations of the ^{40}Ca core associated with particle-hole excitations across the $N = 20$ and $Z = 20$ magic gaps.

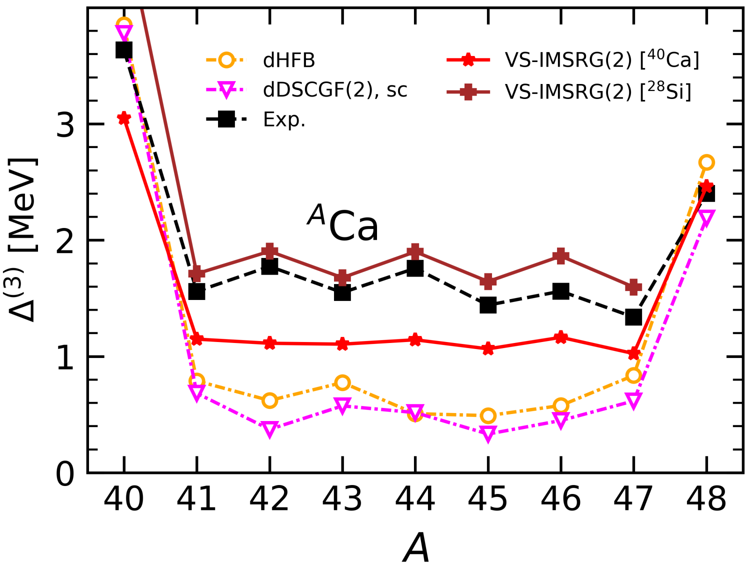

Figure 7.3. Three-point mass difference for even-even and even-odd isotopes between ^{40}Ca and ^{48}Ca for dHF, dDSCGF(2), VS-IMSRG(2) [^{40}Ca] and VS-IMSRG(2) [^{28}Si] calculations against experimental data.

7.2.2. Pairing gap

Figure 7.3 compares theoretical and experimental three-point mass differences. Clearly, low-order dynamical correlations captured by dDSCGF(2)* do not improve the situation over dHF, $\Delta^{(3)}$ remaining essentially unchanged. Performing the full diagonalization within the fp shell, neutron pairing gaps delivered by VS-IMSRG(2) [^{40}Ca] calculations are significantly enhanced, reaching about $\approx 60 - 70\%$ of the experimental $\Delta^{(3)}$, the improvement increasing slightly but steadily as neutrons are added into the $0f_{7/2}$ shell.

Eventually, a decisive improvement is obtained by opening the ^{40}Ca core. Indeed, VS-IMSRG(2) [^{28}Si] calculations provide essentially perfect pairing gaps throughout the shell by allowing the ^{40}Ca core to oscillate collectively[3]. This key result is consistent with the fact that superfluidity is expected to originate for a large part from the exchange of *collective* medium fluctuations between paired particles (in analogy to what happens for normal superconductors) [66–69]. While the present results demonstrate that reaching a quantitative description of pairing gaps from first principles is possible, doing so at polynomial cost still constitutes a major challenge for *ab initio* nuclear structure theory [65, 142, 143].

7.2.3. Charge radius

The experimental mean-square charge radius shown in the top panel of Fig. 7.4 displays the infamous bell-shaped curve between ^{40}Ca and ^{48}Ca, both isotopes exhibiting the same charge radius in spite of differing by eight neutrons.

---

[3] One observes that the sign and amplitude of the odd-even staggering of $\Delta^{(3)}$ is now also perfectly reproduced. This in fact does not come as a surprise given that such a staggering reflects nothing but the curvature of the energy [140].

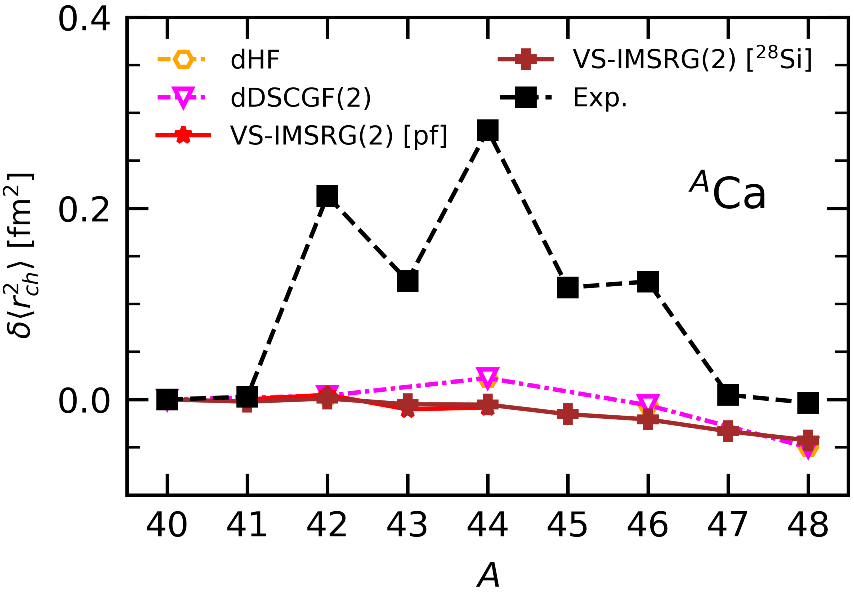

Figure 7.4. Isotopic shift of the mean-square charge radius of even-even and even-odd isotopes between ^{40}Ca and ^{48}Ca for dHF, dDSCGF(2), VS-IMSRG(2) [^{40}Ca] and VS-IMSRG(2) [^{28}Si] calculations against experimental data.

The parabolic trend of the mean-square charge radius is not reproduced by any of the *ab initio* calculations whose results are flat throughout the $0f_{7/2}$ shell. In particular, the opening of the ^{40}Ca core in VS-IMSRG(2) [^{28}Si] calculations, which solves the two first elements of the three-fold puzzle, does not at all improve the behavior. This is surprising given that such an opening of the ^{40}Ca core was put forward as the key ingredient to reproduce the parabolic curve within the frame of the phenomenological shell model [73]. In the context of *ab initio* VS-IMSRG(2) calculations, this feature does not constitute a sufficient condition to do so.

Even though the bell-shape curve is completely missed, the similar sizes of ^{40}Ca and ^{48}Ca are well accounted for by all calculations. As a matter of fact, this property is already captured at the mean-field level and is not deteriorated by the addition of dynamical correlations.

7.3. Conclusions

(i) the curvature of the energy, (ii) the three-point mass differences and (iii) the charge radius between ^{40}Ca and ^{48}Ca constitute a unique playground to study the role of various categories of many-body correlations in atomic nuclei. Indeed, these three features are qualitatively wrong at the mean-field level based on realistic nuclear interactions such that the inclusion of many-body correlations is mandatory to achieve a correct *ab initio* description. Three key lessons can be learnt from the (preliminary) above analysis.

- The curvature of the energy and neutron pairing gaps can be qualitatively (quantitatively) described via VS-IMSRG(2) calculations, i.e. by performing the full diagonalization in an appropriately chosen valence space on top of the ^{40}Ca (^{28}Si) core.

It is thus crucial to open the ^{40}Ca core to explicitly allow for collective fluctuations via particle-hole excitations across the $N = 20/Z = 20$ magic gaps.

- The curvature of the energy and the neutron pairing gaps can (cannot) be qualitatively (quantitatively) described at low order in polynomially-scaling methods. Achieving a quantitative description will require to capture higher-order processes associated with collective fluctuations of the nucleus. This constitutes an interesting challenge for the future development of expansion many-body methods.
- While the similar sizes of ^{40}Ca and ^{48}Ca are well accounted for, the parabolic behavior of the charge radius between both closed-shell isotopes is entirely missed. In particular, opening the ^{40}Ca core to account for its collective fluctuations is probably a necessary but not sufficient condition to achieve a correct description.

Eventually, the reproduction of the charge radius between ^{40}Ca and ^{48}Ca remains a real challenge for all methods. It was conjectured [144] that, while the similar sizes of ^{40}Ca and ^{48}Ca reflect the decreasing collectivity of the first 3_1^- excitation going from ^{40}Ca to ^{48}Ca, the parabolic curve in between correlates with the collectivity of the first 2_1^+ and 0_2^+ excitations as the $0f_{7/2}$ shell is being filled. In the phenomenological shell model [73], the opening of the ^{40}Ca core was key to describe the evolution of those low-lying collective states and thus account for the behavior of the charge radius. In present *ab initio* calculations, the opening of the ^{40}Ca core is probably necessary but not sufficient per se to achieve the same result.

The next step of the analysis will thus consist of computing excitation energies and reduced transition probabilities to the ground state of the first 3_1^-, 2_1^+ and 0_2^+ states. In order to disentangle the various sources of uncertainty, these calculations will be performed for:

- both the EM 1.8/2.0 Hamiltonian and its novel variants better describing absolute charge radii [47];
- both VS-IMSRG(2) and the more advanced VS-IMSRG(3f2) approximation [145];
- both the ^{40}Ca and ^{28}Si cores.

Based on the outcome of such a study, a better understanding of how the evolution of the charge radius between ^{40}Ca and ^{48}Ca can be most efficiently achieved via polynomially-scaling expansion methods can hopefully be achieved.

Overall conclusions

Upon the culmination of this extensive journey, the hope is that the reader will be thoroughly persuaded that *ab initio* methods represent a robust and valid approach for the first-principles description of different typologies of nuclear systems.

The present work focused mainly on the study of correlation-expansion methods that, given their polynomial-scaling, constitute an optimal route toward heavy nuclei. While the efficiency of such techniques has long been validated for spherical systems, their extension to doubly open-shell systems constitutes a recent development and remains only partially explored. Such an application poses significant numerical challenges, in particular due to the m-scheme framework employed. Importantly, one needs to incorporate long-range correlations, playing a crucial role in open-shell systems, from the outset to lift the emerging particle-hole degeneracy, as discussed in Ch. 1.

In the study of doubly open-shell systems, this can be achieved by breaking rotational symmetry. Conversely, singly open-shell systems are generally analyzed through the sole breaking of particle-number symmetry. Such approach requires a dedicated formalism, the Bogoliubov setting, which has been summarized in Ch. 2. Furthermore, the breaking of $SU(2)$ and $U(1)$ can be combined. At mean-field level, this leads to the dHFB method. The simplest extension of such approach to the beyond mean-field description of atomic nuclei is given by perturbation theory, dBMBPT.

The impact of the successive inclusion of beyond mean-field correlations has been studied in detail along Calcium and Chromium isotopic chains and discussed in Ch. 3. dBMBPT was shown to give an excellent reproduction of the total energy of deformed nuclei as well as more refined quantities such as the two-neutron separation energy and the two-neutron shell gap.

While further systematic calculations were being set up, the results of a recent experimental campaign providing accurate mass measurements of neutron-rich Sodium and Magnesium isotopes offered the occasion to test dBMBPT in a challenging region, namely the $N = 20$ island of inversion where deformation and collective effects dominate. Chapter 4 presented such application, where the comparison to experimental data and VS-IMSRG results highlighted at the same time the qualitative merits and some quantitative shortcomings of dBMBPT calculations.

The primary limitation of perturbation theory is that the number of particle-hole excitations that are taken into account is limited. More sophisticated (and expensive) techniques must be then developed in order to take into in account for further correlations. Such goal has been accomplished in Ch. 5, where the development of a novel *ab initio* technique, dDSCGF at second order, was presented. The existing Dyson formalism has been tailored to the case of systems breaking rotational symmetry (under the constraint of axial symmetry) and thoroughly tested in all numerical aspects. Associated results are encouraging and bring a quantitative improvement with respect to dBMBPT. However, the non-perturbative and self-consistent character of such method poses practical limitations, especially in terms of the truncation of the one-body Hilbert space.

To address these limitations, Ch. 6 proposed a dedicated version of NAT bases specifically designed for the study of open-shell systems and provided an in-depth analysis of this advancement. The chapter also examined the benefits of combining NAT bases with other cutting-edge techniques, such as IT. While primarily used in combination with dBMBPT calculations, NAT were proven to be beneficial also for the dDSCGF method. For future extensions of dDSCGF to higher orders, such numerical optimizations will be crucial to manage computational costs.

Lastly, Ch. 7 presented an intriguing threefold puzzle that emerges in *ab initio* calculations along Calcium isotopes. In particular, between ^{40}Ca and ^{48}Ca, i.e. when neutrons fill the $0f_{7/2}$ shell: (i) the curvature of the energy, (ii) the pairing gap and (iii) the charge radii obtained experimentally are not reproduced by simple mean-field calculations. The successive inclusion of beyond mean-field correlations qualitatively improves the situation for the first two points, reaching quantitatively the experiment only with a very recent and advanced version of the VS-IMSRG method. However, the failure in the reproduction of charge radii remains and constitutes a challenge for future theoretical developments. Importantly, finding a polynomially-scaling method capable of incorporating the necessary correlations to address these three features remains an important open problem.

Several of the techniques discussed in this work are still at an early stage of development and currently present some limitations. Nevertheless, ongoing efforts to tackle the main identified obstacles suggest a promising future for *ab initio* methods. The field is advancing rapidly, with significant improvements at the horizon.

Appendix A.

Bohr-Mottelson shell model

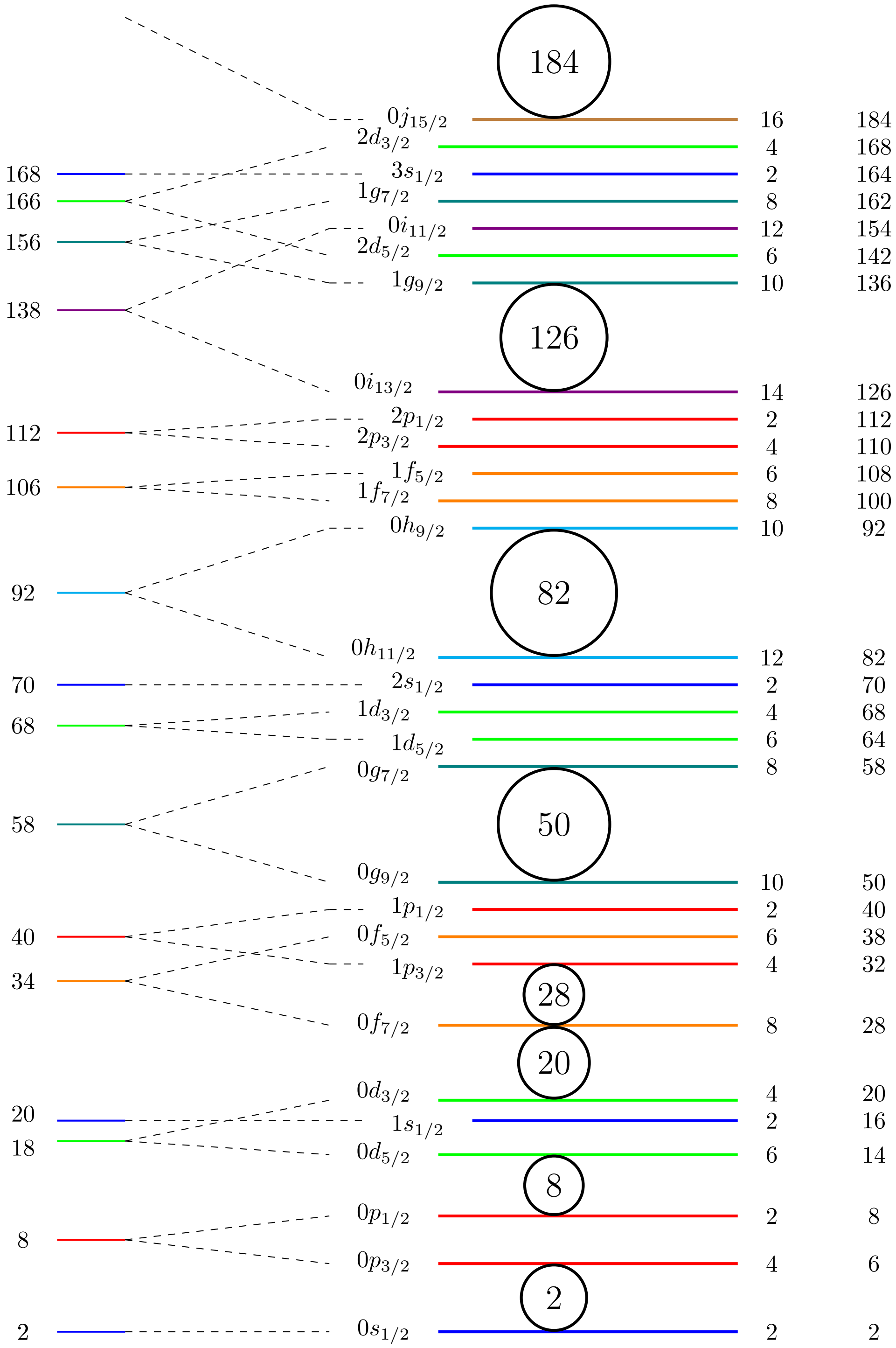

Figure A.1. The Bohr-Mottelson shell model for the sHO basis. Colored lines on the left represent energy levels with the assumption that the spin-orbit coupling is not active. Numbers on the left label the total number of particles included from below to above. Colored lines on the right labels energy levels obtained from the lines on the left by including the spin-orbit splitting. Numbers on the right label the number of particles included for each level and the total one. Numbers in circles in between of different levels label the magic numbers [83, 84] that signal the presence of wide energy gaps in the sHO model.

Appendix B.

Zero-pairing description

The present work shows that χEFT-based interactions typically lead to a mean-field approximation displaying very weak pairing correlations in open-shell nuclei. This property is intimately linked to the fact that the total HFB energy is concave rather than convex throughout long (enough) degenerate spherical shells. This connection can be validated analytically by considering that the system is in the extreme zero-pairing limit.

The zero-pairing mean-field description of an open-shell system can be meaningfully achieved on the basis of two different many-body formalisms, i.e. the Hartree-Fock-Bogoliubov theory in the zero-pairing limit (HFB-ZP) [49] or the Hartree-Fock theory in the equal filling approximation (HF-EFA) [70]. The two cases are worked out analytically below to validate the results obtained through realistic sHFB calculations in the body of the text.

B.1. Hartree-Fock-Bogoliubov

The fully-paired HFB vacuum associated with a time-reversal symmetric system is written in its canonical, i.e., BCS-like, form as [36]

$$|\Phi\rangle \equiv \prod_{\kappa>0} \left[u_\kappa + v_\kappa c^\dagger_\kappa c^\dagger_{\bar\kappa}\right] |0\rangle \, . \tag{B.1}$$

Operators $\{c^\dagger_\kappa, c_\kappa\}$ characterize the so-called canonical one-body basis in which pairs of conjugate states $(\kappa, \bar\kappa)$ are singled out by the Bogoliubov transformation via a quantum number m_κ such that $\kappa \equiv (\breve\kappa, m_\kappa)$ and $\bar\kappa \equiv (\breve\kappa, -m_\kappa)$. The state $\bar\kappa$ (κ) corresponds to the time-reversal state of κ ($\bar\kappa$) up to a sign η_κ ($\eta_{\bar\kappa}$) such that $\eta_{\bar\kappa}\eta_\kappa = -1$.

The BCS-like occupation numbers $u_\kappa \equiv u_{\breve\kappa}$ and $v_\kappa = \eta_\kappa v_{\breve\kappa}$ fulfilling $u^2_\kappa + v^2_\kappa = 1$ are expressed in terms of the positive m_κ-independent coefficients $(u_{\breve\kappa}, v_{\breve\kappa})$. Employing the latter, the non-zero elements of the normal and anomalous density matrices read in the canonical basis as

$$\begin{aligned} \rho_{\kappa\kappa} =& \rho_{\bar\kappa\bar\kappa} = v^2_{\breve\kappa} \, , \\ \kappa_{\kappa\bar\kappa} =& - \kappa_{\bar\kappa\kappa} = \eta_\kappa u_{\breve\kappa} v_{\breve\kappa} \, . \end{aligned} \tag{B.2}$$

Based on the above and given the nuclear Hamiltonian in Eq. (2.3)[1], the total HFB

---

[1] For the present analysis, center-of-mass corrections to the nuclear Hamiltonian are neglected.

energy reads in the canonical basis as

$$\begin{aligned} E_{\text{HFB}} \equiv& \langle\Phi|H|\Phi\rangle \\ \equiv& E^{\text{kin}}_{|\Phi\rangle} + E^{\text{HF}}_{|\Phi\rangle} + E^{\text{B}}_{|\Phi\rangle} \\ =& \sum_{\kappa} t_{\kappa\kappa}\, v^2_{\breve{\kappa}} \\ &+ \frac{1}{2}\sum_{\kappa\kappa'} \bar{v}^{NN}_{\kappa\kappa'\kappa\kappa'}\, v^2_{\breve{\kappa}}\, v^2_{\breve{\kappa}'} \\ &+ \frac{1}{4}\sum_{\kappa\kappa'} \bar{v}^{NN}_{\kappa\bar{\kappa}\kappa'\bar{\kappa}'}\, \eta_\kappa\eta_{\kappa'}\, u_{\breve{\kappa}}v_{\breve{\kappa}}\, u_{\breve{\kappa}'}v_{\breve{\kappa}'} \\ &+ \frac{1}{6}\sum_{\kappa\kappa'\kappa''} \bar{w}_{\kappa\kappa'\kappa''\kappa\kappa'\kappa''}\, v^2_{\breve{\kappa}}\, v^2_{\breve{\kappa}'}\, v^2_{\breve{\kappa}''} \\ &+ \frac{1}{4}\sum_{\kappa\kappa'}\sum_{\kappa''} \bar{w}_{\kappa\bar{\kappa}\kappa''\kappa'\bar{\kappa}'\kappa''}\, \eta_\kappa\eta_{\kappa'}\, u_{\breve{\kappa}}v_{\breve{\kappa}}\, u_{\breve{\kappa}'}v_{\breve{\kappa}'}\, v^2_{\breve{\kappa}''} \,. \end{aligned} \tag{B.3}$$

Canonical single-particle states further gather in degenerate shells. All states belonging to a given shell share the same set of quantum numbers $\breve{\kappa}$ and only differ by the value of m_k such that the single-particle energy defining the shell is independent of it, i.e. $\varepsilon_\kappa = \varepsilon_{\breve{\kappa}}$.

In the zero-pairing limit [49], states belonging to three categories of shells need to be distinguished according to:

1. $\varepsilon_{\breve{h}} - \lambda < 0$, casually denoted as 'hole states',
2. $\varepsilon_{\breve{v}} - \lambda = 0$, casually denoted as 'valence states',
3. $\varepsilon_{\breve{p}} - \lambda > 0$, casually denoted as 'particle states' ,

where λ denotes the chemical potential. Accordingly, it can be shown that canonical states display the following average occupations:

1. hole state: $v^2_{\breve{h}} = 1$,
2. valence state: $0 < v^2_{\breve{v}} \leq 1$,
3. particle state: $v^2_{\breve{p}} = 0$.

The valence shell gathers $p_v = d_v/2$ pairs of conjugated states such that the number of valence states d_v (pairs p_v) is equal to the number of m_v ($|m_v|$) different values. Consequently, the A nucleons making up the system are exhausted in such a way that $0 \leq a_v \leq d_v$ of them sit in the valence shell whereas $A - a_v$ occupy the hole states. Consequently, the occupation of each of the d_v valence states is

$$v^2_{\breve{v}} \equiv o_{\breve{v}} = \frac{a_v}{d_v}\,, \tag{B.4}$$

thus leading to

$$u_{\breve{v}}v_{\breve{v}} = \sqrt{o_{\breve{v}}(1 - o_{\breve{v}})}\,. \tag{B.5}$$

Based on the above, the HFB energy (Eq. B.3) of an open-shell system with a_v nucleons in the valence shell can be computed relatively to the CS core in the zero-pairing limit. After a lengthy but straightforward derivation, one obtains

$$\Delta E^{\text{HFB-ZP}}(a_v) \equiv E^{\text{HFB-ZP}}(a_v) - E^{\text{HFB-ZP}}(0) \tag{B.6}$$

$$= \alpha_{\breve{v}} a_v + \frac{\beta_{\breve{v}}}{2} a_v^2 + \frac{\gamma_{\breve{v}}}{6} a_v^3 \,, \tag{B.7}$$

where

$$\begin{aligned}
\alpha_{\breve{v}} &\equiv \varepsilon_{\breve{v}}^{\text{CS}} + \frac{\Delta_{\breve{v}}}{4} \,, && \text{(B.8a)}\\
\beta_{\breve{v}} &\equiv \frac{U_{\breve{v}}}{d_v} - \frac{1}{2d_v} \left(\Delta_{\breve{v}} - Z_{\breve{v}} \right) \,, && \text{(B.8b)}\\
\gamma_{\breve{v}} &\equiv \frac{1}{d_v^2} \left(X_{\breve{v}} - \frac{3}{2} Z_{\breve{v}} \right) \,, && \text{(B.8c)}
\end{aligned}$$

where the valence-shell single-particle energy computed in the CS core

$$\varepsilon_{\breve{v}}^{\text{CS}} \equiv t_{vv} + \sum_{h} \bar{v}^{NN}_{vhvh} + \frac{1}{2} \sum_{hh'} \bar{w}_{vhh'vhh'} \,, \tag{B.9}$$

and the m_v-independent quantities[2]

$$\begin{aligned}
U_{\breve{v}} &\equiv \sum_{m_{v'}}^{d_v} \left(\bar{v}^{NN}_{vv'vv'} + \sum_{h} \bar{w}_{vv'hvv'h} \right) \\
&= \sum_{m_{v'}}^{d_v} \bar{\boldsymbol{v}}_{vv'vv'} \,, && \text{(B.10a)}\\
\Delta_{\breve{v}} &\equiv \eta_v \sum_{m_{v'}}^{d_v} \left(\bar{v}^{NN}_{v\bar{v}v'\bar{v}'} + \sum_{h} \bar{w}_{v\bar{v}hv'\bar{v}'h} \right) \eta_{v'} \\
&= \eta_v \sum_{m_{v'}}^{d_v} \bar{\boldsymbol{v}}_{v\bar{v}v'\bar{v}'} \eta_{v'} \,, && \text{(B.10b)}\\
X_{\breve{v}} &\equiv \sum_{m_{v'}}^{d_v} \sum_{m_{v''}}^{d_v} \bar{w}_{vv'v''vv'v''} \,, && \text{(B.10c)}\\
Y_{\breve{v}} &\equiv \sum_{m_{v'}}^{d_v} \sum_{m_{v''}}^{d_v} \bar{w}_{vv'\bar{v}'vv''\bar{v}''} \, \eta_{v'} \eta_{v''} \,, && \text{(B.10d)}\\
Z_{\breve{v}} &\equiv \eta_v \sum_{m_{v'}}^{d_v} \sum_{m_{v''}}^{d_v} \bar{w}_{v\bar{v}v''v'\bar{v}'v''} \, \eta_{v'} \,, && \text{(B.10e)}
\end{aligned}$$

have been introduced to express the results in a compact way. Equations (B.10a)–(B.10b) make use of the effective valence-shell two-body matrix elements

$$\bar{\boldsymbol{v}}_{vv'v''v'''} = \bar{v}^{NN}_{vv'v''v'''} + \sum_{h} \bar{w}_{vv'hv''v'''h} \,, \tag{B.11}$$

incorporating the contribution from the initial three-body interaction associated with an averaging over the CS core.

---

[2] The quantities introduced in Eq. B.10 being independent of m_v, an additional sum over m_v simply delivers a factor d_v.

As demonstrated by Eqs. (B.7)–(B.8), the HFB-ZP energy is manifestly[3] cubic with the number of valence nucleons. While the cubic term originates entirely from the three-nucleon interaction, the curvature $\beta_{\breve{v}}$ of the HFB-ZP energy relates to a specific linear combination of two- and three-body matrix elements that can be extracted from actual HFB calculations. The sign of this combination of matrix elements determines the convexity or concavity character through the open shell, under the assumption that the cubic term is subleading, which can also be directly checked from a subset of three-body matrix elements.

The two-neutron separation energy of open-shell nuclei is given, for $a_v \geq 2$, by

$$\begin{aligned} S_{2n}^{\text{HFB-ZP}}(a_v) \equiv& \Delta E^{\text{HFB-ZP}}(a_v-2) - \Delta E^{\text{HFB-ZP}}(a_v) \\ =& -2(\alpha_{\breve{v}} - \beta_{\breve{v}} + \frac{2}{3}\gamma_{\breve{v}}) - 2(\beta_{\breve{v}} - \gamma_{\breve{v}})a_v - \gamma_{\breve{v}}\, a_v^2 \, . \end{aligned} \tag{B.12}$$

Under the (realistic) assumption that $|\alpha_{\breve{v}}| \gg |\beta_{\breve{v}}| \gg |\gamma_{\breve{v}}|$, S_{2n} starts at $-2\alpha_{\breve{v}}$ and evolves linearly throughout the open shell with a negative (positive) slope $-2\beta_{\breve{v}}$ when the energy is convex (concave).

Following Eq. (B.12), the two-neutron shell gap is given, for $a_v \geq 2$, by

$$\begin{aligned} \Delta_{2n}^{\text{HFB-ZP}}(a_v) \equiv& S_{2n}^{\text{HFB-ZP}}(a_v) - S_{2n}^{\text{HFB-ZP}}(a_v)(a_v+2) \\ =& 4\beta_{\breve{v}} + 4\gamma_{\breve{v}} a_v \, . \end{aligned} \tag{B.13}$$

Under the (realistic) assumption that $|\beta_{\breve{v}}| \gg |\gamma_{\breve{v}}|$, Δ_{2n} is constant throughout the open shell with a positive (negative) value when the energy is convex (concave).

Eventually, the evolution of the valence-shell single-particle energy as a function of a_v is given by

$$\begin{aligned} \varepsilon_{\breve{v}}^{\text{HFB-ZP}}(a_v) =& \varepsilon_{\breve{v}}^{\text{CS}} \\ &+ \frac{1}{d_v}\left(U_{\breve{v}} + \frac{1}{4}Y_{\breve{v}}\right) a_v \\ &+ \frac{1}{2d_v^2}\left(X_{\breve{v}} - \frac{1}{2}Y_{\breve{v}}\right) a_v^2 \, . \end{aligned} \tag{B.14}$$

The valence-shell single-particle energy contains linear and quadratic contributions in a_v, the coefficient of the former (latter) being closely related to the curvature (cubic coefficient) of the HFB-ZP energy.

B.2. Equal-filling approximation

While the previous section provides analytical expressions derived within the frame of the HFB formalism in the zero-pairing limit [49], a simpler mean-field treatment of open-shell systems in absence of pairing correlations is provided by the HF theory in the equal filling approximation. While their results are closely related, the two formalisms are

---

[3] Equation B.7 displays the explicit dependence of $\Delta E^{\text{HFB-ZP}}$ on a_v. However, additional implicit dependences are in fact at play in Eq. B.7. First, the two-body part of the center-of-mass kinetic energy correction included in the two-body interaction matrix elements actually depends on A. Second, all matrix elements at play carry an implicit dependence on a_v through the nature of their indices. Indeed, canonical single-particle states are nucleus-dependent and thus evolve as the valence shell is being filled, i.e. with a_v. However, it was checked numerically that both effects are largely subleading.

fundamentally different. Indeed, while HFB describes the system via a pure quantum state, the EFA is formulated within the frame of statistical quantum mechanics, i.e. the system is described in terms of a statistical density operator [70].

Effectively, EFA results can be trivially obtained by setting $\Delta_{\breve{v}} = Y_{\breve{v}} = Z_{\breve{v}} = 0$ in the HFB-ZP formulae. Thus, Eqs. (B.7), (B.12) and (B.14) apply, but with the modified coefficients

$$\alpha_{\breve{v}} = \varepsilon^{\text{CS}}_{\breve{v}} \,, \tag{B.15a}$$

$$\beta_{\breve{v}} = \frac{1}{d_v} U_{\breve{v}} \,, \tag{B.15b}$$

$$\gamma_{\breve{v}} = \frac{1}{d_v^2} X_{\breve{v}} \,. \tag{B.15c}$$

B.3. Discussion

As already mentioned, numerical applications deliver $\gamma_{\breve{v}} = 0$ in all cases under scrutiny. Furthermore, the pairing contributions to $\alpha_{\breve{v}}$ and $\beta_{\breve{v}}$ are also negligible such that the HF-EFA results for $\gamma_{\breve{v}} = 0$ give an excellent account of HFB-ZP under the form

$$\Delta E^{\text{HF-EFA}}(a_v) = \varepsilon^{\text{CS}}_{\breve{v}} a_v + \frac{\beta_{\breve{v}}}{2} a_v^2 \,, \tag{B.16a}$$

$$S^{\text{HF-EFA}}_{2n}(a_v) = -2\varepsilon^{\text{CS}}_{\breve{v}} - 2\beta_{\breve{v}}(a_v - 1) \,, \tag{B.16b}$$

$$\varepsilon^{\text{HF-EFA}}_{\breve{v}}(a_v) = \varepsilon^{\text{CS}}_{\breve{v}} + \beta_{\breve{v}} a_v \,, \tag{B.16c}$$

$$\Delta^{\text{HF-EFA}}_{\breve{v}}(a_v) = 4\beta_{\breve{v}} \,. \tag{B.16d}$$

The evolutions of the total binding energy, the two-nucleon separation and the valence-shell single-particle energy, as one fills the valence shell, are strictly correlated and entirely driven by the valence-shell single-particle energy computed in the core $\varepsilon^{\text{CS}}_{\breve{v}}$ (diagrammatically represented in Fig. 3.3) and by $\beta_{\breve{v}}$ that is nothing but the average diagonal matrix elements of the effective valence-shell two-body interaction (diagrammatically represented in Fig. 3.4)

$$\beta_{\breve{v}} = \frac{1}{d_v} \sum_{m_{v'}}^{d_v} \bar{\boldsymbol{v}}_{vv'vv'} \,. \tag{B.17}$$

More specifically, while the total energy is quadratic in a_v, the two-nucleon separation energy and the valence-shell single-particle energy are linear. The coefficient of the linear (quadratic) term in the former drives the initial value (slope) of the latter, knowing that the slopes of the two-nucleon separation energy and of single-particle energy are opposite.

B.4. Second-order MBPT

Having semi-analytical expressions as a function of a_v for the mean-field results in the zero-pairing limit, it is now relevant to investigate the addition of dynamical correlations.

This is presently done by evaluating the MBPT(2) corrections to the valence-shell single-particle energy computed in the CS core and to the valence-shell effective two-body interaction. To do so, the valence shell is taken to be doubly degenerate (v, v')[4] and the total energy is computed at the MBPT(2) level for both the CS core and the system with two more particles in order to compute the two-nucleon separation energy.

After a lengthy but straightforward derivation, the separation energy between the two even isotopes is obtained as

$$\begin{aligned} S^{(2)}_{2n}(2) &= E^{(2)}(0) - E^{(2)}(2) \\ &= -2\left(\varepsilon^{\text{CS}}_{\check{v}} + \Sigma^{(2)}_{\check{v}}(\varepsilon^{\text{CS}}_{\check{v}})\right) \\ &\quad - \left(\bar{\boldsymbol{v}}_{vv'vv'} + \bar{\boldsymbol{v}}^{(2)}_{vv'vv'}(\varepsilon^{\text{CS}}_{\check{v}})\right) , \end{aligned} \tag{B.18}$$

where the (on-shell) valence-shell self-energy and two-body effective interaction corrections are given by

$$\begin{aligned} \Sigma^{(2)}_{\check{v}}(\varepsilon^{\text{CS}}_{\check{v}}) &= +\frac{1}{2}\sum_{hh'p} \frac{|\bar{\boldsymbol{v}}_{hh'vp}|^2}{\varepsilon^{\text{CS}}_{p} + \varepsilon^{\text{CS}}_{\check{v}} - \varepsilon^{\text{CS}}_{h} - \varepsilon^{\text{CS}}_{h'}} \\ &\quad - \frac{1}{2}\sum_{pp'h} \frac{|\bar{\boldsymbol{v}}_{vhpp'}|^2}{\varepsilon^{\text{CS}}_{p} + \varepsilon^{\text{CS}}_{p'} - \varepsilon^{\text{CS}}_{h} - \varepsilon^{\text{CS}}_{\check{v}}} , \end{aligned} \tag{B.19a}$$

$$\begin{aligned} \bar{\boldsymbol{v}}^{(2)}_{vv'vv'}(\varepsilon^{\text{CS}}_{\check{v}}) &= +\frac{1}{2}\sum_{hh'} \frac{|\bar{\boldsymbol{v}}_{hh'vv'}|^2}{2\varepsilon^{\text{CS}}_{\check{v}} - \varepsilon^{\text{CS}}_{h} - \varepsilon^{\text{CS}}_{h'}} \\ &\quad - \frac{1}{2}\sum_{pp'} \frac{|\bar{\boldsymbol{v}}_{vv'pp'}|^2}{\varepsilon^{\text{CS}}_{p} + \varepsilon^{\text{CS}}_{p'} - 2\varepsilon^{\text{CS}}_{\check{v}}} , \end{aligned} \tag{B.19b}$$

and displayed diagrammatically in Figs 3.8 and 3.9, respectively. The second-order corrections to the total binding energy translate for the two-neutron separation energy into a correction of the mean-field valence-shell single-particle energy and of the effective valence-shell two-body interaction.

Extending candidly the situation to a d_v-fold degenerate valence-shell in a EFA-like spirit, S_{2n} and Δ_{2n} evolve for $a_v \geq 2$ as

$$S^{(2)}_{2n}(a_v) = -2\alpha^{(2)}_{\check{v}} - 2\beta^{(2)}_{\check{v}}(a_v - 1) , \tag{B.20a}$$

$$\Delta^{(2)}_{2n}(a_v) = 4\beta^{(2)}_{\check{v}} , \tag{B.20b}$$

with

$$\alpha^{(2)}_{\check{v}} \equiv \varepsilon^{\text{CS}}_{\check{v}} + \Sigma^{(2)}_{\check{v}}(\varepsilon^{\text{CS}}_{\check{v}}) , \tag{B.21a}$$

$$\beta^{(2)}_{\check{v}} \equiv \frac{1}{d_v}\sum_{m_{v'}}^{d_v} \left(\bar{\boldsymbol{v}}_{vv'vv'} + \bar{\boldsymbol{v}}^{(2)}_{vv'vv'}(\varepsilon^{\text{CS}}_{\check{v}})\right) , \tag{B.21b}$$

the latter being the averaged valence-shell interaction at second order in perturbation theory.

As seen in Eq. (B.20) and (B.21), dynamical correlations modify both the starting value of the $S^{(2))}_{2n}$ in the valence-shell and the slope governing its evolution, i.e. the self-energy correction impacts the former whereas the correction to the valence-shell interaction modifies the latter.

---

[4] This setting is mandatory to compute the energy of two successive even isotopes via MBPT, i.e. to avoid actually dealing with open-shell systems given that pairing was shown to be negligible for the present discussion and given that no perturbation theory based on a HF-EFA statistical operator is available to date.

Appendix C.

Two-neutron shell gap Δ_{2n}

The two-neutron shell gap defined in Eq. (3.2) explicitly reads as

$$\Delta_{2n}(N,Z) = E(N-2,Z) - 2E(N,Z) + E(N+2,Z). \tag{C.1}$$

The second derivative of the total energy centered around N can be written through finite difference coefficients as

$$\frac{\partial^2 E(N,Z)}{\partial N^2} = \frac{1}{4}\left(E(N-2,Z) - 2E(N,Z) + E(N+2,Z)\right), \tag{C.2}$$

which proves that

$$\frac{\partial^2 E(N,Z)}{\partial N^2} = \frac{\Delta_{2n}(N,Z)}{4}\,. \tag{C.3}$$

Appendix D.

Axial tensors

D.1. The 'reduced' Wigner-Eckart theorem

An *irreducible spherical tensor* (IST) T_k^μ of rank k and component μ can be defined as the mathematical object satisfying the two relations:

$$[J_z, T_k^\mu] = \mu T_k^\mu, \tag{D.1a}$$

$$[J_\pm, T_k^\mu] = \{(k \mp \mu)(k \pm \mu + 1)\}^{1/2} T_k^{\mu \pm 1}, \tag{D.1b}$$

where J_+ (J_-) represents the rising (lowering) operator and is defined as

$$J_\pm \equiv J_x \pm i J_y, \tag{D.2}$$

and J_z satisfies the eigenvalue equation

$$J_z \left|jm\right\rangle = m \left|jm\right\rangle . \tag{D.3}$$

Expectation values of ISTs obey the Wigner-Eckart theorem

$$\langle j_f m_f | T_k^\mu | j_i m_i \rangle = \langle j_i m_i k \mu | j_f m_f \rangle \langle j_f || T_k || j_i \rangle , \tag{D.4}$$

which allows to isolate the m-dependency out of the bracket.

Consider now an object that satisfies Eq. (D.1a) and that will be henceforth referred to as *axial tensor* (AT), denoted as $\widetilde{T}^\mu$. The expectation value over the states $|m_i\rangle$ and $|m_f\rangle$ of its commutator with J_z reads

$$\langle m_f | [J_z, \widetilde{T}^\mu] m_i \rangle = \mu \langle m_f | \widetilde{T}^\mu | m_i \rangle . \tag{D.5}$$

Expanding the commutator and exploiting the self-adjointness of J_z, one finds

$$\begin{aligned} \langle m_f | [J_z, \widetilde{T}^\mu] | m_i \rangle &= \langle m_f | J_z \widetilde{T}^\mu - \widetilde{T}^\mu J_z | m_i \rangle \\ &= (m_f - m_i) \langle m_f | \widetilde{T}^\mu | m_i \rangle . \end{aligned} \tag{D.6}$$

The combination of Eqs. (D.5) and (D.6) leads to

$$(\mu - m_f + m_i) \langle m_f | \widetilde{T}^\mu | m_i \rangle = 0, \tag{D.7}$$

which highlights the following simplification in the expectation value of an AT:

$$\langle m_f | \widetilde{T}^\mu | m_i \rangle = \delta_{m_i + \mu, m_f} \langle m_f | \widetilde{T}^\mu | m_i \rangle . \tag{D.8}$$

Eq. (D.8) can be taken as a 'reduced' version of the Wigner-Eckart theorem for states and operators not characterized by good angular-momentum and it is nothing else than a selection rule on the projection of angular momenta.

D.2. Creation and annihilation operators

Creation operators $c^\dagger_\alpha$ can be shown to satisfy Eq. (D.1a). To prove it, consider separately the action of the two members of Eq. (D.1a) on a vacuum state $|0\rangle$:

$$[J_z, c^\dagger_\alpha]\,|0\rangle = J_z c^\dagger_\alpha\,|0\rangle - c^\dagger_\alpha J_z\,|0\rangle = J_z\,|m_\alpha\rangle - 0 = m_\alpha\,|m_\alpha\rangle \tag{D.9}$$

and

$$m_\alpha c^\dagger_\alpha\,|0\rangle = m_\alpha\,|m_\alpha\rangle\,. \tag{D.10}$$

In contrast, the annihilation counterpart c_α does not satisfy Eq. (D.1a). Instead, the operator $\eta_\alpha c_{\bar{\alpha}}$ does, with $\eta_\alpha = (-1)^{1/2-m_\alpha}$. This can be proven similarly to what seen in the case of the creation operator, acting on a single-particle state $|m'\rangle$:

$$\begin{aligned}[J_z, \eta_\alpha c_{\bar{\alpha}}]\,|m'\rangle &= \eta_\alpha \delta_{-m_\alpha,m'} J_z\,|0\rangle - \eta_\alpha c_{\bar{\alpha}} m'\,|m'\rangle \\ &= -\eta_\alpha m' \delta_{-m_\alpha,m'}\,|0\rangle \\ &= \eta_\alpha m_\alpha\,|0\rangle\end{aligned} \tag{D.11}$$

and

$$m_\alpha \eta_\alpha c_{\bar{\alpha}}\,|m'\rangle = m_\alpha \eta_\alpha \delta_{-m_\alpha,m'}\,|0\rangle = m_\alpha \eta_\alpha\,|0\rangle\,. \tag{D.12}$$

The two operators set $\{c^\dagger_\alpha\}$ and $\{\eta_\alpha c_{\bar{\alpha}}\}$ are then (m_α)-th components of ATs and satisfy Eq. (D.8).

Appendix E.

Multi-pivot Lanczos algorithm

The Lanczos algorithm constitutes the numerical tool employed to implement the Krylov projection in practical calculations. It is a recursive method that allows to extract the extreme (i.e. highest and lowest) eigenvalues from an input matrix E of dimensions $N_s \times N_s$. Its importance arises when N_s is so big that not all the eigenvalues of E can be determined for computational time constraints and the interest is only in the 'most useful' ones. A full explanation of such algorithm can be found in [17] and is here summarized.

E.1. Workflow of the multi-pivot algorithm

Let $\mathcal{H}_{LG}$ be the space spanned by the eigenstates of E, with $\dim(\mathcal{H}_{LG}) = N_s$, and let $\boldsymbol{p}$ be the pivot vector of dimension N_s. The *Krylov subspace* can be defined as the linear subspace of $\mathcal{H}_{LG}$ spanned by the vectors obtained by applying the first r powers of E to $\boldsymbol{p}$:

$$\mathcal{K}^{(r)} \equiv \text{span}\{\boldsymbol{p}, E\boldsymbol{p}, E^2\boldsymbol{p}, E^3\boldsymbol{p}, \ldots, E^{r-1}\boldsymbol{p}\}. \tag{E.1}$$

In the limit where $r = N_s$, one finds

$$\mathcal{K}^{(N_s)} = \mathcal{H}_{LG}, \tag{E.2}$$

since the Krylov projection reduces to a unitary transformation of the initial space. The output of the Lanczos algorithm is an orthonormal basis $\boldsymbol{v}_j$, with $j = 1, 2, \ldots, r$ of $\mathcal{K}^{(r)}$. The vectors of such basis are obtained through a recursive procedure where the vector determined at the previous step is employed in the next one:

$$\begin{aligned}
\boldsymbol{v}_1 &\equiv \boldsymbol{p}\,, \\
E\boldsymbol{v}_1 &\equiv e_{11}\boldsymbol{v}_1 + e_{21}\boldsymbol{v}_2\,, \\
E\boldsymbol{v}_2 &\equiv e_{12}\boldsymbol{v}_1 + e_{22}\boldsymbol{v}_2 + e_{32}\boldsymbol{v}_3\,, \\
&\ldots \\
E\boldsymbol{v}_{r-1} &\equiv e_{1(r-1)}\boldsymbol{v}_1 + \cdots + e_{r(r-1)}\boldsymbol{v}_r\,.
\end{aligned} \tag{E.3}$$

The new vectors $\boldsymbol{v}_j$ are further normalized at each step. By construction, it follows that

$$e_{ij} = (e_{ji})^* = \boldsymbol{v}_i^\dagger E \boldsymbol{v}_j = 0 \qquad\qquad \text{for}|i-j| \geq 2, \tag{E.4}$$

which implies that the projection E' of E on the Krylov subspace is tridiagonal. So far, a single pivot $\boldsymbol{p}$ has been considered. In view of a generalization of the procedure above to the case of multiple pivots, consider now a set of linearly independent vectors $\boldsymbol{p}_i$, with $i = 1, \ldots, N_p$. A new Krylov subspace can be generated through the multi-pivot approach taking N_p orthonormal bases $\boldsymbol{v}_j$, henceforth denoted as $\boldsymbol{v}_j^i$, with $i = 1, \ldots, N_p$. Eq. (E.1) is then generalized to:

$$\begin{aligned}\mathcal{K}^{(r)} \equiv \text{span}\{&\boldsymbol{v}_1^{(1)}, E\boldsymbol{v}_1^{(1)}, E^2\boldsymbol{v}_1^{(1)}, \ldots, E^{r_1-1}\boldsymbol{v}_1^{(1)},\\ &\boldsymbol{v}_1^{(2)}, E\boldsymbol{v}_1^{(2)}, E^2\boldsymbol{v}_1^{(2)}, \ldots, E^{r_2-1}\boldsymbol{v}_1^{(2)},\\ &\ldots\\ &\boldsymbol{v}_1^{(N_p)}, E\boldsymbol{v}_1^{(N_p)}, E^2\boldsymbol{v}_1^{(N_p)}, \ldots, E^{r_{N_p}-1}\boldsymbol{v}_1^{(N_p)}\}.\end{aligned} \tag{E.5}$$

The procedure is also generalized as follows. After N_l iterations are performed with the first pivot, the second pivot is orthogonalized with respect to all the previous ones through the Gram-Schmidt procedure[1]:

$$\boldsymbol{p}^{(2)} \equiv \sum_{r=1}^{r_1} c_i^{(1)} \boldsymbol{v}_i^{(1)} + d^{(1)} \boldsymbol{v}_1^{(2)}, \tag{E.6}$$

and after a further normalization, $\boldsymbol{v}_1^{(2)}$ is taken as the new pivot. $c_i^{(1)}$ and $d^{(1)}$ are constrained by the set of vectors with respect to which $\boldsymbol{p}^{(2)}$ has to be orthogonalized. Equations analogous to Eqs. (E.3) are then applied until the addition of a new pivot or the end of the procedure. Eq. (E.4) holds at each iteration except when a new pivot is added, giving rise to the fishbone-like structure of the projected matrix E' (see Fig. 5.6). The pseudo-code below summarizes the main steps of the procedure.

Algorithm 1 Multi-pivot Lanczos algorithm

```
Input: matrix of pivot vectors $\boldsymbol{p}$ of dimension $m \times N_p$
while $0 \leq i < N_p$ do                                  ▷ loop over the pivots
    $\boldsymbol{p}^{(i)} \leftarrow \boldsymbol{p}^{(i)}/|\boldsymbol{p}^{(i)}|$                                  ▷ normalize
    $\boldsymbol{v}^{(i\times N_l)} \leftarrow \boldsymbol{p}^{(i)}$                        ▷ add the pivot to the Lanczos matrix
    Gram-Schmidt($\boldsymbol{w}^{(i\times N_l)}$)                 ▷ orthogonalize w.r.t. previous vectors
    while $1 \leq j < N_l$ do
        $\boldsymbol{v}^{(i\times N_l+j)} \leftarrow A * \boldsymbol{v}^{(i\times N_l+j)}$             ▷ build Lanczos vectors $w$
        Gram-Schmidt($\boldsymbol{v}^{(i\times N_l+j)}$)         ▷ orthogonalize w.r.t. previous vectors
        $\boldsymbol{v}^{(i\times N_l+j)} \leftarrow \boldsymbol{v}^{(i\times N_l+j)}/|\boldsymbol{v}^{(i\times N_l+j)}|$                  ▷ normalize
Output: matrix of Lanczos vectors $\boldsymbol{w}$ of dimension $m \times (N_pN_l)$
```

---

[1] Given the high numerical instability of the Lanczos algorithm arising from the limited numerical precision that computers employ to represent decimal numbers, the Gram-Schmidt orthogonalization procedure is applied not only when a new pivot is added but also when a new vector $\boldsymbol{v}_j$ is determined from the Lanczos iterations.

Appendix F.

Spectroscopic factors

F.1. ^{40}Ca with ADC(2)

The only difference when passing from the ADC(1) to ADC(2) approximation is the fact that beyond mean-field correlations cause a fragmentation of the particles and holes such that the spectroscopic factors represented in Fig. F.1 are now between 0 and 1.

F.2. ^{46}Ca with ADC(2)

The $\beta_2 = 0.08$ deformation that characterizes ^{46}Ca is big enough to prevent identification of good angular momenta for each peak in analogy of what done in Sec. 5.5.3. Figure F.2 highlights this problem and calls for a future restoration of symmetries for a proper description of open-shell nuclei in the SCGF frame (see the Sec. 5.6 for details).

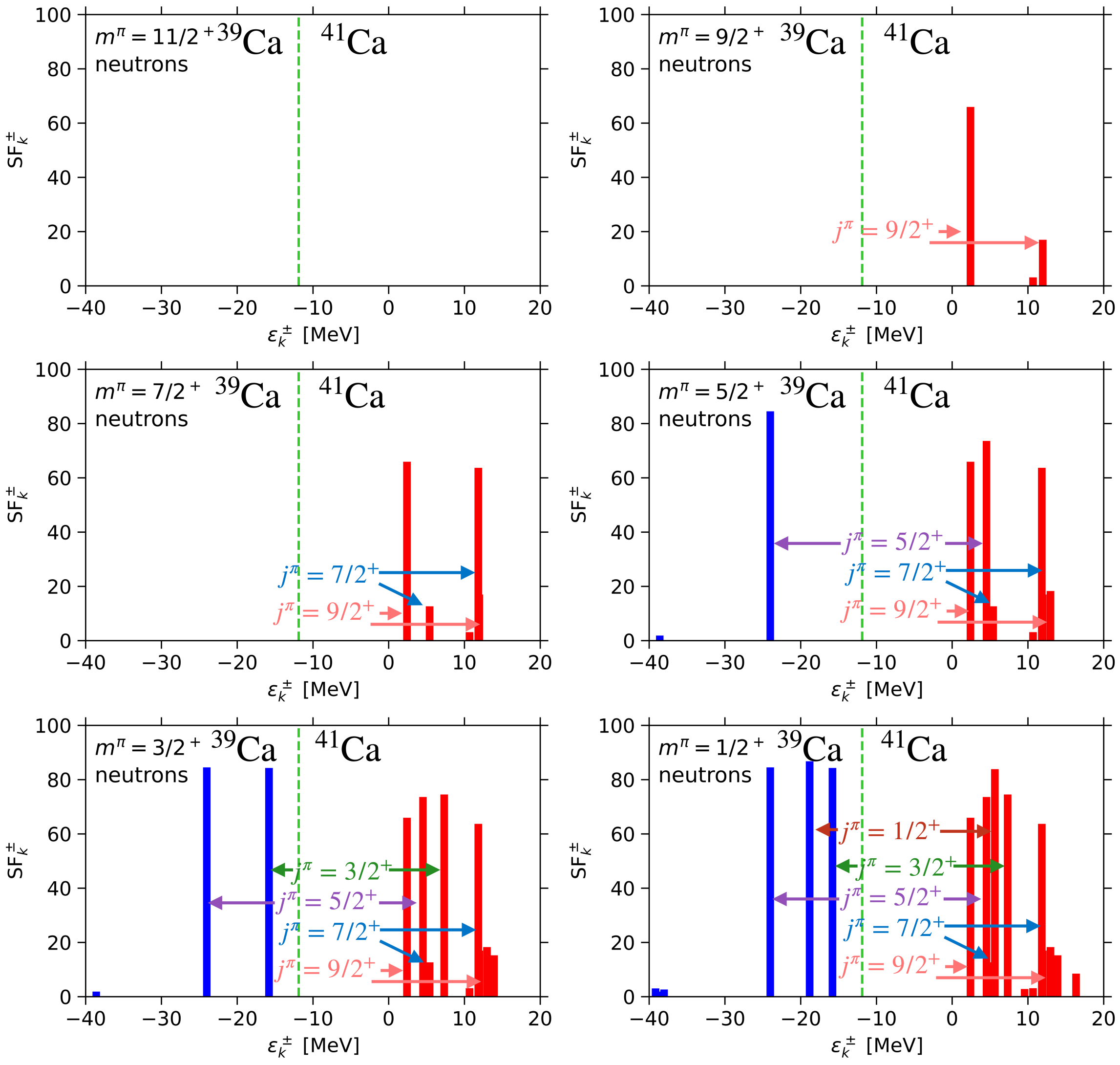

Figure F.1. Same as Fig. 5.19 for the ADC(2) approximation.

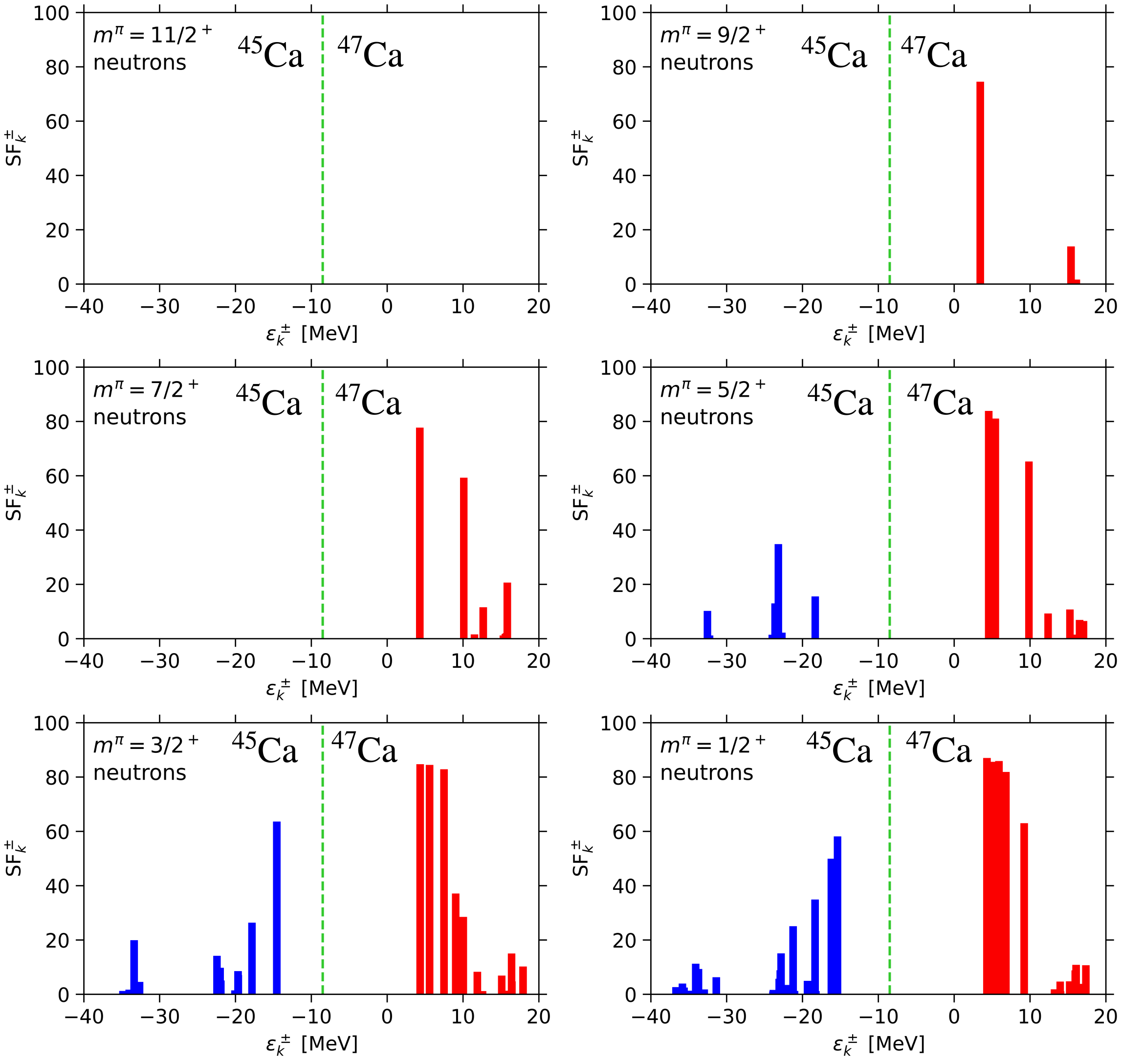

Figure F.2. Same as Fig. F.1 for ^{46}Ca.

Appendix G.

Single-particle wave functions in axially-deformed bases

A generic spherical wave function defined using a so-called j-coupling representation

$$\langle r\theta\phi\sigma\tau|njm\pi t\rangle \equiv \psi_{njm\pi t}(r,\theta,\phi,\sigma,\tau)\,, \tag{G.1}$$

can be represented onto a basis employing a ls-coupling scheme through

$$\begin{aligned}&\psi_{njm\pi t}(r,\theta,\phi,\sigma,\tau)\\ &= \sum_{lm_l sm_s} \psi_{nlm_l}(r,\theta,\phi)\chi_{m_s}(\sigma)\chi_t(\tau)\langle lm_l sm_s|jm\rangle,\end{aligned} \tag{G.2}$$

where m_l is constrained by the sum rule in the Clebsch-Gordan coefficient ($m = m_l + m_s$), $s = 1/2$ for fermions and l is constrained by the knowledge of j and π ($l = |j-s|, j+s$). As a consequence, the summation in Eq. (G.2) is limited to a summation over the spin projection m_s. Clebsch-Gordan coefficients assume a particularly simple expression for the few values of j and m_s allowed, which are summarized in Tab. G.1 (see Ref. [146] for more details).

j	$m_s = 1/2$	$m_s = -1/2$
$l+1/2$	$\sqrt{\dfrac{l+m+1/2}{2l+1}}$	$\sqrt{\dfrac{l-m+1/2}{2l+1}}$
$l-1/2$	$-\sqrt{\dfrac{l-m+1/2}{2l+1}}$	$\sqrt{\dfrac{l+m+1/2}{2l+1}}$

Table G.1. Analytical expression for the Clebsch-Gordan coefficients entering Eq. (G.2).

In general the ls-scheme wave function in Eq. (G.2) can also depend on m_s and t quantum numbers. However, sHO wave functions are independent on the spin and isospin projections (i.e. $\psi_{nlm_l m_s t} = \psi_{nlm_l}$). Eventually the j-scheme wave function can be written as a function of the two spin components ($m_s = +1/2 = \uparrow$ and $m_s = -1/2 = \downarrow$) according to

$$\begin{aligned}&\Psi_{njm\pi t}(r,\theta,\phi,\sigma,\tau) = \begin{pmatrix}\Psi_{njm\pi t}(r,\theta,\phi,\sigma,\tau)_\uparrow\\ \Psi_{njm\pi t}(r,\theta,\phi,\sigma,\tau)_\downarrow\end{pmatrix}\\ &= \sqrt{\frac{1}{2}+\frac{2(j-l)m}{2l+1}}\psi_{nl(m-1/2)}(r,\theta,\phi)\chi_{1/2}(\sigma)\chi_t(\tau)\\ &+ (-1)^{1/2+l-j}\sqrt{\frac{1}{2}-\frac{2(j-l)m}{2l+1}}\psi_{nl(m+1/2)}(r,\theta,\phi)\\ &\times \chi_{-1/2}(\sigma)\chi_t(\tau)\,,\end{aligned} \tag{G.3}$$

which is a two-dimensional vector whose components are scalar wave functions. The wave function ψ_{nlm_l} can be split into radial and angular contributions

$$\psi_{nlm_l}(r,\theta,\phi) = f_{nl}(r) Y_{lm_l}(\theta,\phi)\,, \tag{G.4}$$

where $Y_{lm_l}(\theta,\phi)$ represents a *spherical harmonic*

$$Y_{lm_l}(\theta,\phi) \equiv \sqrt{\frac{2l+1}{4\pi}\frac{(l-m_l)!}{(l+m_l)!}} P_l^{m_l}(\cos\theta) e^{im_l\phi}. \tag{G.5}$$

Eventually, the dependencies on the three spatial coordinates separate as

$$\begin{aligned}&\psi_{nlm_l}(r,\theta,\phi)\\ &= \underbrace{f_{nl}(r)}_{r} \underbrace{\sqrt{\frac{2l+1}{4\pi}\frac{(l-m_l)!}{(l+m_l)!}} P_l^{m_l}(\cos\theta)}_{\theta} \underbrace{e^{im_l\phi}}_{\phi}\,.\end{aligned} \tag{G.6}$$

A single-particle scalar wave function in j-scheme is characterized by the set of quantum numbers n, j, π, m and m_s. The radial function $f_{nl}(r)$ in Eq (G.6) is often re-written as a function of the *reduced radial wave function* $u_{nl}(r)$

$$f_{nl}(r) = \frac{u_{nl}(r)}{r}. \tag{G.7}$$

Introducing the quantity

$$F^{\text{SPH}}_{nlm_l}(r,\theta) = u_{nl}(r)\sqrt{\frac{2l+1}{4\pi}\frac{(l-m_l)!}{(l+m_l)!}} P_l^{m_l}(\cos\theta)\,, \tag{G.8}$$

its j-scheme version is given by

$$\begin{aligned}F^{\text{SPH}}_{njm\pi t}(r,\theta,\sigma) &= \begin{pmatrix} F^{\text{SPH}}_{njm\pi t}(r,\theta,\sigma)_\uparrow \\ F^{\text{SPH}}_{njm\pi t}(r,\theta,\sigma)_\downarrow \end{pmatrix}\\ &= \begin{pmatrix} \sqrt{\frac{1}{2}+\frac{2(j-l)m}{2l+1}} F^{\text{SPH}}_{nlm-1/2}(r,\theta) \\ (-1)^{1/2+l-j}\sqrt{\frac{1}{2}-\frac{2(j-l)m}{2l+1}} F^{\text{SPH}}_{nlm+1/2}(r,\theta)\,. \end{pmatrix}\end{aligned} \tag{G.9}$$

Considering the coefficient $C^{[m\pi t]}_{njN}$ introduced in Eq. (6.4) for the change of basis between sHO and NAT, such a coefficient can be used to mix sHO quantum numbers n and j to give an expression for the deformed NAT wave functions

$$F^{\text{dNAT}}_{Nm\pi t}(r,\theta,\sigma) \equiv \sum_{nj} F^{\text{sHO}}_{njm\pi}(r,\theta,\sigma) C^{[m\pi t]}_{njN}\,. \tag{G.10}$$

This transformation conserves quantum numbers m, π and t.

Eventually re-expressing $(r,\,\theta)$ in terms of cylindrical coordinates

$$\begin{cases} r_\perp = r\sin\theta\,,\\ z = r\cos\theta\,,\end{cases} \tag{G.11}$$

previous equations can be recast in terms of such new coordinates, i.e. $F_{Nm\pi t}(r,\theta,\sigma) \equiv F_{Nm\pi t}(r_\perp,z,\sigma)$.

Figure G.1 represents selected sHO and NAT wave functions $F(r_\perp,z)$, the latter being computed in (spherical) ^{16}O, (prolate) ^{20}Ne and (oblate) ^{28}Si. While the $l=0$ wave functions in ^{16}O display a symmetry along the main diagonal of the square, deformed orbitals in ^{20}Ne and ^{28}Si are distorted in opposite ways.

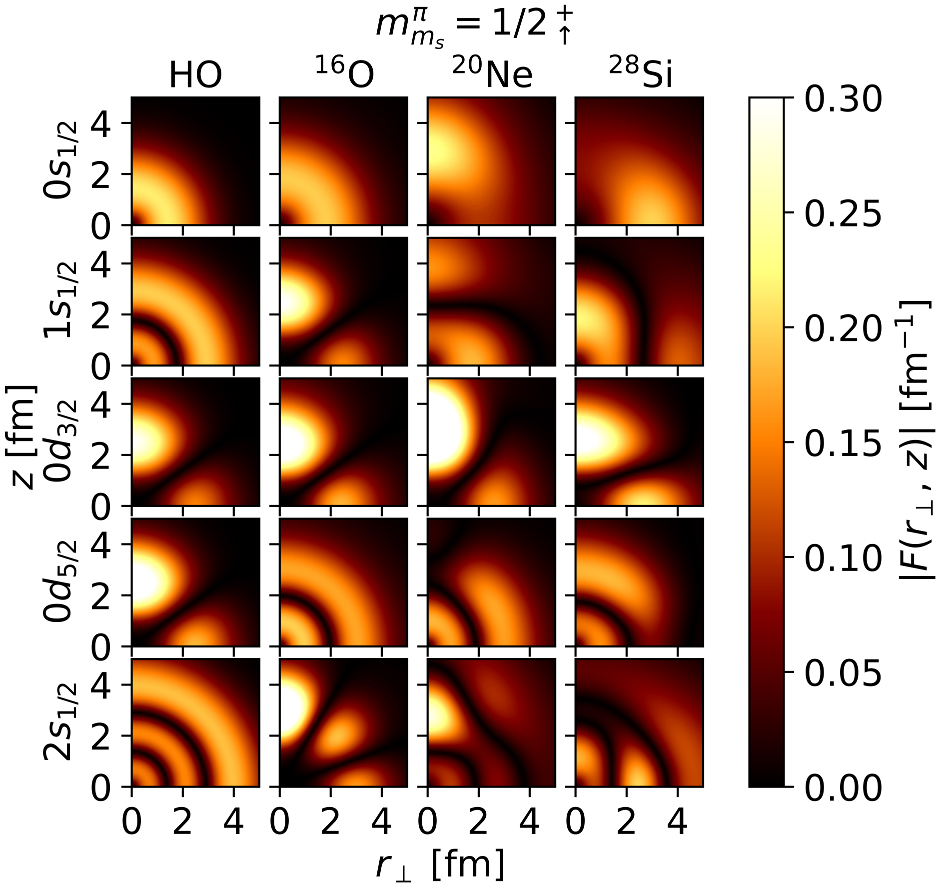

Figure G.1. Two-dimensional representation of deformed orbitals in the $[m\pi t] = [1/2{+}p]$ block. While the first column displays sHO wave functions with $\hbar\omega = 18\,\text{MeV}$ corresponding to a given set of quantum numbers, the following columns corresponds to NAT[dMBPT(2)] wave functions in three different nuclei obtained using the NNLO$_{\text{sat}}$ (bare) Hamiltonian and ordered from top to bottom according to their decreasing average occupations.

List of Figures

List of Tables

Bibliography

[1] H. -W. Hammer, S. König, and U. van Kolck. "Nuclear effective field theory: status and perspectives". In: *Rev. Mod. Phys.* 92.2 (2020), p. 025004. DOI: 10.1103/RevModPhys.92.025004.

[2] U. van Kolck. "Effective field theory of nuclear forces". In: *Prog. Part. Nucl. Phys.* 43 (1999), pp. 337–418. DOI: https://doi.org/10.1016/S0146-6410(99)00097-6.

[3] R. Machleidt and D. R. Entem. "Chiral effective field theory and nuclear forces". In: *Phys. Rep.* 503.1 (2011), pp. 1–75. DOI: https://doi.org/10.1016/j.physrep.2011.02.001.

[4] S. Weinberg. "Nuclear forces from chiral Lagrangians". In: *Phys. Lett. B* 251 (1990), pp. 288–292. DOI: 10.1016/0370-2693(90)90938-3.

[5] H. Hergert. "A Guided Tour of *ab initio* Nuclear Many-Body Theory". In: *Front. in Phys.* 8 (2020), p. 379. DOI: 10.3389/fphy.2020.00379.

[6] A. Scalesi et al. in preparation. 2024.

[7] M. Frosini et al. "Multi-reference many-body perturbation theory for nuclei: I. Novel PGCM-PT formalism". In: *Eur. Phys. J. A* 58.4 (2022), p. 62. DOI: 10.1140/epja/s10050-022-00692-z.

[8] M. Frosini et al. "Multi-reference many-body perturbation theory for nuclei: III. Ab initio calculations at second order in PGCM-PT". In: *Eur. Phys. J. A* 58.4 (2022), p. 64. DOI: 10.1140/epja/s10050-022-00694-x.

[9] S. J. Novario et al. "Charge radii of exotic neon and magnesium isotopes". In: *Phys. Rev. C* 102.5 (2020), p. 051303. DOI: 10.1103/PhysRevC.102.051303.

[10] S. K. Bogner, R. J. Furnstahl, and A. Schwenk. "From low-momentum interactions to nuclear structure". In: *Prog. Part. Nucl. Phys.* 65 (2010), pp. 94–147. DOI: 10.1016/j.ppnp.2010.03.001.

[11] A. Tichai, R. Roth, and T. Duguet. "Many-body perturbation theories for finite nuclei". In: *Front. in Phys.* 8 (2020), p. 164. DOI: 10.3389/fphy.2020.00164.

[12] T. D. Crawford and H. F. Schaefer III. "An Introduction to Coupled Cluster Theory for Computational Chemists". In: *Rev. Comput. Chem.* 14 (2000), p. 33. DOI: 10.1002/9780470125915.ch2.

[13] H. Hergert et al. "The In-Medium Similarity Renormalization Group: A novel ab initio method for nuclei". In: *Phys. Rep.* 621 (2016), pp. 165–222. DOI: https://doi.org/10.1016/j.physrep.2015.12.007.

[14] V. Somà. "Self-consistent Green's function theory for atomic nuclei". In: *Front. in Phys.* 8 (2020), p. 340. DOI: 10.3389/fphy.2020.00340.

[15] M. Bender, P.-H. Heenen, and P.-G. Reinhard. “Self-consistent mean-field models for nuclear structure”. In: *Rev. Mod. Phys.* 75 (1 Jan. 2003), pp. 121–180. DOI: `10.1103/RevModPhys.75.121`.

[16] V. Somà, T. Duguet, and C. Barbieri. “Ab initio self-consistent Gorkov-Green’s function calculations of semimagic nuclei: Formalism at second order with a two-nucleon interaction”. In: *Phys. Rev. C* 84 (6 Dec. 2011), p. 064317. DOI: `10.1103/PhysRevC.84.064317`.

[17] V. Somà, C. Barbieri, and T. Duguet. “*Ab initio* self-consistent Gorkov-Green’s function calculations of semi-magic nuclei: Numerical implementation at second order with a two-nucleon interaction”. In: *Phys. Rev. C* 89 (2 Feb. 2014), p. 024323. DOI: `10.1103/PhysRevC.89.024323`.

[18] T. Duguet. “Symmetry broken and restored coupled-cluster theory: I. Rotational symmetry and angular momentum”. In: *J. Phys. G* 42.2 (2015), p. 025107. DOI: `10.1088/0954-3899/42/2/025107`.

[19] T. Duguet and A. Signoracci. “Symmetry broken and restored coupled-cluster theory: II. Global gauge symmetry and particle number”. In: *J. Phys. G* 44.1 (2017), p. 015103. DOI: `10.1088/0954-3899/44/1/015103`.

[20] H. Hergert and R. Roth. “Treatment of the Intrinsic Hamiltonian in Particle-Number Nonconserving Theories”. In: *Phys. Lett. B* 682 (2009), pp. 27–32. DOI: `10.1016/j.physletb.2009.10.100`.

[21] A. Ekström et al. “Accurate nuclear radii and binding energies from a chiral interaction”. In: *Phys. Rev. C* 91 (5 May 2015), p. 051301. DOI: `10.1103/PhysRevC.91.051301`.

[22] A. Porro et al. “Importance truncation in non-perturbative many-body techniques: Gorkov self-consistent Green’s function calculations”. In: *Eur. Phys. J. A* 57.10 (2021), p. 297. DOI: `10.1140/epja/s10050-021-00606-5`.

[23] W. G. Jiang et al. “Accurate bulk properties of nuclei from $A = 2$ to ∞ from potentials with Δ isobars”. In: *Phys. Rev. C* 102 (5 Nov. 2020), p. 054301. DOI: `10.1103/PhysRevC.102.054301`.

[24] K. Hebeler et al. “Improved nuclear matter calculations from chiral low-momentum interactions”. In: *Phys. Rev. C* 83 (3 Mar. 2011), p. 031301. DOI: `10.1103/PhysRevC.83.031301`.

[25] D. R. Entem and R. Machleidt. “Accurate charge-dependent nucleon-nucleon potential at fourth order of chiral perturbation theory”. In: *Phys. Rev. C* 68 (4 Oct. 2003), p. 041001. DOI: `10.1103/PhysRevC.68.041001`.

[26] V. Somà et al. “Novel chiral Hamiltonian and observables in light and medium-mass nuclei”. In: *Phys. Rev. C* 101 (1 Jan. 2020), p. 014318. DOI: `10.1103/PhysRevC.101.014318`.

[27] K. Kravvaris et al. “Ab initio informed evaluation of the radiative capture of protons on 7Be”. In: *Phys. Lett. B* 845 (2023), p. 138156. DOI: `https://doi.org/10.1016/j.physletb.2023.138156`.

[28] N. Tajima. “Canonical-basis solution of the Hartree-Fock-Bogoliubov equation on a three-dimensional Cartesian mesh”. In: *Phys. Rev. C* 69.034305 (2004). DOI: `10.1103/PhysRevC.69.034305`.

[29] G. Hagen, T. Papenbrock, and D. J. Dean. “Solution of the Center-Of-Mass Problem in Nuclear Structure Calculations”. In: *Phys. Rev. Lett.* 103 (6 Aug. 2009), p. 062503. DOI: `10.1103/PhysRevLett.103.062503`.

[30] T. Miyagi. “NuHamil : A numerical code to generate nuclear two- and three-body matrix elements from chiral effective field theory”. In: *Eur. Phys. J. A* 59 (2023). DOI: `10.1140/epja/s10050-023-01039-y`.

[31] K. Hebeler et al. “Efficient calculation of chiral three-nucleon forces up to N3LO for ab initio studies”. In: *Phys. Rev. C* 91.044001 (2015). DOI: `10.1103/PhysRevC.91.044001`.

[32] A. Scalesi, C. Barbieri, and E. Vigezzi. “Expansion of one-, two- and three-body matrix elements on a generic spherical basis for nuclear ab initio calculations”. In: *Annals Phys.* 467 (2024), p. 169688. DOI: `10.1016/j.aop.2024.169688`.

[33] R. Roth et al. “Medium-Mass Nuclei with Normal-Ordered Chiral NN+3N Interactions”. In: *Phys. Rev. Lett.* 109 (5 July 2012), p. 052501. DOI: `10.1103/PhysRevLett.109.052501`.

[34] E. Gebrerufael, A. Calci, and R. Roth. “Open-shell nuclei and excited states from multireference normal-ordered Hamiltonians”. In: *Phys. Rev. C* 93.3 (2016), p. 031301. DOI: `10.1103/PhysRevC.93.031301`.

[35] M. Frosini et al. “In-medium k-body reduction of n-body operators: A flexible symmetry-conserving approach based on the sole one-body density matrix”. In: *Eur. Phys. J. A* 57.4 (2021), p. 151. DOI: `10.1140/epja/s10050-021-00458-z`.

[36] P. Ring and P. Schuck. *The Nuclear Many-Body Problem.* New-York: Springer-Verlag, 1980.

[37] G. C. Wick. “The Evaluation of the Collision Matrix”. In: *Phys. Rev.* 80 (2 Oct. 1950), pp. 268–272. DOI: `10.1103/PhysRev.80.268`.

[38] P. Arthuis et al. “ADG: Automated generation and evaluation of many-body diagrams I. Bogoliubov many-body perturbation theory”. In: *Comput. Phys. Commun.* 240 (2019), p. 202. DOI: `10.1016/j.cpc.2018.11.023`.

[39] J. Goldstone. “Derivation of the Brueckner many-body theory”. In: *Proc. R. Soc. Lond. A* 239 (Feb. 1957), pp. 267–279. DOI: `10.1098/rspa.1957.0037`.

[40] M. Frosini. “Ab initio description of doubly-open shell nuclei via a novel resolution method of the quantum many-body problem”. PhD thesis. Paris-Saclay university, 2021.

[41] M. Frosini, T. Duguet, and P. Tamagno. “Tensor factorization in ab initio many-body calculations: Triaxially-deformed (B) MBPT calculations in large bases”. `https://arxiv.org/abs/2404.08532`. 2024.

[42] T. Duguet et al. “Pairing correlations. I. Description of odd nuclei in mean-field theories”. In: *Phys. Rev. C* 65 (1 Dec. 2001), p. 014310. DOI: `10.1103/PhysRevC.65.014310`.

[43] B. Hu et al. “Ab initio predictions link the neutron skin of ^{208}Pb to nuclear forces”. In: *Nature Phys.* 18.10 (2022), pp. 1196–1200. DOI: `10.1038/s41567-022-01715-8`.

[44] T. Miyagi et al. “Converged ab initio calculations of heavy nuclei”. In: *Phys. Rev. C* 105.1 (2022), p. 014302. DOI: `10.1103/PhysRevC.105.014302`.

[45] K. Hebeler et al. “Normal ordering of three-nucleon interactions for ab initio calculations of heavy nuclei”. In: *Phys. Rev. C* 107 (2 Feb. 2023), p. 024310. DOI: `10.1103/PhysRevC.107.024310`.

[46] A. Tichai, P. Demol, and T. Duguet. “Towards heavy-mass ab initio nuclear structure: Open-shell Ca, Ni and Sn isotopes from Bogoliubov coupled-cluster theory”. In: *Phys. Lett. B* 851 (2024), p. 138571. DOI: `10.1016/j.physletb.2024.138571`.

[47] P. Arthuis, K. Hebeler, and A. Schwenk. “Neutron-rich nuclei and neutron skins from chiral low-resolution interactions”. `https://arxiv.org/abs/2401.06675`. 2024.

[48] G. Hagen et al. “Angular-momentum projection in coupled-cluster theory: Structure of ^{34}Mg”. In: *Phys. Rev. C* 105 (6 June 2022), p. 064311. DOI: `10.1103/PhysRevC.105.064311`.

[49] T. Duguet, B. Bally, and A. Tichai. “Zero-pairing limit of Hartree-Fock-Bogoliubov reference states”. In: *Phys. Rev. C* 102.5 (2020), p. 054320. DOI: `10.1103/PhysRevC.102.054320`.

[50] A. Ekström et al. “Bayesian optimization in ab initio nuclear physics”. In: *J. Phys. G: Nucl. Part. Phys.* 46.9 (July 2019), p. 095101. DOI: `10.1088/1361-6471/ab2b14`.

[51] I. Svensson, A. Ekström, and C. Forssén. “Bayesian estimation of the low-energy constants up to fourth order in the nucleon-nucleon sector of chiral effective field theory”. In: *Phys. Rev. C* 107 (1 Jan. 2023), p. 014001. DOI: `10.1103/PhysRevC.107.014001`.

[52] E. Epelbaum, H. Krebs, and U. G. Meißner. “Improved chiral nucleon-nucleon potential up to next-to-next-to-next-to-leading order”. In: *Eur. Phys. J. A* 51.5 (2015), p. 53. DOI: `10.1140/epja/i2015-15053-8`.

[53] S. Binder et al. “Ab initio calculations of medium-mass nuclei with explicit chiral $3N$ interactions”. In: *Phys. Rev. C* 87 (2 Feb. 2013), p. 021303. DOI: `10.1103/PhysRevC.87.021303`.

[54] M. Frosini et al. “Multi-reference many-body perturbation theory for nuclei: II. Ab initio study of neon isotopes via PGCM and IM-NCSM calculations”. In: *Eur. Phys. J. A* 58.4 (2022), p. 63. DOI: `10.1140/epja/s10050-022-00693-y`.

[55] R. J. Furnstahl, G. Hagen, and T. Papenbrock. “Corrections to nuclear energies and radii in finite oscillator spaces”. In: *Phys. Rev. C* 86 (3 Sept. 2012), p. 031301. DOI: `10.1103/PhysRevC.86.031301`.

[56] S. N. More et al. “Universal properties of infrared oscillator basis extrapolations”. In: *Phys. Rev. C* 87 (4 Apr. 2013), p. 044326. DOI: `10.1103/PhysRevC.87.044326`.

[57] T. Papenbrock. “Effective field theory of pairing rotations”. In: *Phys. Rev. C* 105 (4 Apr. 2022), p. 044322. DOI: `10.1103/PhysRevC.105.044322`.

[58] S. R. Stroberg et al. “Ab Initio Limits of Atomic Nuclei”. In: *Phys. Rev. Lett.* 126 (2 Jan. 2021), p. 022501. DOI: `10.1103/PhysRevLett.126.022501`.

[59] A. Tichai et al. “Bogoliubov Many-Body Perturbation Theory for Open-Shell Nuclei”. In: *Phys. Lett. B* 786 (2018), pp. 195–200. DOI: `10.1016/j.physletb.2018.09.044`.

[60] A. Signoracci et al. “Ab initio Bogoliubov coupled cluster theory for open-shell nuclei”. In: *Phys. Rev. C* 91 (6 June 2015), p. 064320. DOI: `10.1103/PhysRevC.91.064320`.

[61] R. J. Furnstahl et al. “Infrared extrapolations for atomic nuclei”. In: *J. Phys. G* 42.3 (2015), p. 034032. DOI: `10.1088/0954-3899/42/3/034032`.

[62] S. R. Stroberg et al. “A nucleus-dependent valence-space approach to nuclear structure”. In: *Phys. Rev. Lett.* 118.3 (2017), p. 032502. DOI: `10.1103/PhysRevLett.118.032502`.

[63] M. Wang et al. “The AME 2020 atomic mass evaluation (II). Tables, graphs and references*”. In: *Chin. Phys. C* 45.3 (Mar. 2021), p. 030003. DOI: `10.1088/1674-1137/abddaf`.

[64] T. Duguet et al. “Rooting the EDF method into the ab initio framework: PGCM-PT formalism based on MR-IMSRG pre-processed Hamiltonians”. In: *Eur. Phys. J. A* 59.1 (2023), p. 13. DOI: `10.1140/epja/s10050-023-00914-y`.

[65] V. Somà et al. “Moving away from singly-magic nuclei with Gorkov Green’s function theory”. In: *Eur. Phys. J. A* 57.4 (2021), p. 135. DOI: `10.1140/epja/s10050-021-00437-4`.

[66] F. Barranco et al. “Many body effects in nuclear structure”. In: *Eur. Phys. J. A* 21 (2004), pp. 57–60. DOI: `10.1140/epja/i2003-10185-0`.

[67] G. Gori et al. “Attractive and repulsive contributions of medium fluctuations to nuclear superfluidity”. In: *Phys. Rev. C* 72 (1 July 2005), p. 011302. DOI: `10.1103/PhysRevC.72.011302`.

[68] A. Pastore et al. “Microscopic calculation and local approximation of the spatial dependence of the pairing field with bare and induced interactions”. In: *Phys. Rev. C* 78 (2 Aug. 2008), p. 024315. DOI: `10.1103/PhysRevC.78.024315`.

[69] A. Idini et al. “Dyson treatment of NFT medium polarization processes in superfluid nuclei”. In: *J. Phys. Conf. Ser.* 312 (2011), p. 092032. DOI: `10.1088/1742-6596/312/9/092032`.

[70] S. Perez-Martin and L. M. Robledo. “Microscopic justification of the Equal Filling approximation”. In: *Phys. Rev. C* 78 (2008), p. 014304. DOI: `10.1103/PhysRevC.78.014304`.

[71] S. Burrello, J. Bonnard, and M. Grasso. “Application of an ab-initio-inspired energy density functional to nuclei: impact of the effective mass and the slope of the symmetry energy on bulk and surface properties”. In: *Phys. Rev. C* 103.6 (2021), p. 064317. DOI: `10.1103/PhysRevC.103.064317`.

[72] U. Vernik et al. Unpublished. 2024.

[73] E. Caurier et al. “Shell model description of isotope shifts in calcium”. In: *Phys. Lett. B* 522 (2001), pp. 240–244. DOI: `10.1016/S0370-2693(01)01246-1`.

[74] A. Tichai et al. “Open-shell nuclei from No-Core Shell Model with perturbative improvement”. In: *Phys. Lett. B* 786 (2018), pp. 448–452. DOI: `https://doi.org/10.1016/j.physletb.2018.10.029`.

[75] M. Leininger et al. “Is Moller–Plesset perturbation theory a convergent ab initio method?” In: *J. Chem. Phys.* 112 (2000), pp. 9213–9222. DOI: `10.1063/1.481764`.

[76] R. Roth and J. Langhammer. "Padé-resummed high-order perturbation theory for nuclear structure calculations". In: *Phys. Lett. B* 683.4 (2010), pp. 272–277. DOI: 10.1016/j.physletb.2009.12.046.

[77] J. Langhammer, R. Roth, and C. Stumpf. "Spectra of Open-Shell Nuclei with Padé-Resummed Degenerate Perturbation Theory". In: *Phys. Rev. C* 86 (2012), p. 054315. DOI: 10.1103/PhysRevC.86.054315.

[78] A. Tichai et al. "Hartree–Fock many-body perturbation theory for nuclear ground-states". In: *Phys. Lett. B* 756 (2016), pp. 283–288. DOI: 10.1016/j.physletb.2016.03.029.

[79] P. Demol et al. "Bogoliubov many-body perturbation theory under constraint". In: *Annals Phys.* 424 (2021), p. 168358. DOI: 10.1016/j.aop.2020.168358.

[80] P. Demol et al. "Improved many-body expansions from eigenvector continuation". In: *Phys. Rev. C* 101.4 (2020), p. 041302. DOI: 10.1103/PhysRevC.101.041302.

[81] J. M. Yao et al. "Ab Initio Treatment of Collective Correlations and the Neutrinoless Double Beta Decay of ^{48}Ca". In: *Phys. Rev. Lett.* 124 (23 June 2020), p. 232501. DOI: 10.1103/PhysRevLett.124.232501.

[82] Z. H. Sun et al. "Multiscale physics of atomic nuclei from first principles". https://arxiv.org/abs/2404.00058. Mar. 2024.

[83] O. Haxel, D. Jensen J. H, and H. E. Suess. "On the 'Magic Numbers' in Nuclear Structure". In: *Phys. Rev.* 75 (11 June 1949), pp. 1766–1766. DOI: 10.1103/PhysRev.75.1766.2.

[84] M. G. Mayer. "Nuclear Configurations in the Spin-Orbit Coupling Model. I. Empirical Evidence". In: *Phys. Rev.* 78 (1 Apr. 1950), pp. 16–21. DOI: 10.1103/PhysRev.78.16.

[85] Y. Kondo et al. "First observation of ^{28}O". In: *Nature* 620.7976 (2023). [Erratum: Nature 623, E13 (2023)], pp. 965–970. DOI: 10.1038/s41586-023-06352-6.

[86] E. M. Lykiardopoulou. in preparation. 2024.

[87] D. S. Ahn et al. "Location of the Neutron Dripline at Fluorine and Neon". In: *Phys. Rev. Lett.* 123 (21 Nov. 2019), p. 212501. DOI: 10.1103/PhysRevLett.123.212501.

[88] W. H. Dickhoff and D. Van Neck. *Many-body theory exposed!* World Scientific, 2005.

[89] W. H. Dickhoff and C. Barbieri. "Self-consistent Green's function method for nuclei and nuclear matter". In: *Prog. Part. Nucl. Phys.* 52 (2004), p. 377. DOI: https://doi.org/10.1016/j.ppnp.2004.02.038.

[90] G. Hagen et al. "Coupled-cluster computations of atomic nuclei". In: *Reports on Progress in Physics* 77.9 (2014), p. 096302. DOI: 10.1088/0034-4885/77/9/096302.

[91] A. L. Fetter and J. D. Walecka. *Quantum Theory of Many-Particle Systems.* McGraw-Hill Book Company, 1971.

[92] F. Capuzzi and C. Mahaux. "Projection Operator Approach to the Self-Energy". In: *Annals Phys.* 245.1 (1996), pp. 147–208. DOI: https://doi.org/10.1006/aphy.1996.0006.

[93] J. Schirmer, L. S. Cederbaum, and O. Walter. “New approach to the one-particle Green’s function for finite Fermi systems”. In: *Phys. Rev. A* 28 (3 Sept. 1983), pp. 1237–1259. DOI: `10.1103/PhysRevA.28.1237`.

[94] M. S. Deleuze et al. “Valence one-electron and shake-up ionization bands of carbon clusters. I. The Cn (n = 3,5,7,9) chains”. In: *J. Chem. Phys.* 111.13 (1999), pp. 5851–5865. DOI: `10.1063/1.479880`.

[95] M. S. Deleuze et al. “Ionization Bands and Electron Affinities of Mixed Boron-Nitrogen BnNn Clusters (n = 3,4,5)”. In: *J. Phys. Chem. A* 104.7 (2000), pp. 1588–1596. DOI: `10.1021/jp993232x`.

[96] F. Raimondi and C. Barbieri. “Algebraic diagrammatic construction formalism with three-body interactions”. In: *Phys. Rev. C* 97 (5 May 2018), p. 054308. DOI: `10.1103/PhysRevC.97.054308`.

[97] C. Barbieri, T. Duguet, and V. Somà. “Gorkov algebraic diagrammatic construction formalism at third order”. In: *Phys. Rev. C* 105.4 (2022), p. 044330. DOI: `10.1103/PhysRevC.105.044330`.

[98] C. Barbieri and A. Carbone. “Self-Consistent Green’s Function Approaches”. In: *An Advanced Course in Computational Nuclear Physics*. Ed. by M. Hjorth-Jensen, M. Lombardo, and U. van Kolck. Vol. 936. Lecture Notes in Physics. Springer, Cham, 2017.

[99] L. P. Gorkov. “On the energy spectrum of superconductors”. In: *Sov. Phys. JETP* 7 (1958), p. 505.

[100] Y. Nambu. “Quasiparticles and Gauge Invariance in the Theory of Superconductivity”. In: *Phys. Rev.* 117 (1960), pp. 648–663. DOI: `10.1103/PhysRev.117.648`.

[101] M. Drissi, A. Rios, and C. Barbieri. “Nambu-covariant many-body theory I: Perturbative approximations”. In: *Annals Phys.* (2024), p. 169729. DOI: `https://doi.org/10.1016/j.aop.2024.169729`.

[102] J. Schirmer and G. Angonoa. “On Green’s function calculations of the static self-energy part, the ground state energy and expectation values”. In: *J. Chem. Phys.* 91 (1989), p. 1754. DOI: `10.1063/1.457081`.

[103] V. Somà et al. “Chiral two- and three-nucleon forces along medium-mass isotope chains”. In: *Phys. Rev. C* 89 (6 June 2014), p. 061301. DOI: `10.1103/PhysRevC.89.061301`.

[104] B. R. Barrett, P. Navratil, and J. P. Vary. “Ab initio no core shell model”. In: *Prog. Part. Nucl. Phys.* 69 (2013), pp. 131–181. DOI: `10.1016/j.ppnp.2012.10.003`.

[105] F. Raimondi and C. Barbieri. “Nuclear electromagnetic dipole response with the self-consistent Green’s function formalism”. In: *Phys. Rev. C* 99 (5 May 2019), p. 054327. DOI: `10.1103/PhysRevC.99.054327`.

[106] M. Baranger. “A definition of the single-nucleon potential”. In: *Nucl. Phys. A* 149 (1970), pp. 225–240. DOI: `10.1016/0375-9474(70)90692-5`.

[107] T. Duguet et al. “Nonobservable nature of the nuclear shell structure: Meaning, illustrations, and consequences”. In: *Phys. Rev. C* 92.3 (2015), p. 034313. DOI: `10.1103/PhysRevC.92.034313`.

[108] V. M. Galitskii and A. B. Migdal. “Application of quantum field theory methods to the many body problem”. In: *Z. Eksp. Teor. Fiz.* 34 (1958), p. 139.

[109] D. S. Koltun. “Total Binding Energies of Nuclei, and Particle-Removal Experiments”. In: *Phys. Rev. Lett.* 28 (1972), p. 182. DOI: `10.1103/PhysRevLett.28.182`.

[110] *CODATA recommended values of the fundamental physical constants: 2018. Proton rms charge radius.* `https://physics.nist.gov/cgi-bin/cuu/Value?rp`.

[111] I. Angeli and K.P. Marinova. “Table of experimental nuclear ground state charge radii: An update”. In: *Atomic Data and Nuclear Data Tables* 99.1 (2013), pp. 69–95. DOI: `http://dx.doi.org/10.1016/j.adt.2011.12.006`.

[112] C. J. Horowitz and J. Piekarewicz. “Impact of spin-orbit currents on the electroweak skin of neutron-rich nuclei”. In: *Phys. Rev. C* 86 (4 Oct. 2012), p. 045503. DOI: `10.1103/PhysRevC.86.045503`.

[113] A. Cipollone, C. Barbieri, and P. Navrátil. “Chiral three-nucleon forces and the evolution of correlations along the oxygen isotopic chain”. In: *Phys. Rev. C* 92 (1 July 2015), p. 014306. DOI: `10.1103/PhysRevC.92.014306`.

[114] Y. L. Sun et al. “Restoration of the natural $E(1/2_1^+) - E(3/2_1^+)$ energy splitting in odd-K isotopes towards $N = 40$”. In: *Phys. Lett. B* 802 (2020), p. 135215. DOI: `10.1016/j.physletb.2020.135215`.

[115] T. Koiwai et al. “A First Glimpse at the Shell Structure beyond ^{54}Ca: Spectroscopy of ^{55}K, ^{55}Ca, and ^{57}Ca”. In: *Phys. Lett. B* 827 (2022), p. 136953. DOI: `10.1016/j.physletb.2022.136953`.

[116] V. Somà and T. Duguet. “On the calculation and use of effective single-particle energies. The example of the neutron $1d_{3/2}$-$1d_{5/2}$ splitting along N = 20 isotones”. In: *Phil. Trans. Roy. Soc. Lond. A* 382.2275 (2024), p. 20230117. DOI: `10.1098/rsta.2023.0117`.

[117] A. O. Macchiavelli et al. “Analysis of spectroscopic factors in ^{11}Be and ^{12}Be in the Nilsson strong-coupling limit”. In: *Phys. Rev. C* 97 (1 Jan. 2018), p. 011302. DOI: `10.1103/PhysRevC.97.011302`.

[118] A. Y. Sokolov. “Multi-reference algebraic diagrammatic construction theory for excited states: General formulation and first-order implementation”. In: *J. Chem. Phys.* 149.20 (2018), p. 204113. DOI: `10.1063/1.5055380`.

[119] K. Chatterjee and A. Y. Sokolov. “Extended Second-Order Multireference Algebraic Diagrammatic Construction Theory for Charged Excitations”. In: *J. Chem. Th. Comp.* 16.10 (2020). PMID: 32877184, pp. 6343–6357. DOI: `10.1021/acs.jctc.0c00778`.

[120] R. Roth. “Importance Truncation for Large-Scale Configuration Interaction Approaches”. In: *Phys. Rev. C* 79 (2009), p. 064324. DOI: `10.1103/PhysRevC.79.064324`.

[121] A. Tichai et al. “Natural orbitals for ab initio no-core shell model calculations”. In: *Phys. Rev. C* 99 (3 Mar. 2019), p. 034321. DOI: `10.1103/PhysRevC.99.034321`.

[122] J. Hoppe et al. “Importance truncation for the in-medium similarity renormalization group”. In: *Phys. Rev. C* 105 (3 Mar. 2022), p. 034324. DOI: `10.1103/PhysRevC.105.034324`.

[123] A. Tichai et al. “Tensor-decomposition techniques for ab initio nuclear structure calculations. From chiral nuclear potentials to ground-state energies”. In: *Phys. Rev. C* 99.3 (2019), p. 034320. DOI: `10.1103/PhysRevC.99.034320`.

[124] A. Tichai, J. Ripoche, and T. Duguet. "Pre-processing the nuclear many-body problem: Importance truncation versus tensor factorization techniques". In: *Eur. Phys. J. A* 55.6 (2019), p. 90. DOI: `10.1140/epja/i2019-12758-6`.

[125] A. Tichai et al. "Low-rank matrix decompositions for ab initio nuclear structure". In: *Phys. Lett. B* 821 (2021), p. 136623. DOI: `10.1016/j.physletb.2021.136623`.

[126] A. Tichai et al. "Low-Rank Decompositions of Three-Nucleon Forces via Randomized Projections". `https://arxiv.org/abs/2307.15572`. July 2023.

[127] E. R. Davidson. "Properties and Uses of Natural Orbitals". In: *Rev. Mod. Phys.* 44 (3 July 1972), pp. 451–464. DOI: `10.1103/RevModPhys.44.451`.

[128] T. Helgaker, P. Jørgensen, and J. Olsen. *Molecular Electron-Structure Theory.* Wiley, Chichester, 2000.

[129] M. A. Caprio, P. Maris, and J. P. Vary. "Coulomb-Sturmian basis for the nuclear many-body problem". In: *Phys. Rev. C* 86.034312 (2012). DOI: `10.1103/PhysRevC.86.034312`.

[130] G. Puddu. "A new single-particle basis for nuclear many-body calculations". In: *J. Phys. G: Nucl. Part. Phys.* 44.105104 (2017). DOI: `10.1088/1361-6471/aa8234`.

[131] G. A. Negoita. "Ab initio nuclear structure theory". PhD thesis. Paris-Saclay university, 2010. DOI: `10.31274/etd-180810-2422`.

[132] A Bulgac and M M Forbes. "Use of the discrete variable representation basis in nuclear physics". In: *Phys. Rev. C* 87.051301 (2013). DOI: `10.1103/PhysRevC.87.051301`.

[133] C. F. Bender and E. R. Davidson. "A Natural Orbital Based Energy Calculation for Helium Hydride and Lithium Hydride". In: *Jour. Phys. Chem.* 70.8 (Aug. 1966), pp. 2675–2685. DOI: `10.1021/j100880a036`.

[134] P. Jeffrey Hay. "On the calculation of natural orbitals by perturbation theory". In: *Jour. Chem. Phys.* 59.5 (Sept. 1973), pp. 2468–2476. DOI: `10.1063/1.1680359`.

[135] P. J. Fasano et al. "Natural orbitals for the ab initio no-core configuration interaction approach". In: *Phys. Rev. C* 105.5 (2022), p. 054301. DOI: `10.1103/PhysRevC.105.054301`.

[136] J. Hoppe et al. "Natural orbitals for many-body expansion methods". In: *Phys. Rev. C* 103.1 (2021), p. 014321. DOI: `10.1103/PhysRevC.103.014321`.

[137] A. Scalesi et al. "Impact of correlations on nuclear binding energies". In: (June 2024).

[138] P.-O. Lowdin. "Expansion Theorems for the Total Wave Function and Extended Hartree-Fock Schemes". In: *Rev. Mod. Phys.* 32 (1960), p. 328. DOI: `10.1103/RevModPhys.32.328`.

[139] V. Rotival and T. Duguet. "New analysis method of the halo phenomenon in finite many-fermion systems. First applications to medium-mass atomic nuclei". In: *Phys. Rev. C* 79 (2009), p. 054308. DOI: `10.1103/PhysRevC.79.054308`.

[140] T. Duguet et al. "Pairing correlations. II. Microscopic analysis of odd-even mass staggering in nuclei". In: *Phys. Rev. C* 65 (1 Dec. 2001), p. 014311. DOI: `10.1103/PhysRevC.65.014311`.

[141] T. Miyagi et al. private communication. 2024.

[142] T. Duguet et al. “Lowest-order contributions of chiral three-nucleon interactions to pairing properties of nuclear ground states”. In: *Mod. Phys. Lett. A* 25 (2010), pp. 1989–1992. DOI: `10.1142/S0217732310000812`.

[143] T. Duguet. “Pairing in finite nuclei from low-momentum two- and three-nucleon interactions”. In: (Apr. 2012). DOI: `10.1142/9789814412490_0017`.

[144] F. Barranco and R.A. Broglia. “Correlation between mean square radii and zero-point motions of the surface in the Ca isotopes”. In: *Phys. Lett. B* 151.2 (1985), pp. 90–94. DOI: `https://doi.org/10.1016/0370-2693(85)91391-7`.

[145] B. C. He and S. R. Stroberg. “Factorized Approximation to the IMSRG(3)”. `https://arxiv.org/abs/2405.19594`. 2024.

[146] D. A. Varshalovich, A. N. Moskalev, and V. K. Khersonskii. *Quantum Theory of Angular Momentum*. World Scientific, 1988.